

# Side-Emitting Fibers: Targeted Light Scattering in Optical Fibers

– Kumulative Dissertation –

zur Erlangung des akademischen Grades  
doctor rerum naturalium

vorgelegt dem Rat der Chemisch-Geowissenschaftlichen Fakultät  
der Friedrich-Schiller-Universität Jena

von Aaron Reupert

geboren am 10.06.1983 in Waldshut

Gutachter 1: Prof.Dr.-Ing. Lothar Wondrazcek Jena

Gutachter 2: Prof.Dr. Stefan Nolte Jena

Gutachter 3: Prof.Dr.-Ing. Edda Rädlein Ilmenau

Tag der Verteidigung: 9. März 2022

*Some vices miss what is right because they are deficient, others because they are excessive, in feelings or in actions, while virtue finds and chooses the mean.*

Aristotle, Nichomachean Ethics



## Abstract

Light scattering in optical fibers was initially regarded as an unwanted loss mechanism, which dampens the desired light transmission. But when used and controlled appropriately, it can transform the optical fiber into a linear light source with customizable emission properties: a side-emitting fiber. Besides their decorative application in interior light design and glowing fabrics, they have several applications in the volumetric illumination of turbid media, where light is extinguished on very short distances due to scattering and absorption. This situation is encountered in microalgae cultivation, laser dentistry, endoscopy antimicrobial application, or interstitial photodynamic therapy. Here, their high surface-to-volume ratio increases the extent of the illuminated volume, and their flexibility allows easy access even into complicated geometries.

Side emitting fibers are light sources with special angular and longitudinal emission characteristics, not generally encountered in other light sources. Even though several types of these fibers are currently manufactured and applied, the effect of these properties on the performance of the fiber has not been studied systematically, and techniques to influence these properties are only scarcely known. As it turns out, these light sources have an untypical angular emission behavior; though they emit radiation in all directions like a diffuse light source, the emission is preferentially directed forward concerning the light's propagation direction in the fiber. This is caused by the scattering mechanism, which is the underlying cause of the side emission. Also, the fiber's surface emission may decrease exponentially or vary along the fiber.

In brief, this dissertation finds that the fiber's surface emission influences the generated light field close to the fiber, and the angular emission influences the field at some distance to it. This means that volumetric illumination in turbid media will be mostly concerned with the surface-emission property, while free space illumination application will also be concerned with the angular property. The dissertation then demonstrates how customized surface and angular-emission profiles can be constructed from light scattering modifications, so-called scattering centers, that can easily be generated in commercial optical fibers with focused femtosecond laser irradiation. These modifications are refractive index distortion filled with stochastic fluctuations. The dissertation shows how their number density in the fiber influences surface emission, how their refractive index difference to the surrounding and their volume influence their scattering power, and how the spectral distribution of their fluctuations and their outer shape influence the angular emission.

The contribution of this dissertation to the literature on side-emitting fibers is twofold; first, it will show how the fiber's emission parameters, namely the longitudinal and the angular emission of light, will influence the generated light field in the proximity and the far field of the fiber for free-space propagation. Second, it will show how to customize the emission properties by using femtosecond laser-generated scattering centers: Arranging these building blocks can generate customized longitudinal emission profiles. Furthermore, it will derive an electromagnetic model of the

scattering behavior of these modifications to show how their stochastic properties, shape, and volume affect the angular emission profile and their scattering power. Building upon this knowledge, future work will be able to create side-emitting fibers with customizable angular and longitudinal emission just by laser processing of regular, commercial glass fibers without any further mechanical handling.

## Acknowledgments

I would like to thank Lothar Wondraczek for giving me the opportunity, the facilities, and the support to write this paper, and Stephan Nolte for his support, making his labs available and introducing me to a top-notch co-author.

I would also like to thank my main coauthor, Maximilian Heck, for performing the femtosecond laser writing experiments with me and contributing to my work, and Eva Schlindwein for encouraging me and teaching me how to write scientifically.

Thomas Kittel, I thank for teaching me microscopy and glass technology and discussing my experimental ideas, Dietmar Güttler for building and programming the instrumentation and fruitful discussions, and Jan Schröder for contributing to my last paper and working with me on the Tailored Optical Fibers project.

I would also like to thank all my students for a great and unforgettable teaching experience and my colleagues for the supportive work environment.

Last but not least, I would like to thank my parents, Karen Reupert, Sascha Berst, Achim Auersch, and Andrea Berst, for their financial and moral support during the completion of my studies and dissertation.





# Contents

<b>List of Figures</b>	<b>x</b>
<b>List of Symbols</b>	<b>xi</b>
<b>1 Introduction</b>	<b>1</b>
1.1 Side-Emitting Fibers . . . . .	2
1.2 The Evolution of Side-Emitting Fiber Research . . . . .	3
1.3 Light Scattering in Optical Fibers . . . . .	5
1.3.1 Radiometric Scattering Model . . . . .	7
1.3.2 Electrodynamic Scattering Model . . . . .	11
<b>2 Results and Discussion</b>	<b>14</b>
2.1 The Radiation Field of a Side-Emitting Fiber . . . . .	14
2.2 The Longitudinal Emission of a Side-Emitting Fiber . . . . .	16
2.3 The Angular Emission of a Side-Emitting Fiber . . . . .	17
<b>3 Publications</b>	<b>19</b>
3.1 Radiation from Side-Emitting Optical Fibers and Fabrics . . . . .	19
3.2 Side-Emission Properties of Scattering Centers . . . . .	36
3.3 Angular Scattering Pattern of Refractive Index Modifications . . . . .	51
<b>4 Summary</b>	<b>63</b>
<b>5 Zusammenfassung</b>	<b>68</b>
<b>Bibliography</b>	<b>73</b>
<b>A Theoretical Background</b>	<b>78</b>
A.1 The Plane Wave . . . . .	78
A.2 The Phasor . . . . .	79
A.3 The Wave Equation . . . . .	80
A.4 The Relation Between Electric and Magnetic Field . . . . .	82
A.5 The Superpositions of Plane Waves . . . . .	82
A.6 Pointing Vector . . . . .	84
A.6.1 Time Average Energy Flux Density of a Plane Wave . . . . .	85
A.7 The Radiometric Approximation . . . . .	86
A.7.1 Electromagnetic Derivation of Radiometry . . . . .	88
A.8 The Volume Current Method . . . . .	91

<b>B</b>	<b>Experimental Methods</b>	<b>97</b>
B.1	Longitudinal Measurement: Motorized Integrating Sphere . . . . .	97
B.2	Angular Measurement: Fourier-Microscopy . . . . .	99
B.2.1	The Fourier Transform Property of an Objective . . . . .	104
<b>C</b>	<b>Supplement: Published Version</b>	<b>106</b>
C.1	Radiation from Side-Emitting Optical Fibers and Fabrics . . . . .	106
<b>D</b>	<b>Anhang</b>	<b>118</b>
D.0.1	Selbständigkeitserklärung . . . . .	118

# List of Figures

1.1	Side-emitting fibers discussed in this thesis: (a) Commercial side-emitting plastic optical fiber. (b) Side-emitting fiber tip with laser-induced scattering centers in the fiber core. (c) Textile band with 19 side-emitting plastic optical fibers. Samples (a) and (c) were provided by the company RAMMER GmbH in Ohorn, Germany. Sample (b) was produced as a part of this dissertation. . . . .	2
1.2	Longitudinal and angular light emission from an optical fiber. Longitudinal emission changes as a function of the $z$ -position on the fiber. Angular emission changes as a function of the emission angle $\theta$ , relative to the fiber $z$ -axis. . . . .	3
1.3	Schematics of the refractive index profile of an optical fiber with the radius $R$ and a core-cladding-coating structure. The refractive index is higher in the core and than in the cladding. The coating can have a higher or a lower refractive index than the cladding, depending on the application. . . . .	6
1.4	Total internal reflection schematics: If the refractive index $n_1$ is larger than $n_2$ , so $n_2 < n_1$ , then light rays are refracted away from the surface normal (dashed), obeying Snell's law $n_1 \sin \alpha_1 = n_2 \sin \alpha_2$ . The incident beam is also partially reflected. If the incident angle becomes critical, $\sin \alpha_{crit} = n_2/n_1$ , the refracted ray is parallel to the boundary, and all light is reflected. All rays with incident angles larger $\alpha_{crit}$ can not refract, and therefore, all power in these rays is reflected. . . . .	7
1.5	Calculated examples of the transmission (a) and emission (b) of a side-emitting fiber with constant scattering coefficients. Larger scattering coefficients lead to a larger decrease in transmission and emission. Smaller scattering coefficients lead to more transmitted and thus not emitted light flux. . . . .	8
1.6	Calculated examples of transmission (a) and emission (b) of a side-emitting fiber with constant scattering coefficient and light coupling on both sides: one at 0 mm and one at 1000 mm. The dashed line shows an example of the two superimposed profiles. Fibers with larger scattering coefficients still show inhomogeneous emission; smaller ones are now more homogeneous. The unemitted light flux is twice as large as with one-sided coupling. . . . .	10

1.7	Calculated examples for the transmission (a) and emission (b) of a side-emitting fiber with constant scattering coefficient and fiber end face-mirror ( $r = 1$ ). The dashed line shows an example of the two superimposed profiles. Fibers with small scattering coefficients improve their performance because the unemitted light flux is greatly diminished. . . . .	11
A.1	Schematics of the wave vector $\mathbf{K}$ . For a plane wave, the scalar product $\mathbf{K}\mathbf{r}_1 = \mathbf{K}\mathbf{r}_2$ is constant for all points $\mathbf{r}_i$ on a plane of constant phase.	79
A.2	Solid angle element $d\Omega$ is defined as the projection of $dA_2$ on the unit sphere around $dA_1$ with the radius $\hat{\mathbf{s}}$ . The projection is calculated by dividing $dA_2$ through the square of the magnitude of the connection vector $\mathbf{d}$ and multiplying by the inclination $\cos\Theta_2 = \hat{\mathbf{n}}_2\hat{\mathbf{s}}$ . . . . .	87
A.3	Solid angle element $d\Omega$ corresponding to the area element $d^2s$ is its projection on the unit sphere, $d^2s = \hat{\mathbf{n}}\hat{\mathbf{s}}d\Omega = \cos\Theta d\Omega$ . . . . .	90
B.1	Integrating sphere with motorized scanning stage for longitudinal emission measurement of side-emitting fibers. The light emitted from the fiber segment $\Delta z$ is distributed homogeneously on the sphere wall through multiple diffuse reflections. The flux on the wall, measured with a fiber-coupled spectrometer, is proportional to the flux emitted by the fiber segment. The baffle protects the detector from direct fiber illumination. After measurement, the sphere is moved to a different $z$ -position, and the measurement is repeated. In this way, the $z$ -dependent emission is recorded. . . . .	98
B.2	Schematics of a ray crossing an aplanatic objective obeying the Abbe-sine condition: Rays emerging from the front focal plane under an angle $\beta$ are converted into rays parallel to the optical axis with the distance $h$ by refraction on the reference sphere with the radius $f$ , the focal length. . . . .	100
B.3	Fourier-microscope images of an opal glass scattering standard (provided by QSIL GmbH Quarzschmelze Ilmenau) in two polarization directions $0^\circ$ and $90^\circ$ with an NA = 1.3 microscope objective oil immersion $n_0 = 1.51$ . The two polarization directions show different back focal plane apodization: $0^\circ$ towards the top and bottom edge; $90^\circ$ towards the left and right edge. The dark outer ring marks region undetectable due to the restrictions in opening angle to $\beta_{max} = \arcsin(1.3/1.51) = 59.4^\circ$ . . . . .	103

## List of Symbols

$\phi$	light flux or light power [W]
$F$	light flux density or irradiance [W/m <sup>2</sup> ]
$L$	radiance [W/(m <sup>2</sup> sr)]
$I$	radiant intensity [W/sr]
$\alpha$	coefficient of absorption [1/mm]
$\sigma$	coefficient of scattering [1/mm]
$\lambda$	wavelength [nm]
$\omega$	angular frequency [rad/s]
$k$	magnitude of the wave vector [1/m]
$n$	refractive index
$\Delta n$	refractive index difference
$dV, d^3r$	volume element [m <sup>3</sup> ]
$V_0$	volume [m <sup>3</sup> ]
$dA, d^2r$	area element [m <sup>2</sup> ]
$A$	area [m <sup>2</sup> ]
$d^2K$	area element in wave vector space [1/m <sup>2</sup> ]
$\Omega$	solid angle [sr]
$d\Omega$	solid angle element [sr]
NA	numerical aperture
$f$	focal length [m]
$h$	distance to optical axis [m]
$\beta$	angle with optical axis [rad]
$t$	time [s]
$x, y, z$	Cartesian spacial coordinates [m]
$R$	fiber radius [m]
$\epsilon$	electric permittivity [F/m]
$\mu$	magnetic permeability [H/m]
$c$	speed of light [m/s]
$\epsilon_0$	vacuum permittivity [F/m]
$\mu_0$	vacuum permeability [H/m]
$c_0$	vacuum speed of light [m/s]
$\hat{e}_i$	unit vector
$\hat{n}$	surface normal vector, unit length
$\nabla$	nabla operator
$\mathbf{r}$	location vector [m]
$\mathbf{K}$	wave vector [1/nm]
$\hat{s}$	direction of the wave vector (unit length)
$\mathbf{E}$	electric field strength [V/m]
$\mathbf{H}$	magnetic field strength [A/m]
$\mathbf{A}$	vector potential [Tm]
$\mathbf{j}$	current density [A/m <sup>2</sup> ]
$\mathbf{F}$	flux density vector [W/m <sup>2</sup> ]
$\mathbf{S}$	Poynting vector [W/m <sup>2</sup> ]



# 1 Introduction

Bringing light into dark spaces is a common challenge encountered in densely populated urban environments to improve living conditions [1]. Here, cheap, abundant, and healthy sunlight is blocked, scattered, or absorbed by concrete structures, leading to detrimental outcomes in well-being and psychological health due to low light exposure for the inhabitants [2]. Similarly, in the microcosm, light can not penetrate far into turbid media, where the light flux is extinct within a short distance due to scattering and absorption. In bioreactors, for example, a thick algae suspension blocks the light and thereby reduces the photosynthetically active volume [3]; a similar situation is encountered for microbes in soil [4], or waste water treatment [5]. In photomedical applications, this effect is caused by the highly scattering and absorbing human tissue. This occurs, for example, in external [6] or internal phototherapy [7] for cancer treatment as well as phototherapy of the neurological disorder epilepsy [8]. In all cases, absorption and scattering extinct the light flux, leading to overexposure close to the irradiated surface and underexposure shortly beneath it.

A linear light source based on targeted light scattering in optical fibers is a promising candidate for these applications, offering low cost and high flexibility. Here, the fiber serves both to guide the light to the desired location and to diffuse it there by scattering. In principle, it has two major advantages over conventional electric light sources in these applications. First, as a fiber, it is thin, long and flexible: it has a small footprint but a high surface-to-volume ratio. This increases the actively illuminated volume even in difficult geometries, as many fibers can be placed inside it simultaneously. Second, it separates the actual electric light source from the emitter, making it chemically and electrically safe without expensive sealing and eliminating thermal loads from the source. These properties make these fibers ideal candidates for sensitive phonic applications in the human brain [7, 8], or for a simple application in an urban environment, where they can be used to transport sunlight from rooftops to low-lying areas and subways, providing inexpensive daylight distribution.

This thesis is organized as follows, in the continuation of the introduction, the basic theoretical concepts and problems concerning side-emitting fibers and their generated light field are presented. In Chapter 2 the results of the experiments and calculations from the publications are described and discussed separately for each publication. The publications that make up the bulk of this dissertation are presented in Chapter 3. In Chapter 4, the results and discussion are summarized with emphasis on their application in the research and development of side-emitting fibers. The german translation of the summary can be found in Chapter 5. Derivations of all theoretical concepts used in the publications but not explicitly required for

understanding are provided in Appendix A. The two experimental methods used primarily to characterize side-emitting fiber radiation are derived and described in Appendix B.

## 1.1 Side-Emitting Fibers

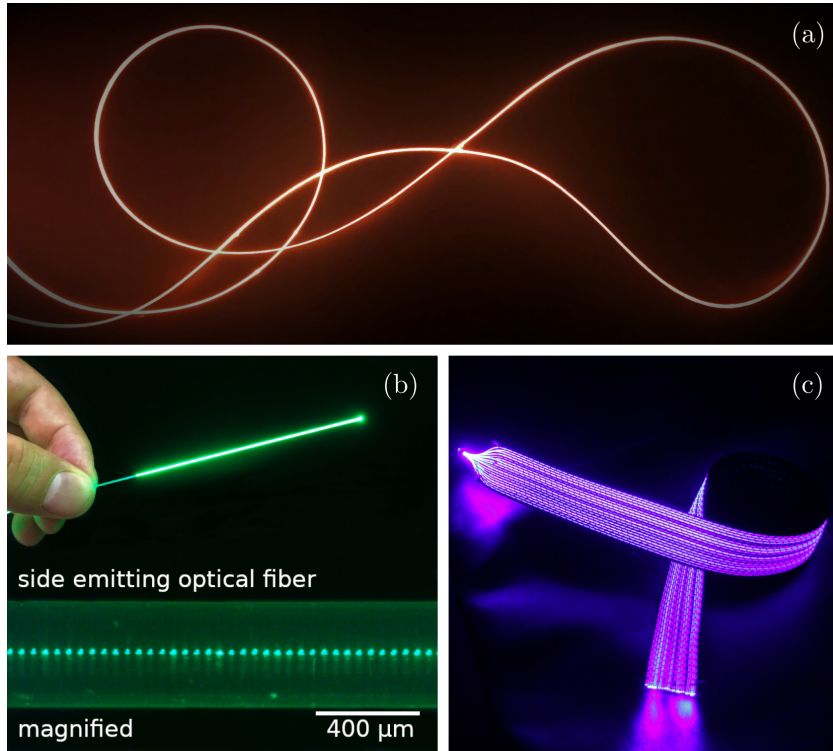


**Figure 1.1:** Side-emitting fibers discussed in this thesis: (a) Commercial side-emitting plastic optical fiber. (b) Side-emitting fiber tip with laser-induced scattering centers in the fiber core. (c) Textile band with 19 side-emitting plastic optical fibers. Samples (a) and (c) were provided by the company RAMMER GmbH in Ohorn, Germany. Sample (b) was produced as a part of this dissertation.

Like optical fibers that guide light by total reflection from start to end, side-emitting fibers guide light but emit some guided radiation through their cylindrical outer surface, the transparent fiber coating. To an observer, they look like a luminous, flexible, linear light source. Examples can be seen in Fig. 1.1. This section introduces how they work in principle and what their important properties are for application and adaptation.

The respective length of a side-emitting fiber can range from a few centimeters, in the case of a glowing fiber tip, to several - or hundreds of - meters. When light is coupled into the fiber end, the fiber lights up and appears to glow, but with varying



intensity along the fiber depending on the fiber type. An exponential decrease in brightness from beginning to end is very common in most commercial products. This characteristic is called *longitudinal dependency* of the fiber (surface) emission (Fig. 1.2a).

If we observe the luminous fiber from different angles, we will find that it is fainter when we observe it at a low angle along the same direction as the light propagation in the fiber. As we increase the angles with the fiber axis, it gets brighter and becomes brightest when we observe it in the direction towards the fiber light coupling, where the light from the light source is coupled into the fiber. This effect is called the *angular dependence* of the emitted radiation (Fig. 1.2b).

On the one hand, the geometry of the light source is an elongated cylinder, but it can be twisted and bent within the limits of its mechanical stability. On the other hand, the aspect ratio of the fiber is very high since the diameter is much smaller than the length. Therefore, it may be advantageous to neglect the diameter altogether and simply treat it as a *line source* rather than a *cylinder source*. This leads to a great simplification in their mathematical handling.

These four properties, namely longitudinal and angular emission and line or cylinder source, will be the primary areas of investigation for side-emitting optical fibers in this work and, as we shall see, are sufficient for understanding and characterizing the radiation properties of side-emitting fibers.

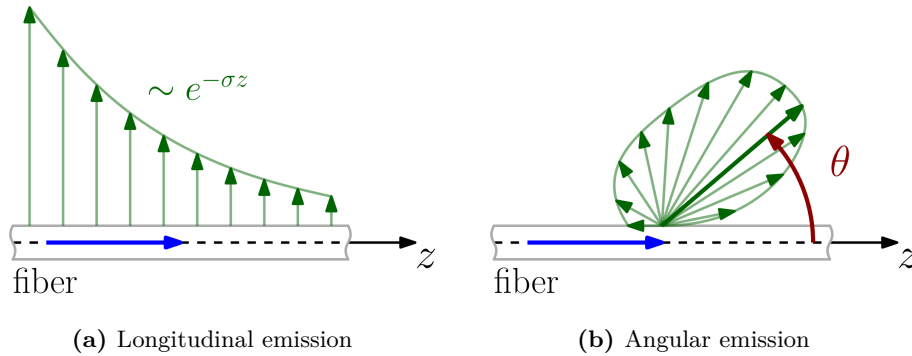


**Figure 1.2:** Longitudinal and angular light emission from an optical fiber. Longitudinal emission changes as a function of the  $z$ -position on the fiber. Angular emission changes as a function of the emission angle  $\theta$ , relative to the fiber  $z$ -axis.

## 1.2 The Evolution of Side-Emitting Fiber Research

Side emitting fibers were first described 31 years ago, and since then, they have an ever-expanding scope of manufacturing and application to novel problems. This section presents the evolution of research on side-emitting fibers to explain what is

## 1 Introduction

already known about their performance, properties, and possible customization and to identify shortcomings in current streams of exploration.

Research on side-emitting fibers can be traced to work on the diffusive optical fiber end by Hasselgren *et al.* (1990) [9], who first described it with regard to possible application to photodynamic therapy. They made their side-emitting fiber by removing the cladding from an ordinary optical fiber and replacing it with a mixture of high refractive index epoxy and very high refractive index  $\text{TiO}_2$  powder. The epoxy's refractive index was higher than the fiber core, which removed the conditions of total internal reflection (see Fig. 1.4) and led to light leaking out in the cladding. There, it was subsequently scattered into the fiber's surrounding by the  $\text{TiO}_2$  powder with very high refractive index.

Spigulis *et al.* gradually build on this idea by extending the tip to a fiber, formulating radiation models, and moving from medical to textile applications in a series of publications from 1994 to 2005 [10, 11, 12, 13, 14]. Here, Spigulis *et al.* identified the exponential decrease in emitted light flux on the surface of the fiber with length as the major challenge in using longer fibers and proposed three different ways to overcome it [14]: The first is to couple the light into the fiber from both sides. The second is to attach a mirror to one end of the fiber to reuse transmitted light. The third is to increase the scattering coefficient as the fiber length increases to compensate for decreasing emission. Although Hasselgren *et al.* and Spigulis *et al.* investigated the angular emission of their light-scattering fiber tips, its impact on applications has not been thoroughly discussed. Older studies that preceded the side-emitting fibers argued that purely radial irradiation could increase the depth of penetration into tissue [15, 16].

In the present day, side-emitting fibers have become increasingly popular, but some areas still need further research. In 2003, Time magazine declared side-emitting fibers as one of "the coolest invention of the year" [10]. This was accompanied by the production and patenting of several types of side-emitting fibers [17, 18, 19] and their dissemination in various fields of application. This process continues to the present day. Although these light sources are not uncommon today, little is known about the radiation field they produce, which would be necessary for a technical application. These fibers represent a new class of light sources that lie between directional and diffuse and have an emissivity that varies longitudinally. Therefore, classical intuitive assumptions such as cosine-dependent (Lambertian) angular emission and constant surface emissivity cannot be taken as valid. Related to this is also the reverse problem: How must the fiber parameters, such as longitudinal and angular radiation, be optimized to produce a specific light field for a specific application?

Existing routes of theory development have focused on simulating the radiation field of side-emitting fibers. For instance, efforts to calculate the generated radiation field have been focused on the medical application, where the distribution of light from the fiber through the complicated human tissue is calculated with the aid of sophisticated Monte Carlo methods [20] or numerical solutions of the diffusion equation [21]. Monte Carlo methods have also been used to calculate the emitted

radiation from the fiber [22, 23]. While simulation methods offer insight into the respective problem, a general understanding of the radiation behavior as a function of fiber parameters is not obtained. Endruweit *et al.* [24] and Pan *et al.* [25], on the other hand, used an approach based on the radiometric approximation to derive the radiation field in terms of its flux density for a cylindrical, Lambertian fiber. This approach provides the ability to insert measured fiber parameters into the model. This work will also follow the radiometric approach, but we will additionally include angular-dependent emission, and we will compare a cylindrical source to a simpler line source model. We will show that the longitudinal dependence is dominant near the fiber and the angular dependence is dominant in the far field. In addition, the line and cylindrical source models show almost no difference in their predicted radiation field.

Efforts on customization of the radiation field have mostly been focused on tailoring the longitudinal properties of side-emitting fibers. The influence of the longitudinal and the angular properties on the fiber's radiation field shows that it is necessary to control both features to generate customized side-emitting fibers for the desired application. Tailoring the longitudinal emission profile is barely explored: The Corning company produces side-emitting fibers with an approximate flat emission profile which can be several meters in length. Their tunable scattering coefficient is based on the twisting and stretching of gas bubbles [17], which unfortunately makes them hard to splice to normal optical fibers. Vesselov *et al.* [26] designed a customizable light-diffusing fiber tip based on long-period fiber gratings and a coating with scattering particles. Bisyarin *et al.* [27] developed a 400 m long homogeneously side-emitting fiber base on a very small increase in scattering caused by adjusting the fiber drawing temperature. This method enables very long, but not short, homogeneous side-emitting fibers.

Regarding the angular-dependent emission, research has focused on achieving Lambertian emission. It is visually more pleasing in lighting applications, but other reasons are barely discussed or are quietly assumed to be beneficial to the application. The possibility of influencing the emission angle of optical fiber radiation is only explored in the relatively different context of tilted fiber gratings [28, 29, 30]; no effort has been made until now to apply something similar to side-emitting fibers.

Regardless of the radiation field property we want to influence, they are all based on the scattering process within the optical fiber that couples the guided light out of the fiber and radiates it into the environment. Therefore, in order to influence the radiation field, we must first understand and control light scattering in optical fibers.

## 1.3 Light Scattering in Optical Fibers

Light scattering in optical fibers is the physical process underlying the operation of most side-emitting fibers. It determines their performance by causing, for example, an exponential decrease in surface emission with increasing distance from the light

## 1 Introduction

input for homogeneously scattering fibers. In this section, we provide an overview of the subject and show how most phenomena in side-emitting fibers can be understood by a relatively simple radiometric approach using a first-order linear differential equation. Here, the light within the fiber is described only by the transmitted power, not by the harmonic eigenmodes [31] of the guided electromagnetic waves. This approach is more accessible than electrodynamic models, which are necessary for a deeper understanding of the scattering process itself, which will be discussed in the following section.

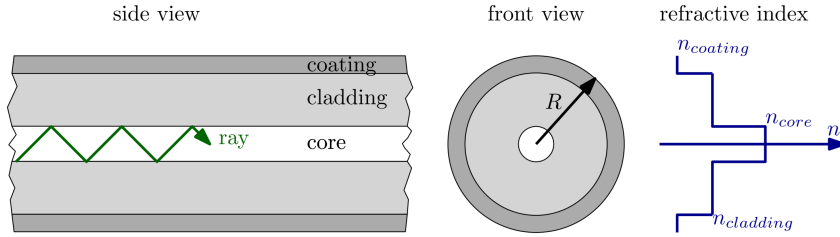


**Figure 1.3:** Schematics of the refractive index profile of an optical fiber with the radius  $R$  and a core-cladding-coating structure. The refractive index is higher in the core and than in the cladding. The coating can have a higher or a lower refractive index than the cladding, depending on the application.

Optical fibers are made to guide light and, in their most basic form, have a cylindrical shape with a core-shell structure, as shown in Fig. 1.3. The principle mode of operation is total internal reflection of light, outlined in Fig. 1.4: when a light ray attempts to cross a boundary from a high refractive index material to a low refractive index material, it is refracted and reflected. However, if the incident angle is larger than a critical angle  $\alpha_{crit}$ , all of its power is reflected, and none is refracted. This phenomenon is called total internal reflection. In an optical fiber, the core consists of a high refractive index material, and the cladding (shell) consists of a low refractive index material. Light rays propagating in the core can not cross the boundary to the cladding if their angle with the boundary normal is larger than the critical angle  $\alpha_{crit}$ . Since the core has a closed and symmetric boundary, each subsequent reflection of the ray is the same. This results in the effect that a light ray can be trapped in the core by total internal reflection, compelled to follow the fiber wherever it may lead.

In general, light scattering occurs in optical fibers where a deviation distorts the ideal core-shell structure, causing guided light to leave the core and radiate into the environment. Conversely, an ideal straight fiber would experience no losses other than absorption [32]. Macroscopic deviations such as fiber curvatures and loops, which occur in practice, result in scattering losses. Microscopic deviations such as microcurvatures due to stresses between the coating and the fiber, oscillation of the core-shell boundary due to fiber fabrication, and refractive index distortions such as bubbles or particles also cause light scattering.

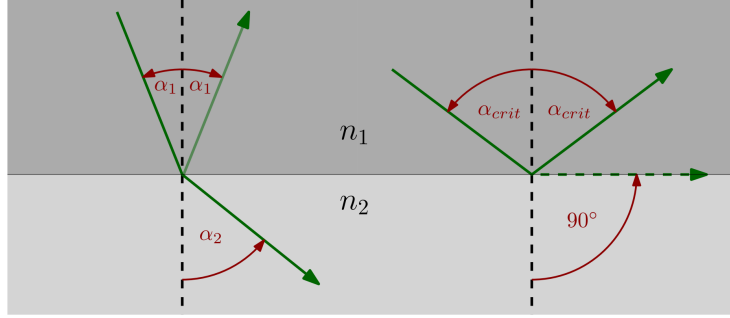


**Figure 1.4:** Total internal reflection schematics: If the refractive index  $n_1$  is larger than  $n_2$ , so  $n_2 < n_1$ , then light rays are refracted away from the surface normal (dashed), obeying Snell's law  $n_1 \sin \alpha_1 = n_2 \sin \alpha_2$ . The incident beam is also partially reflected. If the incident angle becomes critical,  $\sin \alpha_{crit} = n_2/n_1$ , the refracted ray is parallel to the boundary, and all light is reflected. All rays with incident angles larger  $\alpha_{crit}$  can not refract, and therefore, all power in these rays is reflected.

### 1.3.1 Radiometric Scattering Model

A general understanding of the loss of scattered light and its relationship to the emissivity of the fiber surface can be obtained from a simplified radiometric model: The decrease in light flux at a point in the core per unit length  $-\frac{d\phi}{dz}$  is proportional to the flux  $\phi$  at that point, which interacts with the loss process. The positive  $z$ -direction is chosen as the longitudinal axis of the fiber and the direction of light propagation. The constant of proportionality, which represents the fraction of flux that is lost from the transmission, is the sum of absorption and scattering, with their respective wavelength-dependent coefficients  $\alpha(\lambda)$  and  $\sigma(\lambda)$ . The first-order linear differential equation

$$\frac{d\phi}{dz} = -(\alpha + \sigma)\phi(z) , \quad (1.1)$$

that summarizes this behavior is called the Lambert–Beer law. It can be integrated, after separation of variables, to yield

$$\phi(z) = \phi_0 \exp \left\{ - \int_0^z [\alpha(z') + \sigma(z')] dz' \right\} . \quad (1.2)$$

Here  $\phi_0$  is the initial flux at the beginning of the fiber. This simple model can be applied to single and multi-mode side-emitting fibers if a steady-state power distribution [32, 31] can be assumed. Otherwise, every mode would have its own scattering loss coefficient. Then the energy exchange would have to be regarded as a coupled system of differential equations, with one equation for every mode.

The emitted flux per unit length will be the scattered fraction  $-\frac{d\phi}{dz} = \sigma\phi(z)$ , since the absorbed fraction of the flux is converted to heat. The scattered flux per unit

## 1 Introduction

length  $dz$  is equal to the total emitted flux of the fiber segment  $dz$ . If we divide the emitted flux  $-d\phi$  by the emitting area  $dA = 2\pi R dz$  of the fiber with radius  $R$ , we obtain the emitted flux per area, the emissivity

$$M(z) = -\frac{d\phi}{dA} = \frac{-1}{2\pi R} \frac{d\phi}{dz} = \frac{\sigma\phi(z)}{2\pi R} . \quad (1.3)$$

To better understand the consequences of these equations, we use this model to derive the exponentially decaying emission of a side-emitting fiber with a constant scattering coefficient, as well as the scattering coefficient of a fiber with constant emission. Then we use it to discuss the effect of different light coupling strategies:

Suppose we have a good quality fiber material with negligible absorption ( $\alpha \approx 0$ ) but homogeneously ( $\sigma \approx \text{const.}$ ) distributed scattering centers, as in a commercial side-emitting fiber, then Eq. (1.2) can be integrated. The result is a  $z$ -dependent exponential decay of the transmitted and emitted flux in the fiber

$$\phi(z) = \phi_0 \exp\{-\sigma z\} , \quad (1.4)$$

$$M(z) = \frac{-1}{2\pi R} \frac{d\phi}{dz} = \frac{\sigma\phi_0}{2\pi R} \exp\{-\sigma z\} , \quad (1.5)$$

which is plotted in Fig. 1.5.

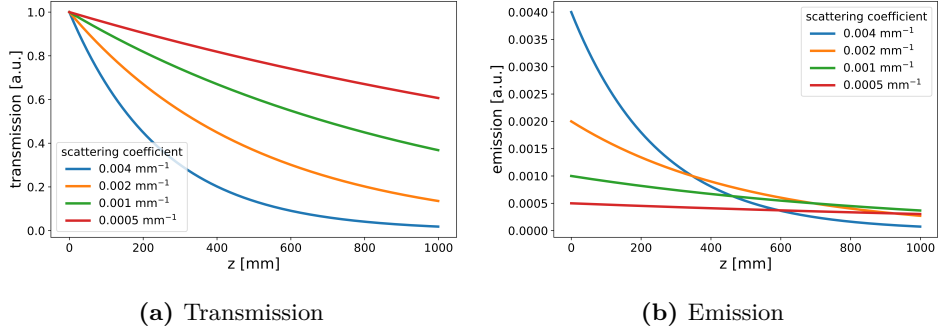


**Figure 1.5:** Calculated examples of the transmission (a) and emission (b) of a side-emitting fiber with constant scattering coefficients. Larger scattering coefficients lead to a larger decrease in transmission and emission. Smaller scattering coefficients lead to more transmitted and thus not emitted light flux.

This example shows the important property that the exponential emission of side-emitting fibers, which leads to an inhomogeneous visual illumination impression, occurs naturally and fundamentally. Therefore, all cheaply manufactured side-emitting fibers with constant scattering coefficient will suffer from this deficiency. Compensating for this effect is therefore the greatest challenge in the manufacture of side-emitting fibers with adjustable emission profiles.

In Figure 1.5 we see calculated plots for the transmitted and emitted light flux for larger and smaller scattering coefficients in the loss-range of  $4 \text{ m}^{-1}$  to  $0.5 \text{ m}^{-1}$  to

visualize different emission and transmission behaviors. If the scattering is constant, both the transmission and the emission of fiber surface decays exponentially. A large scattering coefficient will lead to a large emission at the start of the fiber, which decays on a short distance. All guided light is emitted but very unevenly. A smaller scattering coefficient stretches the exponential function and results in a flatter emission profile. Unfortunately, much light is transmitted through the fiber and is lost at the fiber end, and is not used for emission.

If one wants a relatively constant emission but also wants to be economical and use as much light as possible in emission, one needs to have a changing scattering coefficient  $\sigma$ . The functional dependence of the scattering coefficient  $\sigma$  for constant emission can also be calculated using the radiometric model. Constant emission  $M(z) = \text{const.}$  means, if we neglect absorption loss  $\alpha \approx 0$ , that the flux change rate in the fiber core must be constant  $\frac{d\phi}{dz} = -\phi_0 C_0$  and thus by integration  $\phi(z) = \phi_0(1 - C_0 z)$ . Setting this equal to Eq. (1.5) and again neglect absorption loss  $\alpha \approx 0$ , we obtain after logarithmization and subsequent differentiation,

$$\sigma(z) = \frac{1}{z - C} , \quad (1.6)$$

as the functional dependency of  $\sigma(z)$  with  $C = 1/C_0$ . To determine the constant  $C$ , one can define how much flux is transmitted through fiber length  $z_{max}$ . For example, if we require zero transmission  $0 = \phi_0(1 - C_0 z_{max})$ , the constant would be  $C = z_{max}$ . But this will be hard to achieve in praxis because, according to Eq. (1.6), it will require the scattering coefficient to go to infinity  $\sigma \rightarrow \infty$ . So one would rather look first, which maximum scattering coefficient  $\sigma_{max}$  is achievable and what is the desired length  $z_{max}$ . Then by applying Eq. (1.6), we get

$$C = z_{max} + \frac{1}{\sigma_{max}} . \quad (1.7)$$

These calculations show that the property of constant side emission is not so easily achievable. It depends on the maximum scattering coefficient  $\sigma$  one can generate inside the fiber and also the ability to tune it. In reality, this is additionally complicated by absorption loss and the core-cladding structure of the fiber, as we will see in Chapter 3.

A more straightforward method, already introduced by Spigulis *et. al* [14], to get a more homogeneous emission is to apply the light-coupling to both sides of the fiber or to use a fiber end face mirror, which reflects unused, transmitted light back into the fiber. To obtain the transmission and emission profile for double coupling, we use Eq. (1.5) and the principle of superposition by adding a second exponential with the same amplitude and decay constant to the transmission profile, which runs in the opposite direction. Then the resulting functional dependency is

$$\phi(z) = \phi_0 (\exp \{-\sigma z\} + \exp \{-\sigma(z_{max} - z)\}) . \quad (1.8)$$

As before, the emission behaves proportional to the flux and is calculated according to Eq. (1.3). We see in Fig. 1.6 that the transmission and emission are now, in

## 1 Introduction

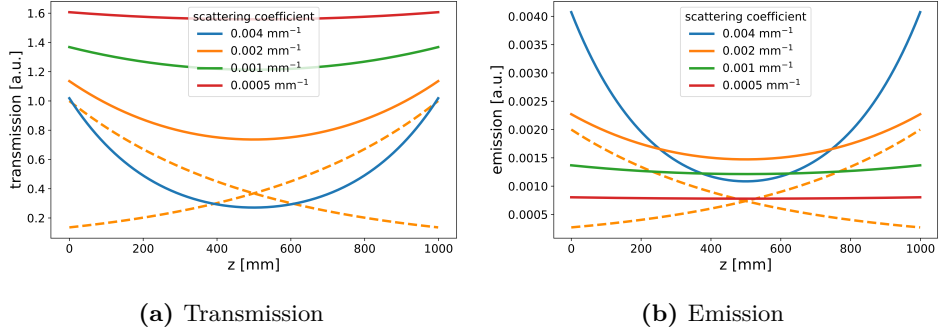


**Figure 1.6:** Calculated examples of transmission (a) and emission (b) of a side-emitting fiber with constant scattering coefficient and light coupling on both sides: one at 0 mm and one at 1000 mm. The dashed line shows an example of the two superimposed profiles. Fibers with larger scattering coefficients still show inhomogeneous emission; smaller ones are now more homogeneous. The unemitted light flux is twice as large as with one-sided coupling.

all cases, symmetric to the middle of the fiber, and most fibers, except the highly scattering one, show a more or less flat profile. This easy technique comes at the cost of double the light sources and couplings; also, double the light flux is lost at the fiber end.

The flux transmission for the end face mirror is derived similarly by superposition, but the amplitude of the added exponent is now the transmitted flux  $\phi_0 \exp\{-\sigma z_{max}\}$  times a reflection coefficient  $r$

$$\phi(z) = \phi_0 (\exp\{-\sigma z\} + r \exp\{-\sigma z_{max}\} \exp\{-\sigma(z_{max} - z)\}) \quad (1.9)$$

$$= \phi_0 (\exp\{-\sigma z\} + r \exp\{-\sigma(2z_{max} - z)\}) \quad (1.10)$$

the emission is again calculated according to Eq. (1.3).

The calculated profiles are shown in Fig. 1.7. Here we see that fibers with low scattering losses benefit most from this technique, since in their case, there is a significant transmitted flux that can be reused. Due to the geometry, the light essentially passes through a fiber twice as long, therefore, the unemitted fraction becomes  $r \exp\{-2\sigma z_{max}\}$ , the square of the value without a mirror times its reflectivity. This effect and the fact that this technique requires the same amount of light couplings as the basic variant make this the most economical strategy, provided a highly reflective fiber end is feasible.

This purely phenomenological treatment, presented in this subsection, helps to understand the general emission behavior of a side-emitting fiber and the problems for lighting applications attached to it. Here we have seen that the exponential decay in emission is a natural consequence of the differential equation that governs the absorption and scattering process. It is, therefore, the main challenge in customization. Unfortunately, this basic model can not describe the angular emission



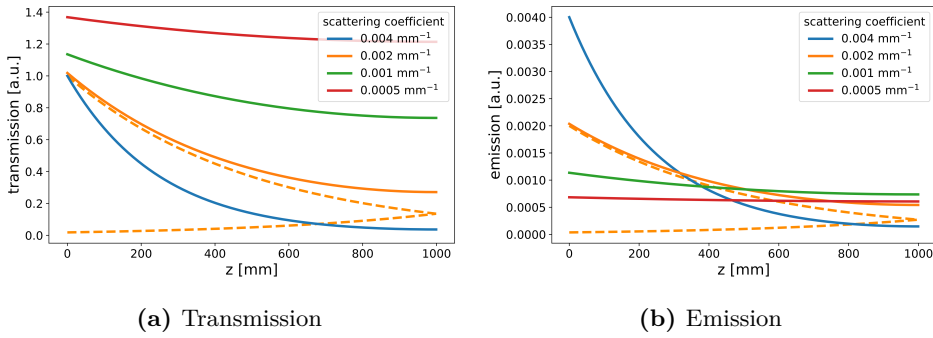


**Figure 1.7:** Calculated examples for the transmission (a) and emission (b) of a side-emitting fiber with constant scattering coefficient and fiber end face-mirror ( $r = 1$ ). The dashed line shows an example of the two superimposed profiles. Fibers with small scattering coefficients improve their performance because the unemitted light flux is greatly diminished.

behavior; for that, we need a more sophisticated electrodynamic scattering model, which will be outlined in the next subsection.

### 1.3.2 Electrodynamic Scattering Model

A deeper understanding of the scattering process is gained from electrodynamics. Here, the guided electric field  $\mathbf{E}_0$  of the light in the fiber induces a polarization current in a refractive index distortion, which in turn radiates light: this is the scattering process. The volume current method allows determining the angular dependency of the scattered radiation and the scattering power. The derivation is sketched here briefly and will continue in the publication in Section 3.3. The detailed mathematical derivation of this *volume current method* can be found in Appendix A.8.

We return to the idea that the ideal core-shell fiber is lossless and has a refractive index distribution  $n_0$  as shown in Fig. 1.3; we can identify and summarize all kinds of (micro) deviations as a distortion  $\Delta n$  of the ideal refractive index distribution. Then the actual fibers refractive index distribution  $n$  is the sum

$$n(\mathbf{r}) = n_0(\mathbf{r}) + \Delta n(\mathbf{r}) \quad (1.11)$$

of idealized fiber plus distortions. Now we take a look at the time free vector wave equation for the electric field strength vector field  $\mathbf{E}$  (vectors are denoted in boldface),

$$\nabla^2 \mathbf{E} + n^2 k^2 \mathbf{E} = i \mu_0 \omega \mathbf{j} . \quad (1.12)$$

We see that the electromagnetic wave with the wavenumber  $k$  is driven by the current density  $\mathbf{j}$ . Here,  $i$  is imaginary unit,  $\mu_0$  is the magnetic permeability of vacuum and  $\omega$  is the angular frequency. The Laplacian  $\nabla^2$  stands for the second

## 1 Introduction

partial derivative in all 3 spacial coordinates. When we observe the wave far from the source, the wave equation becomes homogeneous

$$\nabla^2 \mathbf{E} + n^2 k^2 \mathbf{E} = 0 . \quad (1.13)$$

Now we insert the distorted refractive index distribution Eq. (1.11) in Eq. (1.13) and split the electric field into the sum  $\mathbf{E} = \mathbf{E}_0 + \mathbf{E}_s$  of a guided wave  $\mathbf{E}_0$  which is a solution of the homogeneous Helmholtz equation Eq. (1.13) and the scattered radiation  $\mathbf{E}_s$ . If we insert this in Eq. (1.13) and neglect the term of higher order in  $\Delta n$  we obtain

$$\nabla^2 \mathbf{E}_0 + n_0^2 k^2 \mathbf{E}_0 + 2n_0 \Delta n k^2 (\mathbf{E}_0 + \mathbf{E}_s) + \nabla^2 \mathbf{E}_s + n_0^2 k^2 \mathbf{E}_s = 0 . \quad (1.14)$$

The sum of the two leading terms on the left-hand side are, by definition, Eq. (1.13) ( $n = n_0$ ) and therefore zero. What remains can be written in the form of the vector wave equation

$$\nabla^2 \mathbf{E}_s + n_0^2 k^2 \mathbf{E}_s = -2n_0 \Delta n k^2 (\mathbf{E}_0 + \mathbf{E}_s) \approx -2n_0 \Delta n k^2 \mathbf{E}_0 . \quad (1.15)$$

In this approximation, the electric field inside the scattering center is dominated by the guided radiation  $\mathbf{E}_0 + \mathbf{E}_s \approx \mathbf{E}_0$ . When we compare this equation to Eq. (1.12), we can see that the scattered radiation is driven by the interaction of the guided electric field with the refractive index perturbation, the source term on the right-hand side. The source can also be written in the form of Eq. (1.12), so we get the result that the scattered radiation is driven by a current density,

$$\mathbf{j} = 2i\omega n_0 \Delta n \epsilon_0 \mathbf{E}_0 \quad (1.16)$$

which, as it turned out, is caused by the interaction of the original guided field  $\mathbf{E}_0$  with the refractive index perturbation. Here,  $\epsilon_0$  is the dielectric permittivity of vacuum.

The point of view has two advantages: First, because the  $\mathbf{E}_0$  field is guided in the fiber, its contribution outside of the fiber is zero, so the electric field that is observed outside is just the scattered fraction  $\mathbf{E}_s$ . Second, the actual refractive index difference between core and cladding is small, so we can now use the solution for the vector wave equation in a homogeneous medium as an approximate solution to get the equations for the far field scattered radiation. The derivation of the equations for the scattered radiation is located in Appendix A.8. In summary the result for the electric and magnetic field strength is

$$\mathbf{E}_s = i\omega \hat{\mathbf{e}}_r \times (\hat{\mathbf{e}}_r \times \mathbf{A}_f) \quad (1.17)$$

$$\mathbf{H}_s = -\frac{ink}{\mu_0} (\hat{\mathbf{e}}_r \times \mathbf{A}_f) \quad (1.18)$$

Where  $\mathbf{A}_f$  is the far field vector potential at the point  $\mathbf{r} = r\hat{\mathbf{e}}_r$  from a superposition of spherical wavelets caused by the currents  $\mathbf{j}(\mathbf{r}')$  enclosed in the volume  $V_0$

$$\mathbf{A}_f(\mathbf{r}) = \frac{\mu_0}{4\pi} \frac{e^{in_0kr}}{r} \int_{V_0} e^{-in_0k\hat{\mathbf{e}}_r \cdot \mathbf{r}'} \mathbf{j}(\mathbf{r}') dV' . \quad (1.19)$$

$\mathbf{j}$  is zero outside of  $V_0$  so we could replace the limits of integration with infinity. Then we would immediately see that the far field vector potential  $\mathbf{A}_f$  is the Fourier transform of the current density inside  $V_0$ . This mathematical property will be very useful in deriving the scattering of the stochastic femtosecond laser-induced scattering centers because it interacts very nicely with convolutions, autocorrelations, and stochastic processes.

Another, more exact, method to solve the scattering problem is mode coupling. In mode-coupling theory, the incident and the scattered field are described with a set of cylindrical eigenmodes. These propagate like a plane wave in  $z$ -direction ( $\propto \exp\{-k_z z\}$ ) and are standing waves or harmonics in radial direction, fulfilling the boundary conditions at the fiber surface and in infinity. This results in a discrete set of bound modes and a continuous set of radiation modes. These modes are all orthogonal to each other, meaning, normally, they can not exchange energy. Only when there is a distortion  $\Delta n$  in the fiber, these modes couple, and energy is transferred; for example, from a bound mode to a radiation mode. This is the scattering process in mode-coupling theory, but it is too complicated for practical use in the scope of this thesis. Other works have shown that the volume current method and mode coupling theory are in good agreement except for low scattering angles [28].

Other derivations and theoretical concepts used in the publications, such as the plane wave expansion, the radiometric approximation, and the derivation of the volume current method, have been moved to the end of this thesis for the interested reader. They are not necessary to understand the publications but show the concepts on which they are based and how these concepts can be derived from Maxwell's equations.

## 2 Results and Discussion

This dissertation aims to understand the functioning of side-emitting fibers as a light source based on the fiber's parameters and then control the parameters to adjust the fiber performance. The considered parameters are the longitudinal emission and the angular emission; Section 2.1 discusses their influence on the radiation field. This will show that the longitudinal property dominates the light field close to the fiber; Section 2.2 shows how this property can be customized with femtosecond laser-induced scattering centers. The angular emission of these scattering centers influences the far field of the fiber; Section 2.3 describes how it is related to the scattering properties of the laser modification.

### 2.1 The Radiation Field of a Side-Emitting Fiber

Side-emitting fiber or fiber fabrics generate the radiation field discussed in this thesis depending on their emission properties. This section presents and discusses how it can be measured and calculated. First, it will show the measurement results of the longitudinal or angular property of the side-emitting fiber radiation. Then, these will be inserted into a radiometric model to calculate the generated radiation field of a side-emitting fiber and then compared with measurements of the radiation field.

When light from a green laser diode was coupled into commercial side-emitting fiber with a constant scattering coefficient, the fiber lit up and looked like a linear light source. Visually, the fiber shows a strong emissivity close to the light coupling, which declines strongly in a short distance and then remains relatively constant. The measured longitudinal emission profile followed a bi-exponential function (sum of two exponentials), with two decay functions and amplitudes. One exponent decays on a short distance of 200 mm, then the second one takes over, which decays comparatively slow.

The perceived brightness changes for the observer if the fiber is seen from different angles: if it is viewed in the direction of light propagation, it is relatively dim compared to when viewed from the opposite direction, or perpendicular to the fiber axis. A measurement of the angular emission showed that the light is preferentially directed forward, with a maximum of emission in between  $32^\circ$  and  $37^\circ$  with respect to the direction of light propagation in the fiber.

The light emitted from a textile band of 19 similar fibers was projected onto a scattering screen parallel to the band at different distances. The radiation distribution on the screen showed a similar bi-exponential decay in scattered radiation as a single fiber, with a maximum close to the laser-coupling. This maximum broadens and moves downwards towards the dim end of the fiber band when the

distance between band and screen was increased.

Radiometric models of line sources and cylinder sources calculated the radiation distribution of the fiber band on the scattering screen from the measured longitudinal and angular fiber parameters. The calculated distribution showed qualitatively the same characteristics, namely bi-exponential decay and downward movement of the maximum, as the radiation pattern on the scattering screen. When the measured angular dependency was replaced by a homogeneous Lambertian cosine dependence, the radiation distribution close to the fiber remained the same. However, the downwards movement of the maximum with increasing distance did not occur.

### Discussion

The bi-exponential longitudinal emission behavior indicates that light is coupled in the cladding and the core simultaneously; the two states have a different scattering coefficient, which results in the sum of two exponentials for the declining emissions. In this case, we assumed that the light in cladding experiences more attenuation because it interacts with the fiber surface and its imperfections. The two amplitudes of the exponents are related to the fraction of light that is coupled into the core compared to the cladding. The sharp drop in emission at the start is visually unpleasant and may lead to overexposure. An absorber could block it, or more effort could be made to put light only into the fiber core with better coupling.

The angular scattering behavior gives insight into the spectrum of the refractive index fluctuations in the fiber responsible for the side emission effect. Refractive index fluctuations with a smaller wavelength than the scattered light cause back-scattering, and fluctuations with longer wavelength cause forward scattering [31, 32]. This shows that in the spectral distribution of these wavelengths, the longer wavelength must be dominant.

The comparison of the calculated with the measured radiation shows that the radiation near the fibers is dominated by the longitudinal emission property of the surface. Here, Lambertian or measured angular emission make almost no difference in the prediction of the radiation field. In the far field, however, angular dependence plays a role: it projects the radiation field downward. Therefore, the maximum of radiation is moving to the bottom of the screen with increasing distance. Furthermore, almost no difference between a line source and a cylinder source could be calculated or observed.

Different illumination strategies for the fiber fabric were calculated, aiming at more homogeneous illumination. Spigulies *et al.* [14] already proposed double coupling and fiber end-face mirror. Here, alternating coupling between adjacent fibers with and without end mirrors, were also tested as alternative schemes. All variants resulted in a more homogeneous radiation field. Nevertheless, the alternating methods provided the most homogeneous fields, although they required the same amount of coupling as the basic one-sided variant.

In conclusion, for the studied case of free space radiation, the line source approximation can safely be used to calculate the radiation field. In the proximity

of the fiber, it is even sufficient to use it together with the Lambertian emission approximation, and only the longitudinal surface-emission has to be considered. This is important for application where the fiber is in direct contact with the illuminated medium. In the far field, the angular dependence of the surface emission must be considered to obtain an accurate description of the radiation field. This is important when the fiber is used as a more classical light source. The presented models can be used to calculate the fiber performance from two parameters for different applications. Fiber manufacturers should make these parameters available in catalogs for lighting designers.

### 2.2 The Longitudinal Emission of a Side-Emitting Fiber

This section shows how side-emitting fibers with a tailored emission profile can be fabricated from a commercial optical fiber by focused femtosecond laser radiation. The femtosecond laser was focused in the fiber core to induce a light scattering refractive index distortion: a scattering center, precisely positioned with a motorized stage. We used two placement methods to show how changing the number density of the scattering centers affects the scattering coefficient. First, we choose a constant distance, and second, we continuously decreased the distance with each subsequent modification. The result of laser irradiation in both cases was a localized ellipsoidal refractive index fluctuation in the fiber core. They were invisible to the naked eye but observable under the microscope with phase contrast. When light was coupled into the fiber, these distortions lit up because they scatter guided light out of the core toward the observer.

The modified section of the fiber was several centimeters long. We measured the transmission of the fiber after each modification and obtained the transmission spectra. It showed bi-exponential decay with an increasing number of scattering centers for both methods of positioning. From the outside, it looked like a glowing fiber segment but with changing emissivity. Measurement of the longitudinal emission profile showed a bi-exponential decay for modifications with constant spacing (similar to transmission) and a U-shaped emission profile for modifications with decreasing spacing.

#### Discussion

The experimental observations can be understood and described with basic radiometric considerations. The bi-exponential decay is caused by two dominant scattering mechanisms, one for the fiber core and one for the fiber cladding: Initially, the core contains all light, but when it is scattered on the first scattering centers, it is not only emitted into the surrounding, it also enters into the cladding. There, the light can still propagate and interact with the scattering centers when passing through the core. These cladding modes are spread out more and have less energy density in the core, so they are less affected by the scattering centers and lose power more slowly.

These phenomena can be described with a three-level energy exchange model that takes into account the coupling of the guided light in the fiber core with the cladding and free space. This model consists of three coupled differential equations whose analytical solution yielded the desired bi-exponential function in transmission and emission. The model was fitted to the transmission and emission spectra for constantly spaced scattering centers. It was also able to predict the longitudinal emission performance for scattering centers with decreasing distances from the transmission measurement. We fitted the transmission data with the model and extracted the scattering coefficients. Then we inserted them in the emission model together with the known positions of the scattering center and reproduced the resulting U-shaped emission profile with adequate accuracy compared to the measurement.

In addition, to predict the emission of the fiber segment, we showed that it is possible to shape the emission profile into arbitrary shapes: The U-shape showed that all desired properties, namely decreasing, constant, and increasing emission along the fiber, can be achieved with the right scattering center distance. This paves the way to fully customizable emission patterns.

## 2.3 The Angular Emission of a Side-Emitting Fiber

This subsection investigates the angular emission properties of the scattering centers introduced in the last subsection experimentally and theoretically. For this purpose, the modified fiber segment was immersed in refractive index matching oil and placed under a microscope where the scattering centers could be observed. Their far field scattering pattern could be studied in the back focal plane of the microscope objective (Fourier-microscopy, see Appendix B.2) when light was coupled into the fiber. Additionally, an approximate electrodynamic scattering model was derived, describing the scattering pattern as the sum of several convolutions of the Fourier-transform of modified volume with the spectral densities of the stochastic processes.

The shape of the scattering center resembles a flat ellipsoid whose interior is filled with stochastic refractive index fluctuations. When light is coupled into the fiber, the refractive index distortions light up because they scatter guided light towards the observer. The back-focal plane observation revealed that one modification's far field scattering pattern has a grainy structure: a speckle pattern. An average of the patterns of 80 modifications yielded the enveloping scattering distribution, which showed that the scattering was more intense for small scattering angles with the fiber axis. Unlike the commercial fiber in air from Section 2.1, there was no maximum emission angle. Additionally, the experiment showed a variation in scattering power around the fiber that was correlated with the shape of the scattering center: when we looked at the flat side of the scattering center, the scattering was brighter than when we looked at the small side.

### Discussion

The outer shape of the scattering center is formed by the refraction of the focused femtosecond laser beam on the cylindrical fiber surface, resulting in this flattened focal spot. The fluctuations inside the modification are caused by the overlap of several femtosecond laser pulses at the same spot, resulting in an evolution of the refractive index fluctuations. The fluctuations also extend to the surface of the modification, which is also stochastically deformed for the same reason.

For a deeper understanding of the scattering process, I developed an approximate electromagnetic scattering model based on the volume current method introduced in Section 1.3.2. It showed that the superposition of spherical wavelets originating from inside the volume of the scattering center causes the far field scattering pattern. The source is a volume current created by the interaction of the guided light with the refractive index distortion. This analysis showed that the speckle pattern is the power spectrum of the volume current. Furthermore, it showed that a three-dimensional Fourier transform relates the volume of the modification and the scattering pattern. The associated stochastic fluctuations act as a convolution of the Fourier transform with its power spectrum.

This model helped to understand that the origin of the forward scattering property is the power spectrum of the refractive index fluctuations: longer wavelength than the scattered light cause forward-scattering, and shorter wavelength cause back-scattering [32, 31]. That means laser processing predominately causes fluctuations with longer wavelengths. Also, the shape of the scattering center plays a role: the reciprocal scaling property [33] of the Fourier transform causes the scattering power to be larger perpendicular to the small side and smaller perpendicular to the broadside, which causes the variation of scattering power around the fiber.

This property could be easily exploited to influence the azimuth scattering dependency around the fiber by changing the outer shape of the scattering center, for example, by rotating the fiber during the writing process [34]. In this way, one can generate rotational symmetric scattering patterns; other shapes are also possible. Unfortunately, influencing the forward scattering property is not as easy since one would have to control the power spectra of the refractive index fluctuations. One possibility would be to intentionally write a grating structure like an imperfect fiber Bragg grating. Or one could focus the laser beam better and thus cut off larger frequencies, in which case the spectrum would be dominated by the outer shape of the scattering center.



## 3 Publications

### 3.1 Radiation from Side-Emitting Optical Fibers and Fiber Fabrics: Radiometric Model and Experimental Validation

Aaron Reupert, Jan Schröder, and Lothar Wondraczek. “Radiation from Side-Emitting Optical Fibers and Fiber Fabrics: Radiometric Model and Experimental Validation.” In: *Advanced Photonics Research* (Apr. 2021). Submitted

Side-emitting optical fibers are diffuse light sources that emit guided light through their cladding. Here, we derive two models to predict the generated radiation field: one for the case of a cylinder source and one for a line source. Our approach is based on the radiometric approximation and considers longitudinal and angle-dependent emission. Experimental validation is provided for the model parameters and the radiation field. We show that the longitudinal characteristic is relevant in proximity to the emitter’s surface and that the angular dependency determines the far field of emission. Comparison to the experiment shows that the cylinder source model allows for only slightly more accurate prediction at the cost of significantly higher computational effort. A combination of model and measurements is then used as a tool to predict the illumination performance of side-emitting fibers and fiber fabrics.

#### Remarks to the notation

In this publication, the vectors were denoted by an arrow above the symbol, e.g.  $\vec{A}$ . The light flux density or irradiance was denoted by its standard representation  $E$  and  $\vec{E}$ , not  $F$  and  $\mathbf{F}$  as in Appendix A.7.

#### Remarks to the publication

This paper, which is the submitted version, was published during the review period of this dissertation. Compared to the submitted version, the published version includes changes in the theory section to clarify the radiometric model and its derivation. Also, the vector notation has been changed from the arrow notation  $\vec{A}$  to the bold notation  $\mathbf{A}$ , which is more consistent with the dissertation. The published version can be found in Appendix C.1.

# Radiation from Side-Emitting Optical Fibers and Fiber Fabrics: Radiometric Model and Experimental Validation

Aaron Reupert, Jan Schröder, Lothar Wondraczek\*

Otto Schott Institute of Materials Research,  
Friedrich-Schiller-Universität Jena,  
Fraunhoferstr. 6, 07743 Jena, Germany  
E-mail: lothar.wondraczek@uni-jena.de

Keywords: *side emitting optical fiber, glowing optical fiber, line source, radiometry, optical fiber fabrics, optical fiber illumination*

Side-emitting optical fibers are diffuse light sources that emit guided light through their cladding. Here, we derive two models to predict the generated radiation field: one for the case of a cylinder source and one for a line source. Our approach is based on the radiometric approximation and considers longitudinal and angle-dependent emission. Experimental validation is provided for the model parameters and the radiation field. We show that the longitudinal characteristic is relevant in proximity to the emitters surface and that the angular dependency determines the far field of emission. Comparison to the experiment shows that the cylinder source model allows for only slightly more accurate prediction, at the cost of significantly higher computational effort. A combination of model and measurements is then used as a tool to predict the illumination performance of side-emitting fibers and fiber fabrics.

## 1 Introduction

Side-emitting optical fibers provide a means to illuminate spaces where common light sources face limitations, for example, in penetration depth, thermal load or volumetric homogeneity. These optical fibers emit a fraction of the guided light through their cladding, acting as a diffuse line source that is separated from the actual light emitter. This makes them easy to deploy, for example, in aquatic or highly humid environments. Additionally, they are thin, long, and flexible which enables easy implementation even in tricky geometries.

Different methods of fabrication and light coupling are established for side-emitting fiber made from inorganic glasses or plastics e.g. [1, 2, 3, 4]. Typically, refractive index distortions (*e.g.* bubbles or particles) are introduced into the fiber to scatter light. Here, the standard case of homogeneously distributed scatterers results in an exponential decay in emission strength alongside the fiber, due to the Lambert-Beer law. In addition, the scattering process causes light emission which is preferentially forward-directed. Both properties result in inhomogeneous illumination; their specific effect on the radiation field is largely unknown.

Previous efforts to model the radiation field assumed that the fiber light emission was constant over all angles (Lambertian emission) [5, 6] or used a stochastic Monte Carlo approach [7, 8]. Building on these methods, we now treat the side-emitting fiber as exhibiting angular scattering properties in between directional and diffuse, combined with a non-uniform longitudinal light emittance profile. Both of these characteristics are obtained from measurements. We will use this approach to discuss the generated radiation field in proximity of the emitting surface, and in the far field.

The primary aim of this work is to develop a parametric model of the radiation field surrounding the fiber. This will be shown in Section 2. Experimental methods of measuring the model parameters are presented in Section 3. The results of these measurements are presented in Section 4, and are subsequently compared to the calculated radiation field in Section 5. Finally, in the same section, we will use the best-performing model to evaluate different strategies to create more uniform illumination from standard side-emitting fibers and fiber fabrics.

## 2 Theory

Side emitting fibers are a light source with special properties: Their surface *emittance*  $M(z)$  changes alongside the fiber and the emitted radiation has an angular dependence, captured by the *phase func-*

tion  $P(\Theta, \Phi)$ . For example, the PMMA side-emitting fiber used in this paper has an exponential decay in emittance and the light is preferentially scattered forward. Hereinafter, we will calculate the monochromatic radiation field of the fiber in terms of its flux density, which is called (*spectral*) *irradiance*  $\vec{E}(\vec{r})$  in one arbitrary frequency interval  $d\nu$ .

## 2.1 Radiance and radiation transfer

Radiometry describes the radiation field by its field quantity the *radiance*  $L_\nu(\vec{r}, \vec{s}, \nu)$ , which is constant along a ray of light in the absence of absorption or scattering [9]. The flux  $\phi_\nu$  exchanged between two surfaces is calculated by superposition of all possible light rays connecting the surface elements: integrating the radiance  $L$  over the emitting surface  $A_1$  and the receiving surface  $A_2$  while considering the respective distance  $d$  and inclinations  $\Theta_i$  of the surface elements normal  $\vec{n}_i$  to the distance vector  $\vec{d}$  [9, 10],

$$\phi_\nu = d\nu \int_{A_2} \int_{A_1} L_\nu(\vec{r}, \vec{s}, \nu) \frac{\cos \Theta_1 \cos \Theta_2}{d^2} dA_1 dA_2. \quad (1)$$

We use the equality  $\cos \Theta_2 dA_2 = (\vec{s} \cdot \vec{n}_2) dA_2 = \vec{s} \cdot d\vec{A}_2$  to insert the scalar product of the ray vector  $\vec{s} = \vec{d}/d$  and the surface normal  $\vec{n}_2$  of  $dA_2$ . Then the total transferred flux can be written as the scalar product of the differential irradiance  $d\vec{E}_\nu = \vec{s} dE_\nu$  and  $d\vec{A}_2$ .

$$\phi_\nu = d\nu \int_{A_2} \int_{A_1} d\vec{E}_\nu \cdot d\vec{A}_2 = d\nu \int_{A_2} \vec{E}_\nu \cdot d\vec{A}_2 \quad (2)$$

The irradiance  $\vec{E}_\nu$  is independent of the receiving surface so it can be calculated in the whole irradiation volume or on any surface by integrating over the surface of the light source  $A_1$ .

$$\vec{E}_\nu(\vec{r}) = d\nu \int_{A_1} L_\nu(\vec{r}, \vec{s}, \nu) \frac{\cos \Theta_1}{d^2} \frac{\vec{d}}{d} dA_1 \quad (3)$$

The spectral radiant quantity  $\vec{E}_\nu(\vec{r})$  (monochromatic case) can be turned into the radiometric quantity  $\vec{E}(\vec{r})$  by performing the integral over all involved frequencies  $\int d\nu$ .

## 2.2 Radiation field of a cylinder source

We model the fiber as a cylinder in the corresponding coordinates  $(x, y, z) = (\rho \cos \varphi, \rho \sin \varphi, z)$ , where the light inside propagates in the positive  $z$ -direction. The surface is defined by setting  $\rho = R$  the radius of the fiber, which gives us the surface location vector  $\vec{r}_s$ .

The radiance is measured at an arbitrary point of observation  $O$ . Because the fiber and its radiation field are rotationally symmetric we chose  $O$  as the point of observation  $(\rho', 0, z')$  with  $\rho' > R$  and the location vector  $\vec{O}$ . The distance vector  $\vec{d}$  from a surface element to the observation point is

$$\vec{d} = \vec{O} - \vec{r}_s = \begin{pmatrix} \rho' - R \cos \varphi \\ -R \sin \varphi \\ z' - z \end{pmatrix}, \quad (4)$$

with the magnitude  $d = |\vec{O} - \vec{r}_s| = \sqrt{\vec{d} \cdot \vec{d}} = \sqrt{\rho'^2 + R^2 - 2R\rho' \cos \varphi + (z' - z)^2}$ .

Every surface element of the fiber radiates depending on  $z$ -position and emission angles  $\Phi, \Theta$ . The latter are defined in a local spherical coordinate system centered around the surface element as shown in Figure 1. They have to be translated into the global cylindrical coordinate system: The vector to the pole of the spherical coordinate system always coincides with the unit vector  $e_\rho$  of the cylindrical coordinate

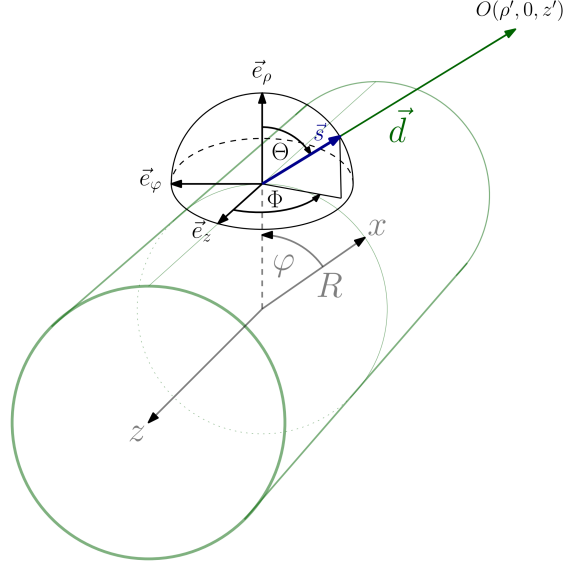


Figure 1: The local spherical coordinate system (black) of a surface element sits on top of the cylindrical coordinate system (green) of the fiber. The  $\vec{d}$  unit vector points from the surface to the point of observation  $O$ . The  $\vec{e}_\rho$  vector coincides with the axis pointing to the north pole of the spherical coordinate system, so  $\vec{e}_\rho \vec{d} = d \cos \Theta$ . The  $\vec{e}_z$  unit vector is the same in both coordinate systems.

system. Thus, the polar angle  $\Theta$  in spherical coordinates can be expressed with  $\vec{e}_\rho = \cos \varphi \vec{e}_x + \sin \varphi \vec{e}_y$  and Equation (4) as

$$\cos \Theta = \vec{e}_\rho \cdot \vec{s} = \frac{\vec{e}_\rho \vec{d}}{d} = \frac{\rho' \cos \varphi - R}{d}. \quad (5)$$

This result becomes zero when  $R = \rho' \cos \varphi$ , then  $\vec{d}$  is a tangent to the surface of the fiber, which we will use as the limits of the surface integration.  $d \sin \Theta \cos \Phi = z' - z$  is the scalar product  $\vec{d} \cdot \vec{e}_z$  expressed in both coordinate systems, in combination with  $\cos^2 \Theta + \sin^2 \Theta = 1$  we obtain

$$\cos \Phi = \frac{z' - z}{d \sqrt{1 - \cos^2 \Theta}} = \frac{z' - z}{\sqrt{d^2 - (\rho' \cos \varphi - R)^2}}. \quad (6)$$

Now all properties of the local spherical coordinate system are expressed in the coordinates of the global cylindrical coordinate system. We insert Equation (5) in Equation (3), with  $\Theta_1 = \Theta$ , replace the surface element by its representation in cylindrical coordinates  $dA_1 = R d\varphi dz$  and obtain the final integral equation for the irradiance vector-field of the cylinder source

$$\vec{E}_\nu(\rho', z') = d\nu \int_0^l \int_{\varphi_0}^{\varphi_1} L_\nu(\vec{r}, \vec{s}, \nu) \frac{(\rho' \cos \varphi - R)}{d^4} \begin{pmatrix} \rho' - R \cos \varphi \\ -R \sin \varphi \\ z' - z \end{pmatrix} R d\varphi dz. \quad (7)$$

From Equation (5) we obtain the limits of integration  $\varphi_0 = -\arccos(R/\rho')$  and  $\varphi_1 = +\arccos(R/\rho')$ ;  $l$  is the length of the fiber.

Two additional remarks to this equation: First, the distance to the surface has to be bigger than zero  $d > 0$ . Second, the symmetry of the formula would cause the second entry of  $\vec{E}_\nu$  always to integrate to zero, because the irradiance passing through this surface element is equal from both sides. This is only true for a virtual surface and not for a real one, which would block radiation from one side of the fiber.

### 2.3 Radiance, emittance, and the phase function

The radiant emittance of a surface element is unequally distributed in all directions on the hemisphere above it. This distribution is a consequence of the heterogeneous scattering process inside the fiber and the refraction and secondary scattering on the fiber surface. To account for this, we separate the radiance into the product of the emittance  $M$  of the fiber surface element with its affiliated phase function  $P$ , which contains the normalized angular information of the emitted radiation.

$$L_\nu(\vec{r}, \vec{s}, \nu) = M_\nu(\vec{r}, \nu) P_\nu(\vec{r}, \vec{s}, \nu) \approx M_\nu(z, \nu) P_\nu(\Theta, \Phi, \nu) \quad (8)$$

We assume an equal scattering mechanism (homogeneously distributed scatterers) throughout the fiber, so only the emittance  $M$  depends on  $z$ . Then we can separate the radiance into the directional  $P$  and the positional contribution  $M$ , which allows us to determine them independently with different experiments.

### 2.4 Line source approximation

The calculation can be greatly simplified by using a line source approximation. Here the light is only emitted radially, therefore its phase function has no angular component everywhere except for  $\Phi = 0$ . This means that we can replace the  $\Phi$ -dependency of the phase function with the delta function

$$P_\nu(\Theta, \Phi, \nu) = P_\nu(\Theta, \nu) \delta(\varphi) \quad (9)$$

Inserting this into Equation (7) and performing the  $\varphi$ -integration leads to the radiant flux density of the line source with an angular dependent emission in  $\Theta$ . Additionally, as a line has no radial extend, we set all resulting  $(\rho' - R) = \rho'$ . The remaining  $R$  from the surface element  $dA = R d\varphi dz$  is combined with the surface emissivity to yield the radial flux emission  $M_\nu(z, \nu) R = I_\nu(z, \nu)$ . The resulting equation for the line source is

$$\vec{E}_\nu(\rho', z') = d\nu \int_0^l I_\nu(z, \nu) P_\nu(\Theta, \nu) \frac{\rho'}{d_l^4} \begin{pmatrix} \rho' \\ 0 \\ z' - z \end{pmatrix} dz, \quad (10)$$

with  $d_l = \sqrt{(\rho')^2 + (z' - z)^2}$ ; the irradiance can now be calculated by integration over  $z$ .

## 3 Experimental

The radiation field of a rotationally symmetric side-emitting fiber can be determined if the radiant emittance  $M(z)$  and the phase function  $P(\Phi, \Theta)$  are known. These parameters are determined experimentally, with two different set-ups: The *side emission measurement* will determine the emittance and the microscopy-based *angular measurement* will measure the phase function. Both methods, except the calibration of the angular measurement, are also described elsewhere in more detail [11, 12]. Additionally, we show how to measure the resulting radiation field of a fiber band with a scattering screen.

The side-emitting optical fibers (PMMA, diameter 500  $\mu\text{m}$ ) and the textile fiber band, containing 19 corresponding fibers oriented parallel to each other with an average distance of 2.6 mm [see Figure 4(c)], were provided by F.J.RAMMER GmbH. For all experiments, we used a 100 mW 520 nm green laser diode which is butt-coupled (direct contact without focusing optics) to the fibers of the band. For micrographs and phase function measurement we used a JenaPol Interphako microscope. The radiation field was imaged with a Canon EOS 650D camera and a EF 18-55 objective focused on a frosted glass plane as a scattering screen.

### 3.1 Side Emission Measurement

A custom-made integrating sphere (see Figure 2a) was used to measure the fiber emittance. It consists of two fiber guides, a baffle to protect the detector port from direct irradiation, and an optical fiber to

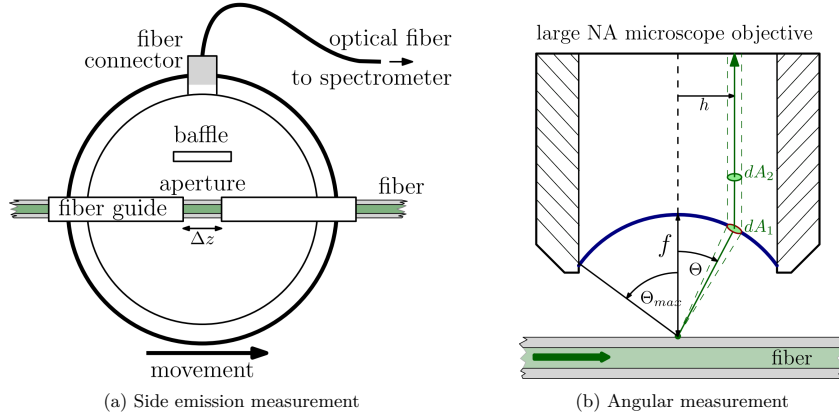


Figure 2: (a) Emittance measurement: Light emitted by the fiber segment  $\Delta z$  (limited by the aperture) is homogeneously distributed on the sphere wall by multiple diffuse reflections. The irradiance on the detector port is proportional to the emitted flux  $E \propto \phi$ . (b) Phase function measurement: Rays spanning an angle  $\Theta$  with the optical axis (dashed) are transformed in parallel rays with a distance  $h$  by refraction on the reference-sphere (blue, radius  $f$ ) according to the Abbe-sine condition Equation (11).

connect the sphere to a spectrometer (Ocean Optics: Maya2000 Pro). The side-emitting fiber was threaded through the sphere with the help of two hollow fiber guides, leaving only a small segment of the length  $\Delta z$  exposed to the interior of the sphere. The emitted flux of the fiber segment  $\Delta\phi(z)$ , which is related to the emissivity by  $\Delta\phi(z) = 2\pi R\Delta z M(z)$ , is distributed homogeneously by multiple diffuse reflections on the sphere walls. Therefore, the measured irradiance  $E_m(z)$  is proportional to the flux collected by the sphere  $\Delta\phi(z)$  [12, 2]. By measuring the flux at different positions along the fiber, we captured the  $z$ -dependence of the emittance of the side-emitting fiber.

### 3.2 Fourier-Microscopy

The angular light distribution on the hemisphere in Figure 1 was captured with a large numerical aperture (NA) objective: In its back focal plane, the light is decomposed into its angular components [13, 11]. The relation between emission angle  $\Theta$  and back focal plane radial distance  $h$ , for infinity-corrected objectives, is sketched in Figure 2b and given by the Abbe sine condition [14]

$$\sin \Theta = \frac{h}{f}. \quad (11)$$

The unknown focal length  $f$  can be replaced by  $f = n_0 h_{max}/\text{NA}$  by using the numerical aperture and Equation (11):  $\text{NA} = n_0 \sin \Theta_{max} = n_0 h_{max}/f$ . Here  $h_{max}$  is the radius of the circular back focal plane image.

All real-world objectives with high NA have angle and polarization-dependent transmission losses [15]. For correction, we use a Lambertian scattering standard (provided by QSIL GmbH Quarzschmelze Ilmenau) which should have an ideal flat irradiance profile in the back focal plane. The correction is performed by dividing the measurement image pixel-wise by the image of the scattering standard.

To show this correctional property, we derive the transfer of a lossless objective with an ideal scattering standard: As shown in Figure 2b), the flux  $\phi$  emerges from the focal point in a cone around the observed ray and is transformed into a non-divergent pencil of rays on the reference sphere while conserving its energy. The flux passing through  $dA_1$  is equal to the flux passing through  $dA_2 = \cos \Theta dA_1$ , so the irradiance has to vary accordingly  $\phi = E_1 dA_1 = E_2 dA_2 = E_2 dA_1 \cos \Theta$ . Therefore, the irradiance in an ideal objective is amplified according to  $E_2(\Theta) = E_1(\Theta)/\cos \Theta$  for increasing  $\Theta$ .

If we insert the irradiance of a Lambertian diffuser  $E_1(\Theta) = E_L \cos \Theta$  into this formula, the cosines cancel, and we obtain  $E_L = E_2(\Theta) = \text{const.}$ : a Lambertian diffuser should have an ideally flat intensity profile in the back focal plane of an objective. This correction was performed separately for both polarization states and then both states are averaged to obtain the corrected unpolarized back focal plane image.

### 3.3 Measurement of the irradiance on a scattering screen

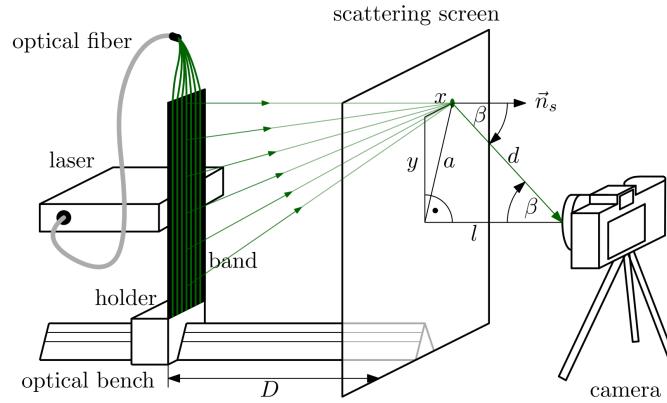


Figure 3: Scattering camera measurement: a CCD-camera is focused ( $l = 900$  mm) on a scattering screen with the surface area  $A_S = 650$  mm  $\times$  450 mm. The fiber band is mounted to a straight holder, which is clamped to an optical bench. A laser is coupled to the side emitting-fibers and the room is darkened. The fibers are moved to different positions  $D$  (10 mm to 800 mm) relative to the glass plate and a picture is taken of the scattering glass plate for each position without changing the focus of the camera.

The radiation field of a band of several side-emitting fibers is measured with a simple set up shown in Figure 3. The idea is that the screen makes the radiation field in its plane visible by secondary scattering. The irradiance  $E_0(x, y) = \vec{n}_s \vec{E}(r)$ , which is intersected by the screen at a certain point is turned into the emissivity on the other side  $M(x, y) \propto E_0(x, y)$  by transmission through the screen. We assume that the screen acts as an ideal Lambertian diffuser: the irradiance which is observed by the camera on the other side of the screen is

$$E(x, y, \alpha) = M(x, y) \frac{\cos \beta}{d^2} \propto E_0(x, y) \frac{\cos \beta}{d^2} . \quad (12)$$

This allows us to measure the light-field at the scattering screen just by taking a picture of it and correct for the angular and distance attenuation: We define the position of the pixel relative to the center of the screen as shown in Figure 3, so  $d = \sqrt{a^2 + l^2} = \sqrt{x^2 + y^2 + l^2}$ . Therefore, the geometric attenuation is

$$\frac{\cos \beta}{d^2} = \frac{l}{d^3} = \frac{l}{(l^2 + x^2 + y^2)^{3/2}} , \quad (13)$$

which is used to correct the measurement for geometric angle and distance attenuation. Because the scattering behavior of the screen is expected to follow the cos-dependence only approximately especially for large angles, it is best to choose a large distance  $l$  between the screen and the camera. Also, the camera response has to be checked for linearity.

## 4 Results

The commercial side-emitting fiber in Figure 4 (a) appears transparent and featureless to the naked eye and under the microscope. When light is butt-coupled in the fiber, as in Figure 4 (b), it lights up and

appears self-luminous. This luminosity is not equally distributed across the fiber, but it is brighter at the fringes and dimmer in the center when observed under the microscope. Additionally, scattering particles in the fiber and small scratches on the fiber surface become visible. The fiber is the brightest close to the coupling, then the brightness decreases quickly towards the fiber end.

The band of equivalent plastic side-emitting fibers in Figure 4 (c) show a similar decline in emission but additionally, the overall brightness varies from one fiber to the next because of difficulties that arise from distributing light equally from one large-diameter fiber to many small ones via butt-coupling.

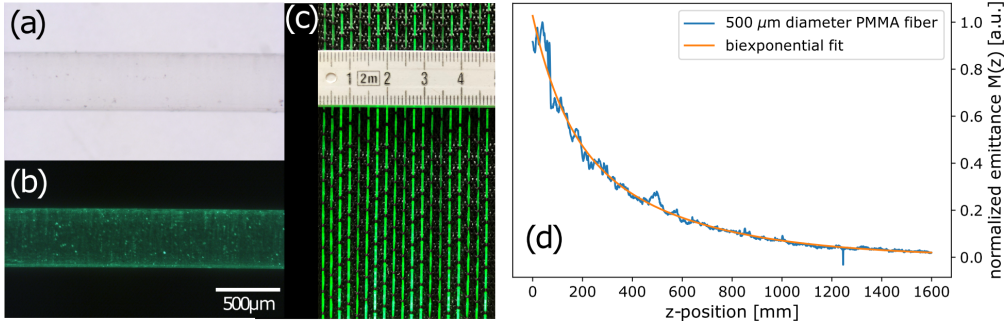


Figure 4: Micrographs of the side-emitting fiber under bright field microscope illumination (a) and dark field self-illumination (b). (c) 19 fibers woven in a fiber band in self-illumination. (d)  $z$ -dependence of the side-emitting fibers emittance  $M$  with increasing distance to the light coupling. A biexponential function with the two decay constants  $\sigma_1 = 0.0021 \text{ mm}^{-1}$  and  $\sigma_2 = 0.0080 \text{ mm}^{-1}$  and the corresponding amplitudes  $A_1 = 0.58$  and  $A_2 = 0.42$  has been fitted to the measurement data.

To quantify the loss in brightness with length, a single fiber is clamped to the side emission set up from Section 3.1, and the relative change in surface emittance is measured. The result in Figure 4 (d) is a monotonous decaying curve that can be fitted with a biexponential decay function.

#### 4.1 Phase function measurement

The emission of light from one fiber segment changes with emission angle, which can easily be verified by observing the fiber (band) from different positions. This angular emission behavior was measured with Fourier-microscopy in two orthogonal polarization directions which are shown in Figure 5 (a) & (b). The radiation is concentrated on the right side of the circle in a half-moon shape, so light scatters preferentially forward under low angles. The remainder of the back focal plane image is dark, which means that comparatively little radiation is scattered in these directions.

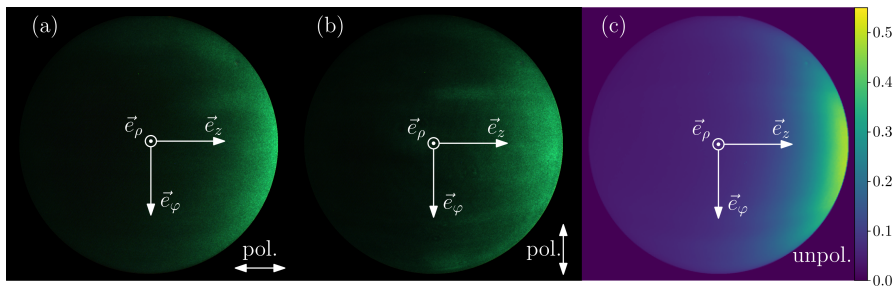


Figure 5: (a) & (b) typical back focal plane images for two orthogonal polarization directions (pol.) and the average corrected image (c) from 100 images, 50 in each polarization direction: the phase function  $P$ . The coordinate system is analogous to Figure 1 when the hemisphere is viewed from the top.



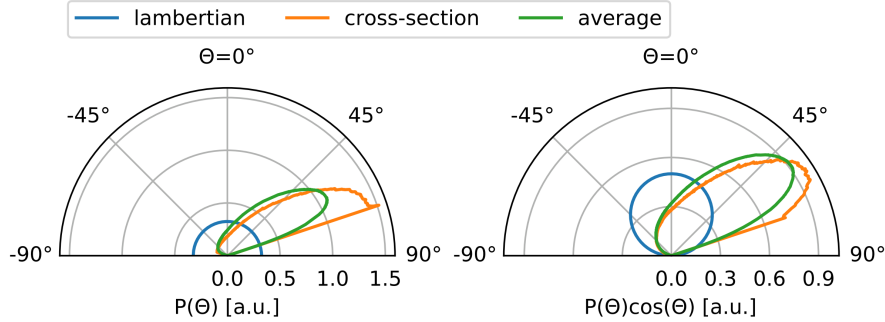


Figure 6: Polar plot of the normalized phase function  $P$  (left) and the projected phase function with  $\cos \Theta$  apodization (right). Lambertian  $P$  is the isotropic case. The cross-section is the data from the  $\vec{e}_\rho$ - $\vec{e}_z$ -plane. The average is calculated by integrating along a rotation around  $\vec{e}_z$  and dividing by arc length.

From these measurements we determine the phenomenological, polarization-independent phase function  $P(\Theta, \Phi)$  by imaging 50 pictures on different positions in each polarization direction, correcting them according to Section 3.2, and averaging all of them. The resulting phase function in Figure 5 (c) is still brighter to the right and is now almost rotationally symmetric with respect to  $\vec{e}_z$ . The half-moon shape brightness, which is caused by the large angle objective amplification, is gone due to the correction procedure. Additionally, the phase function was normalized so that the integral over the hemisphere is equal to one.

To better illustrate the forward scattering of the fiber surface we present it in Figure 6 as a polar plot in the  $\vec{e}_\rho$ - $\vec{e}_z$ -plane from Figure 5. This data will also serve as the phenomenological phase function  $P(\Theta)$  of the line source. Here we see an isotropic Lambertian surface compared to the  $\vec{e}_\rho$ - $\vec{e}_z$ -cross-section of the phase function and the average scattering. The average was calculated by integrating over the surface of the hemisphere in a rotation around the  $\vec{e}_z$  vector and then dividing by the arc length.

In the graph on the left in Figure 6, we see the Lambertian phase function, which is constant over all angles ( $P(\Theta) = 1/\pi$ ). The cross-section of the phase function has its maximum value before it drops rapidly for angles greater than  $71^\circ$ . This cut-off is due to the limited opening angle of the objective. The average function shows a similar behavior but decreases after its maximum at  $60^\circ$  before the cut-off angle.

When we multiply the phase function with the  $\cos \Theta$  projection factor (Equation (3)), we see how much radiation is really scattered in a given direction from a surface element: the isotropic Lambertian surface is now turned into a circle with its maximum emission at  $0^\circ$ . The average curve and the cross-section curve become more similar in shape with their respective maxima now at  $53^\circ$  and  $58^\circ$ . The influence of the cut-off angle is strongly diminished by the  $\cos \Theta$ -factor. This shows that the phase function can be satisfactorily determined even with a limited aperture because the projection factor dampens the missing large-angle phase function components.

## 4.2 Making the radiation field visible

A scattering screen intercepts the radiation field of the fiber band at different distances  $D$  and makes it visible. Black and white camera images of the screen are shown in Figure 7 and display the behavior of the radiation field: At close distance, we can almost distinguish single fibers when the band is closest to the screen. Analogous to a single fiber, this distribution is bright at the start and then decays rapidly towards the fiber end.

When the distance between the screen and band increases, as shown in Figure 7 from left to right, the radiation fields of the single fibers overlap and form a continuous enveloping distribution. Here we observe a distinct maximum of brightness close but not at the very start. Increasing the distance further leads to a downwards movement of the maximum which broadens, spreads out, and fills more and more

area of the screen. In the largest observed distance  $D$  of 870 mm (Figure 9d), the maximum brightness has traveled the whole distance of the screen and is now located at the lower end.

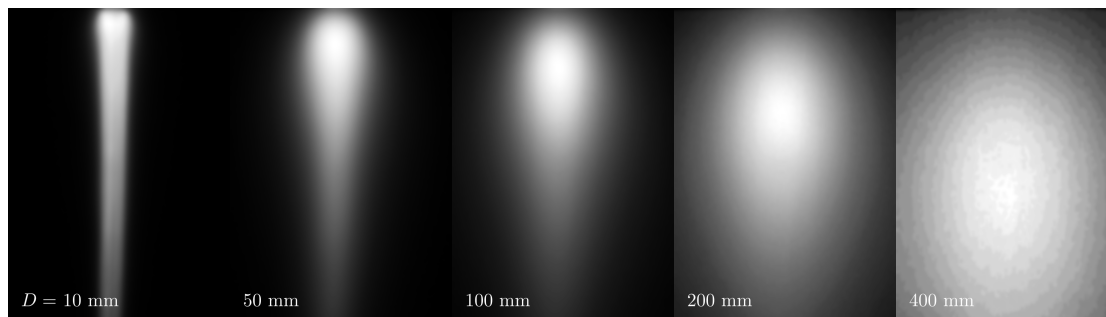


Figure 7: Black and white images of the scattering screen reveal the radiation distribution of a side-emitting fiber band for several distances (increasing from left to the right) according to Figure 3. The light is coupled into the fiber from the top and loses its emissivity, due to the constant out-scattering of light, towards the end. Increasing the distance  $D$  between the band and screen leads to a broadening of the light distribution.

## 5 Discussion

The fiber in Figure 4 (d) shows a biexponential decay in emitted radiation with increasing distance from the light entry point. This corresponds to a fiber where some light is guided in the core and some is guided in the cladding [12], each with its respective scattering coefficients  $\sigma_1$  &  $\sigma_2$  and amplitude  $\phi_1$  &  $\phi_2$ . This is the result of the butt-coupling which excites core and cladding modes simultaneously. In the present case, we expect the cladding modes to experience stronger dampening because they interact with the fiber surface.

$$\phi(z) = \phi_1 e^{-\sigma_1 z} + \phi_2 e^{-\sigma_2 z} \quad \leftrightarrow \quad -\frac{d\phi}{dz} = \phi_1 \sigma_1 e^{-\sigma_1 z} + \phi_2 \sigma_2 e^{-\sigma_2 z} \quad (14)$$

If we neglect absorption loss, we see how this leads to exponentially decaying emission (assuming flux conservation): any loss in transmitted flux is turned into out-scattered radiation  $M(z) \propto -d\phi/dz$ . So, the amplitudes extracted from the fit in Figure 4 are  $A_1 = \phi_1 \sigma_1$  and  $A_2 = \phi_2 \sigma_2$ . They give us a ratio of cladding- to core flux of  $\phi_2/\phi_1 = 0.2$  at the start of the measurement. This strong initial decay is visually unpleasing and can lead to overexposure in technical applications. A costly solution would be to optimize the optical coupling to the fiber core; a simpler solution is to cover this part of the fiber with an absorber (but at the expense of emission efficiency).

### 5.1 Angular emission

The measurement of the angular distribution of the radiation emitted from a fiber surface element in Figure 5 and 6 shows a clear preference for forward scattering which points to the presence of long-period refractive index distortions: Generally, all deviations from the ideal core-cladding structure in a step-index optical fiber cause light scattering [16]. These deviations can be thought of as refractive index fluctuations which can be decomposed into a spectrum of mechanical waves [17, 11]. Each wavelength is responsible for light scattering under a certain angle: longer wavelengths than the guided light causes forward scattering and vice versa. Therefore, the dominant wavelengths of the fluctuations are much longer than the wavelength of the green laser diode.

## 5.2 Calculated radiation field

Comparing the numerically calculated fields close to the fiber for the two fiber models, namely cylinder source and line source, together with the two different phase functions, namely Lambertian and the measured phenomenological phase function, reveals two properties: first the irradiance in all four variants shows a reciprocal dependency on distance ( $\rho^{-1}$ ). Second, the phase functions result in different magnitudes of irradiance close to the fiber: the two Lambertian models are congruent and also the two phenomenological phase function are congruent but result in a slightly higher irradiance.

The numerical results are plotted in Figure 8. The cylinder source was calculated by numerical integrating Equation (7) and the line source by integrating Equation (10). In both cases, the length-dependent decay in emittance was modeled using Equation (14) with the parameters from the fit to the measured values in Figure 4. The Lambertian phase function for the cylinder had the constant value  $P(\Theta, \Phi) = (2\pi)^{-1}$  and for the line  $P(\Theta) = \pi^{-1}$ . The data for phenomenological phase function was either taken from Figure 5 for the cylinder or from Figure 6 (average) for the line.

The discretization of the surface in  $\varphi$  was done by dividing the angular interval  $[\varphi_0, \varphi_1]$  into 20 equal pieces. For  $z$  we converted interval  $[0, l]$  for every  $z$ -position into the angular interval  $[\arctan(z/(\rho - R)), \arctan((l - z)/(\rho - R))]$  divided it into 100 equal angles and converted the angles back into  $z$ -coordinates. This was done to improve numerical stability for small distances.

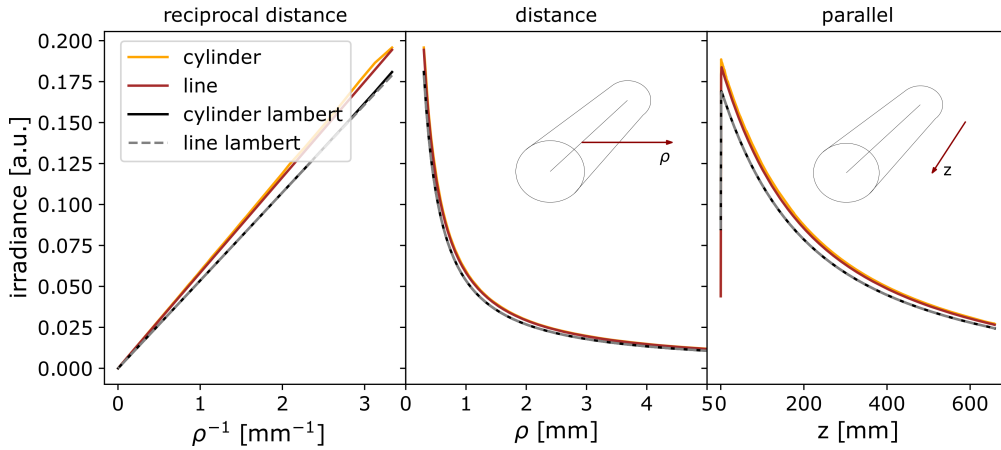


Figure 8: Comparison of the irradiance of the line source and the cylinder source close to the fiber for the phenomenological and the Lambertian phase function. At  $z = 100$  mm in reciprocal distance (left) or in distance (middle). Irradiance in a line parallel to the fiber in a distance of  $\rho = 0.5$  mm.

The deviation between phenomenological and Lambertian models close to the fiber is contradictory to the expected behavior in that all models should converge to the emissivity  $M(z)$  of the fiber surface when  $\rho \rightarrow R$ . Three features of our phenomenological phase function are probably responsible for this: First, the phase function is only known for  $\Theta < 71^\circ$  due to the NA limitation. Second, the normalization of the phase functions can only be performed up to a certain numerical accuracy using our present approach (float 64bit). Third, the discretization of the phase function leads to angular intervals with constant scattering.

Interestingly, the line source and the cylinder source give the same result in the Lambertian case, which indicates a property known for the Lambertian sphere, whose irradiance shows the same behavior ( $\propto \rho^{-2}$ ) as an ideal point source [10]. The conclusion is that the Lambertian cylinder's irradiance behaves like that of a line source, although this remains to be proven mathematically.

We conclude that the Lambertian approximation is adequate to describe the irradiance close to the fiber, justifying the approach of Endruweit *et al.* [6] to calculate the field of a fiber from a Lambertian cylinder. However, it is even sufficient to solely use the line source. This is, of course, just possible in the ab-

sence of absorption and scattering in the surrounding medium. In the latter case, the irradiance of line source and the cylinder source would deviate.

### 5.3 Comparison to the measured radiation field

In the preceding subsection, we concluded that the line source and the cylinder source differ only for different phase functions. Now we compare the calculations for all four models to the measured field of a fiber band and find that in principle the cylinder source with the phenomenological phase function performs best in the observed measurement range, although only slightly better than the phenomenological line source. Lambertian fibers, which performed adequately in the proximity to the fiber, perform worse for larger distances.

We use the same procedure as in Section 5.2 to numerically integrate the four models and obtain the radiation field for the half-space next to the fiber, which corresponds to the volume spanned by the scattering screen measurement in Figure 7. Then we used the principle of superposition to calculate the radiation field of the fiber band from a single fiber: we made 19 duplicates of the calculated field, moved their  $x$ -coordinates to the respective positions of fibers on the band in Figure 4, and added them up. Additionally, we accounted for different coupling efficiencies by weighting the fields. This was done for all observed distances. Exemplary results of these calculations of the cylinder source with the phenomenological phase function are shown in Figure 9 next to the measured values.

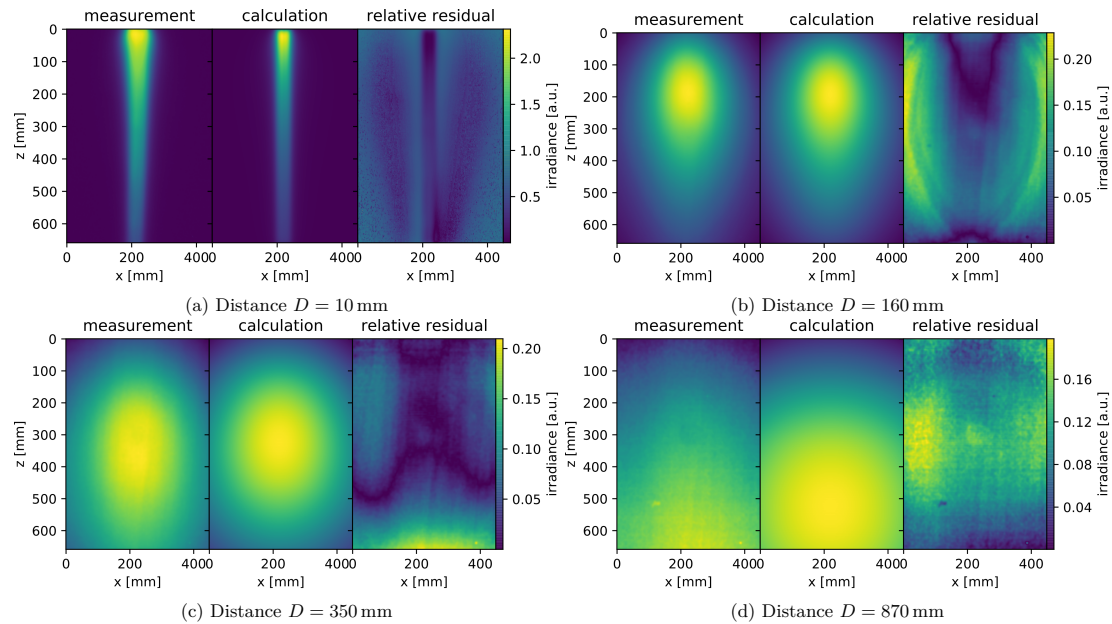


Figure 9: Comparison between measured  $E_m$  and the calculated irradiance field  $E_c$  (phenomenological cylinder source) of fiber band for the distances 10 mm, 160 mm, 350 mm, and 870 mm. The pictures on the right show the relative residual  $|E_m - E_c|/E_m$  which is the relative deviation between measurement and calculation.

The calculated irradiance of the fiber band with the phenomenological phase function in Figure 9 shows two properties that match the measurement: First, the field in proximity to the fiber is dominated by the exponential decay of the radiant emission of the fiber surface. Second, the forward scattering property of the fiber causes a downwards movement (away from the coupling) of the maximum of irradiance with increasing distance  $D$ . That this is caused by the forward scattering property of  $P$  can be inferred by comparison with a Lambertian fiber, which does not show a movement of the maximum (not shown).

For a quantitative comparison of the models with the measurement, we calculated the *relative residual* as the absolute difference between the measured  $E_m$  and the calculated  $E_c$  irradiance divided by the measured irradiance  $|E_m - E_c|/E_m$  for every pixel. This gives the pictures on the right in the subfigures in Figure 9. For a more comprehensive depiction, we calculated the average residual and the standard deviation of the relative residual for each plane of observation, this is shown in Figure 10. Here we see that all models start with the highest residual but only the ones with a phenomenological phase function surpass an error of 10% while the Lambertian level off at around 30%.

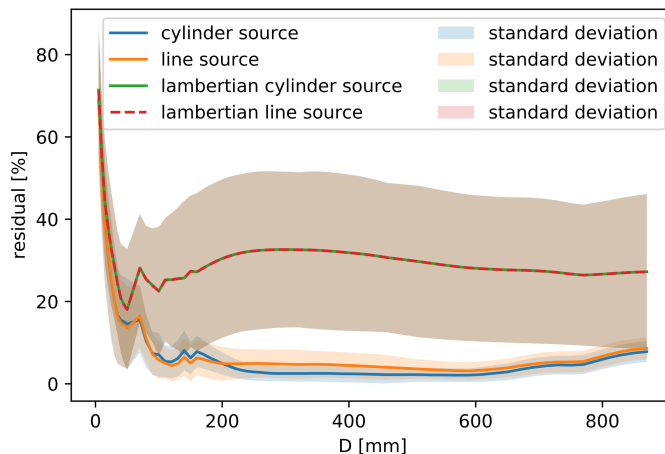


Figure 10: Comparison of the average residual and its standard deviation between cylinder source and line source with the Lambertian or phenomenological phase function. The relative residual is calculated analogously to Figure 9 as  $|E_m - E_c|/E_m$  for every pixel. All pixels are then averaged, and the standard deviation is calculated. The Lambertian curves are congruent in average and standard deviation.

The cause of the high residual for small distances between screen and band is shown in Figure 9: we see that the residual directly above the band is small but next to it is large. In this plane, the fibers will block the light from each other because fibers and the screen are approximately situated in the same plane. Additionally, a possible interaction between scattering screen and fiber band makes the measured scattering more diffuse than in the calculation: some light is scattered back and forth between band and screen, causing additional diffuse irradiation. Also, the screen has no real Lambertian transmission for large incident angles. We conclude that the scattering screen measurement is unfit to measure the irradiance in proximity to the fiber.

With increasing distance  $D$  between screen and band, the aforementioned effects weaken, so the calculation and the measurement converge. Still, the line source shows slightly higher residuals and standard deviation. This shows that the cylinder source is the slightly more precise way of calculating the radiation field in intermediate distances and large distances if a phenomenological phase function is used. The line source can be used in combination with a phenomenological phase function at almost the same precision and comes with the benefit of less computational effort. The Lambertian approximation should not be used for larger distances or only if no phenomenological phase function is available and larger uncertainties can be tolerated.

#### 5.4 Testing alternative fiber coupling schemes by superposition

At last, we explore alternative light coupling schemes with the best performing fiber model, the cylinder source with the phenomenological phase function, to see if they create a more homogeneous illumination

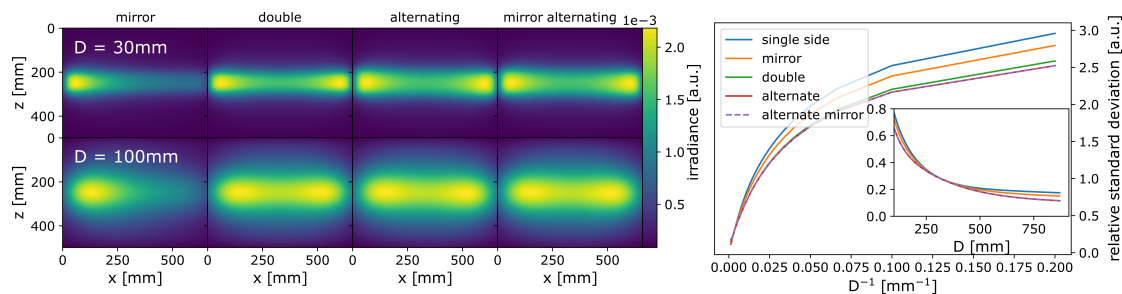


Figure 11: Comparison of calculated irradiance field (phenomenological cylinder source) of a fiber band for four different light coupling schemes in two distances (left). Relative standard deviation in reciprocal presentation (right) and linear representation in the insert (right).

from a fiber band than basic single side coupling. We use the relative standard deviation of irradiance for each calculated plane as a quantitative comparison. From the four proposed schemes we do explore, three perform almost equally well to create a much more homogeneous irradiance field. The exponential decay in emittance and the forward scattering property hinder side-emitting fibers from application because they lead to uneven illumination and optical unpleasing looks. Spigulis *et al.* [5] proposed two methods to mediate the exponential decay without having to resort to fibers with self-compensating scattering coefficient  $\sigma(z)$ : First, double coupling, where light is coupled in both ends of the fiber, and second, a fiber end face mirror, to re-use the transmitted light by reflecting it back into the fiber. We additionally propose two more schemes: alternating, where light is coupled alternating from one side or the other in neighboring fibers, and a combination of alternating with end-mirror. We can now easily test these schemes for a fiber band with the calculated irradiance field of one fiber and the principle of superposition: For the double coupling, we use the result from the previous subsection duplicate it, rotate the duplicate by  $180^\circ$ , and add it to the original calculated field. For the end mirror we proceed in the same manner but weigh the duplicate with the appropriate attenuation caused by the fiber transmission loss. Alternating these methods for every single fiber gives the other two schemes. The relative standard deviation is obtained by dividing the standard deviation of the irradiance in each plane of observation by the average irradiance in that plane. In Figure 11 (left) we show an example for every scheme in two distances (30 mm and 100 mm) and the relative standard deviation (right). As it turns out, three of the four schemes lead to comparable uniform irradiance fields: alternating and alternating with mirror both provide the most homogeneous illumination with the same amount of couplings as the basic one-sided version. Double coupling is third but requires more couplings. Just using an end mirror on one side results in a more homogeneous illumination than single-sided coupling but shows the same disadvantages of having a strong difference in irradiance from start to end.

## 6 Conclusion

We considered two methods to calculate the emitted light field of a side-emitting fiber in the radiometric approximation: A cylinder source and a line source. We validated experimentally that a standard side-emitting fiber possesses a position and angle-dependent radiance which is properly represented in these models. The two contributions influence the emitted light field in two ways: The  $z$ -position dependence of the emittance is dominant close to the side-emitting fiber, and the angular dependence influences the field in the distance. We showed this by comparing calculated data from both approaches with real world measurements of the radiation field. Both models are in good agreement with the measurement of the light field for distances larger than 80 mm from the emitter. Here the cylinder source possesses slightly better predictive capability compared to the line source at the expense of higher computational effort. From the presented models, the radiation field of complicated arrangements of side-

emitting fibers can be calculated by superposition. This was used to show that alternating the side of the light coupling between neighboring, parallel fibers in a fiber fabric, can greatly improve the homogeneity of the generated radiation field.

## Funding

This work received funding from the Carl Zeiss Foundation within the program “Intelligent Substrates”, and was further supported by the Deutsche Forschungsgemeinschaft under Germany’s Excellence Strategy –EXC 2051– “Balance of the Microverse”.

## Acknowledgments

We thank Eva Schlindwein for fruitful discussions, Dietmar Güttler for assistance with the PC based automated measurement system, Thomas Kittel for assistance with the Fourier-microscopy, Christian Zeitler for electrical work, Lutz Preiser for metalwork & set-up engineering and Annkathrin Schwarze for providing the side-emitting fiber and the fiber band.

## Disclosures

The authors declare that there are no conflicts of interest related to this article.

## References

- [1] J. Alkemper, B. Hoppe, B. Schultheis, S. M. Ritter, I. Henze, D. Wolff, A. Curdt, Side-emitting step index fiber, **2013**, US Patent 8,582,943.
- [2] J. F. Clare, *JOSA A* **1998**, *15*, 12 3086.
- [3] T. Wang, K. Watanabe, Side emitting optical fiber, **1999**, US Patent 5,905,837.
- [4] L. J. Button, A. Kobayakov, S. A. Kuchinsky, S. L. Logunov, A. Zakharian, Light diffusing fibers and methods for making the same, **2013**, US Patent 8,620,125.
- [5] J. Spigulis, D. Pfafruds, M. Stafeckis, W. Jelinska-Platace, In *Optical Inorganic Dielectric Materials and Devices*, volume 2967. International Society for Optics and Photonics, **1997** 231–236.
- [6] A. Endruweit, A. Alobaidani, D. Furniss, A. Seddon, T. Benson, M. Johnson, A. Long, *Optics and Lasers in Engineering* **2008**, *46*, 2 97.
- [7] M. Zajkowski, In *Photonics Applications in Astronomy, Communications, Industry, and High-Energy Physics Experiments III*, volume 5775. International Society for Optics and Photonics, **2005** 440–445.
- [8] M. Zajkowski, In *Photonics Applications in Astronomy, Communications, Industry, and High-Energy Physics Experiments*, volume 5125. International Society for Optics and Photonics, **2003** 322–327.
- [9] J. M. Palmer, B. G. Grant, *The art of radiometry*, **2009**.
- [10] B. Grant, SPIE, **2011** .
- [11] A. Reupert, M. Heck, S. Nolte, L. Wondraczek, *Advanced Optical Materials* **2020**, 2000633.
- [12] A. Reupert, M. Heck, S. Nolte, L. Wondraczek, *Optical Materials Express* **2019**, *9*, 6 2497.

- [13] J. A. Kurvits, M. Jiang, R. Zia, *J. Opt. Soc. Am. A* **2015**, *32*, 11 2082.
- [14] M. Born, E. Wolf, *Principles of optics: electromagnetic theory of propagation, interference and diffraction of light*, Elsevier, **2013**.
- [15] M. Leutenegger, R. Rao, R. A. Leitgeb, T. Lasser, *Optics express* **2006**, *14*, 23 11277.
- [16] D. Marcuse, *Principles of optical fiber measurements*, Academic Press, **1981**.
- [17] D. Marcuse, *Theory of dielectric optical waveguides*, Elsevier, **2013**.

## List of Figures

- 1 The local spherical coordinate system (black) of a surface element sits on top of the cylindrical coordinate system (green) of the fiber. The  $\vec{d}$  unit vector points from the surface to the point of observation  $O$ . The  $\vec{e}_\rho$  vector coincides with the axis pointing to the north pole of the spherical coordinate system, so  $\vec{e}_\rho \vec{d} = d \cos \Theta$ . The  $\vec{e}_z$  unit vector is the same in both coordinate systems. . . . . 3
- 2 (a) Emittance measurement: Light emitted by the fiber segment  $\Delta z$  (limited by the aperture) is homogeneously distributed on the sphere wall by multiple diffuse reflections. The irradiance on the detector port is proportional to the emitted flux  $E \propto \phi$ . (b) Phase function measurement: Rays spanning an angle  $\Theta$  with the optical axis (dashed) are transformed in parallel rays with a distance  $h$  by refraction on the reference-sphere (blue, radius  $f$ ) according to the Abbe-sine condition Equation (11). . . . . 5
- 3 Scattering camera measurement: a CCD-camera is focused ( $l = 900$  mm) on a scattering screen with the surface area  $A_S = 650$  mm $\times$ 450 mm. The fiber band is mounted to a straight holder, which is clamped to an optical bench. A laser is coupled to the side emitting-fibers and the room is darkened. The fibers are moved to different positions  $D$  (10 mm to 800 mm) relative to the glass plate and a picture is taken of the scattering glass plate for each position without changing the focus of the camera. . . . . 6
- 4 Micrographs of the side-emitting fiber under bright field microscope illumination (a) and dark field self-illumination (b). (c) 19 fibers woven in a fiber band in self-illumination. (d)  $z$ -dependence of the side-emitting fibers emittance  $M$  with increasing distance to the light coupling. A bi-exponential function with the two decay constants  $\sigma_1 = 0.0021$  mm $^{-1}$  and  $\sigma_2 = 0.0080$  mm $^{-1}$  and the corresponding amplitudes  $A_1 = 0.58$  and  $A_2 = 0.42$  has been fitted to the measurement data. . . . . 7
- 5 (a) & (b) typical back focal plane images for two orthogonal polarization directions (pol.) and the average corrected image (c) from 100 images, 50 in each polarization direction: the phase function  $P$ . The coordinate system is analogous to Figure 1 when the hemisphere is viewed from the top. . . . . 7
- 6 Polar plot of the normalized phase function  $P$  (left) and the projected phase function with  $\cos \Theta$  apodization (right). Lambertian  $P$  is the isotropic case. The cross-section is the data from the  $\vec{e}_\rho$ - $\vec{e}_z$ -plane. The average is calculated by integrating along a rotation around  $\vec{e}_z$  and dividing by arc length. . . . . 8
- 7 Black and white images of the scattering screen reveal the radiation distribution of a side-emitting fiber band for several distances (increasing from left to the right) according to Figure 3. The light is coupled into the fiber from the top and loses its emissivity, due to the constant out-scattering of light, towards the end. Increasing the distance  $D$  between the band and screen leads to a broadening of the light distribution. . . . . 9
- 8 Comparison of the irradiance of the line source and the cylinder source close to the fiber for the phenomenological and the Lambertian phase function. At  $z = 100$  mm in reciprocal distance (left) or in distance (middle). Irradiance in a line parallel to the fiber in a distance of  $\rho = 0.5$  mm. . . . . 10



---

9	Comparison between measured $E_m$ and the calculated irradiance field $E_c$ (phenomenological cylinder source) of fiber band for the distances 10 mm, 160 mm, 350 mm, and 870 mm. The pictures on the right show the relative residual $ E_m - E_c /E_m$ which is the relative deviation between measurement and calculation. . . . .	11
10	Comparison of the average residual and its standard deviation between cylinder source and line source with the Lambertian or phenomenological phase function. The relative residual is calculated analogously to Figure 9 as $ E_m - E_c /E_m$ for every pixel. All pixels are then averaged, and the standard deviation is calculated. The Lambertian curves are congruent in average and standard deviation. . . . .	12
11	Comparison of calculated irradiance field (phenomenological cylinder source) of a fiber band for four different light coupling schemes in two distances (left). Relative standard deviation in reciprocal presentation (right) and linear representation in the insert (right). . . . .	13

## 3.2 Side-Emission Properties of Femtosecond Laser Induced Scattering Centers in Optical Fibers

Aaron Reupert et al. “Side-emission properties of femtosecond laser induced scattering centers in optical fibers.” In: *Optical Materials Express* 9.6 (2019), pp. 2497–2510. DOI: <https://doi.org/10.1364/OME.9.002497>

Fiber optical light diffusers that enable interstitial light delivery have become a useful tool for various illumination tasks, such as in photodynamic therapy. However, existing methods based on light diffusing fiber tips are not applicable for spatially selective light delivery in more complex structures. Here, we employ femtosecond laser induced scattering centers without mechanical manipulation and removal of the outer coatings for generating customized emission patterns. Tailoring of the cumulative emission profile is achieved through controlling the step-width between modification spots. An in-depth evaluation shows that the side-emission pattern is the result of an interplay of several scattering mechanisms that interact with cladding and core modes.



# Side-emission properties of femtosecond laser induced scattering centers in optical fibers

AARON REUPERT,<sup>1</sup> MAXIMILIAN HECK,<sup>2</sup> STEFAN NOLTE,<sup>2</sup> AND  
LOTHAR WONDRAKZEK<sup>1,\*</sup> 

<sup>1</sup>*Otto Schott Institute of Materials Research, Friedrich Schiller University, Fraunhoferstr. 6, Jena, 07743, Germany*

<sup>2</sup>*Institute of Applied Physics, Friedrich Schiller University, Albert-Einstein-Str. 15, Jena, 07745, Germany*  
\**lothar.wondraczek@uni-jena.de*

**Abstract:** Fiber optical light diffusers that enable interstitial light delivery have become a useful tool for various illumination tasks, such as in photodynamic therapy. However, existing methods based on light diffusing fiber tips are not applicable for spatially selective light delivery in more complex structures. Here, we employ femtosecond laser induced scattering centers without mechanical manipulation and removal of the outer coatings for generating customized emission patterns. Tailoring of the cumulative emission profile is achieved through controlling the step-width between modification spots. An in-depth evaluation shows that the side-emission pattern is the result of an interplay of several scattering mechanisms that interact with cladding and core modes.

Published by The Optical Society under the terms of the [Creative Commons Attribution 4.0 License](https://creativecommons.org/licenses/by/4.0/). Further distribution of this work must maintain attribution to the author(s) and the published article's title, journal citation, and DOI.

## 1. Introduction

Photodynamic therapy has become widely applied in treating superficial cancers, for example in skin, lung, esophagus, and bladder, with good clinical and cosmetic outcomes. This method of treatment employs light of a defined wavelength to activate a photosensitizing drug which causes localized cell death or tissue necrosis [1]. Beyond surface treatments, however, the method is difficult to apply to voluminous tumors because of the low light penetration depth in tissue due to scattering and absorption. Interstitial light delivery, which is a more efficient illumination method for such tissues, employs light scattering optical fiber tips which are placed directly inside the tumors [2]. Such tips are usually fabricated by fixing a mixture of epoxy resin and light-scattering particles (quartz, TiO<sub>2</sub>) to the exposed core at the fiber end [3,4]. These diffusers provide for a flat emission profile over a length of several centimeters, but are mechanically stiff and have a large diameter; both factors may result in unwanted tissue damage. In addition, the maximum length of the light diffusing region is limited [3]. In recent years, several authors have hypothesized that effective light delivery, especially in organs or tumors of complex shape, could benefit from specifically tailored light emission profiles on the diffusive fiber tip [2,5,6]. For example, it was estimated that collateral damage on healthy tissue could be reduced in the range of 15% to 58% in terms of tissue volume when using adapted light sources for treating brain cancer tissue [5].

Current technology for tailored light diffusers employs long period fiber gratings, which couple light from guided core modes to cladding modes [3]. This light is eventually scattered out of the fiber by a layer of TiO<sub>2</sub> particles, which is applied as a coating to the modified region after the grating is written. This technique is able to generate 250 μm thin and flexible light diffuser tips with a flat or customized longitudinal emission profile. Unfortunately, this mode of fabrication can neither generate point-like emission in the fiber nor emission profiles with large peak powers towards the fiber end [2].

To address the limitations of current approaches, here, we study tailored light diffusion from a commercial optical fiber which is modified through focused femtosecond laser irradiation. Contrary to continuous laser writing, the high energy density of this method enables the creation of local variations in the refractive index of any transparent fiber material due to nonlinear absorption processes [7]. The irradiation pulse generates a rapid increase in temperature followed by rapid cooling, which results in a refractive index change of the material. Repeated focused irradiation of a single spot by the laser pulses then create localized refractive index perturbations which scatter light guided in the fiber.

Using established technology, such scattering centers can be arranged in periodic or aperiodic longitudinal chains, thereby resulting in a light emitting fiber segment as shown in Fig. 1. The emission profile could be tailored by the number of pulses per spot, by the employed pulse energy and by the step-width between the scattering centers. Since the first two methods include non-linear processes in the creation of the scattering effect, which are difficult to control, we chose the latter to demonstrate the feasibility of our approach. We created two series of modifications under similar irradiation conditions: one with constant step-width, and another one with decreasing step-width. In this way, we make use of the usually undesired light scattering properties of femtosecond laser induced refractive index perturbations. According to this purpose, the writing process itself underlies less critical constraints in terms of writing accuracy and aberrations of the focal spot as compared to the established writing process of fiber gratings. Most noteworthy, this enables to perform the writing procedure in a non-contact process without removal of the fiber coating or other mechanical handling. On the one hand, we retain almost all benefits of light scattering by a long period fiber grating [3], in particular, the possibility to manufacture thin and long filaments which are able to illuminate large volumes of tissue (or other media [8,9]) with low laser power and very high spacial selectivity. On the other hand, the advantages of retaining an intact cladding (by placing the emission centers into the fiber core) also come with the challenge to include the light guiding ability of the cladding into the conception of efficient side-emission designs.

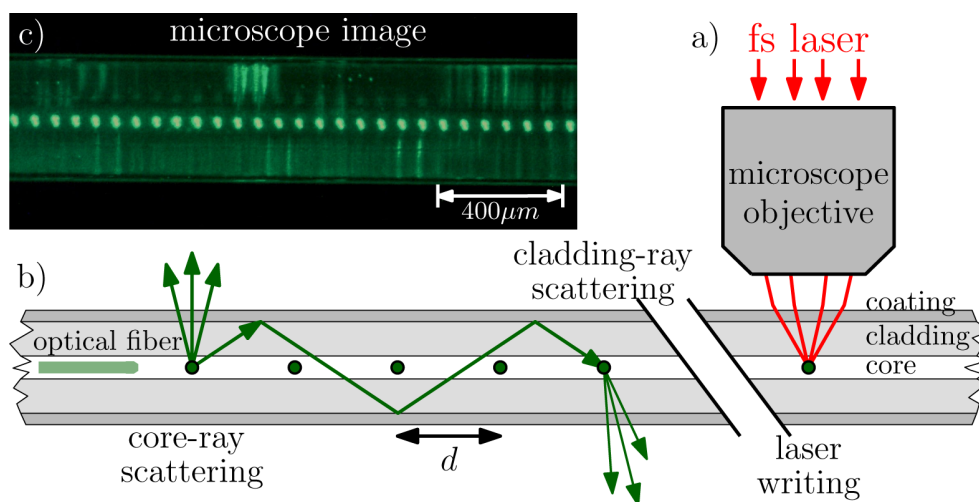


**Fig. 1.** Schematics and microscope image of light scattering on femtosecond laser modifications. a) Creation of scattering centers through focused femtosecond laser irradiation of the fiber core. b) Light scattering on the laser modifications in a two stage process: Light is scattered out of the core into free space and into the cladding, where it is again guided by total internal reflection or, eventually, scattered out into the environment. c) Microscope image of light scattering on laser modifications.

The paper is organized as follows: Section 2 presents the three-level light flux exchange between core, cladding and surrounding in comparison to the common one-level light flux exchange considerations. In Section 3, we describe the experimental parameters as well as the measurement device for quantifying fiber transmission and emission. Section 4 examines the scattering centers and the measured emission and transmission profiles of modified fibers. Building on these analyses, in Section 4 we discuss singular as well as chains of scattering centers. Further, we test the theoretical analysis by applying it to a customized emission profile.

## 2. Theory

### 2.1. General

We initially analyze the interaction of scattering centers with guided light in an optical fiber. The proposed model is based on the Lambert-Beer law, which is expanded to describe the interaction of discrete scattering events with a core-cladding optical fiber structure. From the result we derive the fiber transmission and emission, which can be experimentally observed. The model to describe the fiber emission and transmission relies on two central assumptions: first, all cladding modes as well as all core modes exist in a *steady state power distribution* [10]. This is warranted by the constant coupling of modes due to light scattering. Second, the scattering centers are independent, *i.e.*, they do not interact with each other. This means that a single total loss function can be applied to all modes in the cladding or in the core (*viz.*, the Lambert-Beer law). This total loss in transmitted *spectral flux*  $\phi$  [W/nm] can be decomposed into scattering  $\sigma$  and attenuation  $\alpha$ , which may or may not vary over distance:

$$\frac{d\phi}{dz} = -(\alpha + \sigma)\phi \longleftrightarrow \phi(z) = \phi_0 \exp \left\{ - \int_0^z \alpha(z') + \sigma(z') dz' \right\}. \quad (1)$$

If the integrand is constant, the result is a simple exponential decline in light flux with increasing distance  $z$ . From this the fiber emission can be deduced from conservation of energy: The absorbed light is transformed to heat and the scattered fraction will leave the fiber through its surface. This results in a simple expression for the emission of the fiber per unit length  $\frac{d\phi_E}{dz} = \sigma\phi$ , which is proportional to the fiber transmission.

Because a regular optical fiber consists of at least two layers with different refractive index, namely, core and cladding, this simple model (which is mostly applied to the transmission of the fiber core) is insufficient to describe the emission behavior of a real fiber. Therefore, we expand Eq. (1) based on similar assumptions, but include the general observation that light scattered from the fiber core partially ends up in the cladding where it is still able to propagate. The exchange of flux between the core  $\phi_1$ , the cladding  $\phi_2$  and the surrounding  $\phi_3$  is now described as the energy exchange between different states where the scattering is responsible for the coupling between the states. Light, which is scattered into free space, is transported away from the fiber so there is no reverse process of light being coupled into the fiber from the outside. This energy exchange is schematically shown in Fig. 2.

The scattering of cladding and core modes is caused by discrete refractive index perturbations (as will be generated by focused laser irradiation). The fiber is a low-loss silica fiber, so we approximate scattering to be the dominant loss mechanism and set all other contributions to zero ( $\alpha \approx 0$ ). Under these conditions, we can make the transition from distance-dependent scattering  $\sigma$  to constant scattering per modification  $s$ . This enables us to write the differential equations governing the energy exchange with the number of scattering centers  $n$  as the independent variable  $z \rightarrow n$ :

$$\frac{d\phi_1}{dn} = -(s_{12} + s_{13})\phi_1 + s_{21}\phi_2, \quad (2)$$

$$\frac{d\phi_2}{dn} = s_{12}\phi_1 - (s_{23} + s_{21})\phi_2, \quad (3)$$

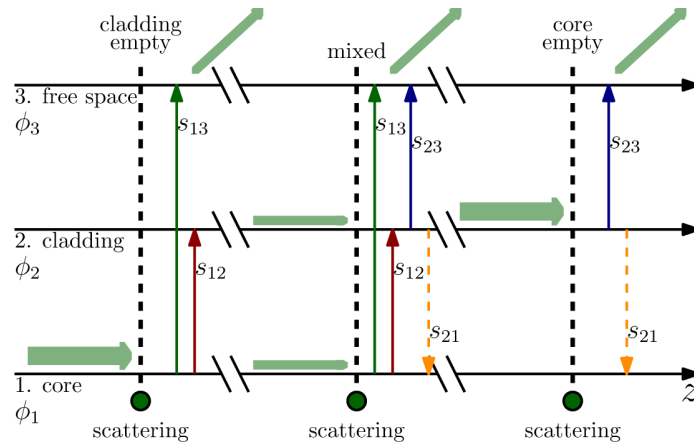


**Fig. 2.** Three-level representation of the energy exchange between the core, the cladding and free space: At first all light is contained in the core and gets scattered into free space (green) and the cladding (red). After some distance this leads to a mixed case where light is also contained in the cladding and scattered into free space (blue) and back into the core (yellow). Because the latter effect is very small, the core is eventually depleted and only the remaining light in the cladding is scattered.

$$\frac{d\phi_3}{dn} = s_{13}\phi_1 + s_{23}\phi_2. \tag{4}$$

Here,  $s_{ab}$  represents the probability for the light to be scattered from state  $a$  to  $b$ . To illustrate the process, the three general cases for energy exchange are shown in Fig. 2. At the start of the modified region the whole light flux is contained within the core; therefore the initial conditions are  $\phi_1(0) = \phi_0$ ,  $\phi_2(0) = 0$  and  $\phi_3(0) = 0$ . The scattering centers are regarded as identical, so all coefficients  $s_{ab}$  are constant. In this experiment, the NA of the fiber core is very small, so the reverse process of scattering light from the cladding into the core is negligibly small ( $s_{21} \approx 0$ ); this approximation decouples Eqs. (2) to (4).

With these conditions, the solutions to the ordinary differential equations can be found by standard methods (e.g. integrating factor). We are only interested in the solutions for  $\phi_1$  and  $\phi_2$  because Eq. (4) already describes the fiber emission at the respective scattering center:

$$\phi_1(n) = \phi_0 \exp\{-(s_{12} + s_{13})n\}, \tag{5}$$

$$\phi_2(n) = \frac{\phi_0 s_{12}}{s_{12} + s_{13} - s_{23}} [\exp\{-s_{23}n\} - \exp\{-(s_{12} + s_{13})n\}]. \tag{6}$$

### 2.2. Observed quantities

The two quantities of this scattering process, which will be measured in the experiment, are the transmitted flux and the emitted flux of the fiber. Both quantities are normalized by the initial flux in the fiber  $\phi_0$  to yield the transmission  $T$  and the emission  $E$ . For the former, we just have to consider that the core as well as the cladding act as light guides, therefore the measured transmitted flux is the sum of flux of the two levels:

$$T(n) = \frac{\phi_1 + \phi_2}{\phi_0} = (1 - A_s) \exp\{-(s_{12} + s_{13})n\} + A_s \exp\{-s_{23}n\}. \tag{7}$$

Here  $A_s$  is substituted for

$$A_s = \frac{s_{12}}{s_{12} + s_{13} - s_{23}}. \tag{8}$$

The fiber emission is described by the normalized flux emitted by the fiber per unit length  $E$ . (In radiometric convention, this would be expressed as the radiant exitance  $M = E/(2\pi R)$  of the fiber surface with the radius  $R$ .) With the general assumption that  $n$  is some function of  $z$  [ $n = n(z)$ ], the relation between the emission per scattering center and the emission per unit length is found via the chain rule.

$$E(z) = \frac{1}{\phi_0} \frac{d\phi_3}{dz} = \frac{1}{\phi_0} \frac{d\phi_3}{dn} \frac{dn}{dz}, \quad (9)$$

$$= [(s_{13} - s_{23}A_s) \exp\{-(s_{12} + s_{13})n(z)\} + s_{23}A_s \exp\{-s_{23}n(z)\}] \frac{dn}{dz}. \quad (10)$$

This is the primary result of this analysis; it means that the functional form of the light scattering per scattering center is always a sum of two exponential functions, regardless of their respective distance to each other. So by placing the scattering centers at different distances, the emission profile can be locally compressed or stretched to yield a customized cumulative profile according to some specific design requirements.

A more sophisticated treatment would expand the consideration further to include the fiber cladding as an additional third light guiding layer and the convolution of the emission signal with the point spread function of the measurement device. Furthermore, it could be considered that light is never coupled out instantaneously but has to undergo several partial reflections which results in an additional exponential decay [11]. These considerations were omitted for clarity.

### 3. Experimental

#### 3.1. Laser writing

A commercially available step-index optical fiber made from fused silica with a germanium doped core and a fluoroacrylate coating (Nufern 20/400 Precision Matched Passive LMA Double Clad Fibers; Core: NA = 0.065, diameter = 20  $\mu\text{m}$ ; Cladding: NA = 0.46, diameter = 400  $\mu\text{m}$ ) was coupled to a super-continuum light source (NKT SuperK) and clamped to a motorized xy-table. Due to the fiber coupling only core modes were excited, so the initial conditions are fulfilled. The femtosecond laser was focused through the transparent coating into the fiber core with an NA = 0.5 microscope objective. The laser, which was employed for writing, was a Ti:sapphire (Spectra Physics, Spitfire) regenerative laser amplifier system emitting pulses at  $\lambda = 800$  nm with a pulse length of 200 fs (FWHM). We used 4  $\mu\text{J}$  pulse energy and a 1 kHz repetition rate. A mechanical shutter was set to 0.4 s, so the number of pulses per scattering center was approximately 400. The transparent fiber coating was not removed for writing.

The free fiber end was connected to an integrating sphere measurement system (see Fig. 3 in the following subsection) in order to record the transmission spectrum after each step of modification. After irradiation, the position of the focal spot was changed and the procedure was repeated until the desired length of the modified region was reached. In one of the examples demonstrated in the following, 1000 modifications with a distance of 60  $\mu\text{m}$  were written. After writing, the fiber was removed from the xy-table and clamped to the linear stage without changing the coupling to the light source, as shown in Fig. 3. We performed the side emission measurement with a longitudinal resolution of 0.2 mm and an aperture  $\Delta z$  of 2 mm. All measurements were normalized to the baseline  $\phi_0$ , which is the transmitted spectral flux of the unmodified fiber. The limited range of the light source and the spectrometer constrained the spectrum to the wavelength interval from 600 nm to 1000 nm.

After the light measurements were finished, we performed optical examination of the refractive index modification with a microscope (ZEISS, JENAPOL interphako). For this, the fiber was immersed in oil ( $n = 1.52$ ) to yield a sharp picture by compensating the aberrations on the cylindrical fiber surface. Then the modifications were imaged with 50 times magnification. We additionally used phase contrast (interphako method) [12] to enhance the image quality, because the refractive index perturbations have a very low contrast with the surrounding glass.

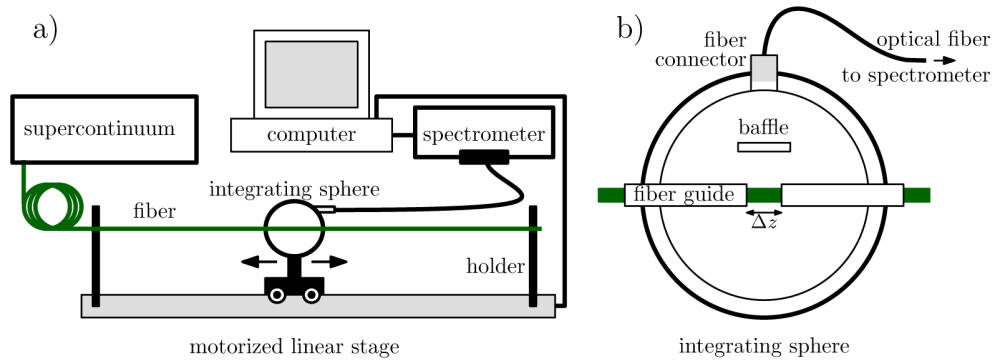


**Fig. 3.** a) Motorized linear stage: The integrating sphere is moved incrementally alongside the optical fiber; the spectrometer measures an emission spectrum for every position. b) Integrating sphere: Light emitted by the fiber segment  $\Delta z$  - limited by the fiber guide - is homogeneously distributed on the sphere wall by multiple diffuse reflections. The irradiance on the detector port is proportional to the emitted flux.

### 3.2. Scanning stage

Quantitative light measurement is notoriously difficult due to many different kinds of instrument attenuation, which are hard to determine. Therefore, we chose a relative measurement approach and normalized all spectra to the transmitted flux of the unmodified fiber. Also, we made as little changes as possible to the measurement device in between the change from the transmission to the emission set-up. This is especially important for the light coupling and the measurement system because they can introduce unknown errors. Under these conditions, we assumed that the constant unknown instrument attenuations will cancel out with the baseline normalization, as shown in Eq. (12).

The measurement device was a fiber coupled spectrometer (Ocean Optics: Maya2000 Pro) with a custom-made integrating sphere for measurement head (Fig. 3). The integration sphere was machined from optical PTFA (Berghof Fluoroplastics) with a reflectivity of  $\rho \approx 0.98$ . It consists of two fiber guides and a baffle to protect the detector port from direct irradiation. An optical fiber connects the sphere to the spectrometer.

The sphere was operated in two modes: In *transmission measurement mode* one fiber guide was blocked with optical PTFA and the cleaved fiber end was put in the middle of the aperture. In this way, the flux emitted from the fiber end is scattered on the blocked fiber guide and captured by the sphere with almost no change in the setup. In *emission measurement mode*, the fiber was threaded through the sphere with the help of both hollow fiber guides, leaving only a small segment of the length  $\Delta z$  exposed to the interior of the sphere. Because the fiber guides limit the size of the measured fiber segment, they also act as the aperture of the integrating sphere. The light flux radiated into the sphere by the fiber is distributed homogeneously by multiple diffuse reflections on the sphere walls. The *irradiance*  $M$  [ $\text{W}/\text{m}^2$ ] measured by the detector of the port area  $A$  is proportional to the flux emitted inside of the sphere [13]:

$$M = \frac{\rho\phi}{A(1 - \rho(1 - f))}. \quad (11)$$

Where  $f$  is the ratio of open port area to total sphere area  $A_{\text{Port}}/A_{\text{Sphere}}$  and  $\rho$  is the coefficient of reflection of the wall material. When  $f$  and  $\rho$  are kept constant between measurement modes, the relation of a measured value to a baseline value will be the same as the relation between the baseline flux value and the measured flux value because the unknown attenuations cancel out. So



the irradiance is proportional to the flux collected by the sphere:

$$\frac{M_i}{M_0} = \frac{\phi_i}{\phi_0}. \quad (12)$$

## 4. Results

### 4.1. Observation

The results of the focused femtosecond laser irradiation are irregular shaped refractive index distortions in the fiber core. Fig. 4 shows microscope images of the core and the modifications viewed perpendicular to the direction of irradiation (side view). In brightfield microscopy the written features show up as faint blurs with irregular but defined boundaries which cover the fiber core partially in a regularly spaced pattern. Phase contrast shows that the modifications consist of a mixture of regions of higher (darker) and lower (brighter) refractive index compared to the surrounding glass matrix. If the fiber is rotated by ninety degrees (top view), the modifications are revealed to be flat, as they cover the core only partially. Here the induced phase shift exceeds the instrument threshold with the consequence that the contrast is inverted. The approximate dimensions of the modifications are  $24 \mu\text{m}$  (length) by  $28 \mu\text{m}$  (height) by  $7 \mu\text{m}$  (width).

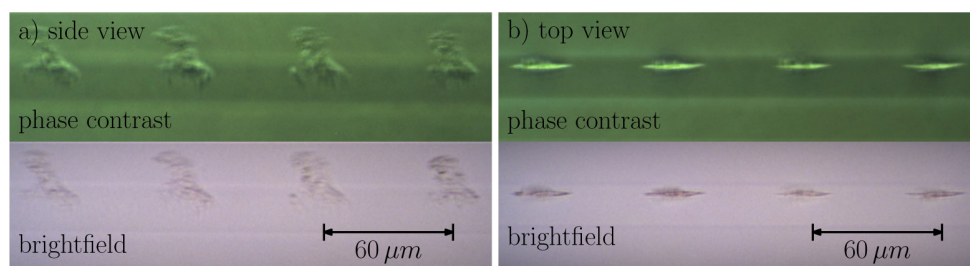


**Fig. 4.** Microscope images of the laser modifications in the fiber core. Top view is in the direction of laser irradiation and side view is orthogonal to it. The contrast of the brightfield images is low, so additional phase contrast images are provided. Here a higher refractive index shows up darker e.g. the fiber core is the dark band in the center of the pictures.

If light is coupled into the fiber, it interacts with the localized modifications and is partially scattered out. This can be seen under the microscope (Fig. 1c), where the modifications appear as clear, bright spots. Without optical magnification, the spots merge into a cumulative continuous emission profile.

For the quantitative investigation of the scattering phenomenon, transmission and emission spectra were recorded. The extensive data set of one series of modifications is displayed in Fig. 5 as two color maps, one for transmission and one for emission. The independent variable is either the number of the modification in the first- or the position in the second case. To better visualize the decline in flux we averaged the data over three different wavelength intervals (which roughly represent the upper-, lower and the whole wavelength range). This is shown in the graphs on top of the corresponding heat maps.

The averaged transmission curves are declining monotonously with increasing number of scattering centers from their highest value at the start to the lowest value at the end of the examined section. The emission (which is zero outside of the modified area) jumps to its highest value at the first modification. Then it declines rapidly for 10 mm before it crosses over into a section where the overall rate of decline is less and several local minima and maxima appear.

The spectrally resolved measurement shows that the transmission as well as the emission is wavelength-dependent. Figure 6 displays both sets of spectra in corresponding stages. In

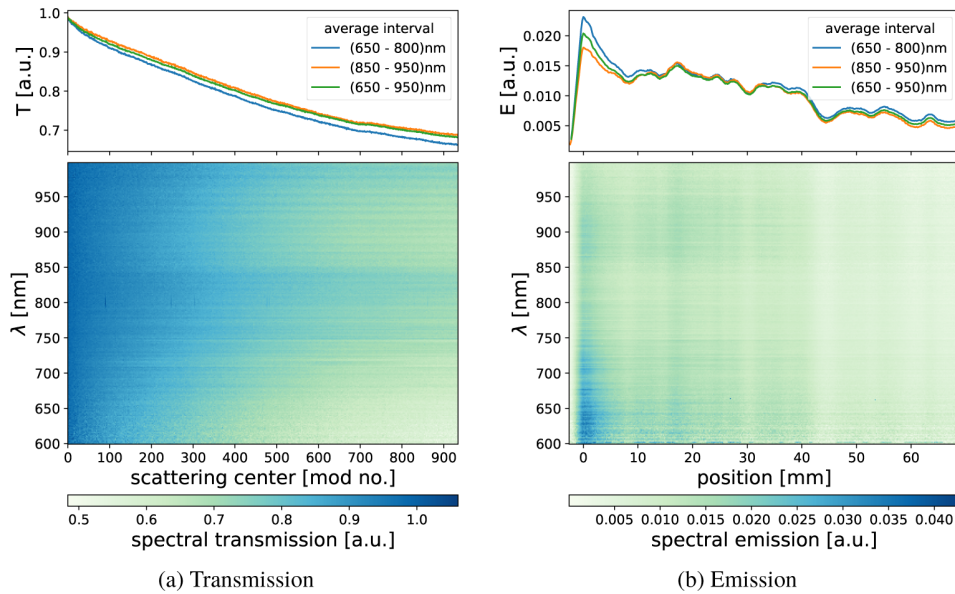


**Fig. 5.** Wavelength-resolved transmission and emission plots for scattering centers with constant spacing. Transmission spectra are plotted as a function of the modification centers number and the emission spectra as a function of position starting from the initial maximum. The top plots show the average spectral flux in certain wavelength intervals. This shows a steady decline in transmitted power with consecutive modifications for in transmission and an overall decline but with local maximums and minimums in emission.

transmission, the strongest decline is found after 1000 modifications at the shortest observed wavelength of 600 nm, where 55% of the initial flux is transmitted through the modified length. Going to higher wavelength, the dampening decreases until its lowest value at around 820 nm where more than 70% is transmitted. Then it declines again to 65% at the local minimum in the near infrared wavelength range at around 900 nm. The shape of the emission curves resembles the shape of the transmission when the order of spectra and the magnitude is inverted: it is approximately a downscaled mirror image. Its highest value of 3% at 600 nm is found at the very start of the modification. Then the emission declines with increasing wavelength to the minimum value of 1.75% at 820 nm and it increases again to 2% at 900 nm which is a local maximum. The magnitude of the emission spectra decreases from the start to the end of the modified length.

#### 4.2. Model fit

For data processing, the analysis from Fig. 2 is applied to the measurements to yield the scattering spectrum of a single modification. According to Eq. (7) and Eq. (9) a double-exponential decay governs both the transmission and emission behavior. This translates to a fit of either Eq. (7) or Eq. (9) to each row in the heat-map of a transmission or emission plot, respectively. To improve the data quality for the fitting, we limited the data range from 0 to 600 modifications. Some selected fit results are shown in Fig. 7. We numerically integrated the data over the wavelength intervals provided in the legend as indicated in the figure captions. This has no consequence for the underlying analysis and was solely done for better visualization.

We obtained three scattering coefficients from every fit which represent the fraction of energy transfer between core, cladding and free space for a single wavelength. These separate values were then stacked and plotted over their respective wavelength to yield the average scattering spectrum per modification  $s_{ab}(\lambda)$  as shown in Fig. 7 for  $s_{23}$ . The initial decay  $s_{12} + s_{13}$  is too short

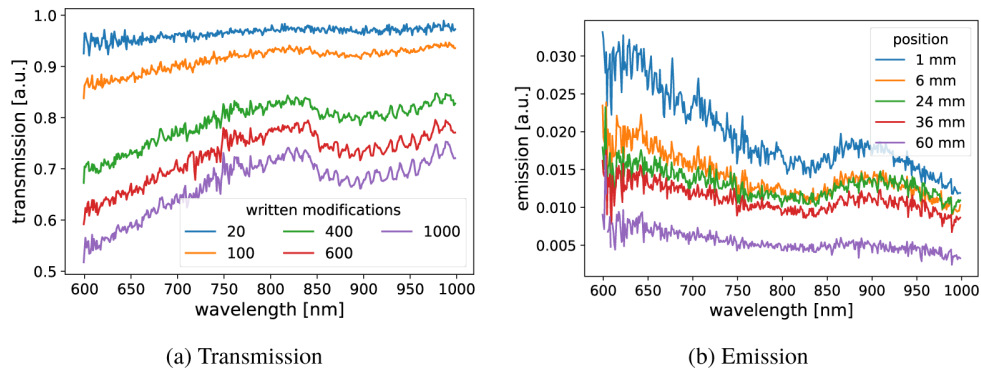


**Fig. 6.** Transmission spectra for increasing amounts of scattering centers (indicated by the labels) with their corresponding emission spectra, measured at the indicated positions.

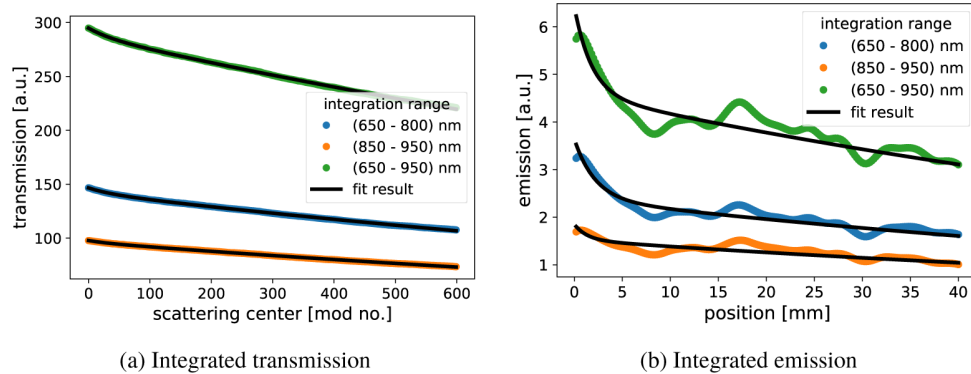


**Fig. 7.** Transmission and emission spectra integrated over three different wavelength ranges and plotted as a function of the number of scattering centers or the position with their respective fits according to Eq. (7) and Eq. (9)

to yield a meaningful spectrum, therefore we give the average value of 0.03 per modification for transmission and emission. The fit results for the  $s_{23}$  scattering spectrum for transmission and emission are plotted in Fig. 8 together with their respective standard error. This represents the scattering spectrum of one modification for cladding modes.

In transmission the highest amount of 0.07% light scattering per modification is found for the lowest measured wavelength of 600 nm. The scattering power then declines with increasing wavelength until the minimum is reached at around 820 nm with 0.035%. Then the scattering increases again up to 0.05% at the local maximum which is located at around 900 nm. The emission spectra show a similar shape and value range as compared to the transmission data. The difference  $\Delta$  of both spectra has the shape of a broad maximum centering around 800 nm. The relative fit error in transmission lies between 1% (740 nm) and 4% (600 nm) with an average value of 2%, which is too small to be visible in Fig. 8. The relative fit error in emission lies between 4% (740 nm) and 20% (600 nm) with an average value of 7%. Here, relative errors greater than 10% are only found for wavelength smaller than (650 nm).

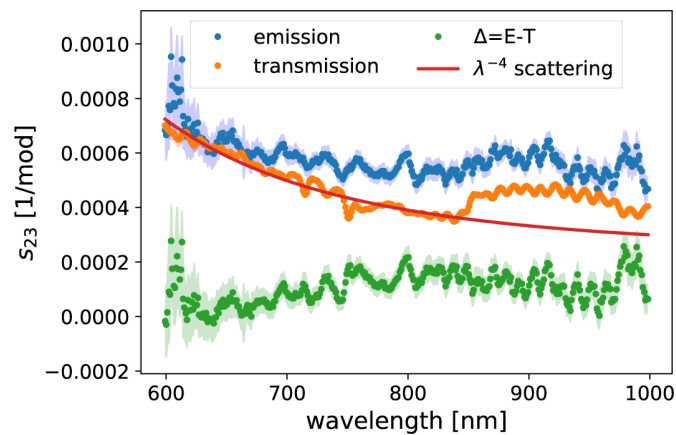


**Fig. 8.** Fit results of Eq. (7) and Eq. (9) to every wavelength of the emission and transmission data set. This yields scattering spectra  $s_{23}$  of a modification in emission or transmission with its corresponding standard error (shaded area). The spectra show an increase in scattering for lower wavelength as well as a local maximum at 900 nm and the difference in magnitude  $\Delta$ . A scattering function  $\propto \lambda^{-4}$  was fitted to the transmission data in the range 600 nm to 840 nm with an  $R^2 = 0.967$ .

## 5. Discussion

### 5.1. Light scattering centers

The combination of microscope imaging and dampening measurement allows us to obtain information on the inner structure of the laser modifications. We can see from the optical images that the modifications consist of refractive index fluctuations, which are contained in a flat but otherwise irregular shaped region. This form is different from a normal focal spot [14] which would be rotationally symmetric when viewed from the top. The straightforward explanation for the derivations is the refraction of the laser on the cylindrical shaped fiber surface. This introduces aberrations which could result in such a shape. Additionally, such aberration depends on the alignment of the fiber with respect to the laser. The outer shape of the modification will probably influence the symmetry of the angular scattering pattern and the total scattering power of the modification. While the former is compensated by the integrating sphere measurement device, which covers the whole solid angle, the latter is determined experimentally by the fitting procedure. Therefore, this asymmetry does not influence the outcome of this experiment and could even be used to customize the angular emission profile.

The emission and transmission data show that the average decay constant of the core flux  $s_{12} + s_{13}$  is approximately 60 times larger than that of cladding flux. This has the effect that the fiber core is rapidly depleted and the second exponent (representing the decay of cladding flux) becomes dominant after about 100 modifications. Then it defines the larger part of the emission and transmission profiles. These different roles are caused by the different diameters of core and cladding. The cross-sectional area of the scattering center is a larger fraction of the core than of the cladding. Therefore, the scattering coefficient is smaller for the cladding flux.

The obtained spectra for  $s_{23}$  provide us with additional insight into the scattering mechanisms of an average modification. Both show similar features but differ by a wavelength dependent amount  $\Delta$ . Because this additional attenuation only affects the light emission, we conclude that it is an effect of the plastic fiber coating, probably true absorption. The remaining distinct features we will investigate further are the local maximum around 900 nm and the increase of scattering

when decreasing the wavelength from 800 nm to 600 nm. Both features are found in transmission and emission, so we infer that they are caused by elastic scattering.

The increase in scattering for decreasing wavelength shows the classical proportionality with  $\lambda^{-4}$  ( $R^2 = 0.967$  over the wavelength range of 600 nm to 840 nm). The maximum around 900 nm indicates the existence of another scattering mechanism. It is probably also caused by fluctuations, but with a period comparable to that of the scattered light: Marcuse showed that the power loss of an optical waveguide with random wall perturbations is at its maximum if the correlation length of the distortions is approximately equal to the wavelength of the guided light [15]. The same idea can be applied to refractive index fluctuations in the fiber core.

These kinds of perturbations should be resolvable with a microscope and indeed, the modifications in Fig. 4 show inner structures with fluctuations in the same order of magnitude. We assume that these inner structures are a result of multiple rapid heating and cooling cycles caused by laser irradiation. Their emergence might be similar to the formation of nanogratings, which are caused by a feedback between the laser beam and the induced microstructure [16]. This interaction leads to a structural evolution from single spots for one laser shot to oriented elongated shapes with increasing number of pulses. A similar process, but with the addition of cylindrical aberrations, might be responsible for the observed fluctuations. To further investigate these scattering phenomena, an evaluation of the angular spectrum of the scattered radiation is necessary. This would yield a distribution of the mechanical frequencies.

## 5.2. Emission profile

In Section 2, we postulated that the scattering centers can be regarded as sufficiently independent of each other to allow for direct shaping of the emission profile by placing the scattering centers at well-controlled step-width.

According to our model, a constant spacing between the modifications should result in a double-exponential decay in transmission and emission, which is also consistent with a longitudinally homogeneous scattering function [17]. This is confirmed by the fit of Eq. (7) and Eq. (9) to both measurement series shown in Fig. 7. In transmission, the curve shape is in good agreement with the theoretical considerations. Regarding emission, Eq. (9) could also be fitted to the data set, except for several local maxima and minima, which cause the scattering spectrum of  $s_{23}$  to be a lot noisier than in transmission. Still, both spectra span the same range and show roughly the same features. This indicates that both procedures record the same effects.

The local extrema we can observe in the emission profile are the result of laser writing errors which are caused by a loss of beam focus. This is due to strong aberrations which are brought about by fluctuations in coating thickness: the affected modifications are either smaller or fainter than the average scattering center, or they have not been written at all. A possible solution to this problem would be to use refractive index matching oil, which would compensate such outer surface irregularities.

Surprisingly, deviations from the ideal exponential curve shape are far stronger in emission than in transmission. This is a counterintuitive consequence of the property discussed in Section 2: contrary to the emission, the transmission is independent of scattering center spacing when there is no interaction. In transmission, only measurements after a successful modification were recorded. Therefore, it shows a double-exponential decay which is in agreement with the model. In emission, the whole length of the chain of modifications was recorded, so missing scattering centers show up as minima. Additionally, according to Eq. (4), the local emission of one modification is determined by the product of its scattering coefficient with the present flux in the core or in the cladding. This makes it even more susceptible to small variations in scattering power.

Besides these irregularities, the model is able to describe the emission and transmission behavior. Nevertheless, the consistency of the theoretical prediction with the measured values

might be coincidental for the special case of constant modification spacing. As an additional test for the proposed approach, we generated an arbitrary emission profiles with aperiodic spacing,

$$d_{n+1} = 0.002(60 \text{ mm} - d_n). \quad (13)$$

Hence, the first distance is  $d_0 = 0.120 \text{ mm}$  and the last is  $d_{1000} = 0.016 \text{ mm}$ . The last interval is smaller than the length of the modification, so at the end of the modified region scattering centers start to overlap. Again, we created 1000 modifications and performed transmission and emission measurements as in the previous section. Results are provided in Fig. 9.

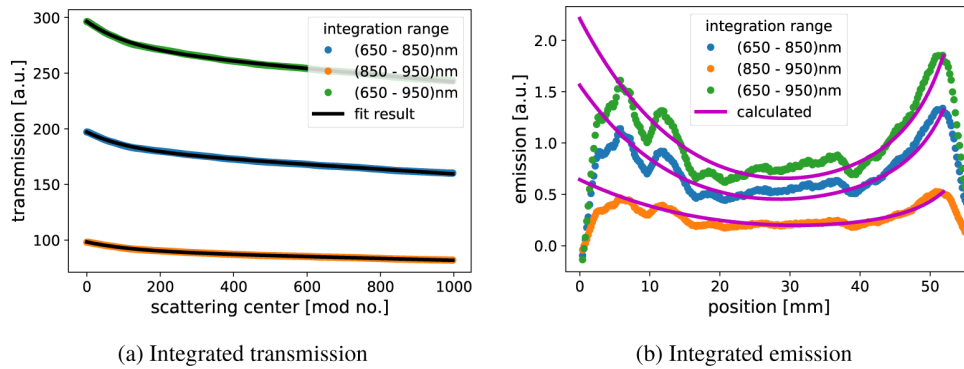


**Fig. 9.** a) Measured transmission with fits according to Eq. (7) at three selected wavelength ranges shows a second degree exponential decay. b) Comparison of the measured emission behavior and the calculated emission profile. The right-side maximum is caused by the decrease of the scattering center distance leading to an increase in emission per unit length.

The measured emission profile in Fig. 9 is U-shaped. This shape is caused by the deformation of the two exponential functions by consecutive decrease of the modification spacing. The high emission values on the left side of the curve correspond to the initial decay of the two exponentials. The increasing line density of scattering centers towards the end of the profile causes the high emission on the right side. An overlap of both effects leads to partial compensation and therefore causes the almost flat emission profile in the central section.

Again, the transmission curve follows a double-exponential decay function, but with lower dampening due to a difference in focal spot position with respect to the fiber core. Qualitatively the overall behavior is in accordance with our hypothesis that the emission profile is shaped by scattering center positioning but the transmission is not.

We extracted the three different scattering spectra  $s_{ab}$  from the transmission measurement by fitting Eq. (7) to the data set. The obtained values were then inserted into Eq. (9) to calculate the emission spectra. To apply this formula, the derivation of the function  $n(z)$  was approximated in the following way:

$$\frac{dn}{dz} \approx \frac{\Delta n}{\Delta z} = \frac{1}{d_n}. \quad (14)$$

This gives the emission per unit length at the position of every modification. The last step was to plot this emission as a function of the position of each modification known from the iterative formula Eq. (13). This calculated emission profile is also shown in Fig. 9. Apart from the irregularities in emission caused by writing errors, the shape of the calculated distribution closely follows the measured one; this holds true for all calculated wavelengths.

Nevertheless, the model shows deviations at the start of the modified length. This is due to the additional effects mentioned in Section 2: the convolution of the measured data with the instruments point spread function and the fiber cladding as a possible third light guiding

layer. Also, the small number of measurement points, where the  $s_{12} + s_{13}$  exponent dominates the transmission profile, makes the fit of this exponent more prone to errors. Despite these shortcomings, the model was capable of predicting the trend of the emission behavior from the transmission data. Therefore, we conclude that the assumption, which leads to the development of the model, *i.e.*, the independence of the scattering centers, can also be applied to modifications of varying distance. This means that arbitrary emission profiles can be designed just by deliberate spacing of similar scattering centers.

This property can also be used to increase the scattering power of the modified area. Figure 6 indicates the range of the transmission through the modified fiber segment after 1000 modifications from 50% to 70%. Depending on the application, this value should be close to zero or at least controllable. In the context of our model, the way to enhance the emission from the fiber and thereby decrease the transmission is to increase the number of scattering centers. This can be achieved either by increasing the length of the light emitting fiber segment or decreasing the distance between the scattering centers. If this is not desired, then another possibility is to make a second chain of scattering centers, which is slightly parallel displaced to the first one. In this way, the number of scattering centers is doubled, therefore just the scattering coefficients  $s_{ab}$  increases but the longitudinal distance of scattering centers stays the same. All these methods results in a double exponential decay with lower transmission but with different longitudinal emission properties. These can again be predicted with the presented model.

However, one needs to acknowledge the possibility that in high light power application, the interaction of the guided light with the scattering centers could cause the destruction of the fiber due to a process called optical fuse [18]. Here, the interaction of the incident light with the backscattered light could lead to the creation of a new defect just in front of the first modification. Repetition of this process may cause a chain reaction in which the defect front moves backward in the optical fiber towards the light source. Driscoll *et al.* [18] gave an approximate threshold value for the radiant flux density  $q$  in the order of  $1\text{MW}/\text{cm}^{-2}$  for the creation of the fuse. Fortunately, radiant flux  $Q$  required for photodynamic therapy lies between 1W and 5W [1], which would lead to an average radiant flux density  $q = Q/(2\pi r)$  between  $0.3\text{MW}/\text{cm}^{-2}$  and  $1.5\text{MW}/\text{cm}^{-2}$  in the present fiber core with a radius  $r$  of  $10\ \mu\text{m}$ . This puts the upper limit of the required flux on the lower end of the threshold value. If necessary, the problem can easily be avoided by taking a fiber with a slightly higher core radius. For example, a core radius of  $15\ \mu\text{m}$  would lead to an average radiant flux density of  $0.7\text{MW}/\text{cm}^{-2}$  while the radiant flux is 5MW.

## 6. Conclusions

In summary, we tested a new method for creating tailorable emission profiles for side-emitting optical fiber segments by focused femtosecond laser irradiation, generating chains of refractive index perturbations alongside the fiber core. The scattering spectrum of each individual such emission center is broadband and wavelength-dependent. Cumulation of all individual scattering centers leads to an overall emission profile which is determined by the employed step-width between the laser-written modifications. Thereby, the writing can be periodic or aperiodic.

Using a model based on simple considerations of Lambert-Beer's law and a three-level transfer process, the emission behavior of longitudinal chains of scattering centers can be predicted with satisfying accuracy, for regular as well as for irregular spacing. As the scattering centers can be treated as acting independent of each other, they can be used as building blocks for creating a virtually arbitrary emission pattern such as required in a certain illumination task.

## Funding

Thüringer Ministerium für Wirtschaft, Wissenschaft und Digitale Gesellschaft (TMWWDG) (41-5507-2016); Leibniz-Institut für Naturstoff-Forschung und Infektionsbiologie – Hans-Knöll-Institut (HKI) (SAS-2015-HKI-LWC); Deutsche Forschungsgemeinschaft (DFG) (GRK2101/1).

## Acknowledgments

This work was supported by a Strategy and Innovation Grant from the Free State of Thuringia (41-5507-2016), the Leibniz ScienceCampus InfectoOptics (SAS-2015-HKI-LWC) and Deutsche Forschungsgemeinschaft (DFG) (GRK 2101/1). We thank Dietmar Güttler for assistance with the PC based automated measurement system and Thomas Kittel for assistance with the phase contrast microscopy.

## Disclosures

The authors declare that there are no conflicts of interest related to this article.

## References

1. B. C. Wilson and M. S. Patterson, "The physics, biophysics and technology of photodynamic therapy," *Phys. Med. Biol.* **53**(9), R61–R109 (2008).
2. A. Rendon, J. C. Beck, and L. Lilge, "Treatment planning using tailored and standard cylindrical light diffusers for photodynamic therapy of the prostate," *Phys. Med. Biol.* **53**(4), 1131–1149 (2008).
3. L. Vesselov, W. Whittington, and L. Lilge, "Design and performance of thin cylindrical diffusers created in ge-doped multimode optical fibers," *Appl. Opt.* **44**(14), 2754–2758 (2005).
4. T. M. Baran and T. H. Foster, "Comparison of flat cleaved and cylindrical diffusing fibers as treatment sources for interstitial photodynamic therapy," *Med. Phys.* **41**(2), 022701 (2014).
5. A.-A. Yassine, L. Lilge, and V. Betz, "Optimizing interstitial photodynamic therapy with custom cylindrical diffusers," *J. Biophotonics* **12**(1), e201800153 (2018).
6. A. Rendon, J. Okawa, R. Weersink, J. Beck, and L. Lilge, "Conformal light delivery using tailored cylindrical diffusers," in *Optical Methods for Tumor Treatment and Detection: Mechanisms and Techniques in Photodynamic Therapy XVI*, vol. 6427 (International Society for Optics and Photonics, 2007), p. 64270M.
7. K. Itoh, W. Watanabe, S. Nolte, and C. B. Schaffer, "Ultrafast processes for bulk modification of transparent materials," *MRS Bull.* **31**(08), 620–625 (2006).
8. L. Wondraczek, E. Tyystjärvi, J. Méndez-Ramos, F. A. Müller, and Q. Zhang, "Shifting the sun: solar spectral conversion and extrinsic sensitization in natural and artificial photosynthesis," *Adv. Sci.* **2**(12), 1500218 (2015).
9. L. Wondraczek, G. Pohnert, F. H. Schacher, A. Köhler, M. Gottschaldt, U. S. Schubert, K. Küsel, and A. A. Brakhage, "Artificial microbial arenas: Materials for observing and manipulating microbial consortia," *Adv. Mater.* **2019**, 1900284 (2019).
10. D. Marcuse, *Principles of Optical Fiber Measurements* (Academic Press, 1981), pp. 11–68.
11. A. W. Snyder and J. Love, *Optical Waveguide Theory* (Springer Science & Business Media, 2012), pp. 135–140.
12. G. Andrehs, H. Beyer, *Theorie und Praxis der Interferenzmikroskopie* (Akademische Verlagsgesellschaft Geest & Portig K.-G., 1974).
13. J. F. Clare, "Comparison of four analytic methods for the calculation of irradiance in integrating spheres," *J. Opt. Soc. Am. A* **15**(12), 3086–3096 (1998).
14. M. Leutenegger, R. Rao, R. A. Leitgeb, and T. Lasser, "Fast focus field calculations," *Opt. Express* **14**(23), 11277–11291 (2006).
15. D. Marcuse, *Light Transmission Optics* (Van Nostrand Reinhold, 1972), pp. 376–387.
16. F. Zimmermann, A. Plech, S. Richter, A. Tunnermann, and S. Nolte, "The onset of ultrashort pulse-induced gratings," *Laser Photonics Rev.* **10**(2), 327–334 (2016).
17. Z. Pan and L. Wondraczek, "Light extraction from fundamental modes in modulated waveguides for homogeneous side-emission," *Sci. Rep.* **8**(1), 9527 (2018).
18. T. Driscoll, J. Calo, and N. M. Lawandy, "Explaining the optical fuse," *Opt. Lett.* **16**(13), 1046–1048 (1991).



### **3.3 Angular Scattering Pattern of Femtosecond Laser-Induced Refractive Index Modifications in Optical Fibers**

Aaron Reupert et al. “Angular Scattering Pattern of Femtosecond Laser-Induced Refractive Index Modifications in Optical Fibers.” In: *Advanced Optical Materials* 8.18 (2020), p. 2000633. DOI: <https://doi.org/10.1002/adom.202000633>

Focused femtosecond laser irradiation is used to induce light scattering modifications in the core of an optical fiber. This turns the fiber into a diffuse, linear light source. The scattering is investigated by imaging almost the full solid angle far-field pattern for the first time. Additionally, an electromagnetic scattering model is developed to explain the observations. The findings herein change how the relationship between light scattering and the refractive index fluctuations is perceived by showing that the far-field scattering pattern is the power spectral density of the polarization current inside the scattering center. Further, the authors contribute to a better estimation of the scattering process by showing that the total scattering power scales quadratically with the laser-induced refractive index change and its volume.

# Angular Scattering Pattern of Femtosecond Laser-Induced Refractive Index Modifications in Optical Fibers

Aaron Reupert, Maximilian Heck, Stefan Nolte, and Lothar Wondraczek\*

**Focused femtosecond laser irradiation is used to induce light scattering modifications in the core of an optical fiber. This turns the fiber into a diffuse, line-shaped light source. The scattering is investigated by imaging almost the full solid angle far-field pattern for the first time. Additionally, an electromagnetic scattering model is developed to explain the observations. The findings herein change how the relationship between light scattering and the refractive index fluctuations is perceived by showing that the far-field scattering pattern is the power spectral density of the polarization current inside the scattering center. Further, the authors contribute to a better estimation of the scattering process by showing that the total scattering power scales quadratically with the laser-induced refractive index change and its volume.**

## 1. Introduction

Light scattering normally constitutes undesired loss in optical fibers. However, if harnessed appropriately, it can be used to turn an optical fiber into a flexible line-shaped light source. Such side-emitting fiber underlies several real and potential applications, for example, in endoscopy where physical access is difficult, and a thin, non-conductive, and chemically stable light source is necessary.<sup>[1–3]</sup>

Early research of light scattering in optical fibers focused on the loss aspect. The field was pioneered by Marcuse, describing intrinsic fiber loss in the framework of electromagnetic theory which he attributed to fluctuations in the core cladding

interface, or in the glass matrix itself.<sup>[4–6]</sup> Rawson measured the angular scattering spectrum of a pristine optical fiber for the first time and linked it to the presence of small needle-like structures for which he also gave a theoretical description.<sup>[7]</sup>

More recent experimental research has turned toward the scattering loss of laser-induced microstructures like fiber Bragg gratings (FBGs) and long-period fiber gratings (LPGs). Fonjallaz et al. and Janos et al. found an azimuthal scattering dependency, where the weakest intensity was measured in the direction of the laser irradiation which created the modifications.<sup>[8,9]</sup> Vesselov et al. on the other hand

used light scattering on long-period fiber gratings to generate customizable side emission.<sup>[10]</sup> We showed previously how deliberately placed femtosecond laser-induced refractive index distortions can be used to create light diffusing fiber segments with a customizable emission profile.<sup>[11]</sup>

Meanwhile, the idea of deterministic scattering on tilted fiber gratings gave rise to further theoretical development of coupling guided to radiation modes. Here, two lines of analysis were followed: the mode coupling theory and the volume current method. While the first is deemed to be more exact, the second offers a more intuitive understanding of the scattering effect. Li et al. showed that both approaches are in good agreement, except for very low scattering angles.<sup>[12]</sup>

Vesselov,<sup>[10]</sup> as well as our prior study<sup>[11]</sup> relied on a phenomenological model of scattering loss which cannot describe the relation between the refractive index modification and the scattering power or the angular emission profile. These shortcomings will be addressed in the present paper, where we develop a new approach to the electromagnetic description of the scattering process based on the volume current method. From this, we are able to explain and predict the angular scattering pattern of refractive index modifications just by using Fourier transforms and convolutions. These mathematical tools are simple to implement with current computer technology. As it turns out, this method can be applied equally well to scattering of all kinds of structures in optical fibers, be it desired or undesired.

For experimental comparison, we study chains of refractive index modifications in the core of a few-mode optical fiber which we created with focused femtosecond laser pulses. Such irradiation has the advantage over a continuous wave laser in that it can modify the refractive index in any transparent material and can induce strong refractive index fluctuations which scatter light.<sup>[13]</sup> The investigation of the refractive index modification and far-field scattering pattern was done with the help of

A. Reupert, Prof. L. Wondraczek  
Otto Schott Institute of Materials Research  
Friedrich-Schiller-Universität Jena  
Fraunhoferstr. 6, Jena 07743, Germany  
E-mail: lothar.wondraczek@uni-jena.de

Dr. M. Heck, Prof. S. Nolte  
Institute of Applied Physics  
Abbe Center of Photonics  
Friedrich-Schiller-Universität Jena  
Albert-Einstein-Str. 15, Jena 07745, Germany

Prof. S. Nolte  
Fraunhofer Institute for Applied Optics and Precision Engineering  
Albert-Einstein-Str. 7, Jena 07745, Germany

 The ORCID identification number(s) for the author(s) of this article can be found under <https://doi.org/10.1002/adom.202000633>.

© 2020 The Authors. Published by WILEY-VCH Verlag GmbH & Co. KGaA, Weinheim. This is an open access article under the terms of the Creative Commons Attribution-NonCommercial License, which permits use, distribution and reproduction in any medium, provided the original work is properly cited and is not used for commercial purposes.

DOI: 10.1002/adom.202000633

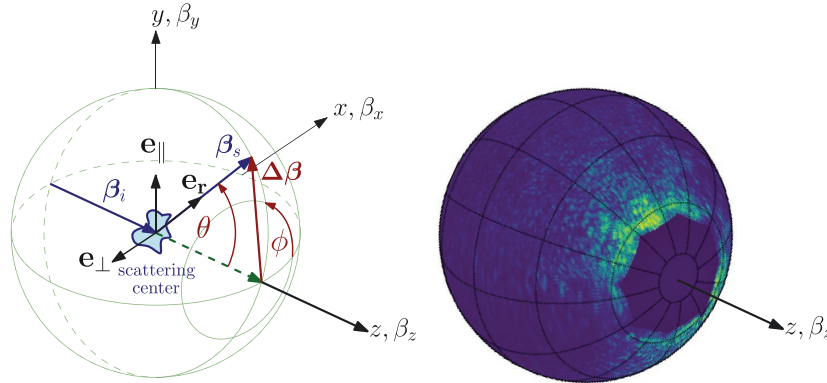


**Figure 1.** Schematics (left) and experimental data (right) of the far-field scattering pattern of a refractive index modification located in the middle of the sphere.  $\beta_i$  is the wave vector of the incoming light with the polarization directions  $\mathbf{e}_\perp$  and  $\mathbf{e}_\parallel$ .  $\beta_s$  is the wave vector of the scattered light, which spans the polar angle  $\theta$  with respect to the incoming wave.  $\Delta\beta$  is the scattering vector.  $\phi$  is the azimuthal angle of the scattered light.

several microscopy methods, that is, shearing, phase-contrast, and Fourier microscopy. A combination with modern digital image processing techniques allowed us to visualize almost the whole solid angle of the far-field scattering pattern of a refractive index modification in an optical fiber for the first time.

The paper is organized as follows: Section 2 presents the derivation of the far-field scattering pattern of a localized refractive index perturbation in a multimode optical fiber. Section 3 describes the experimental conditions for the creation of the refractive index modification as well as the microscopy techniques for measuring the far-field scattering pattern. Section 4 examines the results of the laser processing and scattering measurements, which we discuss in Section 5 and compare the results with the theory from Section 2.

## 2. Theory: Light Scattering on Stochastic Distortions

When guided light interacts with a (laser-induced) refractive index modification  $\Delta n$  in an optical fiber it is scattered in all directions with varying power. This results in an angular spectrum of the scattered radiation which can be pictured on the unit sphere (Figure 1).

In this section, we show that this spectrum is closely related to the power spectrum and the shape of the refractive index distortion by applying a perturbation technique called volume current method.<sup>[14,15]</sup> Here, the interaction of the distortion  $\Delta n$  with the guided electromagnetic field  $\mathbf{E}_0$  induces a polarization current density  $\mathbf{j}$  inside the volume (boldface letters denote vectors). This current radiates light  $\mathbf{E}_s$  which effectively results in power being removed from the incident field. This scattering process is described by the inhomogeneous Helmholtz equation:

$$\nabla \times (\nabla \times \mathbf{E}_s) - n_0^2 k^2 \mathbf{E}_s = 2n_0 \Delta n k^2 \mathbf{E}_0 = -i\omega \mu_0 \mathbf{j} \quad (1)$$

where the refractive index difference between fiber core and cladding has been neglected for simplicity. The interaction of the guided electric field with the perturbation causes a

scattered electromagnetic field which is driven by the current density  $\mathbf{j} = 2i\omega n_0 \Delta n \epsilon_0 \mathbf{E}_0$ . Outside the perturbation  $\Delta n$  is zero and the differential equation is homogeneous, so the solution is the standard eigenmode expansion of the incoming incident field

$$\mathbf{E}_0(\mathbf{r}) = \sum_{\mu}^{\max} c_{\mu}(z) \mathbf{E}_{\mu}(x, y) e^{i\beta_{\mu} z} \quad (2)$$

which we assume to be transversal and unpolarized or circularly polarized. For the scattered field we use a standard procedure to solve the inhomogeneous Helmholtz equation with the aid of a vector potential  $\mathbf{A}$  and the Lorentz gauge.<sup>[15]</sup> The solution outside of the fiber core in terms of the scattered electric and magnetic field strength is

$$\mathbf{E}_s = i\omega \mathbf{e}_r \times (\mathbf{e}_r \times \mathbf{A}_f), \quad \mathbf{H}_s = -\frac{in_0 k}{\mu_0} (\mathbf{e}_r \times \mathbf{A}_f) \quad (3)$$

Here  $\mathbf{A}_f$  is the far-field vector potential, made up by the superposition of outgoing spherical wavelets caused by the currents  $\mathbf{j}(\mathbf{r}')$  enclosed in the volume  $V_0$  of our scattering center:

$$\mathbf{A}_f = \frac{\mu_0}{4\pi} \frac{e^{in_0 k r}}{r} \int_{V_0} e^{-in_0 k \mathbf{e}_r \cdot \mathbf{r}'} \mathbf{j}(\mathbf{r}') dV' \quad (4)$$

Now, we calculate the pointing vector  $\mathbf{S} = 1/2(\mathbf{E}_s \times \mathbf{H}_s^*)$  to obtain the direction and intensity of the far-field scattered radiation (\* denotes the complex conjugate). For that, we perform the integration from Equation (4) two times, which we donate with the two integration variables  $\mathbf{r}_1$  and  $\mathbf{r}_2$  and their corresponding differential volume elements  $dV_1$  and  $dV_2$ :

$$\mathbf{S} = \frac{1}{2} (\mathbf{E}_s \times \mathbf{H}_s^*) = \mathbf{e}_r \frac{\omega n_0 k}{2\mu_0} (\mathbf{e}_r \times \mathbf{A}_f) (\mathbf{e}_r \times \mathbf{A}_f^*) \quad (5)$$

$$= \mathbf{e}_r \frac{\omega n_0 k}{2\mu_0} \frac{\mu_0^2}{16\pi^2 r^2} \iint_{V_0 V_0} [\mathbf{e}_r \times \mathbf{j}(\mathbf{r}_1)] [\mathbf{e}_r \times \mathbf{j}^*(\mathbf{r}_2)] e^{-in_0 k \mathbf{e}_r \cdot (\mathbf{r}_1 - \mathbf{r}_2)} dV_1 dV_2 \quad (6)$$

$$= \mathbf{e}_r \frac{\omega n_0 k \mu_0}{64 \pi^2 r^2} (1 + \cos \theta)^2 \int_{V_0} \int_{V_0} j(\mathbf{r}_1) j^*(\mathbf{r}_2) e^{-i n_0 k \mathbf{e}_r \cdot (\mathbf{r}_1 - \mathbf{r}_2)} dV_1 dV_2 \quad (7)$$

In Equation (5), we used the vector triple product where one term is equal to zero due to orthogonality. For Equation (6), we used that  $\mathbf{j}$  has the same direction as  $\mathbf{E}_0$  (Equation (1)) which is unpolarized or circularly polarized, therefore  $\mathbf{E}_0 = 1/\sqrt{2}(\mathbf{e}_\perp + \mathbf{e}_\parallel)E_0 \rightarrow \mathbf{j} = 1/\sqrt{2}(\mathbf{e}_\perp + \mathbf{e}_\parallel)j$ . This leads to two cross products  $\mathbf{e}_r \times \mathbf{e}_\perp = 1$  and  $\mathbf{e}_r \times \mathbf{e}_\parallel = \sin(\pi/2 - \theta) = \cos \theta$ , as shown in Figure 1.

Next, we introduce the cutoff function  $V$  which is  $V(\mathbf{r}) = 1$  if  $\mathbf{r}$  is inside  $V_0$  and zero elsewhere and acts as a 3D aperture. It represents the shape and the volume of the modification and removes the limits of integration.

Furthermore, we perform a change of variables and get the corresponding volume element with the aid of the Jacobian  $\mathbf{r}_2 = \mathbf{r}_1 - \mathbf{r} \rightarrow dV_2 = dV$ . Also, the shorthand for the propagation constant  $n_0 k = \beta$  is introduced in the exponent, and we write the integral from Equation (7) as

$$\int_{-\infty}^{\infty} \int_{-\infty}^{\infty} e^{-i\beta \mathbf{e}_r \cdot \mathbf{r}} V(\mathbf{r}_1) j(\mathbf{r}_1) V(\mathbf{r}_1 - \mathbf{r}) j^*(\mathbf{r}_1 - \mathbf{r}) dV_1 dV \quad (8)$$

$$= \int_{-\infty}^{\infty} e^{-i\beta \mathbf{e}_r \cdot \mathbf{r}} [(Vj) \star (Vj)] dV = |\mathcal{F}^3\{Vj\}|^2 \quad (9)$$

One group of functions just depends on  $\mathbf{r}_1$  and the other, which is complex conjugate, on  $\mathbf{r}_1 - \mathbf{r}$ , therefore the integral in  $dV_1$  is actually the autocorrelation function  $\int P(\mathbf{r}_1) P^*(\mathbf{r}_1 - \mathbf{r}) dV_1 = P \star P$ . The second integral in  $dV$  turns out to be the 3D Fourier transform  $\mathcal{F}^3$ . At last, we make use of the Wiener–Khinchin theorem  $\mathcal{F}^3\{P \star P\} = \mathcal{F}^3\{P\} \mathcal{F}^3\{P\}^* = |\mathcal{F}^3\{P\}|^2$  and find that the far-field scattering pattern is proportional to the power spectrum of the current density in the volume.

To our knowledge, this elegant result has been derived for the first time but it has one disadvantage in it requiring knowledge of the specific realization of the stochastic functions  $j(\Delta n, E_0)$ . To deal with this inconvenience we will compute the expected scattering behavior of one scattering center by taking the ensemble average  $\langle \mathcal{S} \rangle$  after inserting the current density. At first, this will deviate from our elegant result, but in the end the structure of this solution will be recovered. The ensemble average

$$\langle \mathcal{S} \rangle = \mathbf{e}_r \sqrt{\frac{\epsilon_0}{\mu_0}} \frac{n_0^3 k^4}{16 \pi^2 r^2} (1 + \cos \theta)^2 \int_{-\infty}^{\infty} e^{-i\beta \mathbf{e}_r \cdot \mathbf{r}} \langle (V \Delta n E_0) \star (V \Delta n E_0) \rangle dV \quad (10)$$

is applied only to the autocorrelation function because it contains the stochastically varying functions  $\Delta n$  and  $E_0$ . We see that the whole scattering power scales with  $k^4$  (and thus  $\lambda^{-4}$ ) similar to Rayleigh-scattering as already mentioned by Marcuse.<sup>[4]</sup>

From this point on, the factor in front of the integral will no longer change, therefore we introduce the shorthand notation

$$Q(\theta) = \sqrt{\frac{\epsilon_0}{\mu_0}} \frac{n_0^3 k^4}{64 \pi^2 r^2} (1 + \cos \theta)^2 \quad (11)$$

We insert the eigenmode expansion Equation (2), where the summation index belonging to  $\mathbf{r}_1$  is denoted with  $\mu$  and the

other one belonging to  $\mathbf{r}_2 = \mathbf{r}_1 - \mathbf{r}$  is denoted with  $\nu$ . Similarly, we denote the dependency of other functions on  $\mathbf{r}_1$  or  $\mathbf{r}_2$  with the subscript 1 or 2:

$$\langle \mathcal{S} \rangle = \mathbf{e}_r Q(\theta) \sum_{\mu, \nu}^{\max} \int_{-\infty}^{\infty} e^{-i\beta \mathbf{e}_r \cdot \mathbf{r}} \int_{-\infty}^{\infty} V_1 V_2 \langle c_\mu c_\nu^* \Delta n_1 \Delta n_2 \rangle E_\mu E_\nu^* e^{i\beta_\mu z_1 - i\beta_\nu (z_1 - z_2)} dV_1 dV \quad (12)$$

Due to their interaction, the only stochastic functions are  $\Delta n$  and  $c$ . Now we follow the argument of Marcuse<sup>[5]</sup> that the amplitudes and the refractive index perturbations are uncorrelated:

$$\langle c_\mu(z_1) \Delta n_1 c_\nu^*(z_2) \Delta n_2 \rangle = \langle c_\mu(z_1) c_\nu^*(z_2) \rangle \langle \Delta n_1 \Delta n_2 \rangle \quad (13)$$

Furthermore, we assume that the phases of the complex field amplitudes are sufficiently random, so their product is always zero for unequal indices  $\langle c_\mu(z_1) c_\nu^*(z_2) \rangle \delta_{\mu\nu} = \langle c_{\mu,1} c_{\mu,2}^* \rangle \delta_{\mu\nu}$ . This property removes the summation over  $\nu$ , and we can express the ensemble average of the pointing vector as

$$\langle \mathcal{S} \rangle = \mathbf{e}_r Q(\theta) \sum_{\mu}^{\max} \int_{-\infty}^{\infty} e^{i(\beta_\mu z - \beta \mathbf{e}_r \cdot \mathbf{r})} \int_{-\infty}^{\infty} V_1 V_2 \langle c_{\mu,1} c_{\mu,2}^* \rangle \langle \Delta n_1 \Delta n_2 \rangle E_{\mu,1} E_{\mu,2}^* dV_1 dV \quad (14)$$

Now we rewrite the exponent as a scalar product of two vectors:

$$i(\beta_\mu z - \beta \mathbf{e}_r \cdot \mathbf{r}) = i(\beta_\mu \mathbf{e}_z - \beta \mathbf{e}_r) \cdot \mathbf{r} = -i \Delta \boldsymbol{\beta}_\mu \cdot \mathbf{r} \quad (15)$$

With this conversion, we recover the 3D Fourier transform  $\mathcal{F}_\mu^3$  which is now dependent on the summation index  $\mu$  and transforms from  $\mathbf{r}$  space to  $\Delta \boldsymbol{\beta}_\mu$  space. This is the space of the scattering vector added to the incident light to produce the change in direction as shown in Figure 1.

$$\langle \mathcal{S}(\Delta \boldsymbol{\beta}) \rangle = \mathbf{e}_r Q(\theta) \sum_{\mu}^{\max} \mathcal{F}_\mu^3 \left\{ \int_{-\infty}^{\infty} V_1 V_2 \langle c_{\mu,1} c_{\mu,2}^* \rangle \langle \Delta n_1 \Delta n_2 \rangle E_{\mu,1} E_{\mu,2}^* dV_1 \right\} \quad (16)$$

The next step is to recover the autocorrelation of the whole integral. We process the autocorrelation function  $\langle \Delta n_1 \Delta n_2 \rangle$  by splitting it into the autocovariance  $C_{nn} = \langle \Delta n_1 \Delta n_2 \rangle - \langle \Delta n_1 \rangle \langle \Delta n_2 \rangle$  and the product of the mean values  $\langle \Delta n_1 \rangle \langle \Delta n_2 \rangle$ . This separates the deterministic mean from the stochastic part which is now represented by the autocovariance. We apply the same procedure to the slowly varying amplitude  $c$  to obtain its autocovariance  $C_{cc}$  and its mean  $\langle c_{\mu,1} \rangle \langle c_{\mu,2}^* \rangle$  and get:

$$\begin{aligned} \langle c_{\mu,1} c_{\mu,2}^* \rangle \langle \Delta n_1 \Delta n_2 \rangle &= [C_{nn} + \langle \Delta n_1 \rangle \langle \Delta n_2 \rangle] [C_{cc} + \langle c_{\mu,1} \rangle \langle c_{\mu,2}^* \rangle] \\ &= C_{nn} C_{cc} + C_{cc} \langle \Delta n_1 \rangle \langle \Delta n_2 \rangle + C_{nn} \langle c_{\mu,1} \rangle \langle c_{\mu,2}^* \rangle \\ &\quad + \langle \Delta n_1 \rangle \langle \Delta n_2 \rangle \langle c_{\mu,1} \rangle \langle c_{\mu,2}^* \rangle \end{aligned} \quad (17)$$

When we insert this result back into Equation (16), we obtain four terms. We now assume that both stochastic processes are homogeneous, so their autocovariance is only dependent on  $\mathbf{r}$  and can be taken out of the integral  $\int dV_1$ . Then what remains inside is in all cases the autocorrelation function. Furthermore, we can write the autocorrelation separate from the autocovariance by using the convolution theorem  $\mathcal{F}_\mu^3\{AB\} = \mathcal{F}_\mu^3\{A\} \star \mathcal{F}_\mu^3\{B\}$

$$\begin{aligned} \langle S(\Delta\beta) \rangle = & \mathbf{e}_r Q(\theta) \sum_{\mu}^{\max} \left[ \mathcal{F}_{\mu}^3 \{C_m\} * \mathcal{F}_{\mu}^3 \{C_{cc}\} * \mathcal{F}_{\mu}^3 \{(VE_{\mu}) * (VE_{\mu})\} \right. \\ & + \mathcal{F}_{\mu}^3 \{C_{cc}\} * \mathcal{F}_{\mu}^3 \{(V\langle\Delta n\rangle E_{\mu}) * (V\langle\Delta n\rangle E_{\mu})\} \\ & + \mathcal{F}_{\mu}^3 \{C_m\} * \mathcal{F}_{\mu}^3 \{(V\langle c_{\mu}\rangle E_{\mu}) * (V\langle c_{\mu}\rangle E_{\mu})\} \\ & \left. + \mathcal{F}_{\mu}^3 \{(V\langle c_{\mu}\rangle \Delta n) E_{\mu}) * (V\langle c_{\mu}\rangle \Delta n) E_{\mu})\} \right] \end{aligned} \quad (18)$$

As the last step to simplify the equation, we use the Wiener–Khinchin theorem to turn the autocovariance into the absolute square of its Fourier transform which we call the variance spectral density function of the refractive index fluctuations  $S_m$  or the mode power amplitude  $S_{cc}$ . The same procedure is applied to the autocorrelations to get their respective spectral densities. We arrive at the final most general result of the scattering problem for the expected scattering pattern:

$$\begin{aligned} \langle S(\Delta\beta) \rangle = & \mathbf{e}_r Q(\theta) \sum_{\mu}^{\max} \left[ S_m * S_{cc} * \left| \mathcal{F}_{\mu}^3 \{VE_{\mu}\} \right|^2 \right. \\ & + S_{cc} * \left| \mathcal{F}_{\mu}^3 \{V\langle\Delta n\rangle E_{\mu}\} \right|^2 + S_m * \left| \mathcal{F}_{\mu}^3 \{V\langle c_{\mu}\rangle E_{\mu}\} \right|^2 \\ & \left. + \left| \mathcal{F}_{\mu}^3 \{V\langle c_{\mu}\rangle \Delta n) E_{\mu}\} \right|^2 \right] \end{aligned} \quad (19)$$

Our solution to the scattering problem is the sum of four terms, which all contain a deterministic diffraction part in the form of several power spectral densities. The influence of the stochastic processes appears as the convolution with the respective variance spectral density of the noise process. If it is far from its maximum value, for example, the dominant fluctuation wavelength is way larger than the wavelength of the scattering light, its shape can be approximated as a normalized radial exponential:  $S_{xx} \propto \exp[-|\Delta\beta|/\tau]$ .<sup>[16]</sup>

The result of the scattering problem includes the transformation from real into  $\Delta\beta$  space which has its point of origin at the pole of the sphere in Figure 1. Geometrically, all permitted vectors  $|\beta_i|$  and  $\beta_s$  have their tips confined to a spherical shell with the radius  $|\beta_i| = |\beta_s|$  centered on the scattering center, also shown in Figure 1. This stems from the restriction to elastic scattering of a monochromatic wave, which must obey the phase matching condition  $\beta_s \mathbf{e}_z + \Delta\beta = \beta_i \mathbf{e}_z$ . This means that the  $\Delta\beta$  vector always has a z-component in the range  $[-2\beta_i, 0]$ , so it is either negative or zero, positive z-values are not accessible.

## 2.1. Approximations to Improve the Usability

The previously derived model is useful to calculate a scattering pattern if all properties of the modification are known. For the experimentally observed scattering patterns the shape of the modification and the power spectral densities depend on a variety of experimental parameters that are partially stochastic. To be able to compare experiment and theory, we need to make some simplifying assumptions.

The first simplification is that the fiber core has only a slightly different refractive index compared to the cladding (which is fulfilled in the experiment, see Section 3), so we can apply the weakly guiding case, where all propagation constants merge into one  $\beta_{\mu} \approx \beta \approx n_0 k$ .<sup>[4]</sup> It follows that the 3D Fourier transform in Equation (19) no longer depends on  $\mu$ . Also, we assume that the electric field across the modification is approximately constant,

which effectively turns all the modes into plane waves with the transversal electric field  $E$  and the amplitude  $\langle c \rangle$ . The induced mean refractive index difference  $\langle \Delta n \rangle$  is also assumed to be constant. This enables us to factor out these constants including the integrated volume  $V^2 = (\int V dV)^2$  from the scattering problem. Additionally, we use the distributive property of the convolution to pull  $|\mathcal{F}^3\{V\}|^2$  out of the brackets. This leaves a term with the  $\delta$ -function as the identity operation of the convolution:

$$\begin{aligned} \frac{\langle S \rangle}{Q(|E| |\langle c \rangle | \langle \Delta n \rangle V)^2} = & \mathbf{e}_r \frac{|\mathcal{F}^3\{V\}|^2}{V^2} \\ & * \left[ \frac{S_m}{\langle \Delta n \rangle^2} * \frac{S_{cc}}{|\langle c \rangle|^2} + \frac{S_{cc}}{|\langle c \rangle|^2} + \frac{S_m}{\langle \Delta n \rangle^2} + \delta \right] \end{aligned} \quad (20)$$

We recall from Equation (10) that the  $\theta$  dependence is due to polarization and can be suppressed by observing the scattering through a polarizer to obtain  $Q(\theta) = Q$ . This formula shows that under these simplifying assumptions the total scattering power of a modification scales quadratically with  $V$ ,  $c$  &  $\Delta n$ . This property can act as a rule of thumb to estimate the scattering power of a modification and how to enhance or diminish the extent of light scattering. Additionally, the plane wave is no longer required to be a guided wave, therefore this formula can also be used to calculate the scattering of external waves, which pass through the fiber cladding from the outside.

## 2.2. Random-Shaped V

The preceding calculations assumed that the volume  $V$  of the ensemble of the scattering centers is always the same. If we want to find the expected value by averaging measurements, we also must consider that the shape of the scattering volume is changing: the surface is fluctuating about a mean. This can be implemented by applying the ensemble average in Equation (12) also to  $V_1 V_2$  and assume it is uncorrelated to the refractive index fluctuations and mode amplitudes in Equation (13). Then  $\mathcal{F}^3\{|V\}|^2$  in Equation (20) has to be replaced by  $\langle \mathcal{F}^3\{|V\}|^2 \rangle \approx \mathcal{F}^3\{|V\}|^2 * S_V$ . We make the approximation, that it is sufficient to convolute the volume with the power spectrum of the surface fluctuations to account for the random shape.

## 3. Experimental Section

The fiber, a commercially available step index optical fiber (Nufern 20/400 Precision Matched Passive LMA Double Clad Fiber: Core [NA = 0.065,  $\varnothing = 20 \mu\text{m}$ ], Cladding [NA = 0.46,  $\varnothing = 400 \mu\text{m}$ ]), was clamped to a motorized xy-table. The transparent plastic fiber coating was removed, and femtosecond laser pulses were focused into the fiber core with an NA = 0.25 microscope objective. The laser was a Ti:Sapphire regenerative laser amplifier system (Spectra Physics, Spitfire) emitting pulses at  $\lambda = 800 \text{ nm}$  with a duration of FWHM = 200 fs. A pulse energy of 2.5  $\mu\text{J}$  and 1 kHz repetition rate was used. A mechanical shutter was set to 2 s opening time, so the number of pulses per scattering center was approximately 2000. After one refractive index modification was induced into the fiber

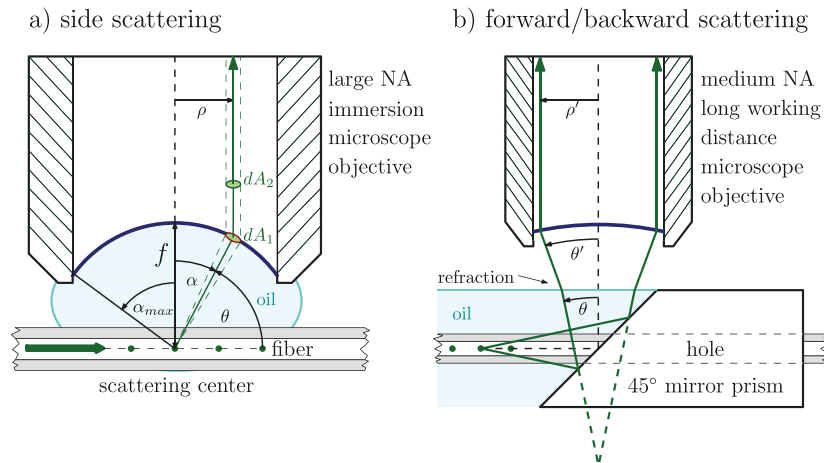


**Figure 2.** Fourier-microscopy for side, forward, and backward scattering. a) Rays spanning an angle  $\alpha$  with the optical axis (dashed) are transformed into parallel rays with a distance  $\rho$  by refraction on the reference sphere (blue) according to the Abbe sine condition  $\sin \alpha = \rho/f$ . Glycerol ( $n_0 = 1.46$ ) immersion eliminates refraction on the fiber surface. b) Rays with small scattering angles are reflected upward ( $\alpha \rightarrow \theta$ ) by a  $45^\circ$  mirror and collected with a long working distance microscope objective. Backscattering is measured by reversing the mirror. Both set ups were calibrated with a diffuse transmittance standard (opal glass Qsil-ilmasil<sup>[17]</sup>) to compensate for the objectives polarization dependent angular attenuation.<sup>[18]</sup>

core, the fiber was moved and the procedure was repeated at a distance of  $200 \mu\text{m}$  along the fiber. In this way, a chain of similar refractive index modifications was created in the fiber core. Sketches and images of the scattering center preparation can be found in ref. [11].

To measure the generated modifications and their scattering performance, the fiber was removed from the laser irradiation set up and coupled a green laser diode ( $\lambda = 520 \text{ nm}$ ) with a maximum power of  $100 \text{ mW}$  into one fiber end. The initial linear polarization of the diode was converted to circular with the aid of a quarter wave plate. The modified fiber segment was then placed under a microscope (Jenapol Interphako), where the scattering of the light on the modifications as well as the refractive index distortions themselves was observed. For real space images, phase contrast objectives ( $\text{NA} = 0.65$ ,  $\text{Mag} = 40$ ) were used to enhance the visibility of the scattering centers.

The principle of the angular scattering measurement is shown in **Figure 2**. Here, the property that light in the front focal plane, by passing through the objective, is decomposed into its angular components whose intensity distribution is then projected onto the back focal plane, was made use of.<sup>[7]</sup> This well-known behavior gives direct access to the far-field scattering pattern; it is often called the Fourier-transform capability of lenses, hence, the name Fourier microscopy. The back focal plane is imaged with the help of a Bertrand lens, which is placed in the beam path of the microscope<sup>[19]</sup> (in polarization microscopy this method is also known as conoscopy). An  $\text{NA} = 1.3$  oil immersion objective with a magnification of 100 was used for side scattering; for forward and backward scattering, a long-working-distance  $\text{NA} = 0.6$  air objective with a magnification of 50 and a custom made mirror prism with a hole for the fiber was employed. Interference microscopy with the immersion objective was also used to approximate the induced refractive index change inside of the modification.

## 4. Results

The focused femtosecond laser irradiation produces a localized refractive index modification in the fiber core, which can be imaged with phase contrast microscopy, as shown in **Figure 3**. In all observed instances, the modifications have a very similar shape, but the interior consists of refractive index fluctuations which differ significantly from one modification to the next. This is readily visible in the side view of **Figure 3**. When comparing top and side-view, we find that the modifications are approximately ellipsoidal, with dimensions of  $11.1 \mu\text{m}$  (length) by  $15.2 \mu\text{m}$  (height) by  $1.7 \mu\text{m}$  (width). In the inner regions, we determined an average refractive index change of  $\langle \Delta n \rangle = 0.023 \pm 0.007$  relative to the fiber core by means of microscope shearing interferometry. When light of the green laser diode is coupled into the fiber, the refractive index distortion visibly scatters the light (**Figure 3** right). From this scattering image as well as the shearing microscopy we observe that the effective scattering volume might be smaller than the limits of the modification visible in phase contrast.

### 4.1. Scattering Pattern of a Single Modification

Light scattered by modifications in the core is transported away from the fiber with almost no refraction due to the index-matching oil. This light eventually forms the far-field scattering pattern of the chain of scattering centers. If one modification is placed in the focus of the high NA objective, its far-field scattering pattern can be observed individually. The two observation directions presented in Fourier space (**Figure 4**) correspond to the real space directions shown in **Figure 3**.

In side view the scattered light forms a pattern of smooth but otherwise random-shaped bright grains which are separated by

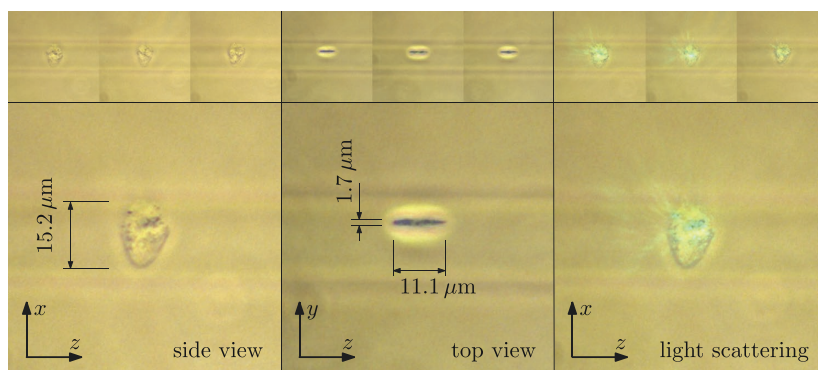


**Figure 3.** Phase contrast microscope images of the laser modifications in the fiber core. Top view is in the direction of laser irradiation and side view is orthogonal to it. Four images of similar scattering centers are provided (zoom in). The boundary of the fiber core shows up as two blurry horizontal lines in the background.

dark boundaries; a structure that is very similar to a laser speckle pattern. The grains are brighter on the right side (small  $\theta$ ) of the picture than on the left side (large  $\theta$ ), which means that the modification is predominately forward scattering.

In top view, we see a similar granular pattern to the broadside but with a wide dark band in the middle, crossing the picture horizontally. In the area of the dark band the grains appear less intense and vertically elongated. Also, the overall brightness in top view is lower than in side view: the imaging required roughly five times the exposure time.

Both pictures were taken with the analyzer polarization perpendicular to the direction of light propagation in the fiber while the light guided in the fiber is circularly polarized. If we set the analyzer polarization parallel to the fiber and look at the broadside of the scattering center, a vertical dark band appears in the center of the back focal plane image, crossing the image from the top to the bottom. This is a damping of the radiation which is strongest if the light is scattered perpendicular to the direction of propagation. The same phenomena of  $\theta$  dependent damping is also observed for the small side and independent of fiber rotation around the z-axis (not shown).

#### 4.2. Forward and Backward Scattering

Light scattered at very small or very large angles cannot be captured with the large NA immersion objective, because its opening angle is limited to  $\alpha_{\max} = \pm 62.9^\circ$  ( $27.1^\circ < \theta < 152.9^\circ$ ). To extend the observable angular range of the microscope, we used a mirror to reflect the forward and backward scattered light into the objective where we again image the back focal plane.

The images in **Figure 5** of forward (left) and backward (right) scattering show a central hole surrounded by concentric rings (very faint in backscattering). This pattern decreases in intensity and in distance in between the rings with increasing radius. Also, the brightness around the hole varies in magnitude: Its angular dependency is characterized by two bright lobes on opposing sides which are separated by a wider and dimmer scattering pattern.

The backward scattering shows almost now distinguishable pattern even though the exposure time in backscattering was 450 times longer than in forward scattering. Contrary to the side scattering in the previous subsection, the forward

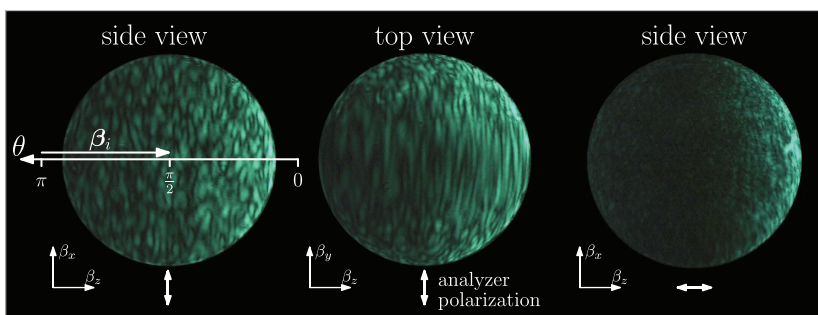


**Figure 4.** Back focal plane images of different perspectives and observation polarizations of the far-field scattering pattern from an excitation wavelength of 540 nm with circular polarization. Brighter colors mean more light exposure. The patterns were enhanced with histogram equalization, so they only allow for qualitative comparison. Views correspond to the real space images in **Figure 3**. Guided light crosses the pictures from the left to the right and is circularly polarized. Light on the right side of the circle is small angle forward scattering and on the left is large angle backward scattering. These images correspond to viewing the sphere from **Figure 1** along the  $\beta_x$ - or  $\beta_y$ -axis.

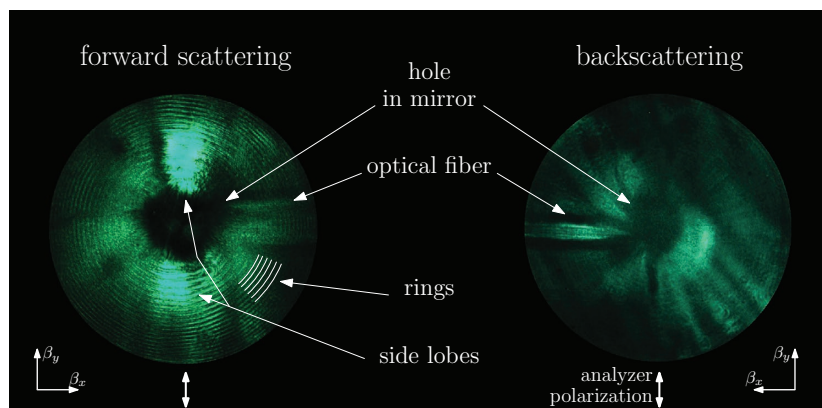


**Figure 5.** Forward and backward scattering pattern captured by reflecting the scattered radiation on a tilted mirror. In the middle of the picture is the hole where the fiber is threaded through the mirror (Figure 2). The optical fiber is bound by two dark horizontal lines and distorts the image beneath it. A pattern of concentric rings is centered on the hole, whose underlying intensity distribution shows an angular dependency: two bright lobes emerging from the hole pointing upward and downward. Rings in backscattering are very faint.

scattering does not show a strong polarization dependency in the intensity distribution on the picture.

The dark irregular shaped hole in the middle of the picture is where the fiber is threaded through the mirror. The fiber itself can be seen as two dark horizontal lines. In Section 5, it will turn out that the rings are probably a diffraction effect caused by the cylindrical shape of the fiber, they are not the main focus of this paper.

## 5. Discussion

The form of the scattering center is a product of overlapping femtosecond laser pulses in the focal spot in the core of the fiber. Before the focal spot is formed, the converging beam undergoes a refraction on the cylindrical fiber surface which introduces aberrations and turns the rotationally symmetric focal spot into a flat ellipsoid. Then, the overlapping of several laser pulses causes an evolutionary process inside the irradiated volume, which results in an average increase of the refractive index and the formation of stochastic fluctuations.<sup>[20]</sup>

The change in refractive index is attributed to the generation of a hot electron plasma which quickly (<10 ps) transfers its energy to the glass matrix. Micro explosions<sup>[21]</sup> for high pulse energies like in the present case produce random density fluctuations. It is well-known that fast heating and quenching leads to an increase in the glass' fictive temperature,<sup>[22,23]</sup> which, in the case of fused silica, is associated with an increase in refractive index.<sup>[13]</sup>

The measured mean value of  $\langle \Delta n \rangle = 0.023$  is very high for a modification in fused silica created with a femtosecond laser. Typical values recorded on optical waveguides are in the range of up to  $10^{-3}$  with a threshold value of  $3 \times 10^{-3}$ .<sup>[24,25]</sup> When higher pulse energies are applied for inscription, the waveguides start to be too strongly scattering to be functional. Both the energy range and the scattering effect are consistent with the present light scattering modifications which were produced at 2.5  $\mu$ J.

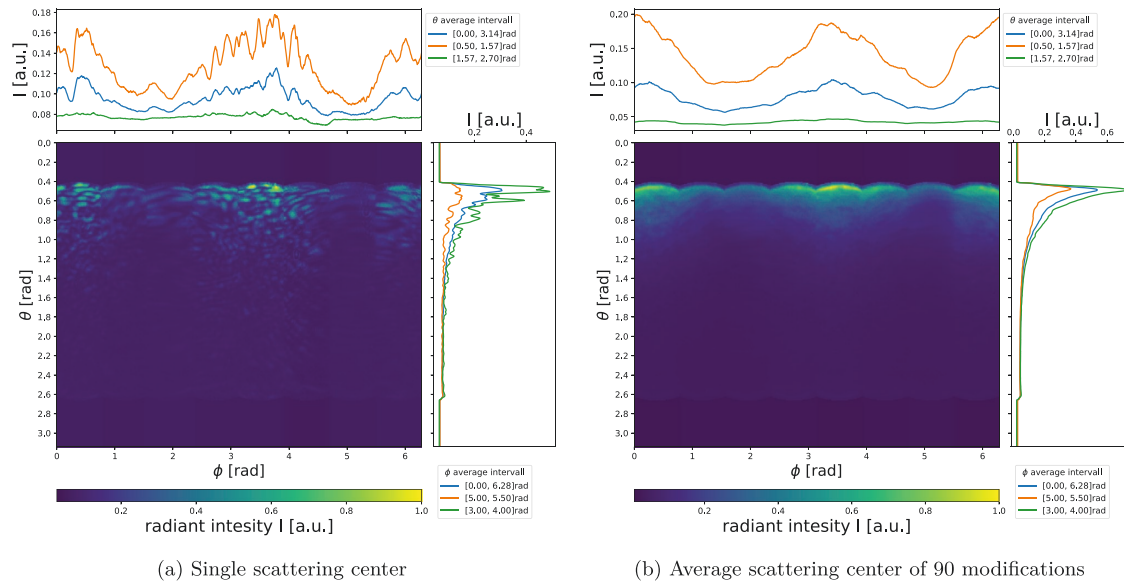
### 5.1. Speckles

The far-field grain pattern which is observed in the back focal plane of the objective as shown in Figure 4 is the result of the interaction of the laser light with the refractive index distortion. The shape of the grains is very similar to a laser speckle pattern which can be observed when a rough surface interacts with coherent monochromatic light.<sup>[26]</sup> Laser speckles are caused by the overlapping spherical wavelets with uncorrelated phase which are generated by multiple scattering regions on a rough surface.

In Section 2, we show that the pattern is a result of overlapping spherical wavelets generated by the interaction of the guided light with the refractive index fluctuations inside the modified volume. Also, due to the finite correlation length of the autocorrelation function, we obtain different contributing regions. We conclude that in the present case we generate volume speckles while common speckles are generated on a surface. The presence of speckles also signifies the spatial limitation of the (stochastic) interior of the modification: if the number of contributing regions would be large enough, the pattern becomes finer and smoothed-out; if there is a directional spatial limitation, the speckles get elongated as in the top view in Figure 4.

We also observe a strong dependency of the speckle pattern on polarization: one direction shows a strong  $\theta$  dependency. This is a result of the  $\cos \theta$  factor stemming from the polarization component  $\mathbf{e}_{\parallel}$  derived in Equation (7). Light, which is polarized parallel to the plane spanned by the incident and the scattered wave vector, cannot be scattered parallel to the polarization direction. This supports our idea that it is sufficient to image the  $\mathbf{e}_{\perp}$  component of the scattering pattern via filtering to obtain an undisturbed picture. Furthermore, this is also in agreement with the observation that forward and backward scattering patterns have no polarization dependence because in this angular range the cosine is almost unity.





(a) Single scattering center

(b) Average scattering center of 90 modifications

**Figure 6.** a) Maps of the far-field scattering pattern of a single modification assembled from eight back focal plane pictures which were imaged by rotating the fiber in steps of  $45^\circ$ . It shows the angular dependency of the far-field grain pattern. b) Average scattering map of 90 modifications. It shows the enveloping distribution which governs all scattering patterns. Both maps have constant spacing in polar  $\theta$  and azimuthal  $\phi$  angle.

## 5.2. Assembling an All-Around View and Averaging

The Fourier-plane images of Figure 4 show only a segment of the whole spherical far-field scattering pattern, which makes it difficult to compare the brightness of the angular distribution around the fiber. To obtain a more complete picture, we assembled a full  $360^\circ$  view in  $\phi$  by stitching together 8 perspectives which were imaged in steps of  $\Delta\phi = 45^\circ$ . The result is shown in Figure 6. It represents a map of the far-field side scattering pattern, which is still limited to  $0.47 < \theta < 2.67$  due to the maximum opening angle of the objective. Wrapping this map on a sphere comes closest to a true representation of the far-field scattering pattern where the modification is in the middle of the sphere as shown in Figure 1. The pattern itself consists of many small speckles. These are present on the whole map, but their brightness follows an enveloping pattern which depends on  $\theta$  and  $\phi$ . Their presence is harder to detect for large scattering angles  $\theta$  without enhancing the contrast of the pictures as in Figure 4. We average the normalized maps of 90 similar modifications for an estimate of the enveloping intensity distribution. This leads to the smooth average distribution in Figure 6b.

Both maps show the same overall features in  $\theta$  and  $\phi$ . A strong increase in scattering power with decreasing polar angle  $\theta$ , which means that the modifications are preferentially forward-scattering. Furthermore, the map shows a sinusoidal dependency of the brightness with the azimuthal angle  $\phi$ . By comparing the real space and the Fourier images we find that the bright lobes coincide with the broad side of the scattering center and the dark bands with the small side of the scattering center. This is consistent with the forward scattering pattern which shows the same feature as the two side lobes.

For very large scattering angles ( $\theta > \pi/2$ ), the far-field intensity approaches a low but constant value. This is the Rayleigh scattering background<sup>[7]</sup> caused by the increase in glass' fictive temperature<sup>[22,27,28]</sup> inside the modified volume. In the framework of our model, this can be treated as white noise background fluctuation which has a flat power spectrum.<sup>[4]</sup> Rayleigh scattering has no angular dependency in the present polarization direction, so it is treated as an additive constant to the angular scattering pattern.

Comparison of the single and the average map shows four important properties: First, the grain pattern is the noisy power spectrum of one realization of the stochastic fluctuations inside the modification (Equation (9)). Second, the feature of two bright and two dark regions in  $\phi$  as well as the increase in scattering for small  $\theta$  is a general property that all scattering centers share. Third, the  $\phi$ -dependency is a consequence of the ellipsoidal shape of scattering volume. Fourth, the decline of scattering power with  $\theta$  is rotational symmetric in  $\phi$  and therefore is caused by the radial functions  $S_{mn}$  and  $S_{cc}$ . The preferential forward scattering indicates that the power spectrum of the fluctuations has its maximum at way larger wavelengths than the scattered light. Therefore, it can be approximated by a radial exponential.

## 5.3. Computed Scattering Pattern

Having obtained the average scattering map, we now show that we can reproduce a qualitatively similar scattering pattern as laid out in Section 2. From Equation (20) we know that the average angular scattering distribution is caused by the superposition of four terms which all consist of a convolution with

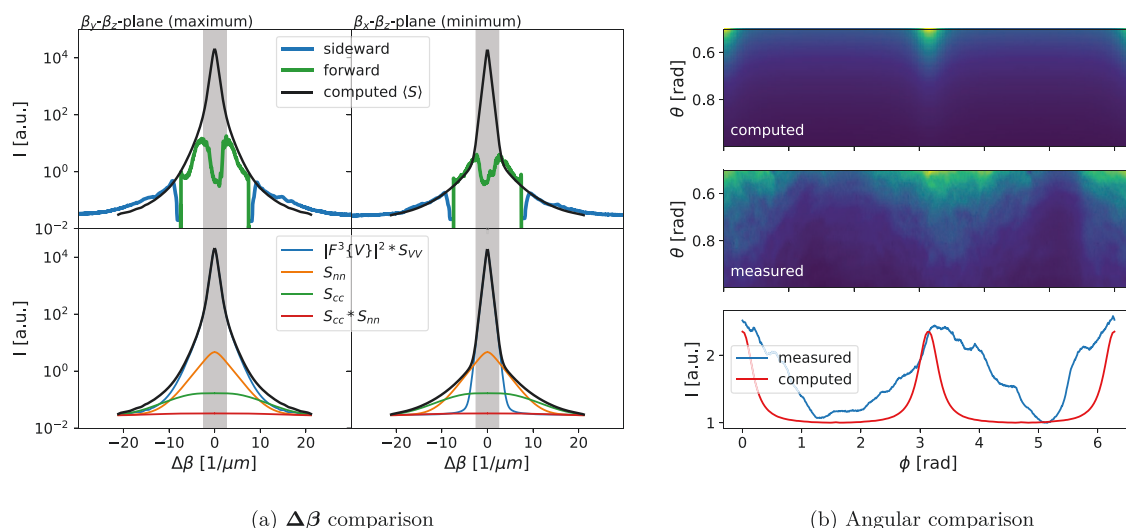


**Figure 7.** Comparison of the calculated scattering pattern with the measurements in forward and sideward scattering. The dip for small  $\Delta\beta$  is due to the hole in the mirror (gray area). Bottom: Contributions of the convolution terms from Equation (20) to the computed cumulative scattering pattern  $\langle S \rangle$ . b)  $\phi$  dependency of the calculated scattering pattern compared to the measured side scattering pattern. The patterns have been integrated with respect to  $\theta$  to yield the graph at the bottom.

the absolute square of the 3D Fourier transforms of the modified volume  $|\mathcal{F}^3\{V\}|^2$ .

The first step of the computation is to define the computational volume: The edge length in real space ( $l = 20 \mu\text{m}$ ) defines the smallest resolvable  $\Delta\beta_{\text{min}} = 1/l$  vector due to the scaling property of the Fourier transform. The relation between the largest  $\Delta\beta_{\text{max}} = \beta_i/2$  and the smallest defines the resolution  $\Delta\beta_{\text{max}}/\Delta\beta_{\text{min}}$ . Here the amount of computer memory available is the limiting factor for increasing the resolution because the data increases with the volume and therefore with resolution to the power of three (for this reason we choose only half of  $\beta_i$  to reduce computational effort). The modification is defined in the center of the computation grid as an ellipsoid ( $1 = x^2/a^2 + y^2/b^2 + z^2/c^2$ ) with the semi-axis corresponding to the measurements from Figure 3:  $a = 15.2 \mu\text{m}$ ,  $b = 1.7 \mu\text{m}$ , and  $c = 11.1 \mu\text{m}$ .

From this, we calculate the discrete Fourier transform and store it into an array. Additionally, we blur it with a normalized radial exponential  $S_{VV}$  ( $\tau = 0.3 \text{ cm}^{-1}$ ) to account for the random surface. Then the three other terms are computed by calculating the convolution with two different normalized exponentials representing  $S_{nn}$  ( $\tau = 2 \text{ cm}^{-1}$ ) and  $S_{cc}$  ( $\tau = 3 \text{ cm}^{-1}$ ) (the latter just acts in the  $z$ -direction). The  $\tau$ -values are chosen by hand to fit the measured curve and the results are weighted and added up. The final result is a 3D array in  $\Delta\beta$ -space, where we find the observed scattering pattern by extracting only the values on the spherical shell from Figure 1 by interpolation.

The general trend for forward and side scattering is reproduced by adjusting the weight of  $S_{nn}$  to 5% and of  $S_{cc}$  to 3.5% of the deterministic diffraction pattern  $\mathcal{F}^3\{V\}^2$ . This is presented in Figure 7 where we compare the calculations to both measurements. Since the angular range for side and forward scattering doesn't overlap, both measured curves require different normalization. Two graphs on the top left show the scat-

tering power over  $\Delta\beta$  in comparison to the calculation viewed as a slice through the maximum ( $\beta_y$ - $\beta_z$ -plane) and minimum ( $\beta_x$ - $\beta_y$ -plane). The contributions of the different convolutions are broken down in the corresponding images below: it shows that the expected scattering pattern for large  $\Delta\beta$  is determined by  $S_{cc}$ ; for intermediate by  $S_{nn}$  and for small by  $\mathcal{F}^3\{V\}^2 * S_{VV}$ . The latter also causes the asymmetry between minimum and maximum. The  $S_{nn} * S_{cc}$  term has almost no effect because it is too spread out.

Still, there are some noticeable deviations between computation and observation especially when we compare the whole map for sideward scattering in Figure 7 on the right. The modeled scattering lobes (maxima) are narrower than the observed ones even though they have almost the same amplitude. This is a consequence of the simple geometry of our calculated scattering center: the high aspect ratio of the ellipsoid leads to a very narrow diffraction pattern due to the reciprocal scaling property of the Fourier transform. This mismatch indicates that the real scattering center has a significantly more complex shape with a broader spectrum of large  $\Delta\beta$  components. Nevertheless, even the chosen simple geometry reproduces the same general properties in  $\phi$  and  $\theta$  which were observed in the experiment.

All deviations from the ideal optical fiber scatter light, therefore the presented model also helps to understand the observations made by other researchers.<sup>[8,9]</sup> Fonjallaz et al. and Janos et al. reported that light scattering of their fiber Bragg grating shows a similar azimuthal dependency with respect to the laser writing direction as in this experiment. We argue that this is also caused by the asymmetry of the refractive index modifications in the optical fiber; it is ultimately a consequence of the asymmetry of the focal volume: it is tighter focused in  $y$  than in  $z$ -direction due to the refraction of the femtosecond laser on the fiber surface. Consequently, the inverse scaling property of the

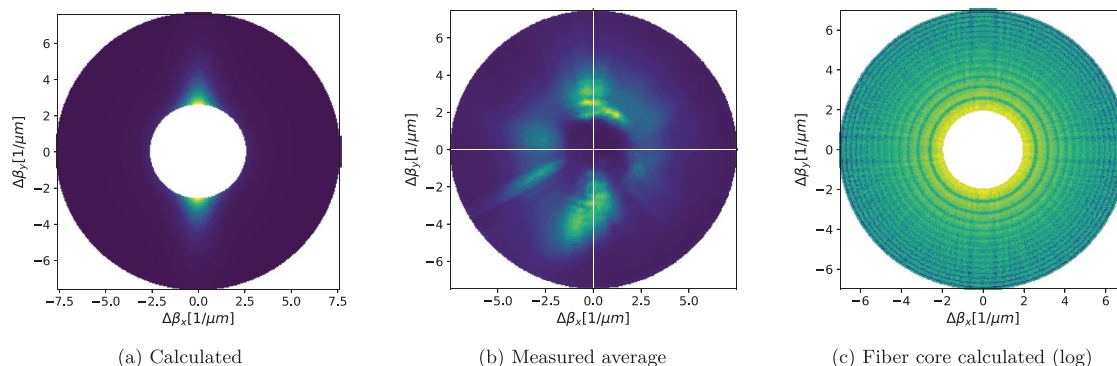


**Figure 8.** Images of the forward scattering pattern: a) Calculated scattering pattern for an ellipsoidal modification shows diffraction lobes but no ring structure. b) Measured average forward scattering pattern shows side lobes with visible rings. The white lines are the min/max cross sections where the forward scattering curves from Figure 7 were taken from. c) Calculated diffraction of a plane wave on the fiber core shows concentric rings (log scale).

Fourier transform turns the scattering pattern brighter in the direction of the smaller extent.

An important consequence of this finding is that the shape of the modification can be used to influence the  $\phi$ -dependency of the scattering pattern: If one wants to have it constant in  $\phi$ , the scattering center should be rotationally symmetric; if one wants to have a certain number of maxima in  $\phi$ , the modification should reflect this requirement in its symmetry. On the other hand, homogeneous scattering in  $\theta$  would require a flat power spectrum of  $S_{mn}$  in the range of the phase matching condition  $[-2\Delta\beta, 0]$ . As of writing this document, it is unknown how to selectively influence the spectra of the refractive index fluctuations with femtosecond laser irradiation. In a previous work,<sup>[11]</sup> we found the maximum scattering loss for similar modifications to be around 900 nm, which means that a maximum of  $S_{mn}$  could be in that range. So, while the modification is predominantly forward scattering in the visible, in the near infrared it could already be homogeneous.

#### 5.4. Forward Scattering Pattern

The concentric rings are the most prominent feature of the forward and backward scattering pattern. They were already observed by Rawson<sup>[7]</sup> in his investigation of scattering loss in unmodified optical fibers. He gave the interpretation that they are the circular symmetric equivalent of laser speckles. If this explanation can also be applied in this case, then averaging several pictures of them should remove the rings and give us the enveloping function like in the previous subsections. The average intensity distribution from 100 different positions is shown in Figure 8b. It shows that even though the rings become less sharp, a visible ring pattern remains, which implies the presence of a deterministic diffraction pattern.

This is unlikely a product of the modifications themselves because when we compute the scattering pattern as in the previous section, we obtain the result shown in Figure 8a. Here, we see two lobes emerging from the center of the computed forward scattering pattern, which neatly correspond to the observed lobes in forward scattering. This is the pattern of the

modification. The two-lobe shape is again due to the reciprocal scaling effect of the Fourier transform, it causes the scattering to be dominant in the direction of the smallest extent of the modification in real space. In this way the elliptical cross section is imprinted on the forward scattering as it was the case for the side scattering. The difference between the computed and the observed scattering pattern is because the shape of the real scattering center is only approximately an ellipsoid as we already mentioned in Section 5.3. We additionally computed the diffraction pattern of two modifications with a distance of 200  $\mu\text{m}$ , which shows the same two-lobe diffraction pattern (not shown), so we can rule out an interaction of several scattering centers.

Regarding an explanation for the circular ring pattern we argue that it originates either from the core-cladding or from the cladding-oil transition because it resembles an Airy disc. To demonstrate this in the framework of our present theoretical approach, we model the diffraction behavior by treating a section of the core itself as a refractive index distortion interacting with a plane wave. For modeling, we chose a cylindrical segment with a diameter of 20  $\mu\text{m}$  and a length of 30  $\mu\text{m}$ . The computational volume in real space was as long as the core segment in the  $z$ -direction but was extended to 80  $\mu\text{m}$  in  $x$  and  $y$ . This zero padding was done in order to increase frequency resolution to help to resolve the ring pattern.

The result of the calculation is shown in Figure 8c. The diffraction pattern shows concentric rings whose distance and intensity decreases from the inside to the outside. From this similarity we conclude that the pattern could be caused by the fiber core itself. The light flux fueling this phenomenon is probably the main diffraction lobe of the modification which is shown in Figure 7a but cannot be observed due to experimental restrictions (the hole in the mirror). This would make this a very low angle scattering effect no longer covered by the volume current method. This almost unknown effect could have implications for the development of long period fiber gratings because it could influence the coupling from core to cladding modes.<sup>[29]</sup>

There is certainly much ambiguity in setting the values of the equations. The problem at hand is that very little independently

measured data are available on the properties involved in the scattering process, especially the mean refractive index change and its variance. Nevertheless, future experiments could extract the power spectrum of the fluctuations from a fiber transmission measurement. Then the volume and the average refractive index change can be measured with microscopy techniques and the resulting scattering pattern could be calculated with less ambiguity and compared to the scattering measurements.

## 6. Conclusions

In conclusion, we derived an equation for the scattering pattern of a stochastic refractive index distortion of arbitrary shape in an optical fiber. This enables the calculation of the angular emission behavior as well as the interpretation of measurements for any kind of refractive index modification. The scattering power scales quadratically with the average induced refractive index change and the volume of the modification, which allows for precise quantitative control of the scattering process.

We experimentally determined the far-field scattering pattern of many similar refractive index modifications created with focused femtosecond laser irradiation: almost the full solid angle far-field scattering pattern was successfully imaged. This showed that while a single pattern is dominated by laser speckles, the average of several patterns follows an enveloping intensity distribution.

Several remarkable features of the scattering process could be assigned to different properties of the refractive index distortion by qualitatively comparing the calculated and the measured scattering patterns. We conclude that it is ultimately the shape of the scattering volume which determines the azimuthal dependency and that the power spectrum of the refractive index fluctuations determines the polar angle dependency. This property can now be used to engineer the angular distribution of the scattering pattern, which paves the way to a completely new class of tailored optical fiber emitters.

## Acknowledgements

This work was funded within the Entrepreneurial Regions scheme of the German Federal Ministry of Science and Education (TOF-Tailored Optical Fibers). Further support was obtained from the Deutsche Forschungsgemeinschaft (DFG) (259607349/GRK2101). The authors thank Eva Schlindwein and Robert Röder for fruitful discussions, Thomas Kittel for assistance with optical microscopy, Lutz Preiser for metalwork, Gabi Möller for fabrication of the prism and Christian Zeidler for electrical work.

## Conflict of Interest

The authors declare no conflict of interest.

## Keywords

femtosecond lasers, light scattering, line sources, refractive index modification, side-emitting optical fibers

Received: April 14, 2020

Revised: May 29, 2020

Published online: June 26, 2020

- [1] A. Rendon, J. Okawa, R. Weersink, J. Beck, L. Lilge, in *Optical Methods for Tumor Treatment and Detection: Mechanisms and Techniques in Photodynamic Therapy XVI* (Ed: D. Kessel), International Society for Optics and Photonics, Proc. SPIE, Vol. 6427, Bellingham, WA 2007, p. 64270M.
- [2] B. C. Wilson, M. S. Patterson, *Phys. Med. Biol.* **2008**, *53*, R61.
- [3] A.-A. Yassine, L. Lilge, V. Betz, *J. Biophotonics* **2018**, *12*, e201800153.
- [4] D. Marcuse, *Principles of Optical Fiber Measurements*, Elsevier, New York 1982.
- [5] D. Marcuse, *Theory of Dielectric Optical Waveguides*, 2nd ed., Academic Press, New York 1991.
- [6] Z. Pan, L. Wondraczek, *Sci. Rep.* **2018**, *8*, 9527.
- [7] E. G. Rawson, *Appl. Opt.* **1972**, *11*, 2477.
- [8] M. Janos, J. Canning, M. G. Sceats, *Opt. Lett.* **1996**, *21*, 1827.
- [9] P. Fonjallaz, H. G. Limberger, R. P. Salathe, *J. Lightwave Technol.* **1997**, *15*, 371.
- [10] L. Vesselov, W. Whittington, L. Lilge, *Appl. Opt.* **2005**, *44*, 2754.
- [11] A. Reupert, M. Heck, S. Nolte, L. Wondraczek, *Opt. Mater. Express* **2019**, *9*, 2497.
- [12] Y. Li, T. G. Brown, *J. Opt. Soc. Am. B* **2006**, *23*, 1544.
- [13] J. W. Chan, T. Huser, S. Risbud, D. M. Krol, *Opt. Lett.* **2001**, *26*, 1726.
- [14] I. White, *IEE J. Microwaves, Opt. Acoust.* **1979**, *3*, 186.
- [15] M. Kuznetsov, H. Haus, *IEEE J. Quantum Electron.* **1983**, *19*, 1505.
- [16] J. Hudson, *Q. J. Mech. Appl. Math.* **1968**, *21*, 487.
- [17] T. Kreuzberger, *US Patent App. 13/687,337*, **2013**.
- [18] M. Leutenegger, R. Rao, R. A. Leitgeb, T. Lasser, *Opt. Express* **2006**, *14*, 11277.
- [19] J. A. Kurvits, M. Jiang, R. Zia, *J. Opt. Soc. Am. A* **2015**, *32*, 2082.
- [20] K. Itoh, W. Watanabe, S. Nolte, C. B. Schaffer, *MRS Bull.* **2006**, *31*, 620.
- [21] E. N. Glezer, E. Mazur, *Appl. Phys. Lett.* **1997**, *71*, 882.
- [22] M. Lancry, E. Réginié, B. Poumellec, *Prog. Mater. Sci.* **2012**, *57*, 63.
- [23] T. Seuthe, A. Mermillod-Blondin, M. Grehn, J. Bonse, L. Wondraczek, M. Eberstein, *Sci. Rep.* **2017**, *7*, 43815.
- [24] D. Homoelle, S. Wielandy, A. L. Gaeta, N. F. Borrelli, C. Smith, *Opt. Lett.* **1999**, *24*, 1311.
- [25] S. Nolte, M. Will, J. Burghoff, A. Tünnemann, *Appl. Phys. A* **2003**, *77*, 109.
- [26] J. C. Dainty, *Laser Speckle and Related Phenomena*, Topics in Applied Physics, Vol. 9, Springer, New York 1975.
- [27] M. Lancry, B. Poumellec, J. Canning, K. Cook, J.-C. Poulin, F. Brisset, *Laser Photonics Rev.* **2013**, *7*, 953.
- [28] B. Champagnon, L. Wondraczek, T. Deschamps, *J. Non-Cryst. Solids* **2009**, *355*, 712.
- [29] M. Heck, G. Schwartz, R. G. Krämer, D. Richter, T. A. Goebel, C. Matzdorf, A. Tünnemann, S. Nolte, *Opt. Express* **2019**, *27*, 4292.

## 4 Summary

The presented dissertation focuses on the development of theoretical and experimental tools for modeling, fabrication, characterization, and optimization of side-emitting optical fibers. For this purpose, phenomenological and electrodynamic models were developed and applied.

In summary, this work establishes that the fiber radiation distribution can be traced to the influence of two parameters, longitudinal emission and angular emission. It shows how to use laser-induced scattering centers and a phenomenological model to shape the longitudinal emission profile of a fiber. Furthermore, the electrodynamic nature of the scattering process is derived. It shows how the stochastic and deterministic properties of the laser-induced modifications can be used to influence the angular scattering pattern and the overall scattering performance. This knowledge paves the way for the generation of fully customizable side-emitting fibers by femtosecond laser processing.

This section summarizes the findings on side-emitting optical fibers in this work as follows: It describes the results of the calculation of *the radiation field* in terms of the influence of two model parameters: *the longitudinal emission* and *the angle-dependent emission*. These parameters are then summarized separately for the specific case of femtosecond laser-induced scattering centers with attention to their tuning.

### The Radiation Field

The findings of this thesis change the way side-emitting fiber radiation can be calculated in free-space lighting applications. The use of a simple line source model and two phenomenological parameters, longitudinal and angular emission, greatly simplifies the calculation of the generated light field and the evaluation of fiber performance for specific applications.

The radiation field was calculated using a radiometric model based on the superposition principle: The field at a point in space is the sum of all rays coming from the side-emitting fiber surface and intersecting at that point. From this method, the flux density, also called irradiance, is obtained. The fiber parameters, longitudinal and angular emission, used in the model were gained from experimental observations. From combining the model and parameters, it was found that longitudinal emission affects the radiance near the fiber, and angular emission influences the field far from the fiber. The calculations showed almost no difference between regarding the fiber as a line source or a cylindrical source, so the simpler line source model can be used to calculate the radiation field.

#### 4 Summary

Commercial side-emitting plastic optical fibers and fiber fabrics were used to test the models and obtain the phenomenological parameters of the model. In addition, the generated radiation field of a side-emitting fiber fabric was measured for comparison with the calculated field. The fibers and band exhibited a bi-exponential decline of the longitudinally emitted radiation and a preferential forward-directed angular radiation.

This angular dependence projected the radiation field forward so that the generated light distribution moved toward the fiber end with increasing radial distance from the fiber. This effect only noticeably affects the field at a certain distance from the fiber and is caused by the refractive index fluctuations inside the fiber, which are responsible for light scattering in the fiber. The forward scattering shows that the spectrum of the fluctuations is dominated by long periodic fluctuations.

The bi-exponential decline in the fiber emission causes a sharp decaying maximum at the beginning, which is visually unpleasing and can lead to overexposure in technical applications (e.g. microalgae reactor). Light coupling causes this effect because cladding and core modes are excited simultaneously but have different attenuations. The cladding modes experience more scattering because they interact with the fiber surface. Either blocking the corresponding sections of the fiber or a more elaborate light source coupling could circumvent this effect.

Alternatively, we devised new strategies for light coupling into fibers, partially based on Spegulis et al. [14]: light coupling from both sides, using a fiber end mirror, switching the coupling side between adjacent fibers, and a combination of the latter strategies. Comparison of the calculated radiation fields showed that alternating coupling between adjacent fibers in fiber fabrics provides a simple solution to obtain more homogeneous illumination by using only the same number of couplings as basic single-sided coupling.

These phenomenological models for side-emitting fibers, along with their comparison to measurements, contributed to the literature on side-emitting fibers in three ways: First, I showed that for free-space applications without absorption, it is sufficient to use the simple line-source approximation to calculate the generated radiation field regardless of distance. So far, only the cylindrical source has been used in the literature [24, 25]. Second, near the fiber, it is sufficient to consider only the longitudinal emission; the parameters of the angle-dependent emission need only be included if the field must be calculated at some distance from the fiber. This influence of the angle-dependent emission characteristics has not yet been studied in the literature. And third, the models can be used to calculate the resulting light field of multiple fibers by superposition, leading to the discovery of a new coupling strategy for fiber fabrics: alternating coupling of the light source. This strategy provides a more homogeneous illumination of a fabric containing fibers with exponentially decreasing emission profiles.

## The Longitudinal Emission

The calculation of the radiation field has shown that the longitudinal emission is the critical factor when using the light field near the fiber. This situation occurs in volumetric illumination of turbid media such as in phototherapy or an algae reactor. For ideal illumination, the goal is to generate arbitrary or flat emission profiles. For this purpose, this thesis presents a new technique for fabricating side-emitting fibers with focused femtosecond laser radiation. These tailored fibers do not require secondary light light-coupling.

The irradiation creates scattering centers in the fiber, which we use as building blocks to change the scattering coefficient as a function of position. Since we can control the density of scattering centers per unit length in the fiber, we have a method to adjust the amount of scattering per unit length. This method demonstrates how side-emitting fibers can be made from standard optical fibers with a transparent coating without further mechanical or chemical preparation. The little preparation required will greatly simplify the fabrication and customization process.

Based on this idea, I derived a phenomenological model to describe the longitudinal emission profile that discrete scattering centers produce. In this case, it was not enough to treat the fiber as a single conducting core; I also had to include the light-guiding ability of the cladding. This led to a model of energy exchange between the core, cladding, and free space, which I described with three coupled differential equations. Here, the scattering coefficients served as coupling coefficients between the states of the model, which must be determined by measurement.

The system of coupled differential equations for constant scattering coefficients yielded a bi-exponential decay of emission and transmission for a fiber with two energy levels. This bi-exponential behavior was observed experimentally for a constant density of scattering centers per unit length (and for commercial side-emitting fibers). The comparison between emission and transmission showed that laser processing introduces negligible absorption losses so that a transmission measurement can determine the scattering coefficients. The model shows that the transmission depends only on the number of scattering centers but not on their placement if the modifications can be treated independently and absorption is neglected. Thus, if the scattering coefficient is known, it can be used to shape the emission profile of the fiber by selective placement of the scattering centers. This leads to a stretching or compression of the two exponents, which can be used to adjust the emission profile.

The experiment and energy exchange model contributes to the literature on side-emitting fibers in two ways: First, it shows that even assuming a steady-state energy distribution in the fiber, two states are still necessary to describe light propagation in the core and cladding, resulting in a striking double exponential decay, even for commercial side-emitting fibers as in Section 2.1. Previously, only a single exponential decay was considered [38, 14, 24]. Second, it has been shown that femtosecond laser-induced scattering centers can be used as building blocks to construct arbitrary emission profiles by controlling their density in the fiber without mechanical preparation. Previous laser processing techniques for side emission used

long-period fiber gratings and required cladding removal and hydrogen loading [26].

### **The Angular Emission**

The calculation of the radiation field has shown that the angular emission determines the far field of the fiber radiation. The findings of this work show a new way to understand the angular scattering of light in optical fibers from general refractive index modifications. It discusses how the scattered radiation represents the spectrum of polarization currents induced in the modification by interaction with the guided light in the fiber. This idea shows how to influence the scattering behavior by controlling the shape, refractive index difference, and stochastic properties of the scattering center.

The interaction of the refractive index change with the guided light in the fiber causes the light emission. Measurements on laser-induced scattering centers show that it is preferentially forward-directed and has two maxima and two minima in the scattering power around the fiber. Since phenomenological models do not provide further insight, I developed an electrodynamic model based on Maxwell's equations to describe the scattering process. It shows the influence of the changes in the refractive index and its stochastic fluctuations on the angular emission. From the calculated scattering patterns, I concluded that dominant large wavelength fluctuations cause the forward scattering and that the asymmetric shape of the scattering center causes the angular dependence around the fiber. This reasoning can also be applied to commercial side-emitting fibers, which also exhibit forward scattering.

I used the volume current method to derive a scattering model of a stochastic refractive index distribution. Under some approximations, the complicated process that generates the far-field scattering pattern was shown to reduce to a Fourier transform and several convolutions. These procedures can be quickly implemented with today's computer technology. The basis is the three-dimensional Fourier transform of the modified volume of the scattering center. This transformed volume is then convolved with several power spectra representing the various stochastic processes that contribute to the scattering. These are the fluctuating envelope of the scattering centers, the refractive index fluctuations within the modifications, and the fluctuation of the power carried by the scattered electromagnetic wave. Furthermore, the model showed that the scattering power scales quadratically with the volume of the scattering center and the refractive index difference from the surroundings.

This thesis contributes to the literature on light scattering in optical fibers by describing localized stochastic refractive index changes using electrodynamics. Previous work described localized periodic structures such as fiber Bragg gratings [39] or nonlocalized stochastic perturbations with zero-mean or Rayleigh scattering [31]. Moreover, the contribution of this work to the literature on customizable side-emitting fibers is fourfold: First, it showed that the forward scattering property



is caused by the power spectrum of the refractive index fluctuation. Second, it showed that the azimuthal scattering depends on the easily changeable external shape of the scattering center. And third, it was shown that the scattering power scales quadratically with the volume of the scattering center and the refractive index change.

## 5 Zusammenfassung

Die vorliegende Dissertation befasst sich mit der Entwicklung von theoretischen und experimentellen Werkzeugen zur Modellierung, Herstellung, Charakterisierung und Optimierung von seitenemittierenden optischen Fasern. Zu diesem Zweck wurden phänomenologische und elektrodynamische Modelle entwickelt und angewendet.

Zusammenfassend stellt diese Arbeit fest, dass die Strahlungsverteilung der Faser auf den Einfluss von zwei Parametern, der longitudinalen Emission und der winkelabhängigen Emission, zurückgeführt werden kann. Sie zeigt, wie man mit Hilfe von laserinduzierten Streuzentren und einem phänomenologischen Modell das longitudinale Emissionsprofil einer Faser gestalten kann. Außerdem wird die elektrodynamische Natur des Streuprozesses abgeleitet. Es wird gezeigt, wie die stochastischen und deterministischen Eigenschaften der laserinduzierten Modifikationen genutzt werden können, um das winklige Streumuster und die Gesamtstreuleistung zu beeinflussen. Dieses Wissen ebnet den Weg für die Erzeugung von vollständig anpassbaren seitenemittierenden Fasern durch Femtosekunden-Laserbearbeitung.

Dieser Abschnitt fasst die Erkenntnisse über seitenemittierende optische Fasern in dieser Arbeit wie folgt zusammen: Er beschreibt die Ergebnisse der Berechnung von *das Strahlungsfeld* in Bezug auf den Einfluss von zwei Modellparametern: *die longitudinale Emission* und *die winkelabhängige Emission*. Diese Parameter werden dann separat für den speziellen Fall von Femtosekundenlaser-induzierten Streuzentren zusammengefasst, mit Augenmerk auf deren Optimierung.

### Das Strahlungsfeld

Die Erkenntnisse dieser Arbeit verändern die Art und Weise, wie seitenemittierende Faserstrahlung in Beleuchtungsanwendungen im freien Raum berechnet werden kann. Die Verwendung eines einfachen Linienquellenmodells und zweier phänomenologischer Parameter, der longitudinalen und der winkelabhängigen Emission, vereinfacht die Berechnung des erzeugten Lichtfeldes und die Bewertung der Faserleistung für spezifische Anwendungen erheblich.

Das Strahlungsfeld wurde mit Hilfe eines radiometrischen Modells berechnet, das auf dem Superpositionsprinzip basiert: Das Feld an einem Punkt im Raum ist die Summe aller Strahlen, die von der seitenemittierenden Faseroberfläche kommen und sich in diesem Punkt kreuzen. Aus dieser Methode ergibt sich die Flussdichte, auch Bestrahlungsstärke genannt. Die im Modell verwendeten Faserparameter, longitudinale und winkelabhängige Emission, wurden aus experimentellen Beobachtungen gewonnen. Durch die Kombination von Modell und Parametern wurde festgestellt, dass die longitudinale Emission die Strahldichte in der Nähe der Faser beeinflusst

und die winkelförmige Emission das Feld fern der Faser. Die Berechnungen zeigten fast keinen Unterschied zwischen der Betrachtung der Faser als Linienquelle oder als zylindrische Quelle, so dass das einfachere Linienquellenmodell für die Berechnung des Strahlungsfeldes verwendet werden kann.

Kommerzielle seitenemittierende optische Kunststofffasern und Fasergewebe wurden verwendet, um die Modelle zu testen und die phänomenologischen Parameter des Modells zu erhalten. Darüber hinaus wurde das erzeugte Strahlungsfeld eines seitenemittierenden Fasergewebes zum Vergleich mit dem berechneten Feld gemessen. Die Fasern und das Band zeigten einen bi-exponentiellen Abfall der längs emittierten Strahlung und eine bevorzugt vorwärts gerichtete Winkelstrahlung.

Diese Winkelabhängigkeit projizierte das Strahlungsfeld nach vorne, so dass sich die erzeugte Lichtverteilung mit zunehmendem radialen Abstand von der Faser in Richtung des Faserendes bewegte. Dieser Effekt wirkt sich nur in einem bestimmten Abstand von der Faser merklich auf das Feld aus und wird durch die Brechungsindexschwankungen innerhalb der Faser verursacht, die für die Lichtstreuung in der Faser verantwortlich sind. Die Vorwärtsstreuung zeigt, dass das Spektrum von langwelligen Fluktuationen dominiert wird.

Der bi-exponentielle Abfall in der Faseremission bewirkt ein scharf abfallendes Maximum am Anfang, was optisch störend ist und bei technischen Anwendungen (z.B. Mikroalgenreaktor) zu einer Überbelichtung führen kann. Die Lichtkopplung verursacht diesen Effekt, weil Mantel- und Kernmoden gleichzeitig angeregt werden, aber unterschiedliche Dämpfungen haben. Die Mantelmoden erfahren mehr Streuung, weil sie mit der Faseroberfläche wechselwirken. Entweder das Blockieren der entsprechenden Abschnitte der Faser oder eine aufwändigere Lichtquellenkopplung könnte diesen störenden Effekt umgehen.

Alternativ haben wir neue Strategien für die Lichteinkopplung in Fasern entwickelt, die teilweise auf Spegulis et al. beruhen: Lichteinkopplung von beiden Seiten, Verwendung eines Faserendspiegels, Wechsel der Einkoppelseite zwischen benachbarten Fasern und eine Kombination der letztgenannten Strategien. Der Vergleich der berechneten Strahlungsfelder zeigte, dass die alternierende Kopplung zwischen benachbarten Fasern in Fasergeweben eine einfache Lösung darstellt, um eine homogenere Ausleuchtung zu erhalten, wobei nur die gleiche Anzahl von Kopplungen verwendet wird wie bei der einfachen einseitigen Kopplung.

Diese phänomenologischen Modelle für seitenemittierende Fasern, zusammen mit ihrem Vergleich mit Messungen, trugen auf drei Arten zur Literatur über seitene-mittierende Fasern bei: Erstens habe ich gezeigt, dass es für Freiraumanwendungen ohne Absorption ausreicht, die einfache Linienquellen-Näherung zu verwenden, um das erzeugte Strahlungsfeld unabhängig vom Abstand zu berechnen. Bislang wurde in der Literatur nur die zylindrische Quelle verwendet [24, 25]. Zweitens ist es in der Nähe der Faser ausreichend, nur die longitudinale Emission zu betrachten; die Parameter der winkelabhängigen Emission müssen nur einbezogen werden, wenn das Feld in einiger Entfernung von der Faser berechnet werden muss. Dieser Einfluss der winkelabhängigen Emissionscharakteristik ist in der Literatur noch nicht untersucht worden. Und drittens kann mit den Modellen das resultierende Lichtfeld

mehrerer Fasern durch Überlagerung berechnet werden, was zur Entdeckung einer neuen Kopplungsstrategie für Fasergewebe führt: die alternierende Kopplung der Lichtquelle. Diese Strategie ermöglicht eine homogenere Ausleuchtung durch ein Gewebe, das Fasern mit exponentiell abnehmenden Emissionsprofilen enthält.

### Die longitudinale Emission

Die Berechnung des Strahlungsfeldes hat gezeigt, dass die longitudinale Emission der kritische Faktor ist, wenn das Lichtfeld nahe der Faser genutzt wird. Diese Situation tritt bei der volumetrischen Beleuchtung von trüben Medien auf, wie z.B. in der Phototherapie oder einem Algenreaktor. Für eine ideale Beleuchtung ist es das Ziel, beliebige oder flache Emissionsprofile zu erzeugen. Zu diesem Zweck wird in dieser Arbeit eine neue Technik zur Herstellung von seitenemittierenden Fasern mit fokussierter Femtosekundenlaserstrahlung vorgestellt. Diese maßgeschneiderten Fasern benötigen keine sekundäre Lichteinkopplung.

Durch die Bestrahlung werden in der Faser Streuzentren erzeugt, die wir als Bausteine nutzen, um den Streukoeffizienten selektiv in Abhängigkeit von der Position zu verändern. Da wir die Dichte der Streuzentren pro Längeneinheit in der Faser kontrollieren können, haben wir eine Methode, um die Menge der Streuung pro Längeneinheit einzustellen. Diese Methode demonstriert, wie seitenemittierende Fasern aus Standard-Lichtleitfasern mit einer transparenten Beschichtung ohne weitere mechanische oder chemische Präparation hergestellt werden können. Die geringe erforderliche Vorbereitung wird den Herstellungs- und Anpassungsprozess erheblich vereinfachen.

Basierend auf dieser Idee habe ich ein phänomenologisches Modell abgeleitet, um das longitudinale Emissionsprofil zu beschreiben, das diskrete Streuzentren erzeugen. In diesem Fall reichte es nicht aus, die Faser als einen einzelnen leitenden Kern zu behandeln; ich musste auch die lichtleitende Fähigkeit des Mantels mit einbeziehen. Dies führte zu einem Modell des Energieaustauschs zwischen Kern, Mantel und freiem Raum, das ich mit drei gekoppelten Differentialgleichungen beschrieb. Dabei dienten die Streukoeffizienten als Kopplungskoeffizienten zwischen den Zuständen des Modells, die durch Messung bestimmt werden müssen.

Das System der gekoppelten Differentialgleichungen für konstante Streukoeffizienten ergab ein bi-exponentielles Abklingen von Emission und Transmission für eine Faser mit zwei Energieniveaus. Dieses bi-exponentielle Verhalten wurde experimentell für eine konstante Dichte von Streuzentren pro Längeneinheit (und für kommerzielle seitenemittierende Fasern) beobachtet. Der Vergleich zwischen Emission und Transmission zeigte, dass die Laserbearbeitung vernachlässigbare Absorptionsverluste mit sich bringt, so dass eine Transmissionsmessung die Streukoeffizienten bestimmen kann. Das Modell zeigt, dass die Transmission nur von der Anzahl der Streuzentren abhängt, nicht aber von deren Platzierung, wenn die Modifikationen unabhängig behandelt werden können und die Absorption vernachlässigt wird. Wenn also der Streukoeffizient bekannt ist, kann er verwendet werden, um das

Emissionsprofil der Faser durch gezielte Platzierung der Streuzentren zu gestalten. Dies führt zu einer Streckung oder Stauchung der beiden Exponenten, die zur Anpassung des Emissionsprofils genutzt werden kann.

Das Experiment und das Energieaustauschmodell tragen in zweierlei Hinsicht zur Literatur über seitenemittierende Fasern bei: Erstens zeigt es, dass selbst unter der Annahme einer stationären Energieverteilung in der Faser immer noch zwei Zustände notwendig sind, um die Lichtausbreitung im Kern und im Mantel zu beschreiben, was zu einem auffälligen doppelten exponentiellen Abklingen führt, selbst für kommerzielle seitenemittierende Fasern wie in Section 2.1. Zuvor wurde nur ein einfacher exponentieller Zerfall betrachtet [38, 14, 24]. Zweitens wurde gezeigt, dass Femtosekundenlaser-induzierte Streuzentren als Bausteine verwendet werden können, um beliebige Emissionsprofile zu konstruieren, indem man ihre Dichte in der Faser ohne mechanische Präparation kontrolliert. Bisherige Laserbearbeitungstechniken für Seitenemission verwendeten langperiodische Fasergitter und erforderten eine Mantelentfernung und Wasserstoffbeladung [26].

## Die winkelabhängige Emission

Die Berechnung des Strahlungsfeldes hat gezeigt, dass die winkelabhängige Emission das Fernfeld der Faserabstrahlung bestimmt. Die Erkenntnisse dieser Arbeit zeigen einen neuen Weg zum Verständnis der Winkelstreuung von Licht in optischen Fasern aus allgemeinen Brechungsindexänderungen. Es wird diskutiert, wie die gestreute Strahlung das Spektrum der Polarisationsströme repräsentiert, die in der Modifikation durch Wechselwirkung mit dem geführten Licht in der Faser induziert werden. Diese Idee zeigt, wie man das Streuverhalten durch Kontrolle der Form, der Brechungsindexdifferenz und der stochastischen Eigenschaften des Streuzentrums beeinflussen kann.

Die Wechselwirkung der Brechungsindexänderung mit dem geführten Licht in der Faser verursacht die Lichtemission. Messungen an laserinduzierten Streuzentren zeigen, dass es bevorzugt vorwärts gerichtet ist und zwei Maxima und zwei Minima in der Streuleistung um die Faser aufweist. Da phänomenologische Modelle keine weiteren Erkenntnisse liefern, habe ich ein elektrodynamisches Modell auf der Basis der Maxwell'schen Gleichungen entwickelt, um den Streuprozess zu beschreiben. Es zeigt den Einfluss der Änderungen des Brechungsindex und seiner stochastischen Fluktuationen auf die Winkelabstrahlung. Aus den berechneten Streumustern habe ich geschlossen, dass dominante große Wellenlängenfluktuationen die Vorwärtsstreuung verursachen und dass die asymmetrische Form des Streuzentrums die Winkelabhängigkeit um die Faser verursacht. Diese Argumentation lässt sich auch auf kommerzielle seitenemittierende Fasern anwenden, die ebenfalls Vorwärtsstreuung aufweisen.

Ich habe die Volumenstrommethode verwendet, um ein Streumodell einer stochastischen Brechungsindexverteilung herzuleiten. Unter einigen Näherungen wurde gezeigt, dass sich der komplizierte Prozess, der das Fernfeld-Streumuster erzeugt, auf

## 5 Zusammenfassung

eine Fourier-Transformation und mehrere Faltungen reduziert. Verfahren, die mit heutiger Computertechnik schnell implementiert werden können. Die Basis ist die dreidimensionale Fourier-Transformation des modifizierten Volumens des Streuzentrums. Dieses transformierte Volumen wird dann mit mehreren Leistungsspektren gefaltet, die die verschiedenen stochastischen Prozesse repräsentieren, die zur Streuung beitragen. Dies sind die fluktuierende Einhüllende der Streuzentren, die Brechungsindexfluktuationen innerhalb der Modifikationen und die Fluktuation der Leistung, die von der gestreuten elektromagnetischen Welle getragen wird. Weiterhin zeigte das Modell, dass die Streuleistung quadratisch mit dem Volumen des Streuzentrums und der Brechungsindexdifferenz zur Umgebung skaliert.

Diese Arbeit trägt zur Literatur über Lichtstreuung in optischen Fasern bei, indem sie lokalisierte stochastische Brechungsindexänderungen mit Hilfe der Elektrodynamik beschreibt. Frühere Arbeiten beschrieben lokalisierte periodische Strukturen wie Faser-Bragg-Gitter [39] oder nichtlokalisierte stochastische Störungen mit Mittelwert Null oder Rayleigh-Streuung [31]. Darüber hinaus ist der Beitrag dieser Arbeit zur Literatur über anpassbare seitenemittierende Fasern vierfach: Erstens zeigte sie, dass die Eigenschaft der Vorwärtsstreuung durch das Leistungsspektrum der Brechungsindexfluktuation verursacht wird. Zweitens wurde gezeigt, dass die azimutale Streuung von der leicht veränderbaren äußeren Form des Streuzentrums abhängt. Und drittens wurde gezeigt, dass die Streuleistung quadratisch mit dem Volumen des Streuzentrums und der Brechungsindexänderung skaliert.

## Bibliography

- [1] Kok-Keong Chong et al. “Design and construction of active daylighting system using two-stage non-imaging solar concentrator.” In: *Applied Energy* 207 (2017). Transformative Innovations for a Sustainable Future – Part II, pp. 45–60. ISSN: 0306-2619. DOI: <https://doi.org/10.1016/j.apenergy.2017.05.188>. URL: <https://www.sciencedirect.com/science/article/pii/S030626191730750X>.
- [2] Irfan Ullah and Allen Jong-Woei Whang. “Development of optical fiber-based daylighting system and its comparison.” In: *Energies* 8.7 (2015), pp. 7185–7201.
- [3] Lothar Wondraczek et al. “Biomimetic light dilution using side-emitting optical fiber for enhancing the productivity of microalgae reactors.” In: *Scientific reports* 9.1 (2019), pp. 1–10.
- [4] Mariana Lanzarini-Lopes et al. “Optical fiber-mediated photosynthesis for enhanced subsurface oxygen delivery.” In: *Chemosphere* 195 (2018), pp. 742–748. ISSN: 0045-6535. DOI: <https://doi.org/10.1016/j.chemosphere.2017.12.089>. URL: <https://www.sciencedirect.com/science/article/pii/S0045653517320593>.
- [5] Mariana Lanzarini-Lopes et al. “Nanoparticle and Transparent Polymer Coatings Enable UV-C Side-Emission Optical Fibers for Inactivation of Escherichia coli in Water.” In: *Environmental science & technology* 53.18 (2019), pp. 10880–10887.
- [6] Serge Mordon et al. “Light emitting fabric technologies for photodynamic therapy.” In: *Photodiagnosis and photodynamic therapy* 12.1 (2015), pp. 1–8.
- [7] Abdul-Amir Yassine, Lothar Lilge, and Vaughn Betz. “Optimizing interstitial photodynamic therapy with custom cylindrical diffusers.” In: *Journal of biophotonics* (2018), e201800153.
- [8] Bram Vandekerckhove et al. “Technological Challenges in the Development of Optogenetic Closed-Loop Therapy Approaches in Epilepsy and Related Network Disorders of the Brain.” In: *Micromachines* 12.1 (2021), p. 38.
- [9] Lennart Hasselgren, Sheila Galt, and Sverker Hard. “Diffusive optical fiber ends for photodynamic therapy: manufacture and analysis.” In: *Applied optics* 29.30 (1990), pp. 4481–4488.
- [10] Janis Spigulis. “Side-emitting fibers brighten our world.” In: *Optics and photonics news* 16.10 (2005), pp. 34–39.

## Bibliography

- [11] Janis Spigulis et al. “Side-emitting optical fibres for clinical applications.” In: *MEDICAL AND BIOLOGICAL ENGINEERING AND COMPUTING* 34 (1996), pp. 285–286.
- [12] Janis Spigulis and Daumants Pfafrods. “Clinical potential of the side-glowing optical fibers.” In: *Specialty Fiber Optics for Biomedical and Industrial Applications*. Vol. 2977. International Society for Optics and Photonics. 1997, pp. 84–88.
- [13] Janis Spigulis, Daumants Pfafrods, and Maris Stafeckis. “Optical fiber diffusive tip designs for medical laser-lightguide delivery systems.” In: *Biomedical Optoelectronic Devices and Systems II*. Vol. 2328. International Society for Optics and Photonics. 1994, pp. 69–75.
- [14] Janis Spigulis et al. “Glowing optical fiber designs and parameters.” In: *Optical Inorganic Dielectric Materials and Devices*. Vol. 2967. International Society for Optics and Photonics. 1997, pp. 231–236.
- [15] Lars O Svaasand, Daniel R Doiron, and Thomas J Dougherty. “Temperature rise during photoradiation therapy of malignant tumors.” In: *Medical physics* 10.1 (1983), pp. 10–17.
- [16] Peter Lenz. “Light distributor for endoscopic photochemotherapy of tumors.” In: *Appl. Opt.* 26.20 (1987), pp. 4452–4456. DOI: 10.1364/AO.26.004452. URL: <http://ao.osa.org/abstract.cfm?URI=ao-26-20-4452>.
- [17] Leslie James Button et al. *Light diffusing fibers and methods for making the same*. US Patent 8,620,125. 2013.
- [18] Jochen Alkemper et al. *Side-emitting step index fiber*. US Patent 8,582,943. 2013.
- [19] Ting Wang and Kojiro Watanabe. *Side emitting optical fiber*. US Patent 5,905,837. 1999.
- [20] Timothy M Baran and Thomas H Foster. “Comparison of flat cleaved and cylindrical diffusing fibers as treatment sources for interstitial photodynamic therapy.” In: *Medical physics* 41.2 (2014).
- [21] Martin D Altschuler et al. “Optimized interstitial PDT prostate treatment planning with the Cimmino feasibility algorithm.” In: *Medical physics* 32.12 (2005), pp. 3524–3536.
- [22] Maciej Zajkowski. “Emission of flux light in side-light fiber optic.” In: *Photonics Applications in Astronomy, Communications, Industry, and High-Energy Physics Experiments*. Vol. 5125. International Society for Optics and Photonics. 2003, pp. 322–327.
- [23] Maciej Zajkowski. “Luminous Flux Emission calculation analysis in side light illumination optical fibers.” In: *Photonics Applications in Astronomy, Communications, Industry, and High-Energy Physics Experiments III*. Vol. 5775. International Society for Optics and Photonics. 2005, pp. 440–445.



- [24] A Endruweit et al. “Spectroscopic experiments regarding the efficiency of side emission optical fibres in the UV-A and visible blue spectrum.” In: *Optics and Lasers in Engineering* 46.2 (2008), pp. 97–105.
- [25] Anpei Pan and Dipak R Biswas. “Light distribution from optical fiber diffusers.” In: *Optical Fibers in Medicine VIII*. Vol. 1893. International Society for Optics and Photonics. 1993, pp. 202–213.
- [26] Leonid Vesselov, William Whittington, and Lothar Lilge. “Design and performance of thin cylindrical diffusers created in Ge-doped multimode optical fibers.” In: *Applied optics* 44.14 (2005), pp. 2754–2758.
- [27] Mikhail A Bisyarin et al. “Light-emitting optical fibers with controllable anomalous small-angle scattering.” In: *JOSA B* 34.11 (2017), pp. 2396–2399.
- [28] Yufeng Li and Thomas G. Brown. “Radiation modes and tilted fiber gratings.” In: *J. Opt. Soc. Am. B* 23.8 (2006), pp. 1544–1555. DOI: 10.1364/JOSAB.23.001544. URL: <http://josab.osa.org/abstract.cfm?URI=josab-23-8-1544>.
- [29] Turan Erdogan and JE Sipe. “Tilted fiber phase gratings.” In: *JOSA A* 13.2 (1996), pp. 296–313.
- [30] Xiaoyi Dong et al. “Tilted fiber Bragg gratings: Principle and sensing applications.” In: *Photonic Sensors* 1.1 (2011), pp. 6–30.
- [31] Dietrich Marcuse. *Theory of dielectric optical waveguides*. Elsevier, 1974.
- [32] Dietrich Marcuse. *Principles of optical fiber measurements*. Elsevier, 2012.
- [33] Ronald Newbold Bracewell and Ronald N Bracewell. *The Fourier transform and its applications*. Vol. 31999. McGraw-Hill New York, 1986.
- [34] Georg Schwartz. “Tailored side emission profile of femtosecond laser induced scattering centers in optical fibers.” Bachelor’s Thesis. Friedrich-Schiller-University Jena, 2020.
- [35] Aaron Reupert, Jan Schröder, and Lothar Wondraczek. “Radiation from Side-Emitting Optical Fibers and Fiber Fabrics: Radiometric Model and Experimental Validation.” In: *Advanced Photonics Research* (Apr. 2021). Submitted.
- [36] Aaron Reupert et al. “Side-emission properties of femtosecond laser induced scattering centers in optical fibers.” In: *Optical Materials Express* 9.6 (2019), pp. 2497–2510. DOI: <https://doi.org/10.1364/OME.9.002497>.
- [37] Aaron Reupert et al. “Angular Scattering Pattern of Femtosecond Laser-Induced Refractive Index Modifications in Optical Fibers.” In: *Advanced Optical Materials* 8.18 (2020), p. 2000633. DOI: <https://doi.org/10.1002/adom.202000633>.
- [38] Dana Kremenakova et al. “Characterization of side emitting polymeric optical fibres.” In: *Journal of Fiber Bioengineering & Informatics* 5.4 (2012), pp. 423–431.

## Bibliography

- [39] Yufeng Li, Mark Froggatt, and Turan Erdogan. “Volume current method for analysis of tilted fiber gratings.” In: *Journal of Lightwave Technology* 19.10 (2001), pp. 1580–1591.
- [40] Andrzej Wolski. “Theory of electromagnetic fields.” In: *arXiv preprint arXiv:1111.4354* (2011).
- [41] Michael I Mishchenko. *Electromagnetic scattering by particles and particle groups: an introduction*. Cambridge University Press, 2014.
- [42] James M Palmer. “Getting intense on intensity.” In: *Metrologia* 30.4 (1993), p. 371.
- [43] Max Planck. *The theory of heat radiation*. Courier Corporation, 2013.
- [44] EW Marchand and E Wolf. “Radiometry with sources of any state of coherence.” In: *JOSA* 64.9 (1974), pp. 1219–1226.
- [45] EW Marchand and E Wolf. “Angular correlation and the far-zone behavior of partially coherent fields.” In: *JOSA* 62.3 (1972), pp. 379–385.
- [46] A Walther. “Radiometry and coherence.” In: *JOSA* 58.9 (1968), pp. 1256–1259.
- [47] IA White. “Radiation from bends in optical waveguides: The volume-current method.” In: *IEE Journal on Microwaves, Optics and Acoustics* 3.5 (1979), pp. 186–188.
- [48] Mark Kuznetsov and H Haus. “Radiation loss in dielectric waveguide structures by the volume current method.” In: *IEEE journal of quantum electronics* 19.10 (1983), pp. 1505–1514.
- [49] Charles Herach Papas. *Theory of electromagnetic wave propagation*. Dover classics of science and mathematics. Mineola, NY: Dover, 1965. Chap. 1, pp. 39–42. URL: <http://cds.cern.ch/record/1356178>.
- [50] Steven H Schot. “Eighty years of Sommerfeld’s radiation condition.” In: *Historia Mathematica* 19.4 (1992), pp. 385–401. ISSN: 0315-0860. DOI: [https://doi.org/10.1016/0315-0860\(92\)90004-U](https://doi.org/10.1016/0315-0860(92)90004-U). URL: <https://www.sciencedirect.com/science/article/pii/031508609290004U>.
- [51] John F Clare. “Comparison of four analytic methods for the calculation of irradiance in integrating spheres.” In: *JOSA A* 15.12 (1998), pp. 3086–3096.
- [52] Jonathan A Kurvits, Mingming Jiang, and Rashid Zia. “Comparative analysis of imaging configurations and objectives for Fourier microscopy.” In: *JOSA A* 32.11 (2015), pp. 2082–2092.
- [53] Max Born and Emil Wolf. *Principles of optics: electromagnetic theory of propagation, interference and diffraction of light*. Elsevier, 2013.
- [54] Bernard Richards and Emil Wolf. “Electromagnetic diffraction in optical systems, II. Structure of the image field in an aplanatic system.” In: *Proceedings of the Royal Society of London. Series A. Mathematical and Physical Sciences* 253.1274 (1959), pp. 358–379.

- [55] Marcel Leutenegger et al. “Fast focus field calculations.” In: *Optics express* 14.23 (2006), pp. 11277–11291.
- [56] A Nickolas Vamivakas et al. “A case study for optics: The solid immersion microscope.” In: *American Journal of Physics* 76.8 (2008), pp. 758–768.
- [57] J Lin et al. “Fast vectorial calculation of the volumetric focused field distribution by using a three-dimensional Fourier transform.” In: *Optics express* 20.2 (2012), pp. 1060–1069.
- [58] Aaron Reupert, Jan Schröder, and Lothar Wondraczek. “Radiation from Side-Emitting Optical Fibers and Fiber Fabrics: Radiometric Model and Experimental Validation.” In: *Advanced Photonics Research* (2022), p. 2100104. DOI: <https://doi.org/10.1002/adpr.202100104>.

# A Theoretical Background

The mathematical description of light distribution through the side-emitting optical fiber relies on wave optics and radiometry, two sub-fields of optics. To link this thesis to the relevant fields, we will briefly derive all concepts used in the publications in Chapter 3 from the Maxwell equations. We will start with plane waves in free space and the representation of a light field as the superposition of plane waves. This will introduce the important concepts of electromagnetic waves: propagation vector, refractive index, light flux density, and Fourier-optics. Then we will derive the concept of radiometry as the limiting case for spatially incoherent light and the scattering of light by a refractive index distortion with the volume current method.

## A.1 The Plane Wave

One of the basic ideas of wave optics is to describe a propagating electromagnetic wave with the vector-valued function  $\mathbf{E}$  periodic in space  $\mathbf{r}$  and in time  $t$ , which represents the electric field

$$\mathbf{E}(\mathbf{r}, t) = \mathbf{E}_0 \exp\{i(\omega t - \mathbf{K}\mathbf{r} - \delta)\} . \quad (\text{A.1})$$

Similarly, we have for the propagating magnetic part of the wave

$$\mathbf{H}(\mathbf{r}, t) = \mathbf{H}_0 \exp\{i(\omega t - \mathbf{K}\mathbf{r} - \delta)\} . \quad (\text{A.2})$$

Throughout the text, vectors are written with boldface. The  $\delta$  represents a possible phase shift. The periodic function could also be represented by angle function (sine or cosine), but the exponential representation allows for easier manipulation because the rules of exponential calculus apply. We see the link to the angular functions by using Euler's formula

$$e^{ix} = \cos(x) + i \sin(x) , \quad (\text{A.3})$$

which also shows that we should only regard the real part when we calculate a measurable observable of the electromagnetic wave in Eq. (A.1). This case will be necessary when we calculate the light flux via the Poynting vector.

From the Eq. (A.1) or Eq. (A.2) alone, we can immediately infer some essential features: first, it represents a plane wave that propagates in the direction of the propagation vector  $\mathbf{K}$ , because the scalar product with the location vector  $\mathbf{r}$ ,  $\mathbf{K}\mathbf{r}$  is maximal when both vectors are parallel. Also, it is constant for all  $\mathbf{r}$  that point on a plane orthogonal to  $\mathbf{K}$ ; this is shown in Fig. A.1, and we can also see it from the scalar product

$$\mathbf{K}\mathbf{r} = |\mathbf{K}||\mathbf{r}| \cos \alpha , \quad (\text{A.4})$$

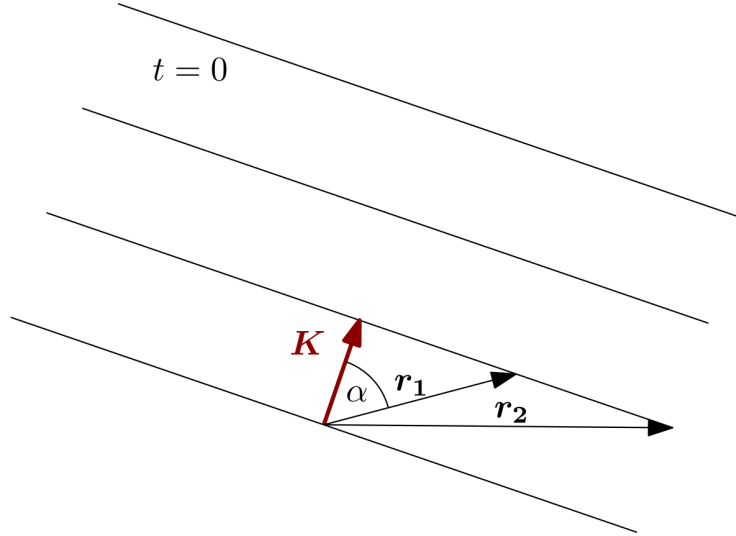


**Figure A.1:** Schematics of the wave vector  $\mathbf{K}$ . For a plane wave, the scalar product  $\mathbf{K}\mathbf{r}_1 = \mathbf{K}\mathbf{r}_2$  is constant for all points  $\mathbf{r}_i$  on a plane of constant phase.

where the modulus  $|\mathbf{K}|$  or  $|\mathbf{r}|$  represents the magnitude of the vectors and  $\alpha$  the angle in between them.

When we freeze time (e.g.  $t = 0$ ) and move parallel to  $\mathbf{K}$ , the distance between two maxima is the wavelength  $|\mathbf{r}| = \lambda$ . Because Eq. (A.3) is periodic when the argument  $x$  is an integer multiple of  $2\pi$ , it follows that the magnitude of  $\mathbf{K}$  is  $|\mathbf{K}| = 2\pi/\lambda$ . We can apply the same argument to the angular frequency  $\omega$ : for constant point in space  $\mathbf{r}$  (e.g.  $\mathbf{r} = 0$ ), the time interval from one wave maximum passing by this point to the next is the period  $T$ , it follows  $\omega = 2\pi/T$  or when we use the frequency  $f = 1/T$  then  $\omega = 2\pi f$ .

## A.2 The Phasor

The phase term  $e^{-i\delta(\omega, \mathbf{K})}$  is often absorbed into the amplitude  $\mathbf{E}_0$  to yield a more compact notation.  $\mathbf{E}_0$  is then called *the phasor* because it contains the phase  $\delta(\omega, \mathbf{K})$ . The same idea can also be applied to the frequency term ( $e^{i\omega t}$ ) or propagation term ( $e^{-i\mathbf{K}\mathbf{r}}$ ) when this dependency is assumed to be stationary or of no greater interest for the problem under consideration. In summary, we have the following equivalent representations for the plane wave

$$\mathbf{E}(\mathbf{r}, t) = \mathbf{E}'_0 e^{i(\omega t - \mathbf{K}\mathbf{r} - \delta(\omega, \mathbf{K}))} = \mathbf{E}_0 e^{i(\omega t - \mathbf{K}\mathbf{r})} = \mathbf{E}_\omega e^{-i\mathbf{K}\mathbf{r}} = \mathbf{E}_\mathbf{K} e^{i\omega t} . \quad (\text{A.5})$$

It should be stressed again that only the real part of this plane wave equation represents the physical wave. This will be important when calculating the carried energy in Appendix A.6.

## A Theoretical Background

The analog representations for the magnetic field are

$$\mathbf{H}(\mathbf{r}, t) = \mathbf{H}'_0 e^{i(\omega t - \mathbf{K}\mathbf{r} - \delta(\omega, \mathbf{K}))} = \mathbf{H}_0 e^{i(\omega t - \mathbf{K}\mathbf{r})} = \mathbf{H}_\omega e^{-i\mathbf{K}\mathbf{r}} = \mathbf{H}_\mathbf{K} e^{i\omega t} . \quad (\text{A.6})$$

### A.3 The Wave Equation

The wave equation is the fundamental relation that underlies the propagation of light waves in the side-emitting optical fiber and its surrounding. Here we will show that the plane wave from the previous subsections is one solution and that the angular frequency  $\omega$  and the wave vector  $\mathbf{K}$  are related by the speed of light  $c = \omega/|\mathbf{K}|$ . Additionally, we will show how the refractive index, the ratio of the speed of light in the medium and in the vacuum can be included in the plane wave equation. For this, we will derive the electromagnetic vector wave equation from Maxwell's equations and insert our proposed solution: the plane wave.

Our goal is the wave equation, which, in its most general form, is a linear, second-order partial differential equation

$$\nabla^2 u - \frac{1}{c} \frac{\partial^2 u}{\partial t^2} = 0 \quad (\text{A.7})$$

where  $c$  represents the speed of the wave and  $u(\mathbf{r}, t)$  some spatially distributed scalar quantity. In the present case, these will be the components of the electric or magnetic field vectors. The triangle with its tip pointing down is the nabla operator  $\nabla = \frac{\partial}{\partial x} \mathbf{e}_x + \frac{\partial}{\partial y} \mathbf{e}_y + \frac{\partial}{\partial z} \mathbf{e}_z$ , here in Cartesian coordinates, which is the partial derivative along all three spatial axis  $x, y, z$ . The square of the nabla operator is the Laplace operator  $\nabla^2 = \frac{\partial^2}{\partial x^2} + \frac{\partial^2}{\partial y^2} + \frac{\partial^2}{\partial z^2}$ .

We start deriving the electromagnetic vector wave equation with the Maxwell equations in the following form:

$$\nabla \times \mathbf{H} = \epsilon \frac{\partial \mathbf{E}}{\partial t} + \mathbf{j} \quad (\text{A.8})$$

$$\nabla \times \mathbf{E} = -\mu \frac{\partial \mathbf{H}}{\partial t} \quad (\text{A.9})$$

$$\mu \nabla \cdot \mathbf{H} = 0 \quad (\text{A.10})$$

$$\epsilon \nabla \cdot \mathbf{E} = 0 \quad (\text{A.11})$$

The vectors  $\mathbf{E}$  and  $\mathbf{H}$  represent the electric and magnetic field strength. The displacement vector  $\mathbf{D}$  and the magnetic flux density  $\mathbf{B}$ , which are normally encountered in Maxwell's equations, have already been replaced with their constitutive counterparts  $\mathbf{D} = \epsilon \mathbf{E}$  and  $\mathbf{B} = \mu \mathbf{H}$ . Here we assumed that the medium is approximately homogeneous, so the electric permittivity  $\epsilon$  and the magnetic permeability  $\mu$  are constant. Additionally, there are no free charges ( $\rho = 0$ ).

First, we use the curl, the vector product of the nabla operator ( $\nabla \times$ ), on Eq. (A.9), and insert Eq. (A.8) on the right-hand side, and this results in

$$\nabla \times \nabla \times \mathbf{E} + \mu \epsilon \frac{\partial^2 \mathbf{E}}{\partial t^2} = -\mu \frac{\partial \mathbf{j}}{\partial t} . \quad (\text{A.12})$$

The double curl in Equation (A.12) can be rewritten by using the vector triple product

$$\nabla \times \nabla \times \mathbf{E} = \nabla(\nabla \cdot \mathbf{E}) - \nabla^2 \mathbf{E} . \quad (\text{A.13})$$

We insert this in Eq. (A.12), use Eq. (A.11), we get the vector wave equation

$$\nabla^2 \mathbf{E} - \mu\epsilon \frac{\partial^2 \mathbf{E}}{\partial t^2} = \mu \frac{\partial \mathbf{j}}{\partial t} , \quad (\text{A.14})$$

which describes the waves generated by the current density  $\mathbf{j}$  in a homogeneous medium in the absence of free charges. Far from the sources, we can drop the term  $\mu \frac{d\mathbf{j}}{dt}$  and get the homogeneous wave equation, the vector Helmholtz equation

$$\nabla^2 \mathbf{E} - \mu\epsilon \frac{\partial^2 \mathbf{E}}{\partial t^2} = 0 . \quad (\text{A.15})$$

The same procedure can be applied to derive the vector wave or Helmholtz equation for  $\mathbf{H}$ : applying the curl to Eq. (A.8) and inserting in Eq. (A.9), then proceed as for the  $\mathbf{E}$ -field. This results in

$$\nabla^2 \mathbf{H} - \mu\epsilon \frac{\partial^2 \mathbf{H}}{\partial t^2} = 0 \quad (\text{A.16})$$

In both cases, the vector wave equation holds for each component of the magnetic or electric field vectors. Therefore, if we compare Eq. (A.15) or Eq. (A.16) to the wave equation A.7 we see that the speed of light in the medium is

$$c = \frac{1}{\sqrt{\epsilon\mu}} . \quad (\text{A.17})$$

From this, we can infer the light speed in vacuum as  $c_0 = (\epsilon_0\mu_0)^{-\frac{1}{2}}$ , where  $\epsilon_0$  and  $\mu_0$  represent the permittivity and permeability of vacuum. The ratio between light speed in vacuum and in the material is the refractive index

$$n = \frac{c_0}{c} = \sqrt{\frac{\epsilon\mu}{\epsilon_0\mu_0}} . \quad (\text{A.18})$$

When we insert our plane wave solutions Eq. (A.1) and Eq. (A.2) into the respective vector wave equations, we get in both cases the dispersion relation

$$|\mathbf{K}| = \omega\sqrt{\epsilon\mu} = \frac{\omega}{c} = \frac{n\omega}{c_0} = nk . \quad (\text{A.19})$$

Here we defined  $k$  as the wave vector's length in a vacuum

$$k = \omega\sqrt{\epsilon_0\mu_0} = \frac{\omega}{c_0} = \frac{2\pi}{\lambda} , \quad (\text{A.20})$$

that has its own dispersion relation. This choice of the wave vector is sometimes more convenient because we can include the refractive index directly in the exponent of the plane wave equation by exchanging  $|\mathbf{K}|$  with  $nk$ . From this comparison, we see that for the same angular frequency  $\omega$ , the wave vector in the material is longer ( $c < c_0$ ) than in a vacuum. This means that light of the same frequency has a shorter wavelength in a material with a refractive index higher than one.

## A.4 The Relation Between Electric and Magnetic Field

The electric field, magnetic field, and direction of the electromagnetic wave propagation are related and mutually orthogonal. Because we got two independent wave equations for  $\mathbf{E}$  and  $\mathbf{H}$ , it seems that both solutions are independent. But from the first-order Maxwell equations, it is clear that this can not be. To check that the first-order equations are also satisfied, we substitute the solution Eq. (A.1) or Eq. (A.2) into Eq. (A.11) or Eq. (A.10) and obtain

$$\nabla \mathbf{E} = -i\mathbf{K}\mathbf{E}_0 e^{i(\omega z - \mathbf{K}\mathbf{r})} = 0, \quad (\text{A.21})$$

$$\nabla \mathbf{H} = -i\mathbf{K}\mathbf{H}_0 e^{i(\omega z - \mathbf{K}\mathbf{r})} = 0. \quad (\text{A.22})$$

Because these equations have to be zero for all points in space  $\mathbf{r}$  and all times  $t$  it follows that  $\mathbf{K}$  and  $\mathbf{E}_0$ , as well as  $\mathbf{K}$  and  $\mathbf{H}_0$ , are orthogonal: the wave is transversal.

For the mutual relation between  $\mathbf{K}$ ,  $\mathbf{E}$  and  $\mathbf{H}$ , we insert the plane wave solutions Eq. (A.1) and Eq. (A.2) into Maxwell's Eq. (A.9) and obtain

$$-i\mathbf{K} \times \mathbf{E} = -i\mu\omega\mathbf{H}. \quad (\text{A.23})$$

So  $\mathbf{H}$  is orthogonal to the plane spanned by  $\mathbf{K}$  and  $\mathbf{E}$ , which are themselves orthogonal to each other. Together with the previous two relations, this shows that they all are orthogonal to each other:  $\mathbf{K}$  points in the direction of propagation, and  $\mathbf{E}$  and  $\mathbf{H}$  are both perpendicular to it, forming an orthogonal trihedron. It also follows that the amplitudes of the electric and the magnetic fields are related by

$$|\mathbf{K}||\mathbf{E}| = \mu\omega|\mathbf{H}| \quad \rightarrow \quad |\mathbf{H}| = \frac{n}{\mu c_0}|\mathbf{E}|, \quad (\text{A.24})$$

by using the dispersion relation, the magnitude of the cross product  $|\mathbf{K} \times \mathbf{E}| = \sin \alpha |\mathbf{K}||\mathbf{E}|$  and the orthogonality ( $\alpha = \pi/2$ ) of  $\mathbf{K}$  and  $\mathbf{E}$ . For the unity vectors  $\hat{\mathbf{s}} = \mathbf{K}/|\mathbf{K}|$ ,  $\hat{\mathbf{e}} = \mathbf{E}/|\mathbf{E}|$ , and  $\hat{\mathbf{h}} = \mathbf{H}/|\mathbf{H}|$  which point in the respective directions of the vectors, it follows, by cyclical permutation

$$\hat{\mathbf{s}} \times \hat{\mathbf{e}} = \hat{\mathbf{h}} \quad \rightarrow \quad \hat{\mathbf{e}} \times \hat{\mathbf{h}} = \hat{\mathbf{s}}. \quad (\text{A.25})$$

The plane electromagnetic wave propagates in the direction of  $\hat{\mathbf{s}}$  and the electric and the magnetic fields are orthogonal to the direction of propagation as well to each other.

## A.5 The Superpositions of Plane Waves

We will use the simple plane wave solution to construct more complex propagating electromagnetic fields, like light pulses or stochastic light fields, by superposition of many plane waves. Waves of different frequencies travel at different velocities due to dispersion, the dependency of the refractive index  $n$  on the frequency of



the waves. If we assume that the dispersion can be neglected, we can predict the way a disturbance  $\mathbf{E}(\mathbf{r}, t)$  (a light pulse) travels through a medium. We express the disturbance as the sum of all its angular frequency components as the Fourier integral or transform

$$\mathbf{E}(\mathbf{r}, t) = \int_{-\infty}^{\infty} \mathbf{E}(\mathbf{r}, \omega) e^{i(\omega t - \mathbf{k}\mathbf{r})} d\omega . \quad (\text{A.26})$$

Which includes forward and backward traveling waves as well as evanescent waves, which do not propagate. The inverse Fourier transform is

$$\mathbf{E}(\mathbf{r}, \omega) = \frac{1}{2\pi} \int_{-\infty}^{\infty} \mathbf{E}(\mathbf{r}, t) e^{-i(\omega t - \mathbf{k}\mathbf{r})} dt , \quad (\text{A.27})$$

where  $(2\pi)^{-1}$  is a normalization constant. From this, the amplitude function  $\mathbf{E}(\mathbf{r}, \omega)$  in Eq. (A.26), which is expanded into the plane waves, is determined by a known shape of the impulse, e.g., in the plane  $z = 0$  ( $\mathbf{r} = 0$ )

$$\mathbf{E}(x, y, 0, t) = \frac{1}{2\pi} \int_{-\infty}^{\infty} \mathbf{E}(x, y, 0, \omega) e^{i(\omega t - k_x x - k_y y)} d\omega \quad (\text{A.28})$$

Inserting this in Eq. (A.26) allows finding the shape of the pulse for all times  $t$ .

We extend this concept to a disturbance that is made up of plane waves, which travel in different directions. Because the wave vector  $\mathbf{K}$  can be chosen freely, there are infinitely many  $\mathbf{K}$ -directions or "(free space) modes" for a plane wave in an isotropic medium. (A mode refers to something that propagates like  $\exp\{-i\mathbf{K}\mathbf{r}\}$ ). Because the wave equation is linear, also superpositions of two or more plane waves are a solution. In fact, the most general solution of a local field  $\mathbf{E}(\mathbf{r})$  will be the sum (or expansion) over all modes, which is presented by the Fourier transform

$$\mathbf{E}(\mathbf{r}, t) = \int_{-\infty}^{\infty} \int_{-\infty}^{\infty} \mathbf{E}(\mathbf{K}, \omega) e^{i(\omega t - \mathbf{K}\mathbf{r})} d\omega d^3 K . \quad (\text{A.29})$$

Here  $dK^3$  is a volume element in wave vector space  $d^3 K = dK_x dK_y dK_z$ . And the inverse transform

$$\mathbf{E}(\mathbf{K}, \omega) = \left(\frac{1}{2\pi}\right)^4 \int_{-\infty}^{\infty} \int_{-\infty}^{\infty} \mathbf{E}(\mathbf{r}, t) e^{-i(\omega t - \mathbf{K}\mathbf{r})} dt d^3 r . \quad (\text{A.30})$$

where we get an additional normalization factor for every integral.  $d^3 r$  is a volume element in real space.

As an additional constrain, we have to demand that the dispersion relation Eq. (A.20) is fulfilled, so not all components of the wave vector are independent:

## A Theoretical Background

The dispersion relation confines the tip of the wave vector to the surface of a sphere, defined by

$$\frac{\omega^2}{c_0^2} = K_x^2 + K_y^2 + K_z^2 = n^2 k^2 (s_x^2 + s_y^2 + s_z^2). \quad (\text{A.31})$$

$\hat{\mathbf{s}} = (s_x, s_y, s_z)$  is the unit vector (ray vector) in the direction of the plane wave, and  $nk$  is its magnitude. From this definition, we can see how evanescent waves are included in the definition: e.g., if  $\sqrt{\frac{\omega^2}{c^2} - K_x^2 - K_y^2} = K_z$  is imaginary, because the expression under the square root is smaller than zero, the exponent becomes real for  $K_z$ , and the wave does not propagate in the  $z$ -direction but decays exponentially. This can be seen if the imaginary  $K_z$  is inserted in Eq. (A.1) or Eq. (A.29).

### A.6 Pointing Vector

Only the time-average power flux of the electromagnetic wave is observable; the rapidly fluctuating magnetic and electric fields themselves are not measurable. To get the relation between the fields and the power flux, we will first calculate the power flux density "Pointing" vector with the help of Pointing's theorem and then its time average in the next subsection. This derivation is based on [40].

First, we take the scalar product of Eq. (A.9) with  $\mathbf{H}$  and the scalar product of Eq. (A.8) with  $\mathbf{E}$ .

$$\mathbf{H} \cdot \nabla \times \mathbf{E} = -\mu \mathbf{H} \cdot \frac{\partial \mathbf{H}}{\partial t} \quad (\text{A.32})$$

$$\mathbf{E} \cdot \nabla \times \mathbf{H} = \mathbf{E} \cdot \mathbf{j} + \epsilon \mathbf{E} \cdot \frac{\partial \mathbf{E}}{\partial t} \quad (\text{A.33})$$

Then we subtract one equation from the other and obtain

$$\mathbf{H} \cdot \nabla \times \mathbf{E} - \mathbf{E} \cdot \nabla \times \mathbf{H} = -\mu \mathbf{H} \cdot \frac{\partial \mathbf{H}}{\partial t} - \epsilon \mathbf{E} \cdot \frac{\partial \mathbf{E}}{\partial t} - \mathbf{E} \cdot \mathbf{j}. \quad (\text{A.34})$$

We can rewrite this using the product rule for the time derivative ( $\mathbf{H}$  analogous)

$$\frac{\partial}{\partial t} \mathbf{E}^2 = \frac{\partial}{\partial t} (\mathbf{E} \cdot \mathbf{E}) = \frac{\partial \mathbf{E}}{\partial t} \cdot \mathbf{E} + \mathbf{E} \cdot \frac{\partial \mathbf{E}}{\partial t} = 2\mathbf{E} \cdot \frac{\partial \mathbf{E}}{\partial t}, \quad (\text{A.35})$$

and the cross product

$$\nabla \cdot (\mathbf{E} \times \mathbf{H}) = \mathbf{H} \cdot \nabla \times \mathbf{E} - \mathbf{E} \cdot \nabla \times \mathbf{H}. \quad (\text{A.36})$$

Inserting this and rearranging the equation gives

$$\frac{\partial}{\partial t} \left( \frac{1}{2} \epsilon \mathbf{E}^2 + \frac{1}{2} \mu \mathbf{H}^2 \right) = -\nabla \cdot (\mathbf{E} \times \mathbf{H}) - \mathbf{E} \cdot \mathbf{j}, \quad (\text{A.37})$$

Pointing's theorem, the work-energy theorem of electrodynamics. To better understand the meaning of this equation, we take the volume integral of the whole

equation and apply Gauss's theorem ( $\int \nabla \mathbf{A} dV = \int \mathbf{A} d\mathbf{S}$ ) to the first term on the right hand side, this gives

$$\frac{\partial}{\partial t} \int_V \left( \frac{1}{2} \epsilon \mathbf{E}^2 + \frac{1}{2} \mu \mathbf{H}^2 \right) dV = - \int_S (\mathbf{E} \times \mathbf{H}) d\mathbf{S} - \int_V \mathbf{E} \cdot \mathbf{j} dV. \quad (\text{A.38})$$

The volume integral on the left-hand side represents the total electromagnetic energy stored in the volume  $V$ , and the time derivative, therefore, means the change of the total energy in the volume. The first term on the right-hand side represents the loss of electromagnetic energy transferred through the surface  $S$  of the volume  $V$ . The second term is the loss of energy due to work on charges in the volume by the field. So Pointings theorem states that energy loss is either caused by work or energy flowing out of the volume.

From this, we see that the energy flux density transported by the field through a surface is

$$\mathbf{S} = \mathbf{E} \times \mathbf{H} \quad (\text{A.39})$$

called the Pointing vector. Deriving this was the goal of this endeavor because it is generally associated (although not uncontroversially [41]) with the measurable radiometric quantity *irradiance*  $\mathbf{F}$ , the light power flux per unit area, or radiant flux density. This value is sometimes (especially in optics) confusingly called *intensity*  $I$ , which is actually the light power per solid angle [42]. To reconcile both concepts, one can imagine the intensity as an area on a unit sphere - then both ideas are again interchangeable.

### A.6.1 Time Average Energy Flux Density of a Plane Wave

Generally, a light wave oscillates very fast, for example, a wave at the wavelength of  $\lambda = 500 \text{ nm}$  oscillates with a frequency of  $f = 6 \times 10^{14} \text{ s}^{-1}$ . Therefore its actual, momentary power is not measured by a light power meter but rather the time average over many, many oscillations. To consider this measurement effect in our concept of flux density, we calculate the time-average pointing vector. For this, we absorb all exponents but the time dependency in the phasor as indicated in Eq. (A.5).

At this point, we have to consider that only the real part of our complex wave solution (see Eq. (A.3)) contributes to the measurable energy flux. The real part will be indicated by  $\text{Re} \{ \mathbf{E}(\mathbf{r}) \}$  and can be calculated by adding the complex conjugated (indicated by  $*$ ) as in  $\text{Re} \{ A \} = (A + A^*)/2$ . Using these properties, we first calculate

## A Theoretical Background

the real part of the pointing vector

$$\mathbf{S} = \mathbf{E} \times \mathbf{H} = \text{Re} \{ \mathbf{E}_{\mathbf{K}}(\mathbf{r})e^{i\omega t} \} \times \text{Re} \{ \mathbf{H}_{\mathbf{K}}(\mathbf{r})e^{i\omega t} \} \quad (\text{A.40})$$

$$= \frac{1}{2} (\mathbf{E}_{\mathbf{K}}(\mathbf{r})e^{i\omega t} + \mathbf{E}_{\mathbf{K}}^*(\mathbf{r})e^{-i\omega t}) \times \frac{1}{2} (\mathbf{H}_{\mathbf{K}}(\mathbf{r})e^{i\omega t} + \mathbf{H}_{\mathbf{K}}^*(\mathbf{r})e^{-i\omega t}) \quad (\text{A.41})$$

$$= \frac{1}{4} (\mathbf{E}_{\mathbf{K}} \times \mathbf{H}_{\mathbf{K}}^* + \mathbf{E}_{\mathbf{K}}^* \times \mathbf{H}_{\mathbf{K}} + \mathbf{E}_{\mathbf{K}} \times \mathbf{H}_{\mathbf{K}}e^{i2\omega t} + \mathbf{E}_{\mathbf{K}}^* \times \mathbf{H}_{\mathbf{K}}^*e^{-i2\omega t}) \quad (\text{A.42})$$

$$= \frac{1}{2} \text{Re} \{ \mathbf{E}_{\mathbf{K}} \times \mathbf{H}_{\mathbf{K}}^* \} + \frac{1}{2} \text{Re} \{ \mathbf{E}_{\mathbf{K}} \times \mathbf{H}_{\mathbf{K}}e^{i2\omega t} \} \quad (\text{A.43})$$

Now we average over one wave period  $T$  to get the time average energy flux

$$\bar{\mathbf{S}} = \frac{1}{T} \int_0^T \mathbf{S} dt = \frac{1}{T} \int_0^T \frac{1}{2} \text{Re} \{ \mathbf{E}_{\mathbf{K}} \times \mathbf{H}_{\mathbf{K}}^* \} + \frac{1}{2} \text{Re} \{ \mathbf{E}_{\mathbf{K}} \times \mathbf{H}_{\mathbf{K}}e^{i2\omega t} \} dt \quad (\text{A.44})$$

The second term integrates to zero due to the double frequency exponent, and the first is constant in time, so the time average complex pointing vector is

$$\bar{\mathbf{S}} = \frac{1}{2} \text{Re} \{ \mathbf{E}_{\mathbf{K}} \times \mathbf{H}_{\mathbf{K}}^* \} \quad (\text{A.45})$$

Finally, we desorb the  $\exp\{-\mathbf{K}\mathbf{r}\}$  from the phasor and calculate the time average flux density contained in a plane electromagnetic wave

$$\bar{\mathbf{S}} = \frac{1}{2} \text{Re} \{ \mathbf{E}_{\mathbf{K}} \times \mathbf{H}_{\mathbf{K}}^* \} = \text{Re} \left\{ \frac{1}{2} \mathbf{E}_0 e^{-i\mathbf{k}\mathbf{r}} \times \mathbf{H}_0^* e^{+i\mathbf{k}\mathbf{r}} \right\} = \hat{\mathbf{s}} \frac{n}{2\mu c_0} |\mathbf{E}_0|^2 \quad (\text{A.46})$$

which is always real as long as the medium is lossless, so we dispensed the  $\text{Re} \{ \dots \}$ . Here we used Eq. (A.25) and Eq. (A.24) in the last step. As expected, the energy flux density of a plane wave points in the direction of propagation and is proportional to the square of the amount of the electric field amplitude. This can also be written as

$$\bar{\mathbf{S}} = (\hat{\mathbf{e}} \times \hat{\mathbf{h}}) \frac{1}{2} |\mathbf{E}(\mathbf{r})| |\mathbf{H}^*(\mathbf{r})| = \hat{\mathbf{s}} \frac{n}{2\mu c_0} \mathbf{E}(\mathbf{r}) \mathbf{E}^*(\mathbf{r}) \quad (\text{A.47})$$

using the definition of the scalar product.

## A.7 The Radiometric Approximation

The radiometric approximation is used in the thesis to calculate the radiation field generated by the fiber in its surroundings by summing the contribution from all surface elements. The classical form of radiometry was founded independently from electromagnetic theory on purely geometrical considerations. The first complete systematic description is attributed to Plank in his work on the black body radiator [43]. The main assumption is that the radiative energy is propagated along light rays and can be described by a scalar function called the *specific intensity* or *radiance*

$L_\nu(\mathbf{r}, \hat{\mathbf{s}})$ . It describes the local distribution of energy at the point  $\mathbf{r}$  over all possible ray directions  $\hat{\mathbf{s}}$ , which is a vector of unit length. By that description, the flux density at  $\mathbf{r}$  coming from the solid angle  $\Omega$  is

$$\mathbf{F}(\mathbf{r}) = \int_{\Omega} L_\nu(\mathbf{r}, \hat{\mathbf{s}}) \hat{\mathbf{s}} d\Omega(\hat{\mathbf{s}}) \quad (\text{A.48})$$

or vice versa: the flux that is passing through a point radiated into the solid angle  $\Omega$ .

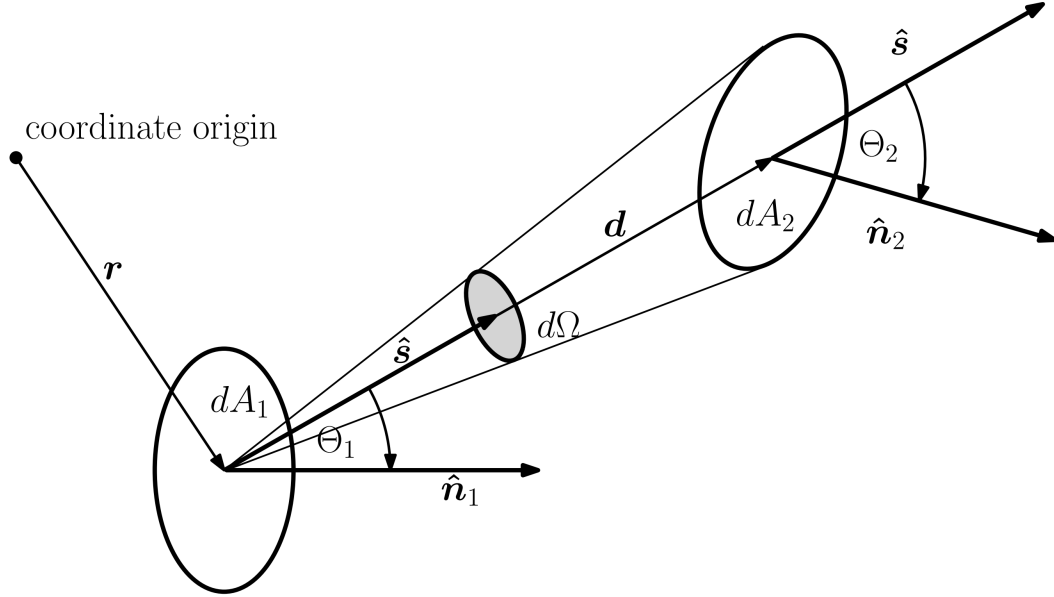


**Figure A.2:** Solid angle element  $d\Omega$  is defined as the projection of  $dA_2$  on the unit sphere around  $dA_1$  with the radius  $\hat{\mathbf{s}}$ . The projection is calculated by dividing  $dA_2$  through the square of the magnitude of the connection vector  $\mathbf{d}$  and multiplying by the inclination  $\cos \Theta_2 = \hat{\mathbf{n}}_2 \cdot \hat{\mathbf{s}}$ .

From this postulated formula, we calculate the flux through a surface element with  $d\phi = \mathbf{F}d\mathbf{A}_1$  and the flux through the whole surface  $A_1$  by the integration

$$\phi = \int_{A_1} \mathbf{F}(\mathbf{r}) d\mathbf{A}_1 = \int_{A_1} \int_{\Omega} L_\nu(\mathbf{r}, \hat{\mathbf{s}}) \hat{\mathbf{s}} d\Omega(\hat{\mathbf{s}}) d\mathbf{A}_1, \quad (\text{A.49})$$

$$= \int_{A_1} \int_{\Omega} F_\nu(\mathbf{r}) P_\nu(\hat{\mathbf{s}}) \hat{\mathbf{s}} d\Omega(\hat{\mathbf{s}}) d\mathbf{A}_1. \quad (\text{A.50})$$

In Eq. (A.50), we assumed that the radiance can be separated into a position-dependent, scalar irradiance  $F$  and an angular-dependent phase function  $P$ , which is normalized. If the flux through the first surface  $A_1$  is coming from another surface

## A Theoretical Background

$A_2$ , for example, the surface of a diffuse light source, we insert  $\hat{\mathbf{s}}d\mathbf{A}_1 = \cos\Theta_1 dA_1$  and the solid angle definition (see Fig. A.2)

$$d\Omega(\hat{\mathbf{s}}) = \frac{\hat{\mathbf{s}}d\mathbf{A}_2}{d^2} = \frac{\hat{\mathbf{n}}_2 dA_2}{d^2} = \frac{\cos\Theta_2 dA_2}{d^2}, \quad (\text{A.51})$$

where  $r$  is the distance between to surface elements that exchange flux. Then replacing the limits of integration ( $\Omega$ ) with the second surface  $A_2$ , gets the energy or flux exchange between two surfaces

$$\phi = \int_{A_1} \int_{A_2} L_\nu(\mathbf{r}, \mathbf{s}) \frac{\cos\Theta_1 \cos\Theta_2}{d^2} dA_1 dA_2, \quad (\text{A.52})$$

$$= \int_{A_1} \int_{A_2} F_\nu(\mathbf{r}) P_\nu(\hat{\mathbf{s}}) \frac{\cos\Theta_1 \cos\Theta_2}{d^2} dA_1 dA_2. \quad (\text{A.53})$$

This double integral describes the mutual energy exchange between all surface elements of the two surfaces  $A_1$  and  $A_2$ , which are connected with a straight light ray.

### A.7.1 Electromagnetic Derivation of Radiometry

Optical coherence theory is the modern description that tries to link electromagnetic theory to radiometry via statistical optics: The light field composed of regular, orderly plane waves is replaced by a more general randomly fluctuating field whose statistical properties determine the transportation of radiant energy - in the limiting case of short correlation length similar to the radiometric approximation. Here we will derive the radiometric equation from statistical optics, inspired by [44, 45].

For partially coherent light  $\mathbf{E}$  and  $\mathbf{H}$  are stochastic functions, we find the flux density of the field by the ensemble average of the time-average Poynting vector  $\langle \mathbf{S} \rangle$ , which is the crosscorrelation

$$\langle \bar{\mathbf{S}} \rangle = \frac{1}{2} \langle \mathbf{E}(\mathbf{r}_1) \times \mathbf{H}^*(\mathbf{r}_2) \rangle \quad (\text{A.54})$$

The Fourier transform relation of this crosscorrelation is

$$\langle \mathbf{E}(\mathbf{r}_1) \times \mathbf{H}^*(\mathbf{r}_2) \rangle = \int \int \langle \mathbf{E}(\mathbf{K}_1) \times \mathbf{H}^*(\mathbf{K}_2) \rangle e^{i(\mathbf{K}_1 \mathbf{r}_1 - \mathbf{K}_2 \mathbf{r}_2)} d^2 K_1 d^2 K_2, \quad (\text{A.55})$$

and its inverse Fourier transform is

$$\langle \mathbf{E}(\mathbf{K}_1) \times \mathbf{H}^*(\mathbf{K}_2) \rangle = \left( \frac{1}{2\pi} \right)^4 \int \int \langle \mathbf{E}(\mathbf{r}_1) \times \mathbf{H}^*(\mathbf{r}_2) \rangle e^{-i(\mathbf{K}_1 \mathbf{r}_1 - \mathbf{K}_2 \mathbf{r}_2)} d^2 r_1 d^2 r_2. \quad (\text{A.56})$$

In the asymptotic far field limit, we can approximate [45]  $\mathbf{K}_1 \approx \mathbf{K}_2 \approx \mathbf{K}$  and use Eq. (A.47), so under the integral, the crosscorrelation can be replaced by the autocorrelation

$$\langle \mathbf{E}(\mathbf{r}_1) \times \mathbf{H}^*(\mathbf{r}_2) \rangle = \hat{s} \frac{n}{2\mu c_0} \langle \mathbf{E}(\mathbf{r}_1) \mathbf{E}^*(\mathbf{r}_2) \rangle . \quad (\text{A.57})$$

Then we perform the change of coordinates,  $\mathbf{r}_2 = \mathbf{r}_1 - \mathbf{r}$  and  $dr_2^2 \rightarrow dr^2$  with the aid of the Jacobian. This results in the flux density in the direction  $\mathbf{K}$  coming from a stochastic electromagnetic field

$$\langle \bar{\mathbf{S}}(\mathbf{K}, \mathbf{K}) \rangle = \frac{1}{2} \langle \mathbf{E}(\mathbf{K}) \times \mathbf{H}^*(\mathbf{K}) \rangle \quad (\text{A.58})$$

$$= \hat{s} \frac{n}{2\mu c_0} \left( \frac{1}{2\pi} \right)^4 \int_{-\infty}^{\infty} \int_{-\infty}^{\infty} \langle \mathbf{E}(\mathbf{r}_1) \mathbf{E}^*(\mathbf{r}_2) \rangle e^{i\mathbf{K}(\mathbf{r}_1 - \mathbf{r}_2)} d^2 r_1 d^2 r_2 \quad (\text{A.59})$$

$$= \hat{s} \frac{n}{32\pi^4 \mu c_0} \int_{-\infty}^{\infty} \int_{-\infty}^{\infty} \langle \mathbf{E}(\mathbf{r}_1) \mathbf{E}^*(\mathbf{r}_1 - \mathbf{r}) \rangle e^{i\mathbf{K}\mathbf{r}} d^2 r_1 d^2 r \quad (\text{A.60})$$

$$= \hat{s} \frac{n}{32\pi^4 \mu c_0} \int_{-\infty}^{\infty} S_{\mathbf{E}\mathbf{E}}(\mathbf{r}_1, \mathbf{K}) d^2 r_1 \quad (\text{A.61})$$

In the last step, we introduced the local power spectrum  $S_{\mathbf{E}\mathbf{E}}(\mathbf{r}_1, \mathbf{K})$ , which is the Fourier transform of the autocorrelation. It still depends on  $\mathbf{r}_1$  because it is not necessarily the same for every point in the plane. When we assume that the purely stochastic part of the fields is indeed stationary (just depends on  $\mathbf{r}$ ) then it can be factored into a strength function  $c$  an autocorrelation  $R_{\mathbf{E}\mathbf{E}}$ . Then we obtain

$$\langle \bar{\mathbf{S}}(\mathbf{K}, \mathbf{K}) \rangle = \hat{s} \frac{n}{8\pi^2 \mu c_0} \int_{-\infty}^{\infty} \int_{-\infty}^{\infty} \langle \mathbf{E}(\mathbf{r}_1) \mathbf{E}^*(\mathbf{r}_1 - \mathbf{r}) \rangle e^{i\mathbf{K}\mathbf{r}} d^2 r_1 d^2 r \quad (\text{A.62})$$

$$= \hat{s} \frac{n}{32\pi^4 \mu c_0} \int_{-\infty}^{\infty} \int_{-\infty}^{\infty} R_{\mathbf{E}\mathbf{E}}(\mathbf{r}) c(\mathbf{r}_1) c^*(\mathbf{r}_1 - \mathbf{r}) e^{i\mathbf{K}\mathbf{r}} d^2 r_1 d^2 r \quad (\text{A.63})$$

$$= \hat{s} \frac{n}{32\pi^4 \mu c_0} \int_{-\infty}^{\infty} c(\mathbf{r}_1) c^*(\mathbf{r}_1) \int_{-\infty}^{\infty} R_{\mathbf{E}\mathbf{E}}(\mathbf{r}) e^{i\mathbf{K}\mathbf{r}} d^2 r d^2 r_1 \quad (\text{A.64})$$

$$= \hat{s} \frac{n}{32\pi^4 \mu c_0} \int_{-\infty}^{\infty} |c(\mathbf{r}_1)|^2 S_{\mathbf{E}\mathbf{E}}(\mathbf{K}) d^2 r_1 \quad (\text{A.65})$$

In the last two steps, we assumed that the autocorrelation length is much shorter than the change of the strength function, therefore  $c^*(\mathbf{r}_1 - \mathbf{r}) \approx c^*(\mathbf{r}_1)$  and could be taken out of the integral in  $d^2 r$ . The result is, under the condition that the strength factor varies much slower than the correlation length and the autocorrelation is stationary, we can separate the positional and the angular part

$$S_{\mathbf{E}\mathbf{E}}(\mathbf{r}_1, \mathbf{K}) = |c(\mathbf{r}_1)|^2 S_{\mathbf{E}\mathbf{E}}(\mathbf{K}) , \quad (\text{A.66})$$

## A Theoretical Background

which is analogous to regarding the radiance as a product of irradiance, which contains the positional dependency, and a phase function which contains the angular dependence. This ties into the general principle of this thesis, to separate the longitudinal (positional) and the angular dependency of the side-emitting fiber.

The last step is to calculate the flux from the observed plane into some solid angle above it. We use

$$\phi = \int \langle \bar{S}(\mathbf{K}, \mathbf{K}) \rangle \hat{\mathbf{n}} d\Omega, \quad (\text{A.67})$$

and express the wave vector with the help of the unit ray vector  $\mathbf{K} = nk\hat{\mathbf{s}} = nk(s_x, s_y, s_z)$  and see that the surface element in wave vector space can be expressed as  $d^2K = n^2k^2 d^2s$ .  $\langle \bar{S}(\mathbf{K}, \mathbf{K}) \rangle$  is expressed as  $n^2k^2 \langle \bar{S}(\mathbf{s}, \mathbf{s}) \rangle$ , the factor  $n^2k^2$  enters because the normalization of the inverse Fourier transform changes in Eq. (A.56). Inserting this and  $\langle \mathbf{S} \rangle = \hat{\mathbf{s}} \langle S \rangle$  we get

$$\phi = n^4k^4 \int \langle \bar{S}(\hat{\mathbf{s}}, \hat{\mathbf{s}}) \rangle \hat{\mathbf{s}} \hat{\mathbf{n}} d\Omega, \quad (\text{A.68})$$

$$= n^4k^4 \int \langle \bar{S}(\hat{\mathbf{s}}, \hat{\mathbf{s}}) \rangle \cos \Theta d\Omega, \quad (\text{A.69})$$

$$= n^4k^4 \int \langle \bar{S}(\hat{\mathbf{s}}, \hat{\mathbf{s}}) \rangle (\cos \Theta)^2 d^2s. \quad (\text{A.70})$$

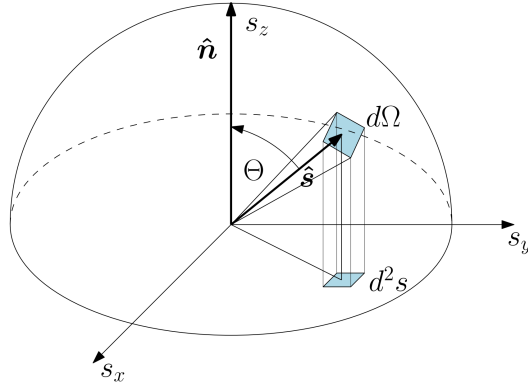


**Figure A.3:** Solid angle element  $d\Omega$  corresponding to the area element  $d^2s$  is its projection on the unit sphere,  $d^2s = \hat{\mathbf{n}} \hat{\mathbf{s}} d\Omega = \cos \Theta d\Omega$

So we obtain  $(\cos \Theta)^2$  in the equation. One  $\cos \Theta$  is from the scalar product of the ray vector with the surface normal, and the other one is from the projection of  $d\Omega$  on the  $s_x, s_y$ -plane, as shown in Fig. A.3. If we insert the pointing vector from Eq. (A.61) with  $\hat{\mathbf{n}} d^2r_1 = d\mathbf{A}_1$  we get

$$\phi = \frac{n^5k^4}{2\mu c_0} \int \int \hat{\mathbf{s}} S_{\mathbf{E}\mathbf{E}}(\mathbf{r}_1, \hat{\mathbf{s}}) d\Omega d\mathbf{A}_1, \quad (\text{A.71})$$

$$= \frac{n^5k^4}{2\mu c_0} \int \int S_{\mathbf{E}\mathbf{E}}(\mathbf{r}_1, \hat{\mathbf{s}}) (\cos \Theta)^2 d^2r_1 d^2s \quad (\text{A.72})$$



Then we see by comparison with Eq. (A.49), that the radiance is  $L = S_{\mathbf{E}\mathbf{E}}(\mathbf{r}_1, \hat{\mathbf{s}})$  and if we express it as  $L = FP = |c(\mathbf{r}_1)|^2 S_{\mathbf{E}\mathbf{E}}(\hat{\mathbf{s}})$ . The phase function is  $P = S_{\mathbf{E}\mathbf{E}}(\hat{\mathbf{s}})$  and the irradiance is  $F = |c(\mathbf{r}_1)|^2$ .

So we have seen that the irradiance is the product of the local power spectral density and the cosine of the emission angle in accordance with the result from Marchant and Wolf [45, 44]. The radiance can be understood as the local power spectral density of the random light field. It can be further factored into an irradiance that contains the local flux density and the phase function, which contains the angular information caused by the stochastic properties of the field. These properties come from the autocorrelation of the fluctuations of the light field.

From frequency analysis, we know that a delta pulse contains all frequencies, so the delta function's Fourier transform is a white spectrum. Similarly, if the field's autocorrelation length is very short, e.g., a delta function, it contains all spatial- $\mathbf{K}$  components (directions) and is therefore radiated in all directions. So a Lambertian surface or source has a very short autocorrelation length across its surface. In praxis, a delta function autocorrelation length is unnecessary to get radiation in all directions because this also contains evanescent waves, which can not leave the source anyway. A  $1/\lambda$  autocorrelation-length is sufficient [46].

## A.8 The Volume Current Method

The light emission from the side-emitting fiber is caused by a scattering process inside it, where guided light interacts with refractive index fluctuations. In this thesis, the refractive index fluctuations are localized femtosecond laser-generated refractive index modifications: scattering centers. This section shows how the fiber's light emission is related to the refractive index fluctuations.

The calculation of radiation loss from dielectric waveguides and optical fibers can be very complicated, and a variety of techniques have been used to approach this problem [47]. Here we apply the volume current method, a perturbation technique used to calculate small radiation loss from small refractive index fluctuations in dielectrics. In this framework, the interaction of the guided light with refractive index fluctuation induces a volume current density. This current density radiates light which results in power being removed from the incident field.

The optical fiber is modeled as normal lossless refractive index distribution  $n_0(\mathbf{r})$  with a small (localized) refractive index distortion  $\Delta n(\mathbf{r})$  which causes the scattering  $n_0(\mathbf{r}) \gg \Delta n(\mathbf{r})$ . The combined refractive index distribution is

$$n(\mathbf{r}) = n_0(\mathbf{r}) + \Delta n(\mathbf{r}) . \quad (\text{A.73})$$

We use the vector wave equation Eq. (A.14) and assume the light to be monochromatic, so the time dependence is stationary and of the form  $\exp\{i\omega t\}$  and the time derivatives can be replaced with  $i\omega$ . Together with the dispersion relation Eq. (A.20) and the refractive index Eq. (A.18), we get the time free wave equation ( $\mu = \mu_0$ )

$$\nabla^2 \mathbf{E} + n^2 k^2 \mathbf{E} = i\mu_0 \omega \mathbf{j} , \quad (\text{A.74})$$

## A Theoretical Background

and the homogeneous, source, and time free Helmholtz equation

$$\nabla^2 \mathbf{E} + n^2 k^2 \mathbf{E} = 0 . \quad (\text{A.75})$$

We insert the distorted refractive index distribution Eq. (A.73) into the latter equation and neglect the term of higher order in  $\Delta n$ . Then we split the electric field into an unperturbed part  $\mathbf{E}_0$  which is a solution of the homogeneous Helmholtz equation Eq. (A.75) with  $n_0$ , and a perturbed part  $\mathbf{E}_s$ , which is the scattered radiation, so  $\mathbf{E} = \mathbf{E}_0 + \mathbf{E}_s$ . This results in a sum of scattered and guided field components

$$\nabla^2 \mathbf{E}_0 + n_0^2 k^2 \mathbf{E}_0 + 2n_0 \Delta n k^2 (\mathbf{E}_0 + \mathbf{E}_s) + \nabla^2 \mathbf{E}_s + n_0^2 k^2 \mathbf{E}_s = 0 . \quad (\text{A.76})$$

The sum two first terms on the right-hand side are by definition Eq. (A.75) and therefore zero. What remains can be written in the form of the vector wave equation

$$\nabla^2 \mathbf{E}_s + n_0^2 k^2 \mathbf{E}_s = -2n_0 \Delta n k^2 (\mathbf{E}_0 + \mathbf{E}_s) \approx -2n_0 \Delta n k^2 \mathbf{E}_0 . \quad (\text{A.77})$$

We applied the perturbation assumption that the electric field inside the scattering center is dominated by the guided radiation  $\mathbf{E}_0 + \mathbf{E}_s \approx \mathbf{E}_0$ . Similarly, to Eq. (A.74), the interaction of the electric field with a small refractive index perturbation causes an electromagnetic field that is driven by a source term. The source can also be written in the form of Eq. (A.74), so we get the result that the scattered radiation can be regarded as driven by a polarization current density, which in turn is caused by the interaction of the original guided field  $\mathbf{E}_0$  with the refractive index perturbation

$$\mathbf{j} = 2i\omega n_0 \Delta n \epsilon_0 \mathbf{E}_0 . \quad (\text{A.78})$$

The advantage point of view is twofold: First, because the  $\mathbf{E}_0$  field is guided in the fiber, its contribution outside of the fiber is zero, so the electric field outside is just the scattered field  $\mathbf{E}_s$ . Second, we can now use the solution for the vector wave equation to get the equations for the far field scattered radiation.

One possibility is to solve Eq. (A.14) with the aid of a vector potential  $\mathbf{A}$  [48, 49]. For this, we use the property of the magnetic field to be source-free (solenoidal), according to Eq. (A.10). Because the divergence of the curl of a vector is always zero  $\nabla(\nabla \times \mathbf{A}) = 0$ , we can define a vector field  $\mathbf{A}$  with the property

$$\mu_0 \mathbf{H}_s = \nabla \times \mathbf{A} . \quad (\text{A.79})$$

Inserting this in the Maxwell equation Eq. (A.9) with monochromatic time dependency, we obtain

$$\nabla \times \mathbf{E}_s = -i\omega \nabla \times \mathbf{A} . \quad (\text{A.80})$$

If we integrate this result, we get

$$\mathbf{E}_s = -i\mu_0 \omega \mathbf{A} - \nabla \Phi . \quad (\text{A.81})$$

Here the divergence of the undetermined scalar potential function  $\Phi$  takes the role of the integration constant because  $\nabla \times (\nabla\Phi) = 0$ . If we insert Eq. (A.79) in Eq. (A.8) and apply the monochromatic condition, we get

$$\nabla \times (\nabla \times \mathbf{A}) = i\omega n^2 \epsilon_0 \mu_0 \mathbf{E}_s + \mu_0 \mathbf{j} = n^2 k^2 \mathbf{A} - i\omega n^2 \epsilon_0 \mu_0 \nabla\Phi + \mu_0 \mathbf{j} . \quad (\text{A.82})$$

Then we expand the vector triple product  $\nabla \times (\nabla \times \mathbf{A}) = \nabla(\nabla\mathbf{A}) - \nabla^2 \mathbf{A}$  and obtain

$$\nabla^2 \mathbf{A} + n^2 k^2 \mathbf{A} = \nabla(\nabla\mathbf{A}) + i\omega n^2 \epsilon_0 \mu_0 \nabla\Phi - \mu_0 \mathbf{j} . \quad (\text{A.83})$$

Because Eq. (A.79) just defined the rotational part of  $\mathbf{A}$ , we can choose its divergence as the Lorentz gauge

$$\nabla(\nabla\mathbf{A}) = -i\omega n^2 \epsilon_0 \mu_0 \nabla\Phi . \quad (\text{A.84})$$

This convenient choice leads to the cancellation of two of the three terms on the right-hand side, and we get the Helmholtz equation for the vector potential

$$\nabla^2 \mathbf{A} + n^2 k^2 \mathbf{A} = -\mu_0 \mathbf{j} . \quad (\text{A.85})$$

The solution to this differential equation is the Helmholtz integral [49] which satisfies Sommerfeld's radiation condition of an outgoing wave at infinity [50]

$$\mathbf{A} = \frac{\mu_0}{4\pi} \int_{V_0} \mathbf{j}(\mathbf{r}') \frac{e^{ink|\mathbf{r}-\mathbf{r}'|}}{|\mathbf{r}-\mathbf{r}'|} dV' . \quad (\text{A.86})$$

It describes the vector potential as the sum of spherical wavelets originating from the polarization current  $\mathbf{j}$  in the volume  $V_0$ .

The electric field of the scattered radiation can be expressed in terms of the vector potential by the combination of Eq. (A.81) and Eq. (A.84).

$$\mathbf{E}_s = -i\omega \mathbf{A} + \frac{\nabla(\nabla\mathbf{A})}{i\omega n^2 \epsilon_0 \mu_0} = -i\omega \left[ \mathbf{A} + \frac{\nabla(\nabla\mathbf{A})}{n^2 k^2} \right] \quad (\text{A.87})$$

To solve it, we have to take a look at  $\nabla(\nabla\mathbf{A})$  and notice that the differential operators can be pulled under the integral

$$\nabla(\nabla\mathbf{A}) = \frac{\mu_0}{4\pi} \int_{V_0} \mathbf{j}(\mathbf{r}') \nabla \left( \nabla \frac{e^{ink|\mathbf{r}-\mathbf{r}'|}}{|\mathbf{r}-\mathbf{r}'|} \right) dV' , \quad (\text{A.88})$$

because they operate on the unprimed coordinates only.

Because of the modulus  $|\mathbf{r}-\mathbf{r}'|$ ,  $\mathbf{r}$  and  $\mathbf{r}'$  can be exchanged, and the differential operators can be changed to primed coordinates as well, so

$$\nabla \left( \nabla \frac{e^{ink|\mathbf{r}-\mathbf{r}'|}}{|\mathbf{r}-\mathbf{r}'|} \right) = \nabla' \left( \nabla' \frac{e^{ink|\mathbf{r}-\mathbf{r}'|}}{|\mathbf{r}-\mathbf{r}'|} \right) . \quad (\text{A.89})$$

## A Theoretical Background

We are interested in the field far from the scattering center, therefore, we use the Fraunhofer limit and approximate the exponent with  $|\mathbf{r} - \mathbf{r}'| \approx r - \hat{\mathbf{e}}_r \mathbf{r}'$  and the denominator with  $1/r$ . Now the gradient and the divergence is easily calculated

$$\nabla' \left( \frac{e^{ink|\mathbf{r}-\mathbf{r}'|}}{|\mathbf{r}-\mathbf{r}'|} \right) \approx \frac{e^{inkr}}{r} \nabla' \left( \nabla' e^{-ink\hat{\mathbf{e}}_r \mathbf{r}'} \right) , \quad (\text{A.90})$$

$$= \frac{e^{inkr}}{r} \nabla' \left( -ink\hat{\mathbf{e}}_r e^{-ink\hat{\mathbf{e}}_r \mathbf{r}'} \right) , \quad (\text{A.91})$$

$$= \frac{e^{inkr}}{r} \left( -n^2 k^2 \hat{\mathbf{e}}_r \hat{\mathbf{e}}_r e^{-ink\hat{\mathbf{e}}_r \mathbf{r}'} \right) . \quad (\text{A.92})$$

Inserting this result back into Eq. (A.87) together with the Fraunhofer approximation and using the vector triple product  $\hat{\mathbf{e}}_r \times (\hat{\mathbf{e}}_r \times \mathbf{A}_f) = \hat{\mathbf{e}}_r (\hat{\mathbf{e}}_r \mathbf{A}_f) - \mathbf{A}_f (\hat{\mathbf{e}}_r \hat{\mathbf{e}}_r)$  will provide the scattered electric field

$$\mathbf{E}_s = -i\omega [\mathbf{A}_f - \hat{\mathbf{e}}_r \hat{\mathbf{e}}_r \mathbf{A}_f] = i\omega [\hat{\mathbf{e}}_r \times (\hat{\mathbf{e}}_r \times \mathbf{A}_f)] , \quad (\text{A.93})$$

with the far field vector potential

$$\mathbf{A}_f = \frac{\mu_0}{4\pi} \frac{e^{in_0kr}}{r} \int_{V_0} e^{-in_0k\hat{\mathbf{e}}_r \mathbf{r}'} \mathbf{j}(\mathbf{r}') dV' , \quad (\text{A.94})$$

which now has the form of outgoing plane waves originating from the current polarization current density inside  $V_0$ .

The next step is to find the associated magnetic field. From the Maxwell equation and the definition of the vector potential Eq. (A.79) we know

$$\mu_0 \mathbf{H}_s = \nabla \times \mathbf{A} . \quad (\text{A.95})$$

Again, the rotation can be taken under the integral because it operates on the unprimed quantities only, so

$$\mu_0 \mathbf{H}_s = \frac{\mu_0}{4\pi} \int_{V_0} \nabla \times \mathbf{j}(\mathbf{r}') \frac{e^{ink|\mathbf{r}-\mathbf{r}'|}}{|\mathbf{r}-\mathbf{r}'|} dV' , \quad (\text{A.96})$$

$$= -\frac{\mu_0}{4\pi} \int_{V_0} \mathbf{j}(\mathbf{r}') \times \nabla \frac{e^{ink|\mathbf{r}-\mathbf{r}'|}}{|\mathbf{r}-\mathbf{r}'|} dV' . \quad (\text{A.97})$$

Now we again use the modulus property to exchange the nabla operator for primed and unprimed coordinates and use the Fraunhofer approximation to perform the

following calculations

$$\mu_0 \mathbf{H}_s = -\frac{\mu_0}{4\pi} \frac{e^{in_0kr}}{r} \int_{V_0} \mathbf{j}(\mathbf{r}') \times (\nabla' e^{-in_0k\hat{\mathbf{e}}_r \cdot \mathbf{r}'} ) dV' , \quad (\text{A.98})$$

$$= -\frac{\mu_0}{4\pi} \frac{e^{in_0kr}}{r} \int_{V_0} \mathbf{j}(\mathbf{r}') \times (-ink\hat{\mathbf{e}}_r e^{-in_0k\hat{\mathbf{e}}_r \cdot \mathbf{r}'} ) dV' , \quad (\text{A.99})$$

$$= \frac{\mu_0}{4\pi} \frac{e^{in_0kr}}{r} \int_{V_0} (-ink\hat{\mathbf{e}}_r) \times \mathbf{j}(\mathbf{r}') e^{-in_0k\mathbf{r}'} dV' , \quad (\text{A.100})$$

$$= -ink(\hat{\mathbf{e}}_r \times \mathbf{A}_f) . \quad (\text{A.101})$$

In summary, the electric and the magnetic fields of the scattered radiation are

$$\mathbf{E}_s = i\omega\hat{\mathbf{e}}_r \times (\hat{\mathbf{e}}_r \times \mathbf{A}_f) , \quad (\text{A.102})$$

$$\mathbf{H}_s = -\frac{ink}{\mu_0} (\hat{\mathbf{e}}_r \times \mathbf{A}_f) . \quad (\text{A.103})$$

Where  $\mathbf{A}_f$  is the far field vector potential at the point  $\mathbf{r}$  from a superposition of spherical wavelets, approximated as plane waves in the Fraunhofer limit, caused by the polarization currents  $\mathbf{j}(\mathbf{r}')$  enclosed in the volume  $V_0$ ,

$$\mathbf{A}_f = \frac{\mu_0}{4\pi} \frac{e^{in_0kr}}{r} \int_{V_0} e^{-in_0k\hat{\mathbf{e}}_r \cdot \mathbf{r}'} \mathbf{j}(\mathbf{r}') dV' . \quad (\text{A.104})$$

Our last objective is to calculate the scattered radiation in the far field, by calculating the time average pointing vector from Eq. (A.46)

$$\bar{\mathbf{S}} = \frac{1}{2} \text{Re} \{ \mathbf{E}_s \times \mathbf{H}_s^* \} = \frac{\omega nk}{2\mu_0} \text{Re} \{ [\hat{\mathbf{e}}_r \times (\hat{\mathbf{e}}_r \times \mathbf{A}_f)] \times (\hat{\mathbf{e}}_r \times \mathbf{A}_f^*) \} . \quad (\text{A.105})$$

The complicated looking multiple cross product can be expanded using the vector triple product

$$[\hat{\mathbf{e}}_r \times (\hat{\mathbf{e}}_r \times \mathbf{A}_f)] \times (\hat{\mathbf{e}}_r \times \mathbf{A}_f^*) = \hat{\mathbf{e}}_r [(\hat{\mathbf{e}}_r \times \mathbf{A}_f^*)(\hat{\mathbf{e}}_r \times \mathbf{A}_f)] - (\hat{\mathbf{e}}_r \times \mathbf{A}_f)[(\hat{\mathbf{e}}_r \times \mathbf{A}_f^*)\hat{\mathbf{e}}_r] , \quad (\text{A.106})$$

where the last term is zero due to orthogonality. Inserting the remaining term, we obtain

$$\bar{\mathbf{S}} = \hat{\mathbf{e}}_r \frac{\omega nk}{2\mu_0} (\hat{\mathbf{e}}_r \times \mathbf{A}) (\hat{\mathbf{e}}_r \times \mathbf{A}^*) = \hat{\mathbf{e}}_r \frac{\omega nk}{2\mu_0} |\hat{\mathbf{e}}_r \times \mathbf{A}|^2 , \quad (\text{A.107})$$

$$= \hat{\mathbf{e}}_r \frac{\omega nk}{2\mu_0} \frac{\mu_0^2}{16\pi^2 r^2} \int_{V_0} \int_{V_0} [\hat{\mathbf{e}}_r \times \mathbf{j}(\mathbf{r}_1)] [\hat{\mathbf{e}}_r \times \mathbf{j}^*(\mathbf{r}_2)] e^{-ink(\mathbf{r}_1 - \mathbf{r}_2)} dV_1 dV_2 . \quad (\text{A.108})$$

which is also real due to the absolute square, so we don't need to remove an imaginary part. When we replace the  $\mathbf{r}_2 = \mathbf{r}_1 - \mathbf{r}$  and notice that  $\mathbf{j}$  is zero outside of  $V_0$ , we

## *A Theoretical Background*

see that this is again the autocorrelation function of the cross product of  $\hat{\mathbf{e}}_r$  with  $\mathbf{j}$  whose Fourier transform again gives the power spectral density as in Appendix A.7. We will use this property to derive the scattering pattern of a refractive index distortion in an optical fiber in Section 3.3.

## B Experimental Methods

The measurement of the light emitted from the side-emitting fiber serves, on the one hand, to obtain parameters to calculate the radiation field and, on the other hand, to compare calculations with the observations. These measurements are divided into longitudinal and angular emission, which gives the corresponding parameters used to calculate and characterize the radiation field in the publications in Chapter 3. For the longitudinal emission, the goal is to measure the total emission of a fiber segment as a function of the  $z$ -position: An integrating sphere moved alongside the side-emitting fiber captures the light emission in all directions. For the angular emission, we want to determine the directional distribution of radiation emitted from a fiber segment or fiber surface element. A microscope objective, focussed on the fiber, decomposes the collected light into its angular components, and a microscope camera images this decomposition. The enveloping angular light distribution from a fiber segment is obtained from the average of many images of the angular pattern.

### B.1 Longitudinal Measurement: Motorized Integrating Sphere

The longitudinal emission from a side-emitting fiber is measured stepwise by capturing it with an integrating sphere moved from the light coupling to the fiber-end: The custom-made integrating sphere encloses the fiber and captures almost the whole solid angle flux emission from a fiber segment with the length  $\Delta z$ . After the flux measurement for one fiber segment is complete, the sphere moves to another, and the procedure is repeated. In this way, the  $z$ -dependency of the emitted flux is measured piece-wise for the whole fiber.

An integrating sphere is a hollow sphere made of a white, highly diffuse reflecting material, which generates a homogeneous irradiation field inside it by multiple diffuse reflections. In Fig. B.1 we see a sketch of the experimental set-up: Two hollow tubes, coated with boron nitride, guide the fiber through the integrating sphere. The guides are separated by a gap  $\Delta z = 2$  mm in the middle of the sphere, which exposes a small fiber segment: this is the aperture of the sphere. The flux emitted from the fiber segment is now homogeneously distributed on the sphere wall by diffuse reflections. There it is measured by an optical fiber, which is placed shortly beneath the sphere's surface. In this way, the sphere material also acts as a cosine corrector, which enlarges the field of view of the optical fiber to a half solid angle. The sphere was made from optical PTFE (polytetrafluoroethylene) [provided by Berghof-Fluoroplastics, Eningen] and had an inner diameter of 40 mm.

There are several ways to derive the measured irradiance on a port that results

## B Experimental Methods

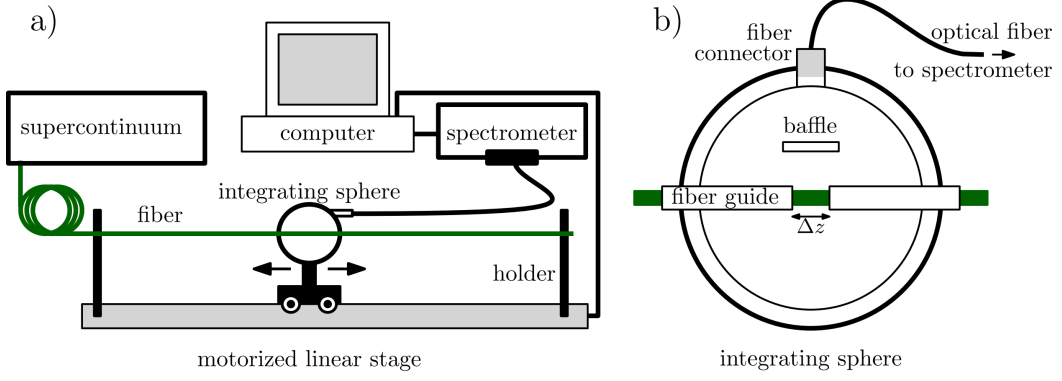


**Figure B.1:** Integrating sphere with motorized scanning stage for longitudinal emission measurement of side-emitting fibers. The light emitted from the fiber segment  $\Delta z$  is distributed homogeneously on the sphere wall through multiple diffuse reflections. The flux on the wall, measured with a fiber-coupled spectrometer, is proportional to the flux emitted by the fiber segment. The baffle protects the detector from direct fiber illumination. After measurement, the sphere is moved to a different  $z$ -position, and the measurement is repeated. In this way, the  $z$ -dependent emission is recorded.

from the multiple diffuse reflections on the sphere wall. The easiest is the energy-balance method provided by Clare [51]. It states, in equilibrium, the flux entering the sphere has to match the flux that drained from it, either by absorption or by leaving the sphere through a port. Let's regard the sphere with the surface area  $A_{tot}$  as composed of  $n$ -zones with the area  $A_n$ , which can be chosen arbitrarily small. Each zone has a diffuse reflection coefficient  $\rho_n$ , which can, for example, either be around 99% for the diffusely reflecting sphere wall or 0% for a port. Now, the drained flux  $D_n$  from the diffuse irradiance  $F_n$  which is irradiating the zone  $A_n$  is

$$D_n = F_n A_n (1 - \rho_n) . \quad (\text{B.1})$$

Here we dispense the vector notation because the resulting flux is always perpendicular to the sphere's surface due to symmetry. In equilibrium, when we sum up all the drained fluxes, they should match the flux  $\phi_0$  injected into the sphere

$$\phi_0 = (1 - \rho_0)\phi_0 + \sum_n D_n = (1 - \rho_0)\phi_0 + \sum_i F_n A_n (1 - \rho_n) . \quad (\text{B.2})$$

Here  $(1 - \rho_0)\phi_0$  signifies the initial diffuse reflection of the primary beam on the sphere wall:  $\rho_0$  can either be the average reflectivity of the initially irradiated wall segment or the average of the whole sphere, if the light source is enclosed and radiating in all directions, as in this thesis.

Now we bring the initial reflection on the left-hand side and split the sphere into



## B.2 Angular Measurement: Fourier-Microscopy

two kinds of zones, wall ( $w$ ) with  $\rho_n = \rho$  and port ( $p$ ) with  $\rho_n = 0$

$$\phi_0 - (1 - \rho_0)\phi_0 = \rho_0\phi_0 = (1 - \rho) \sum_w F_w A_w + \sum_p F_p A_p, \quad (\text{B.3})$$

$$= (1 - \rho)W\bar{F}_w + P\bar{F}_p. \quad (\text{B.4})$$

In the last step, we have replaced the two sums by the respective average irradiances  $\bar{F}$  times the associated total wall  $W$  or total port  $P$  area.

In equilibrium, the irradiance is approximately the same on all surface elements  $\bar{F}_w \approx \bar{F}_p \approx F$  because of the spherical symmetry. When we insert this, we can solve the equation and find the average irradiance on every wall segment as well as on the measurement port

$$F = \frac{\rho_0\phi_0}{(1 - \rho)W + P} = \frac{\rho_0\phi_0}{A_{tot}[1 - \rho(1 - a)]}. \quad (\text{B.5})$$

Where  $A_{tot} = W + P$  is the surface of the sphere, and  $a = P/A_{tot}$  is the fraction of the port area. So we found that the integrating sphere is not just distributing the incoming radiation over the inner surface, which would result in  $F = \phi_0/A_{tot}$ , but it boosts the signal by a factor of  $\rho_0/[1 - \rho(1 - a)]$ . For example, if we assume  $\rho_0 \approx \rho$  and  $a \approx 0$ , the resulting boost would be 49 for  $\rho = 0.98$ , 99 for  $\rho = 0.99$  and 999 for  $\rho = 0.999$ : the last percent to 100% diffuse reflectivity makes a huge difference! Therefore, the sphere should always be made of a highly diffuse reflecting material and kept very clean. For the custom-made integrating sphere in this thesis, I choose optical PTFE (polytetrafluoroethylene - also known as Teflon), which is easy to machine into a hollow sphere and has a diffuse reflectivity of 99% in the visible range. It must also be stressed that this equation only holds for diffuse reflections, not for direct illumination with the primary beam, which is therefore blocked with a diffuses reflective but intransparent baffle Fig. B.1.

From the derived equation, we see that the measured irradiance at the port is proportional to the flux injected into the sphere. In measuring the side-emitting fiber, we use this to determine the flux  $\Delta\phi$  from the fiber segment  $\Delta z$ . But because the light coupling to the optical fiber and the spectrometer causes unknown systematic errors, we choose to perform relative measurements by normalizing all measured values to the start value at  $z = 0$ . In this way, all the sphere parameters and unknown systematic attenuation factors cancel out by the normalization

$$\frac{F(z)}{F(0)} = \frac{\Delta\phi(z)}{\Delta\phi(0)}. \quad (\text{B.6})$$

However, the dependency on  $z$  of  $\Delta\phi$  is unaffected by this normalization and can be examined undisturbed.

## B.2 Angular Measurement: Fourier-Microscopy

The angular emission of a fiber segment is measured by capturing the radiation with a microscope objective, which decomposes it into its angular components and

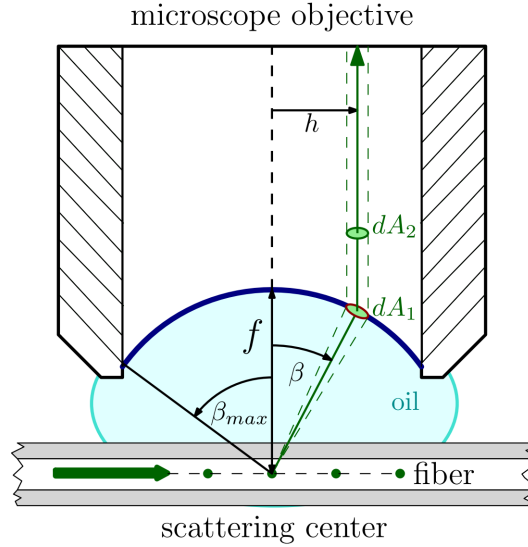


**Figure B.2:** Schematics of a ray crossing an aplanatic objective obeying the Abbe sine condition: Rays emerging from the front focal plane under an angle  $\beta$  are converted into rays parallel to the optical axis with the distance  $h$  by refraction on the reference sphere with the radius  $f$ , the focal length.

imaging the decomposition with a microscope camera. This method is referred to as Fourier-microscopy: the light field in the front focal plane or object space is decomposed into its angular components in the back focal plane or Fourier space. This thesis uses this property to analyze the light emitted by a side-emitting fiber surface or scattering center for its angular emission- or scattering pattern. To image the back focal plane and not the object plane, a Bertrand-lens is inserted into the beam path of a microscope [52] (alternatively, the ocular can be removed for a quick glimpse).

When we take a picture of the back focal plane with some scattering object in front of the lenses, we see a light-filled circle surrounded by darkness. When we image a plane wave, we see a point inside the circle with some distance to the optical axis depending on the plane wave's inclination. To understand these phenomena, we will use this section to derive how the angles of rays are represented in the back focal plane and how certain corrections have to be performed to turn the image into a quantitative measurement. These derivations will show us that the back focal plane image is essentially the projection of the hemispherical far field scattering pattern on a plane while conserving its energy.

To derive the relation between the angle of the ray and its position in the back focal plane, we use the property that every infinity-corrected aplanatic microscope objective should obey the Abbe sine condition in the following form [53, 54]

$$\sin \beta = \frac{h}{f} . \quad (\text{B.7})$$

It states that a ray emerging from the front focal plane under the angle  $\beta$  is transformed into a parallel ray with the distance  $h$  to the optical axis by the imaging system. This is schematically shown in Fig. B.2. The focal length  $f$  is not necessarily known, but all microscope objectives have their numerical aperture NA engraved, which is defined by [53]

$$\text{NA} = n_0 \sin \beta_{max} , \quad (\text{B.8})$$

the product of the refractive index of the medium between objective and front focal plane  $n_0$  and the sine of the maximum opening angle  $\beta_{max}$ , which is the maximum angle of a ray with the optical axis accepted by the objective.

Using the maximum opening angle in the sine condition, we can equate it to the numerical aperture and get

$$\sin \beta_{max} = \frac{h_{max}}{f} = \frac{\text{NA}}{n_0} \rightarrow \frac{1}{f} = \frac{\text{NA}}{n_0 h_{max}} . \quad (\text{B.9})$$

We use this to replace the unknown focal length in the sin condition and obtain

$$\sin \beta = \frac{h}{h_{max}} \frac{\text{NA}}{n_0} . \quad (\text{B.10})$$

So the angle of a light ray can readily be determined from a picture of the back focal plane by its relative distance to the optical axis, which is the center of the circular back-focal plane with the radius  $h_{max}$ . The numerical aperture ratio to the refractive index accounts for the immersion medium (e.g., air/water/oil) and the largest accepted angle.

The spherical shell in Fig. B.2 with the radius  $f$ , which refracts tilted rays into parallel rays, is called the reference sphere. It represents the actions of the many lenses of the objective. In essence, the Abbe sine condition acts as if the reference sphere is projected on a plane while conserving the energy of the rays: the flux passing through  $dA_1$  on the reference sphere with the radius  $f$  is equal to the flux through  $dA_2$ , which is its projection on the back focal plane. This is geometrically expressed as

$$d\phi = \mathbf{F}_1 d\mathbf{A}_1 = \mathbf{F}_2 d\mathbf{A}_2 = F_1 dA_1 = F_2 dA_2 . \quad (\text{B.11})$$

Both flux densities are in both cases parallel to the surface normal  $\hat{\mathbf{s}}_1 \hat{\mathbf{n}}_1 = \hat{\mathbf{s}}_2 \hat{\mathbf{n}}_2 = 1$  so we obtain

$$\frac{F_1}{F_2} = \frac{dA_2}{dA_1} \quad (\text{B.12})$$

To calculate the flux-density ratio we use that  $dA_2$  is the projected area of  $dA_1$  or, in vector notation, the projection of  $d\mathbf{A}_1$  on the surface unit vector  $\hat{\mathbf{n}}_2$ . So by

## B Experimental Methods

exploiting the definition of the scalar product

$$d\mathbf{A}_1 \hat{\mathbf{n}}_2 = dA_1 \hat{\mathbf{n}}_1 \hat{\mathbf{n}}_2 = \cos \beta dA_1 = dA_2 . \quad (\text{B.13})$$

Due to the symmetry of the problem, the angle between the surface normals  $\beta$  is the same as the angle of the light ray with the optical axis. Inserting Eq. (B.13) in Eq. (B.12) we obtain

$$F_2 = \frac{F_1}{\cos \beta} . \quad (\text{B.14})$$

This shows that the flux density in large  $\beta$  angles will be amplified to conserve energy in the process of projecting the reference sphere on the back focal plane. This amplification compensates the loss of surface area. So if one is interested in the flux contained in a light ray, this needs to be corrected by multiplying the image of the back focal plane with  $\cos \beta$ . But we also need to correct for apodization.

Real-world objectives will suffer from an angle and polarization-dependent loss according to the Fresnel equations because rays entering the objective at large  $\beta$ -angles will undergo large-angle refraction [55]. These losses are generally unknown, and therefore one needs to perform a calibration if one wants to use the Fourier-microscope as a quantitative angular radiation measurement device.

As a calibration standard, we will choose a Lambertian diffuser because it theoretically has a constant irradiance in the back focal plane, and very good real-world substitutes are readily available in the form of diffuse reflection and transmission standards.

To show that a Lambertian diffuser has a constant back focal plane irradiance distribution, we calculate the irradiance on the reference sphere: In radiometry, a Lambertian diffuser is characterized by its constant radiance  $L(\mathbf{r}, \hat{\mathbf{s}}) = L = \text{const.}$  Inserting this into Eq. (A.48), only the solid angle remains in the equation. We replace it with the definition of the solid angle Eq. (A.51) and integrate it over the emitting surface, in this case, the front focal plane  $\Delta A$  whose surface normal  $\hat{\mathbf{n}}_o$  is parallel to the optical axis

$$\mathbf{F} = L \int_{\Omega} \hat{\mathbf{s}} d\Omega(\hat{\mathbf{s}}) = L \hat{\mathbf{s}} \int_{\Delta A} \frac{\hat{\mathbf{s}} \hat{\mathbf{n}}_o dA_s}{f^2} , \quad (\text{B.15})$$

$$= \hat{\mathbf{s}} \frac{L \cos \beta \Delta A}{f^2} = \hat{\mathbf{s}} \frac{I \cos \beta}{f^2} . \quad (\text{B.16})$$

We replaced  $I \approx L \Delta A$  with the intensity  $I$  because  $f$  is much larger than the dimensions of the surface  $\sqrt{\Delta A}$ , so it can be regarded as a point source. Here we see why this is referred to as Lambert's cosine law: the radiance is constant over all directions, but the projected area of the emitting surface varies with viewing angle. That is also the reason why a Lambertian source is equally bright from all viewing angles.

If we insert this result in Eq. (B.11) and use the angular amplification Eq. (B.13), the cosine cancel, and we obtain

$$F_2 = \frac{I}{f^2} = \text{const.} , \quad (\text{B.17})$$

the objective conserves the intensity, or the intensity of an ideal Lambertian diffuser should be ideally flat in the back focal plane. This ideal property can now be used for calibration in the following way. The real world measured flux of a good Lambertian diffuser should follow the equation but has an  $h$  and  $\varphi$  dependent apodization  $A(h, \varphi)$ , the real measured flux density distribution  $F_m$  in the back focal plane is

$$F_m(h, \varphi) = A(h, \varphi)F_2(h, \varphi) , \quad (\text{B.18})$$

so when measuring a Lambertian surface, we can assume  $F_2$  to be constant. Therefore  $F_m(h, \varphi)$  is directly proportional to  $A(h, \varphi)$ . All measurements can be apodization corrected by dividing through the appropriately normalized back focal plane image of a Lambertian diffuser  $A(h, \varphi)/|A(h, \varphi)|$ .

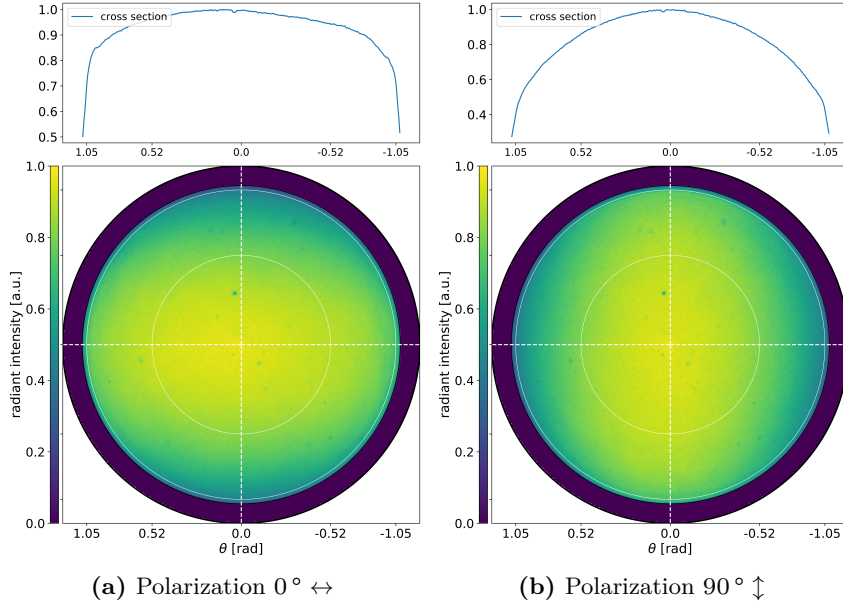


**Figure B.3:** Fourier-microscope images of an opal glass scattering standard (provided by QSIL GmbH Quarzschmelze Ilmenau) in two polarization directions  $0^\circ$  and  $90^\circ$  with an  $\text{NA} = 1.3$  microscope objective oil immersion  $n_0 = 1.51$ . The two polarization directions show different back focal plane apodization:  $0^\circ$  towards the top and bottom edge;  $90^\circ$  towards the left and right edge. The dark outer ring marks region undetectable due to the restrictions in opening angle to  $\beta_{max} = \arcsin(1.3/1.51) = 59.4^\circ$ .

In Fig. B.3, we see an example of the back focal plane image of a Lambertian scattering standard in two polarization directions. Here we see a filled circle, the back focal plane image, surrounded by a dark ring, representing the cutoff at  $\text{NA} = 1.3$  to the limit of  $\text{NA} = 1.51$  in oil ( $n_0 = 1.51$ ). We see that the irradiance profile inside the back focal plane is almost flat parallel to the polarisation direction, only for very large angles, there is a noticeable deviation. But orthogonal to the polarisation

direction, the irradiance drops continuously towards the edge. This distribution is a direct representation of the objectives polarization-dependent apodization function. Dividing pictures of the back focal plane by these distributions in the corresponding polarisation direction will yield the corrected versions. In this thesis, this has been done for all back focal plane images.

### B.2.1 The Fourier Transform Property of an Objective

This last section will show that the back focal plane is indeed the Fourier transform of the electric field in the front focal plane of the objective times an angular amplification factor. We assume that the Abbe sine condition Eq. (B.7) holds and that it means the rays coming from the front focal plane are refracted at the reference sphere. The directions of rays in the sine condition are associated with the wave vector  $\mathbf{K}$  coming from the front focal plane. Therefore, the measured flux on the reference sphere is the Pointing vector as a function of the wave vector.

We compute the pointing vector for the wave vector and insert the inverse Fourier transform of the electric field

$$\bar{\mathbf{S}}(\mathbf{K}_1, \mathbf{K}_2) = \frac{1}{2} \text{Re} \{ \mathbf{E}(\mathbf{K}_1) \times \mathbf{H}^*(\mathbf{K}_2) \} \quad (\text{B.19})$$

$$= \left( \frac{1}{2\pi} \right)^2 \frac{1}{2} \int_{-\infty}^{\infty} \mathbf{E}(\mathbf{r}_1) e^{i\mathbf{K}_1 \mathbf{r}_1} dr_1^2 \times \left( \frac{1}{2\pi} \right)^2 \int_{-\infty}^{\infty} \mathbf{H}^*(\mathbf{r}_2) e^{-i\mathbf{K}_2 \mathbf{r}_2} dr_2^2 \quad (\text{B.20})$$

$$= \frac{1}{2} \left( \frac{1}{2\pi} \right)^4 \int_{-\infty}^{\infty} \int_{-\infty}^{\infty} \mathbf{E}(\mathbf{r}_1) \times \mathbf{H}^*(\mathbf{r}_2) e^{i(\mathbf{K}_1 \mathbf{r}_1 - \mathbf{K}_2 \mathbf{r}_2)} dr_1^2 dr_2^2 \quad (\text{B.21})$$

The radius of the reference sphere is much larger than the front focal plane, therefore all contributing plane waves are almost parallel, and we can use the far field limit  $\mathbf{K}_1 \approx \mathbf{K}_2 \approx \mathbf{K}$ . Using Eq. (A.47), we find the pointing vector on the reference sphere

$$\bar{\mathbf{S}}(\mathbf{K}, \mathbf{K}) = \frac{1}{32\pi^4} \frac{1}{2} (\hat{\mathbf{e}} \times \hat{\mathbf{h}}) \int_{-\infty}^{\infty} \int_{-\infty}^{\infty} |\mathbf{E}| |\mathbf{H}^*| e^{i\mathbf{K}(\mathbf{r}_1 - \mathbf{r}_2)} dr_1^2 dr_2^2 \quad (\text{B.22})$$

$$= \hat{\mathbf{s}} \frac{n}{64\pi^4 \mu c_0} \int_{-\infty}^{\infty} \int_{-\infty}^{\infty} \mathbf{E}(\mathbf{r}_1) \mathbf{E}^*(\mathbf{r}_2) e^{i\mathbf{K}(\mathbf{r}_1 - \mathbf{r}_2)} dr_1^2 dr_2^2 \quad (\text{B.23})$$

Which we can write as the autocorrelation function with the usual change of coordinates  $\mathbf{r}_1 - \mathbf{r}_2 = \mathbf{r} \rightarrow dr_2^2 = dr^2$  from Appendix A.7 and get the Fourier transform of the autocorrelation of the electric field

$$\bar{\mathbf{S}}(\mathbf{K}, \mathbf{K}) = \hat{\mathbf{s}} \frac{n}{64\pi^4 \mu c_0} \int_{-\infty}^{\infty} \int_{-\infty}^{\infty} \mathbf{E}(\mathbf{r}_1) \mathbf{E}^*(\mathbf{r}_1 - \mathbf{r}) e^{i\mathbf{K}\mathbf{r}} dr_1^2 dr^2, \quad (\text{B.24})$$

$$= \hat{\mathbf{s}} \frac{n}{64\pi^4 \mu c_0} |\mathcal{F}\{\mathbf{E}\}|^2, \quad (\text{B.25})$$

In the second step, we applied the autocorrelation theorem and obtained the absolute square of the Fourier transform: the power spectrum of the electric field. So we see that the flux density on the reference sphere is indeed the Fourier transform of the electric field in the front focal plane.

If we now project this pointing vector on the back focal plane, we introduce the factor  $\cos \beta = \hat{\mathbf{s}} \hat{\mathbf{n}}_2$

$$\bar{\mathbf{S}}(\mathbf{K}, \mathbf{K}) \hat{\mathbf{n}}_2 = \bar{\mathbf{S}}(\mathbf{K}, \mathbf{K}) \hat{\mathbf{s}} \hat{\mathbf{n}}_2 = \bar{\mathbf{S}}(\mathbf{K}, \mathbf{K}) \cos \beta \quad (\text{B.26})$$

but we have already established in Eq. (B.14) that the Abbe-sine condition tells that the energy is conserved along rays. To account for this, an additional factor  $(\cos \beta)^{-1}$  has to be put in front of the integral Eq. (B.24). In the present case, this seems trivial because it just removes the cosine dependency in Eq. (B.26). But for the inverse transform, for example, when a laser beam is focused with the objective, this generates large-angle amplification, as in [56, 57, 54] and [55].

In summary, an objective performs Fourier transform in combination with an angular amplification. The radiant flux density distribution observed in the back focal plane is the absolute square of the Fourier transform of the electric field, or its power spectrum, multiplied with an angular amplification factor that conserves the flux density.

## C Supplement: Published Version

### C.1 Radiation from Side-Emitting Optical Fibers and Fiber Fabrics: Radiometric Model and Experimental Validation

Aaron Reupert, Jan Schröder, and Lothar Wondraczek. “Radiation from Side-Emitting Optical Fibers and Fiber Fabrics: Radiometric Model and Experimental Validation.” In: *Advanced Photonics Research* (2022), p. 2100104. DOI: <https://doi.org/10.1002/adpr.202100104>

Side-emitting optical fibers are diffuse light sources that emit guided light through their cladding. Here, we derive two models to predict the generated radiation field: one for the case of a cylinder source and one for a line source. Our approach is based on the radiometric approximation and considers longitudinal and angle-dependent emission. Experimental validation is provided for the model parameters and the radiation field. We show that the longitudinal characteristic is relevant in proximity to the emitter’s surface and that the angular dependency determines the far field of emission. Comparison to the experiment shows that the cylinder source model allows for only slightly more accurate prediction at the cost of significantly higher computational effort. A combination of model and measurements is then used as a tool to predict the illumination performance of side-emitting fibers and fiber fabrics.

#### Remarks to the notation

In this publication, the light flux density or irradiance was denoted by its standard representation  $E$  and  $\mathbf{E}$ , not  $F$  and  $\mathbf{F}$  as in Appendix A.7.

#### Remarks to the publication

This paper is the published version. Compared to the submitted version, the published version includes changes in the theory section to clarify the radiometric model and its derivation. Also, the vector notation has been changed from the arrow notation  $\vec{A}$  to the bold notation  $\mathbf{A}$ , which is more consistent with the dissertation. The submitted version can be found in Section 3.1.



# Radiation from Side-Emitting Optical Fibers and Fiber Fabrics: Radiometric Model and Experimental Validation

Aaron Reupert, Jan Schröder, and Lothar Wondraczek\*


Side-emitting optical fibers are diffuse light sources that emit guided light through their cladding. Herein, two models to predict the generated radiation field are derived: one for the case of a cylinder source and one for a line source. The approach is based on the radiometric approximation and considers longitudinal and angle-dependent emission. Experimental validation is provided for the model parameters and the radiation field. It is shown that the longitudinal characteristic is relevant in proximity to the emitter's surface and that the angular dependency determines the far field of emission. Comparison to the experiment shows that the cylinder source model allows for only slightly more accurate prediction at the cost of significantly higher computational effort. A combination of model and measurements is then used to predict the illumination performance of side-emitting fibers and fiber fabrics.

## 1. Introduction

Side-emitting optical fibers provide a means to illuminate spaces where common light sources face limitations, for example, in light penetration depth, thermal load, or volumetric homogeneity. These optical fibers emit a fraction of the guided light through their cladding, acting as a diffuse line source that is separated from the actual light emitter. This makes them easy to deploy, for example, in aquatic or highly humid environments.<sup>[1–3]</sup> Additionally, they are thin, long, and flexible, which enables easy implementation even in tricky geometries.

Different methods of fabrication and light coupling are established for side-emitting fiber made from inorganic glasses or plastics, e.g.<sup>[4–9]</sup> Typically, refractive index distortions (e.g., bubbles or particles) are introduced into the fiber to scatter light. Here, the standard case of homogeneously distributed scatterers results in an exponential decay in emission strength alongside the fiber, due to the Lambert–Beer law. In addition, the scattering process causes light emission, which is preferentially forward-

A. Reupert, J. Schröder, L. Wondraczek  
Otto Schott Institute of Materials Research  
Friedrich-Schiller-Universität Jena  
Fraunhoferstr. 6, 07743 Jena, Germany  
E-mail: lothar.wondraczek@uni-jena.de

 The ORCID identification number(s) for the author(s) of this article can be found under <https://doi.org/10.1002/adpr.202100104>.

© 2022 The Authors. Advanced Photonics Research published by Wiley-VCH GmbH. This is an open access article under the terms of the Creative Commons Attribution License, which permits use, distribution and reproduction in any medium, provided the original work is properly cited.

DOI: 10.1002/adpr.202100104

directed. Both properties result in inhomogeneous illumination; their specific effect on the radiation field is largely unknown.

Previous efforts to model the radiation field assumed that the fiber light emission was constant over all angles (Lambertian emission)<sup>[10,11]</sup> or used a stochastic Monte Carlo approach.<sup>[12–14]</sup> Building on these methods, we now treat the side-emitting fiber as exhibiting angular scattering properties in between directional and diffuse, combined with a nonuniform longitudinal light emittance profile. Both of these characteristics are obtained from measurements. We will use this approach to discuss the generated radiation field in the proximity of the emitting surface and in the far field.

The primary aim of this work is to develop a parametric model of the radiation field surrounding the fiber. This will be shown in Section 2. Then, experimental methods of measuring the model parameters are presented in Section 3. The results of these measurements are presented in Section 4, and are subsequently compared to the calculated radiation field in Section 5 Discussion. Finally, in the same section, we will use the best-performing model to evaluate different strategies to create more uniform illumination from standard side-emitting fibers and fiber fabrics.

## 2. Theory

Side-emitting fibers are a light source with special properties: Their surface “emittance”  $M(z)$  changes alongside the fiber, and the emitted radiation has an angular dependence, captured by the “phase function”  $P(\Theta, \Phi)$ . For example, the side-emitting poly(methyl methacrylate) optical fiber (PMMA fiber) used in this work exhibits an exponential decrease in emittance with length. In addition, the light is emitted preferentially at small angles to the fiber axis. Hereinafter, we will calculate the monochromatic radiation field surrounding the fiber in terms of its flux density, which is called “(spectral) irradiance”  $E_\nu(\mathbf{r})$  in one arbitrary frequency interval  $(\nu, \nu + d\nu)$ . Vector quantities will be denoted in boldface. We will use this to calculate the radiation field of single fibers or fiber fabrics, consisting of many side-emitting fibers.

### 2.1. Radiance, Irradiance, and Radiation Transfer

We use the radiometric approximation to calculate the radiation field generated by the side-emitting fiber and assume no absorption or scattering in the surrounding medium. In this case, the

radiometric field quantity “radiance”  $L_\nu(\mathbf{r}, \hat{\mathbf{s}}, \nu)$  is constant along a ray of light,<sup>[15,16]</sup> basically representing its energy. The usual starting point for the radiometric derivation is to use the radiance to express the differential radiant flux  $d\phi$  in the frequency interval  $d\nu$  transported through an element of area  $dA_1$  at an angle  $\Theta_1$  and confined to an element of solid angle  $d\Omega$  as

$$d\phi_\nu = L_\nu(\mathbf{r}, \hat{\mathbf{s}}, \nu) \cos \Theta_1 d\Omega dA_1 d\nu \quad (1)$$

This defines the flux of a pencil of light rays as sketched in Figure 1. With the scalar product  $\hat{\mathbf{s}} \cdot \hat{\mathbf{n}}_1 = \cos \Theta_1$  between the ray vector  $\hat{\mathbf{s}}$  and the surface normal  $\hat{\mathbf{n}}_1$  of  $dA_1$ , we can express the differential flux as the scalar product of the differential irradiance  $d\mathbf{E}_\nu = dE_\nu \hat{\mathbf{s}}$  and the surface element  $d\mathbf{A}_1 = \hat{\mathbf{n}}_1 dA_1$  as

$$d\phi_\nu = L_\nu(\mathbf{r}, \hat{\mathbf{s}}, \nu) \hat{\mathbf{s}} \cdot \hat{\mathbf{n}}_1 d\Omega dA_1 d\nu = d\mathbf{E}_\nu(\mathbf{r}, \hat{\mathbf{s}}, \nu) \cdot d\mathbf{A}_1 \quad (2)$$

The vectorial irradiance describes both the spatial distribution of the flux density of the radiation field (light power per unit area) and the direction of the radiation. Therefore, we argue that it is the most useful quantity to describe the directional radiation field surrounding a side-emitting fiber with angle-dependent emission. For example, if one were to shine the radiation from the fiber onto a piece of paper, the observable brightness distribution would be the projected irradiance distribution.

To calculate the irradiance at a point in space  $\mathbf{r}_1$ , we only need to integrate the differential irradiance over the solid angle  $\Omega$  surrounding it. Therefore the flux density of all rays intersecting at this point is summed up, which we write as the integral

$$E_\nu(\mathbf{r}_1) = \int d\mathbf{E}_\nu(\mathbf{r}_1, \hat{\mathbf{s}}, \nu) = d\nu \int_{\Omega} L_\nu(\mathbf{r}_1, \hat{\mathbf{s}}, \nu) \hat{\mathbf{s}} d\Omega(\hat{\mathbf{s}}) \quad (3)$$

In the present case, the light only originates from the surface of the side-emitting fiber. Therefore, the irradiance at  $\mathbf{r}_1$  is

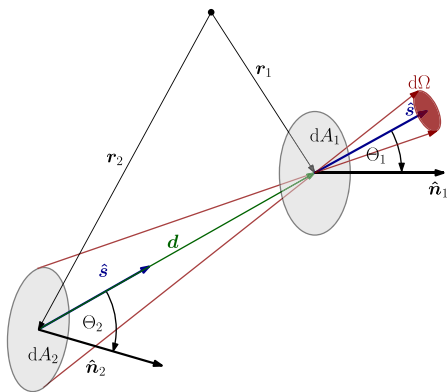


**Figure 1.** A pencil of radiation, confined to the solid angle interval  $\Omega$ , is transmitted through a surface element  $dA_1$  at the angle  $\Theta_1$  with its surface normal  $\hat{\mathbf{n}}_1$ . It originates from a surface  $dA_2$ , emitted at the angle  $\Theta_2$  with its surface normal  $\hat{\mathbf{n}}_2$ . The solid angle is equal to the projected area of the radiating surface according to  $d\Omega = \cos \Theta_2 dA_2 / d^2$ . The distance  $d = |\mathbf{d}|$  is the magnitude of the connection vector  $\mathbf{d} = \mathbf{r}_1 - \mathbf{r}_2$ .

calculated by integrating all the intersecting light rays coming from the fiber’s surface. The relationship between the solid angle element and a surface element of the side-emitting fiber is

$$d\Omega(\hat{\mathbf{s}}) = \frac{\hat{\mathbf{s}} \cdot \hat{\mathbf{n}}_2 dA_2}{d^2} = \frac{\cos \Theta_2 dA_2}{d^2} \quad (4)$$

This relation is also sketched in Figure 1: the pencil of rays crossing the observation point has its origin in the surface element  $dA_2$  at the distance  $\mathbf{d} = \mathbf{r}_1 - \mathbf{r}_2$  on the fiber. This area spans the solid angle element  $d\Omega$  when seen from  $\mathbf{r}_1$ .<sup>[17]</sup> Substituting Equation (4) and the ray vector  $\hat{\mathbf{s}} = \mathbf{d}/d$  into Equation (3), we obtain the formula for calculating the irradiance in the volume surrounding the fiber by integration over its surface  $A_F$ .

$$E_\nu(\mathbf{r}_1) = d\nu \int_{A_F} L_\nu(\mathbf{r}_1, \hat{\mathbf{s}}, \nu) \frac{\cos \Theta_1}{d^2} \frac{\mathbf{d}}{d} dA_2 \quad (5)$$

The spectral (monochromatic) radiant quantity  $E_\nu(\mathbf{r})$  can be turned into the radiometric quantity  $\mathbf{E}(\mathbf{r})$  by performing the integral over all involved frequencies  $\int E_\nu d\nu$ . One should keep in mind that the scattering process causing the light emission depends on the frequency and, therefore, the radiance’s angular distribution does too.

## 2.2. Radiation Field of a Cylinder Source

To perform the fiber surface integral in Equation (5), we model the fiber as a cylinder in the corresponding cylindrical coordinates  $\mathbf{r} = (x, y, z) = (\rho \cos \varphi, \rho \sin \varphi, z)$ . The coordinate origin is the center of the start of the fiber; the light inside propagates in the positive  $z$ -direction. The fiber surface is defined by setting  $\rho = R$ , the radius of the fiber, which gives us the surface location vector  $\mathbf{r}_2 = (R \cos \varphi, R \sin \varphi, z)$ . The radiance is measured at an arbitrary point of observation  $O$ . Because the fiber and its radiation field are rotationally symmetric, we chose  $O(\varphi' = 0)$  as the point of observation with the location vector  $\mathbf{r}_1 = (\rho', 0, z')$  and  $\rho' > R$ . The distance vector  $\mathbf{d}$  from a surface element to the observation point is

$$\mathbf{d} = \mathbf{r}_1 - \mathbf{r}_2 = \begin{pmatrix} \rho' - R \cos \varphi \\ -R \sin \varphi \\ z' - z \end{pmatrix} \quad (6)$$

with the magnitude  $d = |\mathbf{r}_1 - \mathbf{r}_2| = \sqrt{\mathbf{d} \cdot \mathbf{d}} = \sqrt{\rho'^2 + R^2 - 2R\rho' \cos \varphi + (z' - z)^2}$ . Consequently, the length and direction of this vector change from surface element to surface element.

Every surface element of the fiber radiates depending on  $z$ -position and emission angles  $\Phi, \Theta$ . The angles are defined in a local spherical coordinate system centered around the surface element, as shown in Figure 2. They have to be translated into the global cylindrical coordinate system for the integration: The surface vector  $\hat{\mathbf{n}}_2$  can be expressed as  $\hat{\mathbf{n}}_2 = \cos \varphi \hat{\mathbf{e}}_x + \sin \varphi \hat{\mathbf{e}}_y$ , as shown in Figure 2. Then, we can express the polar angle  $\Theta$  in spherical coordinates with the aid of Equation (6) as

$$\cos \Theta = \hat{\mathbf{n}}_2 \cdot \hat{\mathbf{s}} = \frac{\hat{\mathbf{n}}_2 \cdot \mathbf{d}}{d} = \frac{\rho' \cos \varphi - R}{d} \quad (7)$$

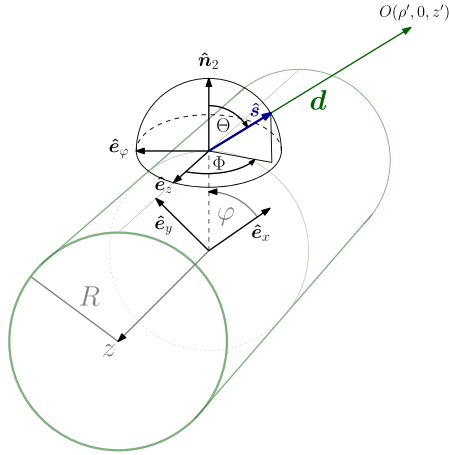


**Figure 2.** The local spherical coordinate system (black) of a surface element sits on top of the cylindrical coordinate system (green) of the fiber with the radius  $R$ . The connection vector  $d$  from Figure 1 points from the surface to the point of observation  $O$ . The surface normal vector  $\hat{n}_1$  written in Cartesian coordinates is  $\hat{n}_1 = \cos \varphi \hat{e}_x + \sin \varphi \hat{e}_y$ . The  $\hat{e}_z$  unit vector is the same in both coordinate systems.

This result becomes zero when  $R = \rho' \cos \varphi$ , then  $\mathbf{d}$  is a tangent to the fiber's surface. We will use this as the limit of the surface integration.

The scalar product  $\mathbf{d} \cdot \hat{e}_z = d \sin \Theta \cos \Phi = z' - z$  between the connection vector  $\mathbf{d}$  and  $\hat{e}_z$  expressed in cylindrical and spherical coordinates gives the relation for  $\Phi$ , and in combination with  $\cos^2 \Theta + \sin^2 \Theta = 1$  we obtain

$$\cos \Phi = \frac{z' - z}{d \sqrt{1 - \cos^2 \Theta}} = \frac{z' - z}{\sqrt{d^2 - (\rho' \cos \varphi - R)^2}} \quad (8)$$

Now all properties of the local spherical coordinate system are expressed in the global cylindrical coordinate system. We insert Equation (7) in Equation (5), with  $\Theta_1 = \Theta$ , replace the surface element by its representation in cylindrical coordinates  $dA_1 = R d\varphi dz$ , and obtain the final Equation for the irradiance vector-field of the cylinder source

$$\mathbf{E}_\nu(\rho', z') = d\nu \int_0^l \int_{\varphi_0}^{\varphi_1} L_\nu(z, \Theta, \Phi, \nu) \frac{(\rho' \cos \varphi - R)}{d^4} \times \begin{pmatrix} \rho' - R \cos \varphi \\ -R \sin \varphi \\ z' - z \end{pmatrix} R d\varphi dz \quad (9)$$

From Equation (7), we obtain the limits of integration  $\varphi_0 = -\arccos(R/\rho')$  and  $\varphi_1 = +\arccos(R/\rho')$ ;  $l$  is the length of the fiber.

Two additional remarks to Equation (9): First, the distance to the surface has to be bigger than zero  $d > 0 \rightarrow \rho' > 0$ . Second,

the symmetry of the formula would cause the second entry of  $\mathbf{E}_\nu$  always to integrate to zero because the irradiance passing through this surface element is equal from both sides. This is only true for a virtual surface and not for a real one, which would block radiation from one side of the fiber.

### 2.3. Radiance, Emittance, and the Phase Function

The radiant emittance of a surface element is distributed on the hemisphere above it. This distribution results from the heterogeneous scattering process inside the fiber and the refraction and secondary scattering on the fiber surface. To account for this, we separate the radiance into the product of the emittance  $M$  of the fiber surface element with its affiliated phase function  $P$ , which contains the normalized angular information of the emitted radiation.

$$L_\nu(z, \Theta, \Phi, \nu) = M_\nu(z, \nu) P_\nu(z, \Theta, \Phi, \nu) \approx M_\nu(z, \nu) P_\nu(\Theta, \Phi, \nu) \quad (10)$$

We assume homogeneous scattering throughout the fiber, so only the emittance  $M$  depends on  $z$ . Then, we can separate the radiance into the directional  $P$  and the positional contribution  $M$ , which allows us to determine them independently with different experiments.

### 2.4. Line Source Approximation

The calculation can be greatly simplified by using a line source approximation. Here, the light is only emitted radially, therefore its phase function has no angular component everywhere except for  $\Phi = 0$ . This means that we can replace the  $\Phi$ -dependency of the phase function with the delta function

$$P_\nu(\Theta, \Phi, \nu) = P_\nu(\Theta, \nu) \delta(\varphi) \quad (11)$$

Inserting this into Equation (9) and performing the  $\varphi$ -integration lead to the radiant flux density of the line source with an angular-dependent emission in  $\Theta$ . Additionally, as a line has no radial extend, we set all resulting  $(\rho' - R) = \rho'$ . The remaining  $R$  from the surface element  $dA = dR\varphi dz$  is combined with the surface emissivity to yield the radial flux emission  $M_\nu(z, \nu)R = I_\nu(z, \nu)$ . The resulting equation for the line source is

$$\mathbf{E}_\nu(\rho', z') = d\nu \int_0^l I_\nu(z, \nu) P_\nu(\Theta, \nu) \frac{\rho'}{d_l^4} \begin{pmatrix} \rho' \\ 0 \\ z' - z \end{pmatrix} dz \quad (12)$$

with  $d_l = \sqrt{(\rho')^2 + (z' - z)^2}$ ; the irradiance can now be calculated by integration over  $z$ .

## 3. Experimental Section

The radiation field of a rotationally symmetric side-emitting fiber can be determined if the radiant emittance  $M(z)$  and the phase function  $P(\Phi, \Theta)$  are known. These parameters are determined experimentally, with two different setups: The "side emission

measurement” will determine the emittance, and the microscopy-based “angular measurement” will measure the phase function. Except for the calibration of the angular measurement, both methods are also described elsewhere in more detail.<sup>[18,19]</sup> Additionally, we show how to measure the resulting radiation field of a fiber band with a scattering screen.

All light measurements are subject to unknown systematic attenuation due to light decoupling or transmission losses. To account for this, all measurements are normalized to the maximum measured value. This does not affect the calculated distributions according to Section 2. If absolute values are required, it is sufficient to measure the maximum brightness with a calibrated device and multiply the calculated distribution by this to obtain the absolute value of the irradiance distribution.

The side-emitting optical fibers (multi-mode, PMMA, diameter 500  $\mu\text{m}$ ) and the textile fiber band, containing 19 corresponding fibers oriented parallel to each other with an average distance of 2.6 mm (see Figure 5c), were provided by F.J.RAMMER GmbH. For all experiments, we used a 100 mW 520 nm green laser diode which is butt-coupled (direct contact without focusing optics) to the fibers of the band. For micrographs and phase function measurement, we used a JenaPol Interphako microscope. The radiation field was imaged with a Canon EOS 650D camera and an EF 18–55 objective focused on a frosted glass plane as a scattering screen.

### 3.1. Side Emission Measurement

A custom-made integrating sphere (see Figure 3a) was used to measure the fiber emittance. It consists of two fiber guides: a baffle to protect the detector port from direct irradiation and an optical fiber to connect the sphere to a spectrometer (Ocean Optics: Maya2000 Pro). The side-emitting fiber was threaded through the sphere with the help of two hollow fiber guides, leaving only a small segment of the length  $\Delta z$  exposed to the interior of the sphere. The emitted flux of the fiber segment  $\Delta\phi(z)$ , which is related to the emissivity by  $\Delta\phi(z) = 2\pi R\Delta z M(z)$ , is distributed homogeneously by multiple diffuse reflections on the sphere walls. Therefore, the measured

irradiance  $E_m(z)$  is proportional to the flux collected by the sphere  $\Delta\phi(z)$ .<sup>[6,19]</sup> By measuring the flux at different positions along the fiber, we captured the  $z$ -dependence of the emittance of the side-emitting fiber. Here, fiber coupling, light transmission, and absorption in the integrating sphere (walls and air) represent systematic sources of error. To take this into account, the measurement is normalized to the maximum value.

### 3.2. Angular Measurement

The angular light distribution on the hemisphere in Figure 2 was captured with a large numerical aperture (NA) objective: In its back focal plane, the light is decomposed into its angular components.<sup>[18,20]</sup> The relation between emission angle  $\Theta$  and back focal plane radial distance  $h$ , for infinity-corrected objectives, is sketched in Figure 3b and given by the Abbe sine condition<sup>[21]</sup>

$$\sin \Theta = \frac{h}{f} \quad (13)$$

The unknown focal length  $f$  can be replaced by  $f = n_0 h_{\max}/\text{NA}$  by using the NA and Equation (13):  $\text{NA} = n_0 \sin \Theta_{\max} = n_0 h_{\max}/f$ . Here,  $h_{\max}$  is the radius of the circular back focal plane image.

All real-world objectives with high NA have angle and polarization-dependent transmission losses.<sup>[22]</sup> For correction, we use a Lambertian scattering standard (provided by QSIL GmbH Quarzschmelze Ilmenau), which should have an ideal flat irradiance profile in the back focal plane. The correction is performed by dividing the measurement image pixel-wise by the image of the scattering standard. To show this correctional property, we derive the transfer of a lossless objective with an ideal scattering standard: As shown in Figure 3b, the flux  $\phi$  emerges from the focal point in a cone around the observed ray and is transformed into a non-divergent pencil of rays on the reference sphere while conserving its energy. The flux passing through  $dA_1$  is equal to the flux passing through  $dA_2 = \cos \Theta dA_1$ , so the irradiance has to vary accordingly  $\phi = E_1 dA_1 = E_2 dA_2 = E_2 dA_1 \cos \Theta$ .

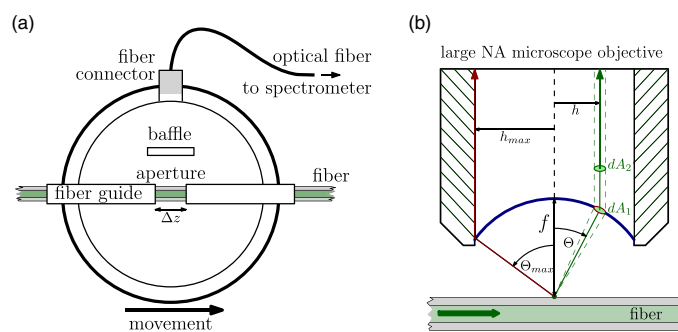


**Figure 3.** a) Emittance measurement: Light emitted by the fiber segment  $\Delta z$  (limited by the aperture) is homogeneously distributed on the sphere wall by multiple diffuse reflections. The irradiance on the detector port is proportional to the emitted flux  $E \propto \phi$ . b) Phase function measurement: Rays spanning an angle  $\Theta$  with the optical axis (dashed) are transformed in parallel rays with a distance  $h$  by refraction on the reference-sphere (blue, radius  $f$ ) according to the Abbe sine condition Equation (13).

Therefore, the irradiance in an ideal objective is amplified according to  $E_2(\Theta) = E_1(\Theta) / \cos \Theta$  for increasing  $\Theta$ .

Suppose we insert the irradiance of a Lambertian diffuser  $E_1(\Theta) = E_L \cos \Theta$  into this formula. In that case, the cosines cancel, and we obtain  $E_L = E_2(\Theta) = \text{const.}$ : a Lambertian diffuser should have an ideally flat intensity profile in the back focal plane of an objective. This correction was performed separately for both polarization states, and then both states were averaged to obtain the corrected unpolarized back focal plane image.

### 3.3. Measurement of the Irradiance on a Scattering Screen

The radiation field of a band of several side-emitting fibers is measured with a simple setup shown in **Figure 4**. The idea is that the screen makes the radiation field in its plane visible by secondary scattering. The irradiance  $E_0(x, y) = \hat{n}_s \cdot \mathbf{E}(\mathbf{r})$ , which is intersected by the screen at a certain point, is turned into the emissivity on the other side  $M(x, y) \propto E_0(x, y)$  by transmission through the screen. We assume that the screen acts as an

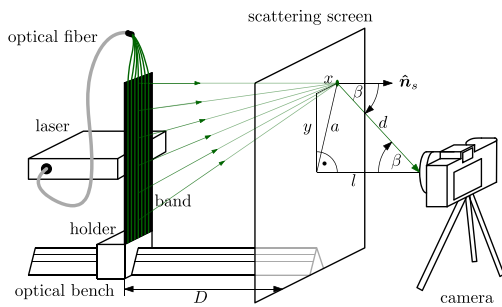


**Figure 4.** Scattering camera measurement: A CCD camera is focused ( $l = 900\text{mm}$ ) on a scattering screen with the surface area  $A_s = 650\text{mm} \times 450\text{mm}$ . The fiber band is mounted to a straight holder, which is clamped to an optical bench. A laser is coupled to the side-emitting fibers, and the room is darkened. The fibers are moved to different positions  $D$  (10–800 mm) relative to the glass plate, and a picture is taken of the scattering glass plate for each position without changing the focus of the camera.

ideal Lambertian diffuser: the irradiance which is observed by the camera on the other side of the screen is

$$E(x, y, \alpha) = M(x, y) \frac{\cos \beta}{d^2} \propto E_0(x, y) \frac{\cos \beta}{d^2} \quad (14)$$

This allows us to measure the light field at the scattering screen just by taking a picture of it and correcting for the angular and distance attenuation: We define the position of the pixel relative to the center of the screen as shown in **Figure 4**, so  $d = \sqrt{a^2 + l^2} = \sqrt{x^2 + y^2 + l^2}$ . Therefore, the geometric attenuation is

$$\frac{\cos \beta}{d^2} = \frac{l}{d^3} = \frac{l}{(l^2 + x^2 + y^2)^{3/2}} \quad (15)$$

which is used to correct the measurement for geometric angle and distance attenuation. Because the scattering behavior of the screen is expected to follow the cos-dependence only approximately, especially for large angles, it is best to choose a large distance  $l$  between the screen and the camera. Also, the camera response has to be checked for linearity.

## 4. Results

The commercial side-emitting fiber in **Figure 5a** appears transparent and featureless to the naked eye and under the microscope. When light is butt-coupled in the fiber, as in **Figure 5b**, it lights up and appears self-luminous. This luminosity is not equally distributed across the fiber, but it is brighter at the fringes and dimmer in the center when observed under the microscope. Additionally, attached particles and small scratches on the fiber surface become visible. The fiber emits strongest close to the coupling, and then the emission decreases quickly toward the fiber end.

The band of equivalent plastic side-emitting fibers in **Figure 5c** shows a similar decline in emission, but additionally, the overall brightness varies from one fiber to the other because of difficulties that arise from distributing light equally from one large-diameter fiber to many small ones via butt-coupling.

To quantify the loss in fiber brightness with length, a single fiber is clamped to the side emission setup from Section 3.1, and

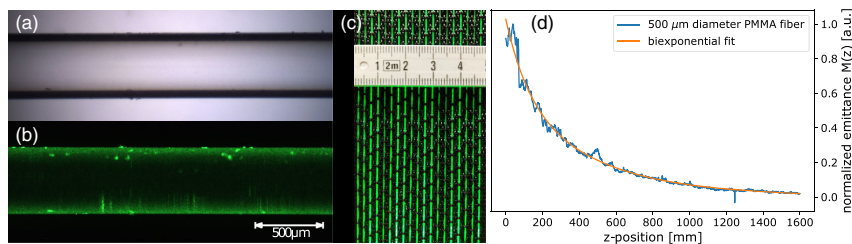


**Figure 5.** Micrographs of the side-emitting fiber under bright field microscope illumination a) and dark field self-illumination b). c) Nineteen fibers woven in a fiber band in self-illumination. d) z-dependence of the side-emitting fiber emittance  $M$  with increasing distance to the light coupling, the data is normalized by the maximum emittance. A biexponential function with the two decay constants  $\sigma_1 = 0.0021\text{mm}^{-1}$  and  $\sigma_2 = 0.0080\text{mm}^{-1}$  and the corresponding amplitudes  $A_1 = 0.58$  and  $A_2 = 0.42$  has been fitted to the measurement data. Panel (b) reproduced from<sup>[1]</sup> under CC-BY 4.0 Licence. Copyright 2019, The authors. Published by Springer Nature.

the relative change in surface emittance is measured. The data was normalized by the maximum value, and the plot in Figure 5d shows a monotonous decaying curve that decreases to 2% of the maximum value at the end of the fiber. This decrease can be fitted with a biexponential decay function.

#### 4.1. Phase Function Measurement

The fiber's light emission depends on the emission angle. This can easily be verified by observing the fiber (band) from different positions. This angular emission behavior was measured with Fourier microscopy in two orthogonal polarization directions, shown in Figure 6a,b. The radiation is concentrated on the right side of the circle in a half-moon shape, so light scatters preferentially forward under low angles. The remainder of the back focal plane image is dark, which means that comparatively little radiation is scattered in these directions.

We determine the phenomenological, polarization-independent phase function  $P(\Theta, \Phi)$  from these measurements by imaging 50 pictures on different positions in each polarization direction, correcting them according to Section 3.2, and averaging all of them. The resulting phase function in Figure 6c is still brighter to the right and is now almost rotationally symmetric with respect to  $\hat{e}_z$ . The half-moon shape brightness, which is caused by the large angle objective amplification, is gone due to the correction procedure. Additionally, the phase function

was normalized so that the integral over the hemisphere is equal to one.

To better illustrate the forward scattering of the fiber surface, we present it in Figure 7 as a polar plot in the  $\hat{n}_1$ - $\hat{e}_z$ -plane from Figure 6. This data will also serve as the phenomenological phase function  $P(\Theta)$  of the line source. Here, we see an isotropic Lambertian surface compared to the  $\hat{n}_1$ - $\hat{e}_z$ -cross section of the phase function and the average scattering. The average was calculated by integrating over the surface of the hemisphere in a rotation around the  $\hat{e}_z$  vector and then dividing by the arc length.

In the graph on the left in Figure 7, we see the Lambertian phase function, which is constant over all angles ( $P(\Theta) = 1/\pi$ ). The cross section of the phase function has its maximum value before it drops rapidly for angles greater than  $71^\circ$ . This cutoff is due to the limited opening angle of the objective. The average function shows a similar behavior, but decreases after its maximum at  $60^\circ$  before the cutoff angle.

When we multiply the phase function with the  $\cos \Theta$  projection factor (Equation (5)), we see how much radiation is really scattered in a given direction from a surface element: the isotropic Lambertian surface is now turned into a circle with its maximum emission at  $0^\circ$ . The average curve and the cross-section curve become more similar in shape, with their respective maxima now at  $53^\circ$  and  $58^\circ$ . The influence of the cutoff angle is strongly diminished by the  $\cos \Theta$  factor. This shows that the phase function can be satisfactorily determined even with a

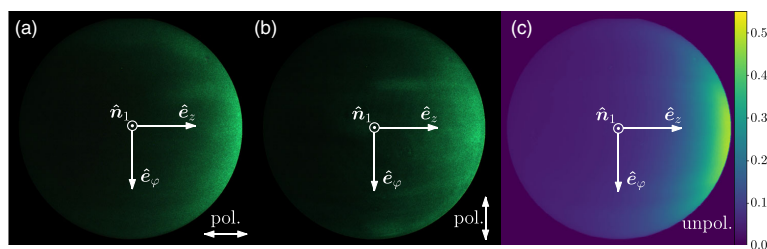


**Figure 6.** a,b) Typical back focal plane images for two orthogonal polarization directions (pol.) and the average corrected image c) from 100 images, 50 in each polarization direction: the phase function  $P$ . The coordinate system is analogous to Figure 2, when the hemisphere is viewed from the top.

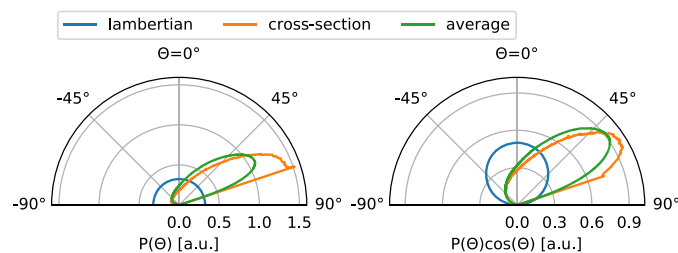


**Figure 7.** Polar plot of the normalized phase function  $P$  (left) and the projected phase function with  $\cos \Theta$  apodization (right). Lambertian  $P$  is the isotropic case. The cross section is the data from the  $\hat{n}_1$ - $\hat{e}_z$ -plane. The average is calculated by integrating along a rotation around  $\hat{e}_z$  and dividing by arc length.

limited aperture because the projection factor dampens the missing large-angle phase function components.

#### 4.2. Making the Radiation Field Visible

A scattering screen intercepts the radiation field of the fiber band at different distances  $D$  and makes it visible. Black and white camera images of the screen are shown in **Figure 8** and display the behavior of the radiation field: At close distance, we can almost distinguish single fibers when the band is closest to the screen. Analogous to a single fiber, this distribution is bright at the start and then decays rapidly toward the fiber end.

When the distance between the screen and band increases, as shown in **Figure 8** from left to right, the radiation fields of the single fibers overlap and form a continuous enveloping distribution. Here, we observe a distinct maximum of brightness close, but not at the very start. Increasing the distance further leads to a downward movement of the maximum, which broadens, spreads out, and fills more and more of the screen area. In the largest observed distance  $D$  of 870 mm (**Figure 10d**), the maximum brightness has traveled the whole distance of the screen and is now located at the lower end.

### 5. Discussion

The fiber in **Figure 5d** shows a biexponential decay in emitted radiation with increasing distance from the light entry point. This corresponds to a fiber where some light is guided in the core, and some are guided in the cladding,<sup>[19]</sup> each with its respective scattering coefficients  $\sigma_1$  and  $\sigma_2$  and amplitudes  $\phi_1$  and  $\phi_2$ . This is the result of the butt-coupling, which excites core and cladding modes simultaneously. In the present case, we expect the cladding modes to experience stronger dampening because they interact with the fiber surface.

$$\begin{aligned} \phi(z) &= \phi_1 e^{-\sigma_1 z} + \phi_2 e^{-\sigma_2 z} \quad \leftrightarrow \\ -\frac{d\phi}{dz} &= \phi_1 \sigma_1 e^{-\sigma_1 z} + \phi_2 \sigma_2 e^{-\sigma_2 z} \end{aligned} \quad (16)$$

If we neglect absorption loss, we see how this leads to exponentially decaying emission (assuming flux conservation): any

loss in transmitted flux is turned into out-scattered radiation  $M(z) \propto -d\phi/dz$ . So, the amplitudes extracted from the fit in **Figure 5** are  $A_1 = \phi_1 \sigma_1$  and  $A_2 = \phi_2 \sigma_2$ . They give us a ratio of cladding to core flux of  $\phi_2/\phi_1 = 0.2$  at the start of the measurement.

This strong initial decay is visually unpleasing and can lead to overexposure in technical applications. A costly solution would be to optimize the optical coupling to the fiber core; a simpler solution is to cover this part of the fiber with an absorber (but at the expense of emission efficiency). One could also choose a fiber with a smaller scattering coefficient to stretch the exponent and obtain a more uniform illumination. However, this would also be at the expense of efficiency as more light would pass through the fiber unused without being scattered and emitted.

#### 5.1. Angular Emission

Under the microscope, no bubbles, particles, or other sources of light scattering can be seen inside the fiber in **Figure 5**. Measurement of the angular distribution of the radiation emitted from a fiber surface element in **Figure 6** and **7** shows a clear preference for forward scattering. This points to the presence of long-period refractive index distortions: Generally, all deviations from the ideal core-cladding structure in a step-index optical fiber cause light scattering.<sup>[23]</sup> These deviations can be thought of as refractive index fluctuations, which can be decomposed into a spectrum of mechanical waves.<sup>[18,24]</sup> Each wavelength is responsible for light scattering under a certain angle: longer wavelengths than the guided light causes forward scattering and vice versa. Therefore, the dominant wavelengths of the fluctuations are much longer than the wavelength of the green laser diode.

Furthermore, the refractive index contrast of the distortion enhances its scattering power.<sup>[18]</sup> In summary, this means that the cause of the scattering inside the fiber is a long periodic fluctuation with low refractive index contrast or a disturbance of the core-cladding boundary with low amplitude, so it cannot be detected with the microscope. The visible scratches and particles on the fiber surface, on the other hand, are signs of wear and have high refractive index contrast. They are responsible for the attenuation of the light guided in the cladding, which

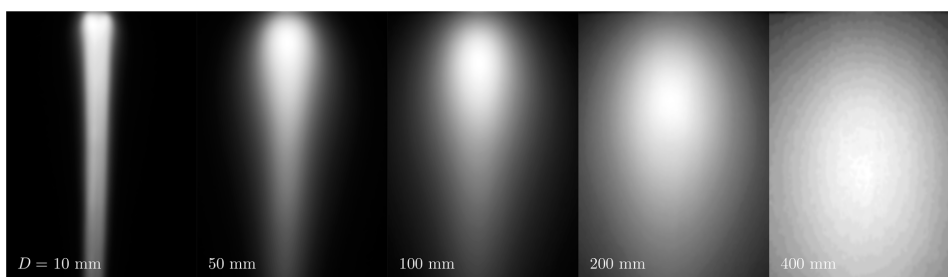


**Figure 8.** Black and white images of the scattering screen reveal the radiation distribution of a side-emitting fiber band for several distances (increasing from left to right), according to **Figure 4**. The light is coupled into the fiber from the top and loses its emissivity, due to the constant out-scattering of light, toward the end. Increasing the distance  $D$  between the band and screen leads to a broadening of the light distribution.

explains the larger scattering coefficient  $\sigma_2$  for the cladding modes.

### 5.2. Calculated Radiation Field

Comparing the numerically calculated fields in **Figure 9** close to the fiber for the two fiber models, namely cylinder source and line source, together with the two different phase functions, namely Lambertian and the measured phenomenological phase function, reveals two properties: first, the irradiance in all four variants shows a reciprocal dependency on distance ( $\rho^{-1}$ ). Second, the phase functions result in different magnitudes of irradiance close to the fiber: the two Lambertian models are congruent, and also, the two phenomenological phase function are congruent but result in a slightly higher irradiance.

These numerical results are plotted in **Figure 9**. The cylinder source was calculated by numerical integrating Equation (9) and the line source by integrating Equation (12). In both cases, the length-dependent decay in emittance was modeled using Equation (16) with the parameters from the fit to the measured values in **Figure 5**. The Lambertian phase function for the cylinder had the constant value  $P(\Theta, \Phi) = (2\pi)^{-1}$  and for the line  $P(\Theta) = \pi^{-1}$ . The data for the phenomenological phase function was taken either from **Figure 6** for the cylinder or from **Figure 7** (average) for the line.

The discretization of the surface in  $\varphi$  was done by dividing the angular interval  $[\varphi_0, \varphi_1]$  into 20 equal pieces. For  $z$ , we converted interval  $[0, l]$  for every  $z$ -position into the angular interval  $[\arctan(z/(rho - R)), \arctan((l - z)/(rho - R))]$  divided it into 100 equal angles and converted the angles back into  $z$ -coordinates. This improves numerical stability for small distances.

The deviation between phenomenological and Lambertian models close to the fiber is contradictory to the expected behavior in that all models should converge to the emissivity  $M(z)$  of the fiber surface when  $\rho \rightarrow R$ . Three features of our phenomenological phase function are probably responsible for this: First, the phase function is only known for  $\Theta < 71^\circ$  due to the NA limitation. Second, the normalization of the phase functions can only be performed up to a certain numerical accuracy using our

present approach (float 64bit). Third, the discretization of the phase function leads to angular intervals with constant scattering.

Interestingly, the line source and the cylinder source give the same result in the Lambertian case, which indicates a property known for the Lambertian sphere, whose irradiance shows the same behavior ( $\propto \rho^{-2}$ ) as an ideal point source.<sup>[17]</sup> Thus, the conclusion is that the Lambertian cylinder's irradiance behaves like that of a line source, although this remains to be proven mathematically.

We conclude that the Lambertian approximation is adequate to describe the irradiance close to the fiber, justifying the approach of Endruweit et al.<sup>[11]</sup> to calculate the field of a fiber from a Lambertian cylinder. However, it is even sufficient to solely use the line source. This is, of course, just possible in the absence of absorption and scattering in the surrounding medium. In the latter case, the irradiance of the line source and the cylinder source would deviate.

### 5.3. Comparison to the Measured Radiation Field

Section 5.2 concluded that the line source and the cylinder source differ only for different phase functions. Now, we compare the calculations for all four models to the measured field of a fiber band. We find that, in principle, the cylinder source with the phenomenological phase function performs best in the observed measurement range, although only slightly better than the phenomenological line source. Lambertian fiber models, which performed adequately in proximity to the fiber, perform worse for larger distances.

We use the same procedure as in Section 5.2 to numerically integrate the four models and obtain the radiation field for the half-space next to the fiber, which corresponds to the volume spanned by the scattering screen measurement in **Figure 8**. Then, we used the principle of superposition to calculate the radiation field of the fiber band from a single fiber: we made 19 duplicates of the calculated field, moved their  $x$ -coordinates to the respective positions of fibers on the band in **Figure 5**, and added them up. Additionally, we accounted for different coupling efficiencies by weighting the fields. This was done for all observed

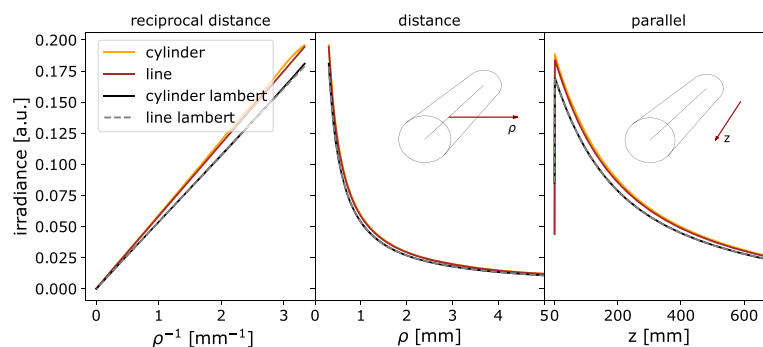


**Figure 9.** Comparison of the irradiance of the line source and the cylinder source close to the fiber for the phenomenological and the Lambertian phase function. At  $z = 100$  mm, in reciprocal distance (left) or in distance (middle). Irradiance in a line parallel to the fiber in a distance of  $\rho = 0.5$  mm.



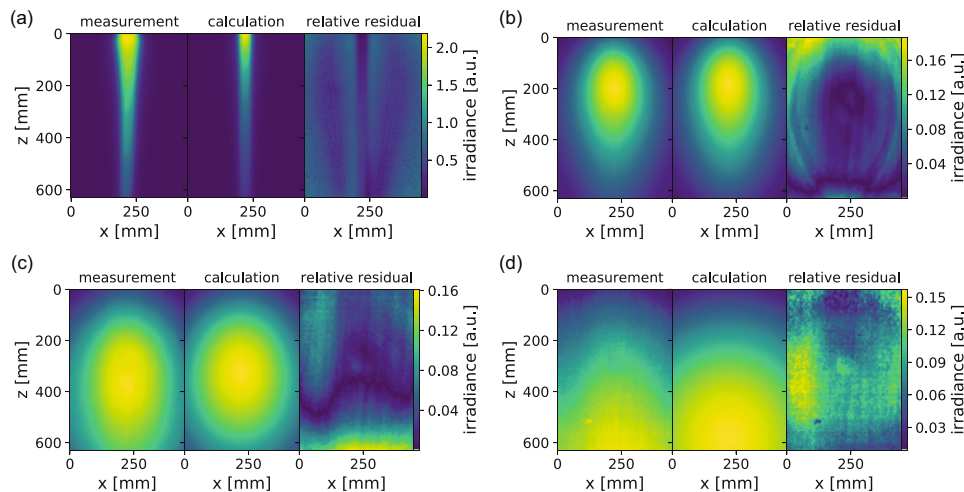


**Figure 10.** Comparison between measured  $E_m$  and the calculated irradiance field  $E_c$  (phenomenological cylinder source) of the fiber band for the distances 10 (a), 160 (b), 350 (c), and 870 mm (d). The pictures on the right show the relative residual  $|E_m - E_c|/E_m$ , the relative deviation between measurement and calculation.

distances. Exemplary results of these calculations of the cylinder source with the phenomenological phase function are shown in **Figure 10** next to the measured values.

The calculated irradiance of the fiber band with the phenomenological phase function in **Figure 10** shows two properties that match the measurement: First, the field in proximity to the fiber is dominated by the exponential decay of the radiant emission of the fiber surface. Second, the forward scattering property of the fiber causes a downward movement (away from the coupling) of the maximum of irradiance with increasing distance  $D$ . That the forward scattering property of  $P$  causes this can be inferred by comparison with a Lambertian fiber, which does not show a movement of the maximum (not shown).

For a quantitative comparison of the models with the measurement, we calculated the “relative residual” as the absolute difference between the measured  $E_m$  and the calculated  $E_c$  irradiance divided by the measured irradiance  $|E_m - E_c|/E_m$  for every pixel. This gives the pictures on the right in the subfigures in **Figure 10**. For a more comprehensive depiction, we calculated the average residual and the standard deviation of the relative residual for each plane of observation, which is shown in **Figure 11**. Here, we see that all models start with the highest residual, but only those with a phenomenological phase function surpass an error of 10% while the Lambertian level off at around 30%.

The cause of the high residual for small distances between screen and band is shown in **Figure 10**: we see that the residual directly above the band is small, but next to it is large. In this plane, the fibers will block the light from each other because fibers and the screen are approximately situated in the same plane. Additionally, a possible interaction between the scattering screen and the fiber band makes the measured scattering more diffuse than in the calculation: some light is scattered back and

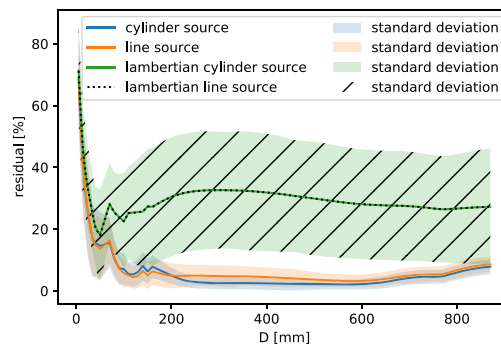


**Figure 11.** Comparison of the average residual and its standard deviation between cylinder source and line source with the Lambertian or phenomenological phase function. The relative residual is calculated analogously to **Figure 10** as  $|E_m - E_c|/E_m$  for every pixel. All pixels are then averaged, and the standard deviation is calculated. The Lambertian curves are congruent in average and standard deviation.

forth between band and screen, causing additional diffuse irradiation. Also, the screen has no real Lambertian transmission for large incident angles. We conclude that the scattering screen measurement is unfit to measure the irradiance in proximity to the fiber.

With increasing distance  $D$  between screen and band, the aforementioned effects weaken, so the calculation and the measurement converge. Still, the line source shows slightly higher residuals and standard deviation. This shows that the cylinder source is the slightly more precise way of calculating the

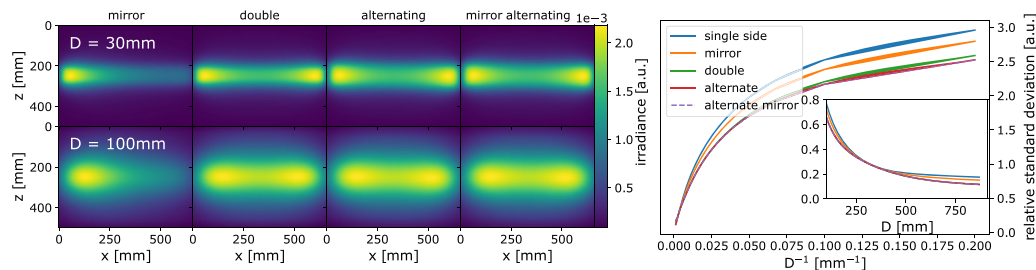


**Figure 12.** Comparison of calculated irradiance field (phenomenological cylinder source) of a fiber band for four different light coupling schemes in two distances (left). Relative standard deviation in reciprocal presentation (right) and linear representation in the insert (right).

radiation field in intermediate distances and large distances if a phenomenological phase function is used. The line source can be used in combination with a phenomenological phase function at almost the same precision and comes with the benefit of less computational effort. The Lambertian approximation should not be used for larger distances or only if no phenomenological phase function is available and larger uncertainties can be tolerated.

#### 5.4. Testing Alternative Fiber Coupling Schemes by Superposition

At last, we explore alternative light coupling schemes with the best performing fiber model, the cylinder source with the phenomenological phase function, to see if they create a more homogeneous illumination from a fiber band than basic single side coupling. We use the relative standard deviation of irradiance for each calculated plane as a quantitative comparison. From the four proposed schemes we do explore, three perform almost equally well to create a much more homogeneous irradiance field.

The exponential decay in emittance and the forward scattering property hinder the application of side-emitting fibers, leading to uneven illumination and a visually displeasing appearance. Spigulis et al.<sup>[10]</sup> proposed two methods to mediate the exponential decay without having to resort to fibers with self-compensating scattering coefficient  $\sigma(z)$ : First, double coupling, where light is coupled in both ends of the fiber, and second, a fiber end face mirror, to reuse the transmitted light by reflecting it back into the fiber. We additionally propose two more schemes: alternating, where light is coupled alternating from one side or the other in neighboring fibers, and a combination of alternating with end mirror.

We can now easily test these schemes for a fiber band with the calculated irradiance field of one fiber and the principle of superposition: For the double coupling, we use the result from Section 5.3, duplicate it, rotate the duplicate by  $180^\circ$ , and add it to the original calculated field. For the end mirror, we proceed in the same manner, but weigh the duplicate with the appropriate attenuation caused by the fiber transmission loss. Alternating these methods for every single fiber gives the other two schemes. The relative standard deviation is obtained by dividing the

standard deviation of the irradiance in each plane of observation by the average irradiance in that plane.

In **Figure 12** (left), we show an example for every scheme in two distances (30 and 100 mm) and the relative standard deviation (right). As it turns out, three of the four schemes lead to comparable uniform irradiance fields: both alternating and alternating with mirror provide the most homogeneous illumination with the same amount of couplings as the basic one-sided version. Double coupling is third but requires more couplings. Just using an end mirror on one side results in a more homogeneous illumination than single-sided coupling, but shows the same disadvantages of having a strong difference in irradiance from start to end.

## 6. Conclusion

We considered two methods to calculate the emitted light field of a side-emitting fiber in the radiometric approximation: A cylinder source and a line source. We validated experimentally that a standard side-emitting fiber possesses a position and angle-dependent radiance, which is properly represented in these models. The two contributions influence the emitted light field in two ways: The  $z$ -position dependence of the emittance is dominant close to the side-emitting fiber, and the angular dependence influences the field in the distance. We showed this by comparing calculated data from both approaches with real-world measurements of the radiation field. Both models are in good agreement with the measurement of the light field for distances larger than 80 mm from the emitter. Here, the cylinder source possesses slightly better predictive capability compared to the line source at the expense of higher computational effort. From the presented models, the radiation field of complicated arrangements of side-emitting fibers can be calculated by superposition. This was used to show that alternating the side of the light coupling between neighboring, parallel fibers in a fiber fabric can greatly improve the homogeneity of the generated radiation field.

## Acknowledgements

The authors thank Eva Schindwein for fruitful discussions, Dietmar Güttler for assistance with the PC-based automated measurement system,

Thomas Kittel for assistance with the Fourier microscopy, Christian Zeitler for electrical work, Lutz Preiser for metalwork and setup engineering, and Annkathrin Schwarze for providing the side-emitting fiber and the fiber band. This work received funding from the Carl Zeiss Foundation within the program "Intelligent Substrates" and was further supported by the Deutsche Forschungsgemeinschaft under Germany's Excellence Strategy –EXC 2051– "Balance of the Microverse".

### Conflict of Interest

The authors declare no conflict of interest.

### Data Availability Statement

The data that support the findings of this study are available from the corresponding author upon reasonable request.

### Keywords

line source, optical fiber fabrics, optical fiber illumination, radiometry, side-emitting optical fiber

Received: April 6, 2021

Revised: November 11, 2021

Published online:

- [1] L. Wondraczek, A. Gründler, A. Reupert, K. Wondraczek, M. A. Schmidt, G. Pohnert, S. Nolte, *Sci. Rep.* **2019**, *9*, 1.
- [2] B. Vandekerckhove, J. Missinne, K. Vonck, P. Bauwens, R. Verplancke, P. Boon, R. Raedt, J. Vanfleteren, *Micromachines* **2021**, *12*, 38.
- [3] M. Lanzarini-Lopes, A. G. Delgado, Y. Guo, P. Dahlen, P. Westerhoff, *Chemosphere* **2018**, *195*, 742.
- [4] J. Kallweit, M. Pätzl, F. Pursche, J. Jabban, M. Morobeid, T. Gries, *Textiles* **2021**, *1*, 337.
- [5] J. Alkemper, B. Hoppe, B. Schultheis, S. M. Ritter, I. Henze, D. Wolff, A. Curdt, *US Patent 8,582,943*, **2013**.
- [6] J. F. Clare, *JOSA A* **1998**, *15*, 3086.
- [7] T. Wang, K. Watanabe, *US Patent 5,905,837*, **1999**.
- [8] L. J. Button, A. Kobayakov, S. A. Kuchinsky, S. L. Logunov, A. Zakharian, *US Patent 8,620,125*, **2013**.
- [9] Z. Zhao, M. Lanzarini-Lopes, E. Westerhoff, X. Long, H. Rho, Y. Bi, L. Ling, P. Westerhoff, *Environ. Sci.: Nano* **2021**, *8*, 2441.
- [10] J. Spigulis, D. Pfafrods, M. Stafekis, W. Jelinska-Platace, *Optical Inorganic Dielectric Materials and Devices*, Vol. 2967, International Society for Optics and Photonics, Bellingham, WA 1997, pp. 231–236.
- [11] A. Endruweit, A. Alobaidani, D. Furniss, A. Seddon, T. Benson, M. Johnson, A. Long, *Opt. Lasers Eng.* **2008**, *46*, 297.
- [12] M. Zajkowski, *Photonics Applications in Astronomy, Communications, Industry, and High-Energy Physics Experiments III*, Vol. 5775, International Society for Optics and Photonics, Bellingham, WA **2005** pp. 440–445.
- [13] M. Zajkowski, *Photonics Applications in Astronomy, Communications, Industry, and High-Energy Physics Experiments*, Vol. 5125, International Society for Optics and Photonics, Bellingham, WA **2003**, pp. 322–327.
- [14] A.-A. Yassine, L. Lilge, V. Betz, *Biomed. Opt. Express* **2021**, *12*, 5401.
- [15] J. M. Palmer, B. G. Grant, *The Art of Radiometry*, SPIE press, Bellingham, Washington USA **2010**.
- [16] S. Chandrasekhar, *Radiative Transfer*, Dover Publications, New York **1960**.
- [17] B. Grant, SPIE, Bellingham, WA **2011**.
- [18] A. Reupert, M. Heck, S. Nolte, L. Wondraczek, *Adv. Opt. Mater.* **2020**, *2000633*.
- [19] A. Reupert, M. Heck, S. Nolte, L. Wondraczek, *Opt. Mater. Express* **2019**, *9*, 2497.
- [20] J. A. Kurvits, M. Jiang, R. Zia, *J. Opt. Soc. Am. A* **2015**, *32*, 2082.
- [21] M. Born, E. Wolf, *Principles of Optics: Electromagnetic Theory of Propagation, Interference and Diffraction of Light*, Pergamon Press, Headington Hill Hall, Oxford OX3 0BW, England, **1980**.
- [22] M. Leutenegger, R. Rao, R. A. Leitgeb, T. Lasser, *Opt. Express* **2006**, *14*, 11277.
- [23] D. Marcuse, *Principles of Optical Fiber Measurements*, Academic Press, New York, **1981**.
- [24] D. Marcuse, *Theory of Dielectric Optical Waveguides*, Academic Press, San Diego, CA **1991**.

## D Anhang

### D.1 Selbständigkeitserklärung

Ich erkläre, dass ich die vorliegende Arbeit selbständig und unter Verwendung der angegebenen Hilfsmittel, persönlichen Mitteilungen und Quellen angefertigt habe.

---

Ort, Datum

---

Aaron Reupert